Improved Performance of Solid Oxide Fuel Cell Operating on Biogas using Tin Anode-infiltration

by

Lina Troskialina

A thesis submitted to
The University of Birmingham
for the degree of

DOCTOR OF PHILOSOPHY

Chemical Engineering
School of Engineering
University of Birmingham
Edgbaston
Birmingham
B15 2TT

December 2015

Abstract

This work presents a novel method of Sn-infiltration on SOFC anodes for SOFC operation in biogas dry reforming. Using commercially available NiYSZ-based anode supported half cells with hand-painted LSM/YSZ cathode layers, Sn-infiltrated NiYSZ SOFCs containing different amounts of Sn were manufactured. These SOFCs were tested for their electrochemical performance and quantity of deposited carbon during operation on simulated biogas of 1:2 volume ratio of CO_2:CH_4 without humidification but with 25% Helium added to the feed stream to enable measurements of the fuel cell outlet gas composition using a quadrupole mass spectrometer. Most of the SOFCs were tested in biogas for 1 day (22 hours), but several cells were tested for 6 days (150 hours) to evaluate performance degradation. The electrochemical performance tests at 750 ^{o}C showed that with H_2 as fuel the non-infiltrated NiYSZ SOFCs were able to reliably generate a moderate level of current of 350 mA cm^{-2} at 0.7 V; however when simulated biogas was introduced, current dropped significantly to 90-200 mA cm^{-2}. Contrary to non-infiltrated cells, a series of Sn-infiltrated cells under the same operating conditions performed equally well both on H_2 and biogas producing 310 to 420 mA cm^{-2} at 0.7 V. Several cells showed stable electrochemical performance over 150 hours of operation both on H_2 and biogas. Using Temperature Programmed Oxidation (TPO), both Sn-infiltrated and non-infiltrated SOFCs showed low quantities of carbon formed during 22 hours operation on biogas. Visual observation and SEM images of the anode surface after 150 hours operation on biogas showed no sign of deposited carbon. The conclusion is that Sn-infiltrated NiYSZ-based SOFC can be operated on simulated biogas with significantly higher electrochemical performance and low carbon deposition, given the anode is adequately modified.

بسم الله الرحمن الرحيم

In The Name of Allah, The Most Beneficent, The Most Merciful

All the praises and thanks be to Allah, Who has sent down to His slave (Muhammad) the Book (the Qur'an), and has not placed therein any crookedness. (QS 18:1)

Say (O Muhammad to mankind). "If the sea were ink for (writing) the Words of my Lord, surely, the sea would be exhausted before the Words of my Lord would be finished, even if we brought (another sea) like it for its aid." (QS 18:109)

(Al-Qur'an, Surah 18. (Al Kahf) verses 1 and 109)

I dedicate this thesis for my family Inten, Kiyai, Hasan, Maryam, Kang Undang, my dearest parents, teachers, students, sisters and brothers

Acknowledgements

All praise is only Allah’s, the Lord of the Worlds, who had allowed me to conduct this study and finish the thesis.

I am grateful to my supervisors Prof. Robert Steinberger-Wilckens and Dr. Aman Dhir for their continuous supports, assistance and invaluable guidance during the final tough years of my study. Thank you also to Prof. Kevin Kendall and the late Dr. Waldemar Bujaski who had been my supervisors during the first few years of my study. Many thanks also to Prof. Tim Button and Dr. Mark Cassidy for their invaluable insight and knowledgeable advice for this thesis writing.

I would like to also thank the Directorate General of Higher Education (DGHE) of the Ministry of Education-Indonesia, and the European Projects for providing the scholarship for me to undertake and finish this study.

This study would not have been possible without the assistance of the administration and technical staffs at the University of Birmingham; namely Mrs Lynn Draper, John Hooper, Robert Sharpe, Paul Stanley, Theresa Morris, Jackie Deans, Steven Williams, Artur Majewski and Jong-Eun Hong. To them I am very grateful.

I would also like to offer my kindest thanks to my colleagues at the Fuel Cells and Hydrogen Research Centre for their supports and helps. Thank you, especially to Nikkia, James, Evan, Tony, Tom, Katie, Ghzzai, Anwar, Fabricio, Fatima, Yaxiang, Vikrant, Sophie, Anisa, Melissa, Putri and Sotiris, to name but a few. Finally, my huge thanks go to my children and husband who have given up their time, days and nights, in order for me to carry out the study and finish this thesis.

List of Publications

- L.Troskialina, A.Dhir, R.Steinberger-Wilckens, *Improved Performance and Durability of Anode Supported SOFC Operating on Biogas*, ECS Transactions, 68 (1) 2503-2513 (2015)
- T.-I. Tsai, L.Troskialina, A.Majewski, R.Steinberger-Wilckens, *Methane internal reforming in solid oxide fuel cells with anode off-gas recirculation*, International Journal of Hydrogen Energy (2015).

Table of Contents

CHAPTER 1 INTRODUCTION 1

1.1 Overview 2

1.2 Motivations 4

1.3 Thesis presentation 6

CHAPTER 2 SOFC OPERATION AND CARBON DEPOSITION 8

2.1 Overview 9

2.2 Solid Oxide Fuel Cells (SOFC) 9

2.2.1 Principle of operation 9

2.2.2 Cell components 14

2.2.3 Cell designs 18

2.2.4 SOFC performance and durability 20

2.3 Fuelling SOFC with hydrocarbons, minimising carbon deposition 29

2.3.1 Chemical reactions at SOFC anodes 29

2.3.2 The modes of reforming in SOFC operation 38

2.3.3 Biogas fuelled SOFCs 42

2.3.4 Modification of catalytic properties of SOFC anodes 57

CHAPTER 3 METHODS & MATERIALS 60

3.1 Overview 61

3.2 Materials 61

3.3 Methods 62

3.3.1 SOFC manufacturing steps 62

3.3.2 Electrochemical performance test 64

3.3.3 SOFC outlet gas monitoring using a quadrupole mass spectrometer 67

3.3.4 Temperature programmed oxidation 67

3.3.5 Anode materials characterisation 69

CHAPTER 4 ELECTROCHEMICAL PERFORMANCE BASELINE WITH HYDROGEN FUEL 72

4.1 Overview 73

4.2 SOFC test set-up 73

4.2.1 Cathode painting and sintering 74

4.2.2 Current collector attachment 74

4.2.3 The sealing of the SOFCs on to the cell holder 75

4.2.4 Observations on SOFC seals 77

4.2.5 SOFC heat-up 78

4.2.6 Sequence of electrochemical performance measurements 81

4.3 Mass spectra of SOFC outlet gases 84

4.4 Electrochemical performance 87

4.4.1 Prediction of electrochemical performance using fuel cell model 87

4.4.2 Measured electrochemical performance 89

4.5 Conclusions 100

CHAPTER 5 TIN-INFILTRATION ON SOFC ANODES 103

5.1 Overview 104

5.2 Overview of Ni/Sn alloy properties and applications 104

5.2.1 Ni/Sn phase diagram 104

5.2.2 Ni/Sn applications 106

5.3 Methods of Ni/Sn alloy formation 107

5.3.1 Previous studies, general methods of Ni/Sn alloy formation 107

5.3.2 Methods of Sn-anode infiltration 109

5.3.3 Characterisation of Sn precursor 114

5.3.4 Chemical reactions involved in the Sn-infiltration stages 116

5.4 Results 117

5.4.1 Gravimetric analysis of Sn-infiltrated SOFC anodes 117

5.4.2 Characterisation of Sn-infiltrated anode 120

5.5 Discussion & Conclusion 124

CHAPTER 6 DRY REFORMING OF BIOGAS ON SOFC ANODES 128

6.1 Overview 129

6.2 Method of dry reforming 129

6.3 Results 130

6.3.1 Anode reduction profile 130

6.3.2 Dry reforming on non-infiltrated anode supports 131

6.3.3 Dry reforming on Sn-infiltrated anode supports 135

6.4 Conclusions 139

CHAPTER 7 ELECTROCHEMICAL PERFORMANCE OF NON-INFILTRATED SOFC FUELLED BY BIOGAS 141

7.1 Overview 142

7.2 Mass spectra of the SOFC outlet gases 142

7.3 Electrochemical Performance 143

7.3.1 Prediction of electrochemical performance using fuel cell model 143

7.3.2 Measured electrochemical performance 145

7.4 Conclusions 154

CHAPTER 8 ELECTROCHEMICAL PERFORMANCE OF TIN-INFILTRATED SOFC FUELLED BY BIOGAS 156

8.1 Overview 157

8.2 Summary of electrochemical performance on H_2 157

8.3 Mass Spectra of SOFC outlet gases 158

8.4 Electrochemical Performance on Biogas 162

8.4.1 Prediction of electrochemical performance using fuel cell model 162

8.4.2 Measured electrochemical performance 164

8.1 SEM images 170

8.2 Summary of SOFC electrochemical performance 171

8.3 Conclusions 172

CHAPTER 9 CARBON DEPOSITION 176

9.1 Overview 177

9.2 Appearance of NiYSZ SOFC anodes **177**

9.2.1 Pre- and post-dry reforming in the quartz tube 177

9.2.2 Appearance of SOFC anodes post-test on biogas 179

9.3 TPO Results **181**

9.3.1 Carbon deposition from non-infiltrated SOFCs 181

9.3.2 Carbon deposition from Sn-infiltrated SOFCs 184

9.4 Discussion and conclusion **186**

CHAPTER 10 CONCLUSIONS & FURTHER WORK **189**

10.1 Overview **190**

10.2 Summary of Conclusions **190**

10.2.1 Establishing the electrochemical performance testing procedure 190

10.2.2 Sn- Anode infiltration 191

10.2.3 Electrochemical performance measurement with outlet gas monitoring 191

10.2.4 Carbon deposition 192

10.3 Main Points **193**

10.4 Further work **194**

REFERENCES **197**

List of Figures

Figure 1.1: Schematic diagram of a SOFC plant that utilises biogas from an anaerobic digester [16]..... 4

Figure 2.1: Operating principle of a solid oxide fuel cell [23] 10

Figure 2.2: A schematic diagram of an SOFC stack showing the stack, the cell, the electrode and location of the TPB [24]..12

Figure 2.3: A view of the 3D anode reconstruction of a tested cell showing the Ni (green), YSZ (grey) and pore (blue) phases [25] 13

Figure 2.4: A schematic diagram of an anode supported SOFC showing five layers including anode inter (functional) layer [32] 17

Figure 2.5: (a) Schematic diagram of Ceres Steel SOFC [14] and (b) materials used in the Ceres Steel SOFC [12] 19

Figure 2.6: Examples of micro tubular anode supported SOFCs (a) µSOFC of 5.5 cm length and (b) µSOFC of 15 cm length 20

Figure 2.7: A typical characteristic curve of an SOFC showing ideal and observed voltages..................27

Figure 2.8: Formation, transformation and gasification of carbon on nickel (a, g, s refer to adsorbed, gaseous and solid states respectively) [46, 47]..36

Figure 2.9: C-H-O ternary diagram at different operating temperature [69]..38

Figure 2.10: Carbon filaments formed on SOFC anode substrate post testing on simulated biogas (1:1 volume ratio of CO_2:CH_4) at 800 °C [129]...49

Figure 3.1: Main stages of SOFC preparation...63

Figure 3.2: SOFC anode side (left) and the ceramic double cylinder SOFC holder (right) 64

Figure 3.3: Step by step SOFC preparation process...64

Figure 3.4: SChematic diagram of the test rig (the diagram courtesy of N. McDonald)........................ 65

Figure 3.5: SOFC test rig with tunnel furnace; insert is the fuel inlet and outlet position.......................65

Figure 3.6: Mass Flow Controllers...66

Figure 3.7:C-H-O ternary diagram, red dot shows the position of the fuel used (CH_4:CO_2=2:1)............66

Figure 4.1: Various cases of seal misfunction and cell cracks at 750-800 °C operating temperature. 76

Figure 4.2: SOFC heat-up profile....79

Figure 4.3: Concentration of H_2 at fuel cell outlet obtained from Case A....85

Figure 4.4: Concentration of H_2 at fuel cell outlet obtained from Case B....85

Figure 4.5: Predicted polarisation curve obtained from Tsai's FCM simulation. 88

Figure 4.6: Measured OCV obtained from SOFC-A1 and SOFC-B1....90

Figure 4.7: Comparison of polarisation curves of Case A and Case B obtained in the lab and predicted by Nernst's equation.....92

Figure 4.8: Electrochemical performance of (a) SOFC-A1 and (b) SOFC-B1 95

Figure 4.9: Current produced at 0.7 V from SOFCs with Case A and Case B....97

Figure 4.10: EIS spectra at (a) OCV and (b) 0.7 V of SOFC-A1 (Case A) and B1 (Case B) 98

Figure 5.1: Ni/Sn phase diagram [157] 105

Figure 5.2: Temperature profile for calcinations of Sn-infiltrated SOFC anodes....110

Figure 5.3: Illustration of pipette-drop, sonic-immersion and powder-blend infiltration methods.....112

Figure 5.4: TG% and DTA of $SnCl_2.2H_2O$ at 10 °C min^{-1} heating rate 114

Figure 5.5: Weight of SnO_2 obtained after Sn infiltration on SOFC anodes 118

Figure 5.6: Weight percent of Sn/Ni in Sn-infiltrated SOFC anodes 119

Figure 5.7: XRD spectra of SOFC anodes, 6D SnNiYSZ and NiYSZ 121

Figure 5.8: (a) a cross sectional area of a reduced Sn-infiltrated NiYSZ cell showing part of the anode support, anode active and electrolyte layers and (b) anode surface showing Ni-rich and Zr-rich parts. 121

Figure 5.9: EDX map of the 6D-SnNiYSZ anode surface showing the distribution of Zr, Ni and Sn......122

Figure 5.10: X-ray fluorescence spectra of 28D-Sn-infiltrated anode....123

Figure 5.11: Schematic model of Sn-infiltration on SOFC anode....125

Figure 5.12: Ni/Sn phase diagram showing the expected Ni/Sn alloy phase which can be obtained from Sn-infiltrated SOFC anode 126

Figure 6.1: The rig configuration used for dry reforming of simulated biogas....130

Figure 6.2: Concentration of H_2 as anode reduction progresses....131

Figure 6.3: Mass spectra of outlet gases from dry reforming of 1:1 CO_2:CH_4 at 750 °C on non-infiltrated anode support 132

Figure 6.4: Mass spectra of outlet gases from dry reforming on non-infiltrated NiYSZ full cells at 650-800 °C..133

Figure 6.5: Percent conversion of CO_2 and CH_4 at 650 - 800 °C..134

Figure 6.6: Partl pressures of CO and H_2 produced at 650 - 800 °C..135

Figure 6.7: Mass spectra of outlet gases during dry reforming on 6D Sn-infiltrated NiYSZ full cell at 650 - 800 °C...136

Figure 6.8: Mass spectra of outlet gases during dry reforming on 4D Sn-infiltrated NiYSZ full cell at 800 °C and varied CO_2 : CH_4 ratio 137

Figure 6.9: Dry reforming product gas fraction on 4D Sn-infiltrated NiYSZ full cell at 800 °C and varied CO_2 : CH_4 ratio..138

Figure 6.10: Ratio of CO : H_2 on 4D Sn-infiltrated NiYSZ full cell at 800 °C and varied CO_2 : CH_4 138

Figure 7.1: Dry reforming product gas composition of the non-infiltrated SOFC-B1 at 750 °C 143

Figure 7.2: First and second FCM simulation results..145

Figure 7.3: Performance of SOFC-Bs compared with results obtained from two simulations 146

Figure 7.4: OCV of four SOFCs fuelled by biogas with OCV in H_2 as reference....................................148

Figure 7.5: Polarisation and power density curves of four SOFCs fuelled by biogas............................149

Figure 7.6: Current produced for 22 hours (at 0.7 V) from four SOFCs fuelled by biogas. 150

Figure 7.7: Current produced for 150 hours (at 0.7 V) from SOFC-B1 fuelled by biogas 151

Figure 7.8: EIS spectra of SOFC-B1 obtained in H_2 (26 hours) and biogas (22 hours) at OCV 152

Figure 7.9: SOFC appearance a) pre-test b) post-test and c) anode side post-22 h test on biogas......153

Figure 7.10: SEM images of SOFC-B3 pre- and post-22 hours test on biogas......................................154

Figure 8.1: Typical mass spectra of outlet gases of a Sn-infiltrated SOFC fuelled by biogas. 159

Figure 8.2: Partial pressures of SOFC outlet gases (a) CO at OCV, (b) CO at OCV and IV curve and (c) H_2 at OCV and IV curve measurements...161

Figure 8.3: Predicted polarisation curves obtained from three modes of simulation. 163

Figure 8.4: Measured vs. predicted polarisation curves of Sn-infiltrated and non-infiltrated SOFCs. .164

Figure 8.5: OCV values obtained from Sn-infiltrated SOFCs fuelled by biogas 165

Figure 8.6: Polarisation and power density curves of Sn-infiltrated SOFCs fuelled by biogas 166

Figure 8.7: Current density at 0.7 V from Sn-infiltrated SOFCs fuelled by biogas................................167

Figure 8.8: Current and power densities at 0.7 V of 10D-Sn-infiltrated SOFC fuelled by biogas 168

Figure 8.9: EIS Spectra at OCV of Sn-infiltrated SOFCs fuelled by biogas 169

Figure 8.10: SEM images of SOFC anode surface pre- and post-22 hours test on and biogas.............170

Figure 8.11: SEM images of SOFC anode surface pre- and post-150 hours test on H_2 and biogas.......171

Figure 8.12: Summary of current density at 0.7 V obtained from all of the tested SOFCs...................172

Figure 9.1: Appearance of catalysts before and after dry reforming in the quartz tube......................178

Figure 9.2: Appearance of SOFC anode surface post testing under dry reforming mode 180

Figure 9.3: SEM images of SOFC-10D-2 post-150 hours test on biogas (a) anode support (b) anode functional layer. 181

Figure 9.4: (a) The TPO reactor and (b) a known amount of graphite for TPO calibration 181

Figure 9.5: CO_2 peaks obtained from TPO calibration of standard carbon (graphite powder).............183

Figure 9.6: CO_2 peaks obtained from TPO of non-infiltrated SOFCs (SOFC-B1, B3 and B4)..................183

Figure 9.7: CO_2 peaks obtained from TPO of Sn-infiltrated SOFCs, first series...................................185

Figure 9.8: CO_2 peaks obtained from TPO of Sn-infiltrated SOFCs, second series..............................186

Figure 9.9: Results of DFT calculations of the rate of C-O, C-H and C-C bond formation on Ni and Sn/Ni surfaces [99]... 187

List of Tables

Table 1 Chemical reactions at SOFC anode [55]..31

Table 2 Forms and reactivities of carbon species on nickel catalyst [46] 36

Table 3 Summary of Literature on Performance of SOFCs fuelled by biogas..55

Table 4 Recent literature involving Ni-bimetallic catalysts and Sn for steam and dry (CO_2) reforming .59

Table 5 List of materials used..62

Table 6 List of sealing types used 76

Table 7 Qualitative results of SOFC sealing trials at 750-800°C operating temperature........................77

Table 8 Rating results of SOFC sealing trials at 750-800°C operating temperature 78

Table 9 Conditions of the two feed flow rates..83

Table 10 SOFC electrochemical performance operating on H_2 at 750 °C (26 hours) 96

Table 11 SOFC resistances obtained from EIS spectra of Case A and Case B 100

Table 12 Enthalpies of formation of different Ni/Sn phases [158]..106

Table 13 Methods of Ni/Sn alloy formation 108

Table 14 Observations of three infiltration techniques 113

Table 15 Proposed reactions occurring during calcinations, reduction and alloying 117

Table 16. Chemical composition of 28D-Sn-infiltrated SOFC anode obtained from XRF....................123

Table 17 Chemical composition of 28D-Sn-infiltrated NiYSZ anode obtained from XPS......................124

Table 18 Summary of Sn content in 28D-SnNiYSZ anode 126

Table 19 SOFC outlet gas composition, measured vs. prediction[#1] (at 750 °C) in equilibrium (OCV) ...144

Table 20 Summary of electrochemical performance on H_2..157

Table 21 SOFC outlet gas composition (in partial pressure), measured vs. prediction[#2] (at 750 °C) in equilibrium (OCV) 162

Abbreviations

AD-SOFC	Anaerobic Digester – Solid Oxide Fuel Cell
AFL	Anode Functional Layer
ALT	Accelerated Lifetime Testing
ASR	Area Specific Resistance
BCZYYb	$BaZr_{0.1}Ce_{0.7}Y_{0.1}Yb_{0.1}O_3$-delta
BSE	Back Scattered Electron
CGO	Ceria-doped Gadolinum Oxide
CHP	Combined Heat And Power
DOE-SECA	Department of Energy – Solid State Energy Conversion Alliance
DRT	Distribution Of Relaxation Time
DSC	Differential Scanning Calorimetry
DTA	Differential Thermal Analysis
EDX	Energy Dispersive X-Ray Spectroscopy
EIS	Electrochemical Impedance Spectroscopy
EMF	Electromotive Force
ER	External Reformer
ETEM	Environmental Transmission Electron Microscopy
f.c.c.	Face Centered Cubic
FCM	Fuel Cell Model
FIB-SEM	Focus Ion Beam-Scanning Electron Microscopy
GC	Gas Chromatography
LHV	Low Heating Value
LSCF	Lanthanum Cobaltite And Ferrite Perovskites
LSM	Lanthanum Strontium Manganite
MS	Mass Spectroscopy

MIEC	Mixed-Ionic-Electronic-Conductor
Mtoe	Mega Ton Electricity
NIMTE	Ningbo Institute Of Material Technology And Engineering
NiYSZ	Nickel-Yttria Stabilised Zirconia
OCV	Open Circuit Voltage
P-blend	Powder-blend
P-drop	Pipette Drop
QMS	Quadrupole Mass Spectrometers
SE	Secondary Electron
SEM	Scanning Electron Microscopy
S-imm	Sonic -Immersion
SOFC	Solid Oxide Fuel Cell
TEM	Transmission Electron Microscopy
TGA	Thermal Gravimetric Analysis
TPB	Triple Phase Boundary
TPH	Temperature Programmed Hydrogenation
TPO	Temperature Programmed Oxidation
XPS	X-Ray Photoelectron Spectroscopy
XRD	X-Ray Diffraction
XRF	X-Ray Fluorescence
YSZ	Yttria Stabilised Zirconia

Chapter 1

Introduction

1.1 Overview

Fuel cell technology is emerging as an attractive alternative to conventional methods of energy generation. Several of the attractive points of fuel cell technology are the lack of pollutant emissions such as NO_x, SO_x and particles, potential high efficiency operation, and the highly modular nature which allows for distributed power generation. However, much investment into research in this field is still needed to bring the costs of materials, manufacturing and infrastructure down [1-3].

The solid oxide fuel cell (SOFC) is one of several types of fuel cell which offer promising clean and efficient energy production with added benefit of being fuel flexible. Generally, SOFCs operate at 600-950 ^{o}C [4-7]. On one hand the high operating temperature nature of SOFC poses challenges with materials manufacturing and long term stability. On the other hand the high operating temperature of SOFC allows for direct use of methane and hydrocarbons through internal reforming, and is also beneficial for recovering heat as a by-product and operating as a combined heat and power (CHP) generator [4-8]. Recent developments in SOFC research have resulted in the capability of operating at lower temperatures of 500-750 ^{o}C which broadens the choice of materials and reduces the manufacturing costs [9-11]. Even low temperature SOFCs still operate at sufficiently high temperature to allow for some internal reforming of hydrocarbons to take place on SOFC anodes and for recovering heat [12, 13]. The state of the art SOFCs, the metal supported cell such as the Ceres Steel Cell stack, operate at 550 ^{o}C. The stacks have demonstrated the ability to turn on and off over 600 times with almost no loss of performance. The stack capacity ranges from 1 to 10 kW. Ceres develops the fuel cells and stacks for its partners to integrate into their power generation systems [14]. Fuelled with natural gas, to date Ceres Steel Cell demonstrated 0.12 kW kg^{-1} power and 47% net electrochemical efficiency in their prototype fuel cell stacks [13, 14]. The highest electrochemical efficiency achieved for SOFCs was obtained by the now defunct company, CFCL Ltd., who achieved 60% net electrochemical efficiency (LHV) and a total thermal efficiency of 85% [15].

The benefit of SOFC in being capable of utilising hydrocarbons as fuel is added especially when the hydrocarbons come from renewable sources. Several types of hydrocarbons are renewable fuels such as biogas or bio-methane generated from anaerobic digesters. Biogas contains mainly CH_4 and CO_2 in various compositions plus other impurities depending on the source of the biomass. Other forms of renewable fuels such as bio-ethanol and glycerol are also potential fuels for SOFC [16]. Utilisation of these renewable fuels in SOFC operation and integrating the SOFC system in a Combined Heat and Power (CHP) generation plan makes SOFC a strong option for low carbon power generation. In fact, recently, through an ongoing EU project coordinated by Politecnico di Torino, a biogas fuelled SOFC system was installed in a waste water treatment plant near Torino (Italy). The project is aimed to deliver a 175 kWe SOFC system that runs on biogas. The efficiency of the SOFC system is predicted to reach 60%. The system will provide clean water, thermal energy and electrochemical energy to the local community with zero emissions. Figure 1.1 represents the schematic diagram of the corresponding SOFC plant [17].

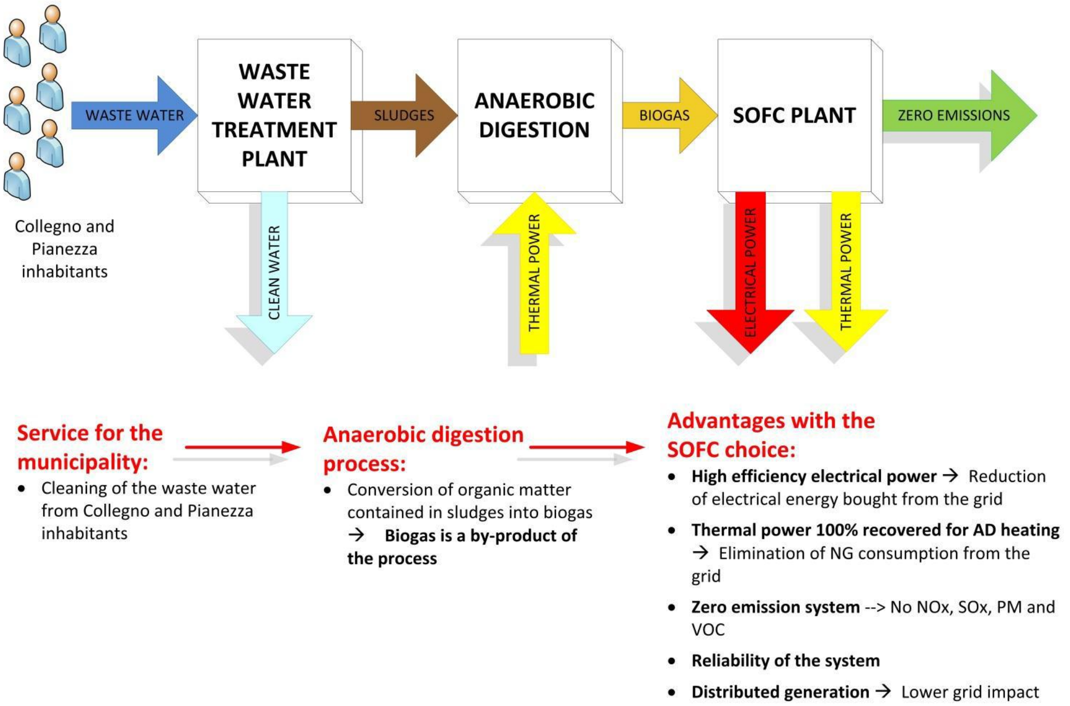

Service for the municipality:

- Cleaning of the waste water from Collegno and Pianezza inhabitants

Anaerobic digestion process:

- Conversion of organic matter contained in sludges into biogas → **Biogas is a by-product of the process**

Advantages with the SOFC choice:

- **High efficiency electrical power** → Reduction of electrical energy bought from the grid
- **Thermal power 100% recovered for AD heating** → Elimination of NG consumption from the grid
- **Zero emission system** --> No NOx, SOx, PM and VOC
- **Reliability of the system**
- **Distributed generation** → Lower grid impact

Figure 1.1: Schematic diagram of a SOFC plant that utilises biogas from an anaerobic digester [16]

1.2 Motivations

The increasing demand for energy and depleting fossil fuel resources need rigorous methods of energy generation. Within 25 years from 1989 to 2014 the world energy consumption increased by 62.5% from 8000 Mtoe to 13000 Mtoe [18]. Coal, oil, and natural gas comprise 85% of the primary sources of energy and nuclear, hydroelectricity and renewable energy comprised the remaining 15%. This global energy demand is predicted to increase by 60% over the next 30 years.

In terms of CO_2 emission, it is the way energy is converted from the primary source to electricity or heat which contributes most to CO_2 emissions. In the EU, 90% of CO_2 emissions are attributed to energy conversions. Therefore finding more efficient ways of supplying energy improves the world situation in many ways such as reducing greenhouse gas emission, postponing depletion of resources, avoiding expenses for energy import and securing regional growth, avoiding import dependencies and contributing to regional political stability [19] [20]

SOFC is an alternative technology for power generation with promising high efficiency and low environmental impact. In addition, the possibility of SOFC to operate on hydrocarbon fuels in internal reforming mode calls for a study of the possibility of operating SOFC fuelled directly by biogas. Biogas, which mainly consists of CH_4 and CO_2 is a product of anaerobic digesters processing wastes and biomass, for instance sludge from water treatment plants. Biogas is available worldwide but it is underutilised. In many cases biogas is just vented to the air contributing as greenhouse gas with a fourfold higher impact than CO_2, or it is utilised in power generation systems with combustion engines or micro turbines with only 20% to 35% electrical efficiency. The ability to fuel an SOFC system with biogas can lead to a substantial increase in efficiency and at the same time to reduction of the carbon footprint.

The challenge for SOFC operation with direct biogas fuel is the low power produced originating from the low heating value of the biogas and the possibility of carbon formation which always accompanies hydrocarbon reforming and can lead to accelerated SOFC performance degradation. Generally, carbon deposition is avoided by adding steam to the fuel feed with a ratio of 2 mole water to 1 mole carbon [21, 22]. This requirement of steam supply adds complexity to the SOFC system. To provide excess steam or carbon dioxide in the fuel feed, additional costs are incurred. Besides, overall fuel cell efficiency will be reduced. Therefore a careful balance should be considered in trying to reduce carbon formation while still keeping the SOFC electrochemical performance and overall efficiency acceptable. This study is aimed at investigating the ability of commercially available anode supported NiYSZ-based SOFC to operate on direct biogas under dry reforming mode (without the addition of steam) and to develop a method of modification of anode catalytic activity to improve the SOFC electrochemical performance and to minimise carbon formation.

1.3 Thesis presentation

This thesis has five major objectives as follows:

i. to establish a procedure for electrochemical performance testing of anode supported NiYSZ-based SOFC disc single cell,
ii. to develop a reliable technique for Sn-infiltration on NiYSZ-based SOFC anodes,
iii. to evaluate catalytic performance of the anodes in biogas dry reforming,
iv. to evaluate electrochemical performance of SOFCs and Sn-infiltrated SOFCs run in dry reforming mode of biogas,
v. to evaluate degradation rate and tendency to form carbon during electrochemical testing.

With the above five major objectives, this thesis is outlined into ten chapters. The first two chapters serve as introduction chapters which consist of Chapter 1 Introduction, and Chapter 2 SOFC Operation and Carbon Deposition. Chapter 3 Materials and Methods presents the materials and general experimental methods used. Parts of the electrochemical testing method are presented in Chapter 4 because the testing procedure is part of the investigation to establish reliable test results. Likewise, some details of the experimental methods for Sn-infiltration are presented in the Sn-infiltration chapter, Chapter 5, to provide a complete and uninterrupted explanation about Sn infiltration methods and material characterisation in one chapter.

The results chapter starts with Chapter 4 which describes the steps to establish a repeatable procedure for planar anode supported SOFC electrochemical testing on H_2. This is followed by Chapter 5 which describes the experimental steps and results of Sn-infiltration on SOFC anode. The subsequent chapter, Chapter 6, presents an evaluation of the SOFC anode catalytic performance in biogas dry reforming performed in a quartz tube; to evaluate the anodes' catalytic activity and the tendency for carbon formation without being influenced by electrochemical reactions.

The next two chapters, Chapter 7 and Chapter 8 describe the electrochemical performance of the non-infiltrated and Sn-infiltrated SOFCs fuelled by biogas under dry reforming mode. Chapter 9 presents collective results of qualitative and quantitative measurements of carbon deposition during SOFC operation, which covers carbon deposition during dry reforming in the quartz tube and during SOFC operations in biogas on non-infiltrated and Sn-infiltrated anodes. Finally Chapter 10 concludes all results of this study and presents several suggestions for future work.

Chapter 2

SOFC Operation and Carbon Deposition

2.1 Overview

This chapter is divided into two major parts; the first part describes the principle of operation of SOFC, the SOFC components and the SOFC electrochemical performance and durability. The second part describes the phenomena of carbon deposition on the anode surface of the SOFC which is observed in operating SOFC with hydrocarbon-based fuels in direct internal reforming.

2.2 Solid Oxide Fuel Cells (SOFC)

2.2.1 Principle of operation

Solid oxide fuel cells produce electricity from electrochemical reactions which readily take place on the electrodes of the cell. An SOFC consists of a dense electrolyte layer sandwiched between two electrode layers, a porous anode layer on one side and a porous cathode layer on the other side. A schematic diagram of a typical solid oxide fuel cell is given in Figure 2.1. Current collectors are attached on the anode and cathode ends. During cell operation, oxygen is reduced to an oxygen ion (O^{2-}) on the cathode side, while hydrogen as fuel is oxidized on the anode side producing H^+ ions (or protons) which further react with the incoming oxygen ion diffusing through the electrolyte to form water at the anode-electrolyte interface. Electrons generated on the anode side are transported through the current collectors and the external electrical circuit to the cathode side. This produces direct current or electricity.

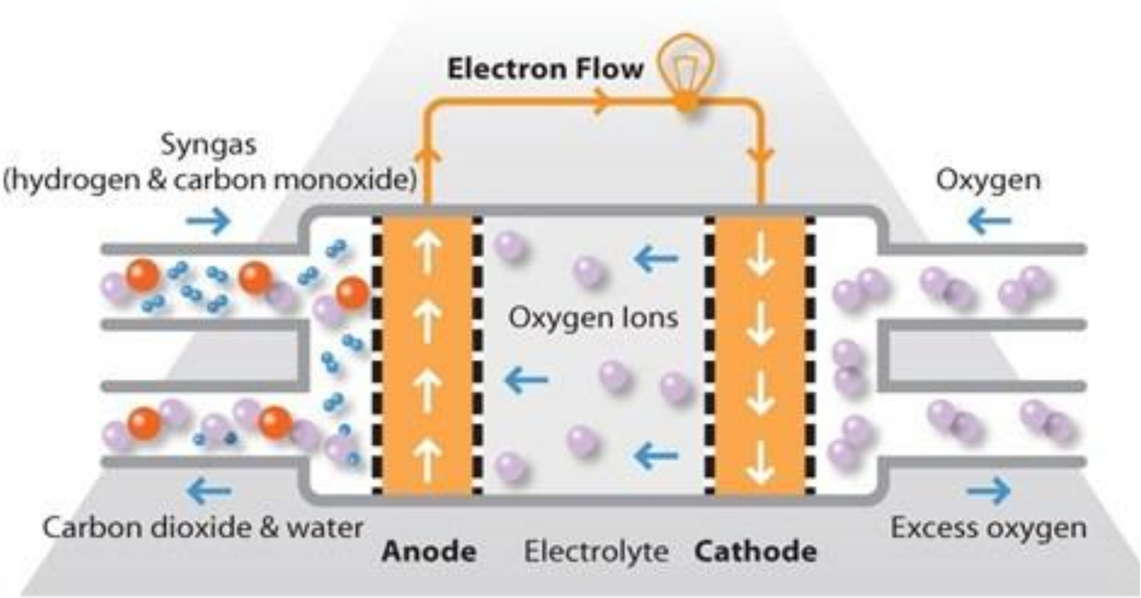

Figure 2.1: Operating principle of a solid oxide fuel cell [23]

Chemical reactions which occur in a H_2 fuelled solid oxide fuel cell can be simplified and represented as follows,

At the anode site	$H_2 + O^{2-}$	$\leftrightarrow$	$H_2O + 2e^-$	**Eq. 2.1**
At the cathode site	$\frac{1}{2} O_2 + 2e^-$	$\leftrightarrow$	O^{2-}	**Eq. 2.2**
Overall reaction	$H_2 + \frac{1}{2} O_2$	$\leftrightarrow$	H_2O	**Eq. 2.3**

In a hydrocarbon fuelled SOFC, the presence of CO and C as the products of methane reforming and cracking reactions in the anode creates an opportunity for CO and C electrochemical oxidation to also take place (Eq. 2.4 and Eq. 2.5). The extent to which CO and C can be oxidised depends on the specific properties of the SOFC components, especially that of the anode material, gas composition and the temperature of the SOFC operation. The oxidation reactions involving C and CO may be written as represented by Eq.2.6 and or Eq. 2.7 depending on the properties of the anode material in catalysing the electrochemical oxidation of C and CO. The extent to which these reactions can occur depends also on the electrolyte property in providing O^{2-}.

At the anode site

$$C + O^{2-} \leftrightarrow CO + 2\ e^- \qquad \textbf{Eq. 2.4}$$

$$CO + O^{2-} \leftrightarrow CO_2 + 2\ e^- \qquad \textbf{Eq. 2.5}$$

Overall reaction at the anode side

$$H_2 + C + 1\tfrac{1}{2}\ O_2 \leftrightarrow H_2O + CO_2 \qquad \textbf{Eq. 2.6}$$

or

$$H_2 + CO + O_2 \leftrightarrow H_2O + CO_2 \qquad \textbf{Eq. 2.7}$$

The above reactions occur at the anode triple phase boundary (TPB). The TPB is where three simultaneous physicochemical changes take place as follows:

i. H_2 molecules undergo electrochemical oxidation releasing 2 electrons,

ii. Oxygen ion being transported from the electrolyte layer combines with H^+ to form H_2O,

iii. Electrons from H_2 oxidation are transported via outer circuit.

For those three processes to take place, anode pores, Ni catalytic sites, YSZ as O^{2-} carrier and Ni metal as electron conductor should be in a very close and continuous contact with each other. The lines in the SOFC anode which allow for those three processes to occur are called the Triple Phase Boundary (TPB). Figure 2.2 represents a schematic diagram of a fuel cell stack, showing the stack, the cell, the electrode and location of the triple phase boundary (TPB) [24].

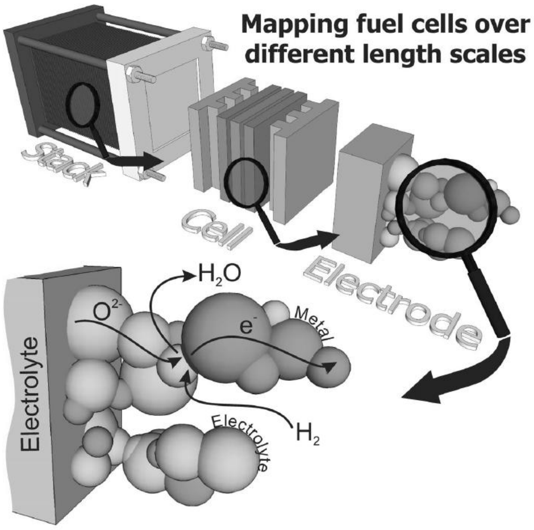

Figure 2.2: A schematic diagram of an SOFC stack showing the stack, the cell, the electrode and location of the TPB [24]

Figure 2.3 shows a 3D view of a NiYSZ anode structure obtained from a tested anode supported SOFC with the microstructure analysed using a dual beam focused ion beam-scanning electron microscopy (FIB-SEM) method [25]. Wilson et al. used the 3D image reconstruction process to calculate each phase volume fraction, TPB length and the pore tortuousity to evaluate the relationship between the manufacturing process, the microstructure obtained, and the SOFC electrochemical performance. From the 3D image reconstruction, they obtained the phase volume fractions of the Ni (green), YSZ (grey), and pores (blue) being 25.9%, 54.6% and 19.5% respectively. According to this work, the SOFC anode used for the FIB-SEM analysis was prepared from a 50:50 weight ratio NiO:YSZ. With a typical LSM composite cathode, operating at 800 ^{o}C and fuelled by $H_{2,}$ the cell produced 1.2 W cm^{-2}. Therefore the illustration of the 3D view in Figure 2.3 represents a typical working NiYSZ SOFC anode.

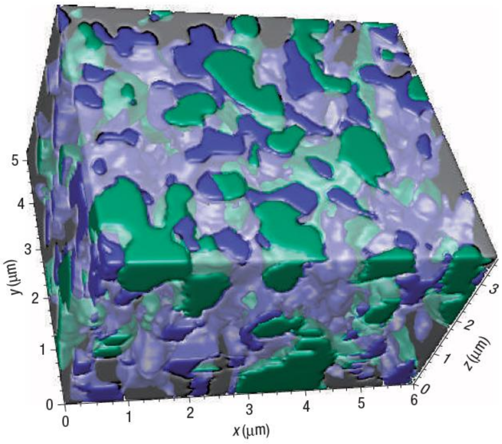

Figure 2.3: A view of the 3D anode reconstruction of a tested cell showing the Ni (green), YSZ (grey) and pore (blue) phases [25]

On the cathode side, similar physicochemical changes occur simultaneously as above but with the reverse order as follows:

i. Electrons from the anode side reach the cathode surface and are transported through the cathode to the electrolyte interface,
ii. At the cathode-electrolyte interface, electrons react with oxygen molecules and electrochemically reduce the oxygen to oxygen ions (O^{2-}),
iii. The oxygen ions produced then diffuse to the anode side through the electrolyte layer.

Because the two electrochemical reactions occur simultaneously, the lower rate between the two determines the overall reaction rate, generally this will be the reduction reaction.

2.2.2 Cell components

2.2.2.1 Electrolyte

An SOFC electrolyte functions as oxygen ion conductor connecting cathode and anode for ionic charge transport. The electrolyte should be dense to prevent fuel leaking from the anode to the cathode side. Ideally, an electrolyte does not conduct electrons; no electron should pass through the electrolyte thus causing an electrical short circuit. Following those requirements, the most important properties for oxygen ion conducting SOFC electrolytes are as follows [6, 9, 26, 27]:

i. able to conduct oxide ions (its structure having vacant O^{2-} sites within the lattice),
ii. dense, impermeable by gases
iii. having negligible electronic conductivity,
iv. having high stability under the required operating conditions,
v. stable within both reducing and oxidizing environments which are experienced at the anode and cathode interfaces, and
vi. having compatible thermal expansion coefficient and mechanical properties with those of the electrodes.

Zirconia doped with 8 mole % yttria (yttria stabilised zirconia – YSZ) is the most commonly used SOFC electrolyte for operation at high temperatures (700-850 ^{o}C). 10Sc/CeSZ scandia doped zirconia in principle displays an ionic conductivity one order of magnitude above that of 8YSZ. The Ce component also promise improved reforming abilities. Nevertheless, this material still poses some challenges in manufacturing anode supported SOFC cells [28]. Other electrolyte materials such as CeO_2 and $LaGaO_3$-based perovskites are attractive for low temperature SOFC (400-600 °C) and as electrolyte interlayer for intermediate temperature (600-700 °C) SOFCs with zirconia electrolytes [6, 26, 29]. Recently an electrolyte made of ceria/bismuth oxide bilayers having excellent high ionic conductivity enabled SOFC to operate at 650 °C with a high power density of 2 W cm^{-2} [9].

2.2.2.2 Cathode

The cathode serves as the oxygen reduction site and electronic conductor for the reduction of oxygen to an oxide ion (O^{2-}). Good cathodes should possess these characteristics [6, 26, 30] :

i. solid porous material with high electronic conductivity and optionally also good ionic conductivity,
ii. refractory, and compliant to thermal cycling to ambient temperature,
iii. enhanced catalytic activity for oxygen reduction,
iv. compatible in thermal expansion coefficient and mechanical properties with the electrolyte and interconnect materials, and
v. chemically stable in an oxygen rich environment.

Lanthanum deficient strontium doped manganite (LSM) is one of the most commonly used cathode materials [6, 26, 30] especially for high temperature SOFC. A mixture of LSM and YSZ is used to form a mixed-ionic-electronic-conductor (MIEC) to provide increased three phase boundary (TPB) length, and is used as a first cathode layer in contact with the YSZ electrolyte. A second layer of porous pure LSM is coated on top of this as a current collector layer to allow for electronic contact with the inter connector plates. For intermediate temperature SOFCs, lanthanum cobaltite and ferrite perovskites

(LSCF) are used as cathodes for its good ionic and electronic conductivities at 600-750 °C [6].

2.2.2.3 Anode

The anode in a solid oxide fuel cell serves to provide the sites for the fuel gas to react with the oxide ion delivered through the electrolyte, within a structure which also facilitates the necessary charge neutralisation by its electronic conductivity [31]. These functional considerations together with the operating environment of the anode are the key factors for the materials selection of the anode. A good anode should possess these characteristics:

i. solid porous material with high electronic conductivity and possibly good ionic conductivity,
ii. refractory, and compliant to thermal cycling to ambient temperature,
iii. enhanced catalytic activity for fuel oxidation,
iv. compatible in thermal expansion coefficient and mechanical properties with the electrolyte and interconnect materials,
v. chemically and physically stable under various compositions of fuel reactants and products during SOFC operation, and
vi. compliant to reduction and re-oxidation cycling during fuel cell operation

Nickel-zirconia cermets (NiYSZ) have been the most commonly used and investigated anode material. This NiYSZ is basically a mixture of around 50:50 wt % of green nickel oxide with YSZ powder, which is made into a slurry, ball milled, tape cast and dried, and sintered at a certain temperature. SOFC anodes are commonly produced in at least two layers, a thin anode functional layer (AFL) with fine microstructure and high surface area to maximise the electrochemical oxidations and a thick anode support layer with coarse particles to provide mechanical strength and current collection. Zhao and Virkar [32] did a study to investigate the effects of anode porosity and each SOFC layer's thickness on SOFC electrochemical performance. Figure 2.4 shows a schematic diagram of an anode supported SOFC with anode support and functional layers and cathode support and functional layers. It also shows an illustration of how partial pressures of H_2, H_2O change across the anode layers and that of O_2 changes across the cathode layers due to the electrochemical oxidation reactions which take place at the electrode-electrolyte interface.

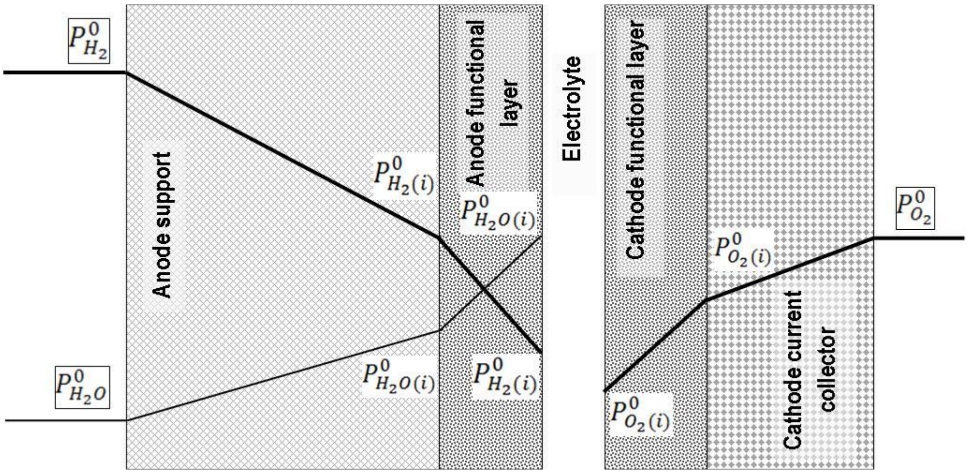

Figure 2.4: A schematic diagram of an anode supported SOFC showing five layers including anode inter (functional) layer [32]

2.2.2.4 Interconnects

The main function of the interconnect is to conduct electrons from one electrochemical cell to the next and then to the external circuit. Interconnect material should be highly electronically conducting, thermally stable under the high SOFC operating temperatures and rapid changes of temperature, and chemically stable under different and extreme partial pressures of the gases at cathode and anode [6, 27, 33]. For high temperature

SOFC, example of interconnect materials are magnesium doped lanthanum chromate and $LaSrCrO_3$-nickel foil. For lower temperature SOFCs, metallic alloys such as ‘inconnel’ type stainless steel has been used as interconnect.

2.2.3 Cell designs

SOFC designs are based around two primary geometries; planar and tubular, and are supported by one of the functional components (electrolyte, anode or cathode) or non-functional components (metal or ceramic supported). In planar cells, components are arranged in a flat orientation and are electrically connected in series [6, 26]. Figure 2.5a. shows a schematic planar cell design from Ceres Power [14] which represents a state of the art planar fuel cell design. Ceres uses ferritic stainless steel foil as the cell support, hence the term metal supported cell, with thick film ceramics deposited on the steel surface. The anode is a ceria-nickel cermet, the electrolyte is of gadolinium doped ceria and the cathode is a composite lanthanum perovskite. Because of the ceria-based electrolyte used, these SOFCs operate at a low temperature range of $500^{-}620$ ^{o}C [10].

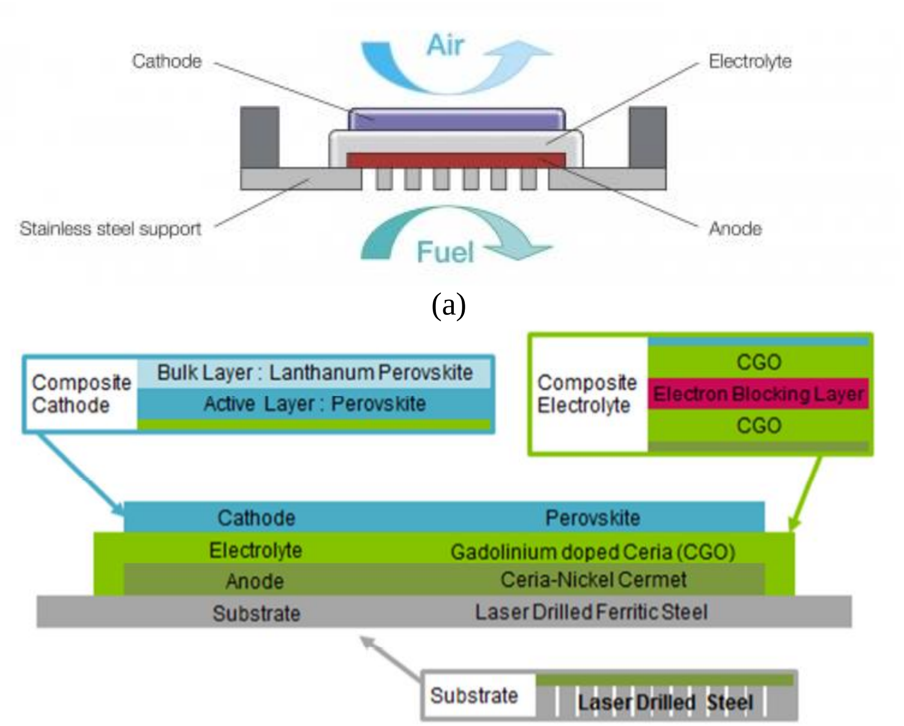

(a)

(b)

Figure 2.5: (a) Schematic diagram of Ceres Steel SOFC [14] and (b) materials used in the Ceres Steel SOFC [12]

Tubular cells can be in the forms of large tubes with >1.5 cm diameter and up to 200 cm length. They were initially developed by Siemens-Westinghouse. Small tubes or micro tubes (µSOFCs), which were initially developed by Kendall [6, 34], have 0.8-2.5 mm diameter and up to 5.5 cm length. Figure 2.6 shows pictures of two sizes of micro tubular SOFCs, the 5.5 cm long µSOFC showing electrolyte and LSM cathode surface with silver wire current collectors [35] and the 15 cm long µSOFC showing electrolyte layer and LSCF cathode showing reduced NiYSZ anode in the inner layer with transparent YSZ electrolyte and black LSM/LSCF cathodes on the outer layer.

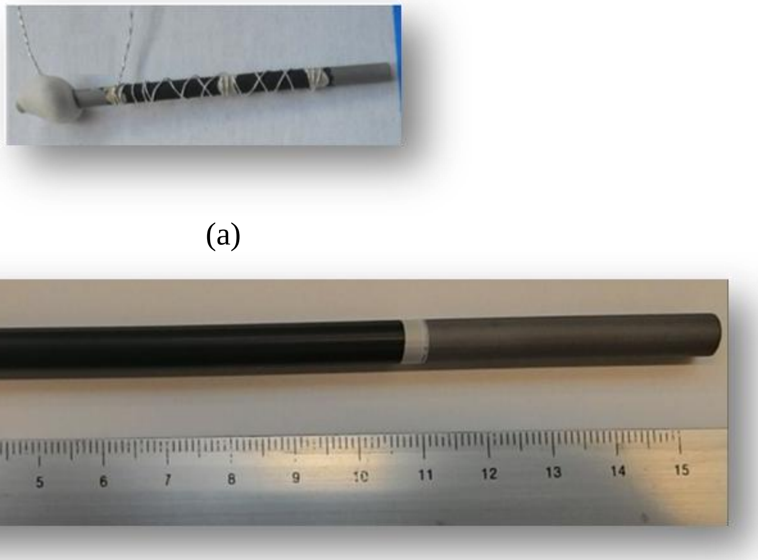

(a)

(b)

Figure 2.6: Examples of micro tubular anode supported SOFCs (a) μSOFC of 5.5 cm length and (b) μSOFC of 15 cm length

2.2.4 SOFC performance and durability

2.2.4.1 How much electricity can be obtained from a fuel cell?

Two electrons are involved in the formation of one molecule of water from one molecule of H_2. To form one mole of water from one mole of H_2, two moles of electron or 2N electrons pass around the external circuit, where N is Avogadro's number. If $-e$ is the charge of one electron, then the charge that flows per mole of H_2 oxidised is

$$-2\,Ne = -2F\ (Coulombs)$$

Eq. 2.8

If E is the voltage of the fuel cell, then the electrical work performed on passing the electrons across anode and cathode will be:

$$Electrical\ Work\ performed = Charge \times Voltage = -2F \times E$$ **Eq. 2.9**

Meanwhile the chemical energy available from the reaction depicted by Eq. 2.3, known as Gibbs free energy, can be obtained from the well-known relationship with enthalpy and entropy:

$$\Delta G_f^0 = \Delta H_f^0 - T\Delta S$$ **Eq. 2.10**

With Δ H_f being enthalpy of formation of one mole of H_2O from H_2 and ΔS being the entropy changes associated with the reaction.

If we assume that the reaction in the fuel cell is reversible (no energy losses) then all the Gibbs free energy is converted to electrical energy, thus:

$$-\Delta G_f = Gibbs\ free\ energy = Electrical\ Work\ produced$$ **Eq. 2.11**

$$-\Delta G_f^0 = -2FE^0$$

$$E^0 = \frac{-\Delta G_f^0}{2F}$$

Therefore the value of the standard potential E^o is determined by the Gibbs free energy of formation of the reaction (Eq. 2.3) at the corresponding temperature. For a reaction condition of pure H_2 and O_2 at 1 atmosphere provided at anode and cathode sides, the Gibbs free energy of formation of the reaction at 298 ^oC is -237.2 kJ mol^{-1}. The value is negative which means that energy is released during the reaction. Therefore E^o, the electromotive force (EMF) or reversible open circuit voltage (OCV), of a H_2 fuel cell operating at 25 ^{o}C (298 K) can be calculated as follows:

$$E^{o}_{298K} = 237.2 \text{ kJ mol}^{-1} / 2*(96485) = 1.23 \text{ V}$$

Similarly, using the values of $-\Delta G_f^{o}$ listed in Appendix A, E^{o} at 80 ^{o}C, 600 ^{o}C and 800 ^{o}C can be calculated as follows:

$$E^{o}_{353K} = 228.2 \text{ kJ mol}^{-1} / 2*(96485) = 1.18 \text{ V}$$

$$E^{o}_{873K} = 199.6 \text{ kJ mol}^{-1} / 2*(96485) = 1.03 \text{ V}$$

$$E^{o}_{1083K} = 188.6 \text{ kJ mol}^{-1} / 2*(96485) = 0.98 \text{ V}$$

However, what if the fuel is not pure H_2 but a mixture of H_2 and other (inert) gases and the oxidant is not pure O_2 but air? For this condition, it is known that for reaction Eq. 2.3

$$\Delta G_f = \Delta G_f^0 - RT \ \ln \frac{\left(P_{H_2} . P_{O_2}^{\frac{1}{2}}\right)}{P_{H_2O}} \qquad \textbf{Eq. 2.12}$$

Following **Eq. 2.11** and **Eq. 2.12** we obtain:

$$E = E^0 + \left(\frac{\mathrm{RT}}{2\mathrm{F}}\right) ln \left[\frac{P_{H_2} . P_{O_2}^{\frac{1}{2}}}{P_{H_2O}}\right] \qquad \textbf{Eq. 2.13}$$

With E, R, T, F and P being equilibrium potential, universal gas constant, absolute temperature, Faraday's constant (96485 C mol^{-1}) and gas pressure respectively.

Eq. 2.13 is known as Nernst equation. In principle, according to thermodynamics explained above, the EMF of a H_2 fuel cell at a condition other than standard temperature and pressure can be calculated using Eq. 2.13.

In practice, other factors also contribute to how much electricity can be obtained from a fuel cell. These are factors relating to the rate of reactions taking place both at anode and at cathode sides. The molar rates of fuels undergoing oxidation reactions at the anode, and that of oxygen undergoing reduction reaction at the cathode depend on the design and physicochemical properties of the reactor (or the fuel cell) materials where these reactions take place. The presence of a high partial pressure of H_2 at the anode alone would not produce much electricity if this H_2 is not being sufficiently oxidised. Thus anodes need to play a role as a catalyst for H_2 electrochemical oxidation. The same case with O_2 at the cathode side; O_2 needs to be reduced at the cathode side at a compatible rate with the rate of H_2 oxidation. The electrolyte should be able to transport anions (or cations) at a comparable rate with the rate of oxidation and reduction reactions. Finally, the current collectors should also be able to transfer electrons at an equivalent rate to the other reactions. The kind of properties which should be demonstrated by these SOFC components to obtain maximum electricity generated from an SOFC operation is already explained in the previous section.

2.2.4.2 SOFC efficiency

In this sub-section, SOFC performance is explained in terms of thermal efficiency, voltage efficiency, net efficiency and power density. For ease of calculation, it is assumed that the overall reaction which occurs in the fuel cell is as written in equation Eq. 2.3, with cell standard potential being 1.18 V [4, 5], and that 100% reactants undergo electrochemical reaction to produce electricity (fuel utilisation is 100%).

Thermal efficiency of a fuel cell conversion device is the ratio of the amount of useful energy produced (=change of Gibbs free energy, ΔG) relative to enthalpy change (ΔH) between product and reactants [4]. For an ideal fuel cell with overall reactions written in Eq. 2.3, using Nernst equation and published thermodynamic data of ΔG^o and ΔH^o, at standard pressure and temperature,

$$\Delta G^0 = 237.1\ kJ\ mol^{-1}\ and\ \Delta H^0 = 285.8\ kJ\ mol^{-1},$$

$$therefore, \qquad \eta_{ideal\ thermal} = \frac{\Delta G^0}{\Delta H^0} = \frac{237.1}{285.8} = 0.83 \qquad \textbf{Eq. 2.14}$$

Calculation of thermal efficiency for an actual fuel cell needs to include values of actual changes of enthalpies of reactants and products, which are not easy to measure. For convenience, the so called voltage efficiency is used. Voltage efficiency is expressed in terms of the ratio of the operating cell voltage to the ideal voltage. Voltage of an actual fuel cell can be easily measured. The actual cell voltage is usually less than ideal because of losses associated with cell polarisation and ohmic losses. By utilising simple calculation, ‘corrected’ voltage efficiency or an actual efficiency can be obtained as follows:

$$Voltage\ Efficiency, \eta_{\text{voltage}} = \frac{V_{actual}}{V_{ideal}} \qquad \textbf{Eq. 2.15}$$

$$\text{according to Eq. 2.9 at STP} \quad \mathrm{V}\,ideal\ = 1.23\,V$$

$$\text{and that actual efficiency, } \eta_{\text{actual}} = \eta_{\text{ideal thermal}} \times \eta_{\text{voltage}} \qquad \textbf{Eq. 2.16}$$

Therefore we can obtain a relationship between efficiency and actual cell voltage as follows:

$$\eta_{\text{actual}} = 0.83 \text{ x } V_{\text{actual}}/V_{\text{ideal}} = 0.83 \text{ x } V_{\text{actual}}/1.23 = 0.68\ V_{\text{actual}}$$

When fuel utilization is not 100%, which is always the case in practice, then the cell efficiency is further reduced. For example, for an SOFC operating at optimistic 80% fuel utilisation (20% fuel is not converted), and voltage of 0.7 V, the net efficiency is 38.1%, as shown by a simple calculation below

$$\text{For } V_{actual} = 0.7\ V,$$

$$\eta_{\text{net}} = \eta_{actual} \times U_f = 0.68 \times 0.7 \times 0.80 = 38.1\% \qquad \textbf{Eq. 2.17}$$

It was shown that the calculation of cell efficiency involves several parameters such as Gibbs free energy, enthalpy changes, actual cell voltage, and fuel utilisation, and that net efficiency of a typical fuel cell operating at low temperature is usually less than 40%. However, since SOFCs operate at high temperature and involve exothermic reactions, it is advantageous for an SOFC system to be built and integrated with other power co-generators to recover the heat and to utilise the un-reacted fuel. In this way, overall SOFC efficiency increases significantly.

SOFC performance may also be expressed in terms of cell power density. This is usually taken as maximum power density which is obtained by plotting voltage and power, on the same graph, against the current density of an SOFC performance testing.

Overall performance of an SOFC is best represented by a characteristic I-V-curve such as presented in Figure 2.7. In Figure 2.7, two cases of efficiency and power density are illustrated, showing increasing voltage and efficiency loss as a fuel cell is operated from low to high current output [4, 36]. The voltage loss can be divided into three regions, at zero current, at relatively low current and at high current. At zero current or at open circuit voltage (OCV) to low currents where $V = E^o$ and the cell is in equilibrium, the voltage loss is associated with the activation losses which is further related to the kinetics of the charge. At medium current, the loss is proportional to the ohmic losses associated with electronic conduction through the various interconnects and the material of the electrodes. At high current, voltage loss is associated with mass transfer or concentration polarisation which is caused by depletion of the fuel and an imbalance between fuels supplied and charge transport as prescribed by the current drawn, due to rapid electrochemical reactions.

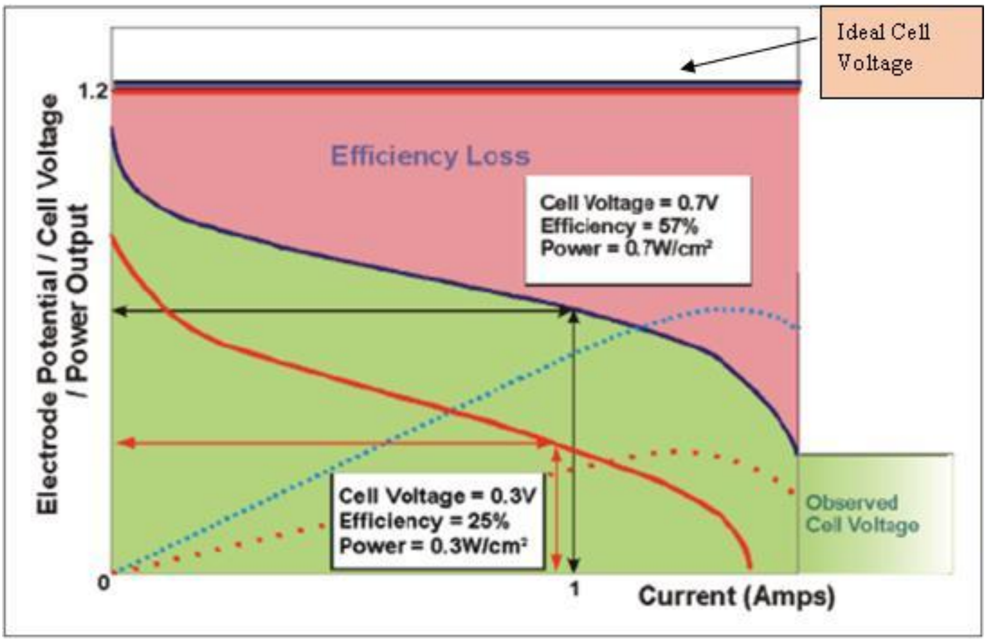

Figure 2.7: A typical characteristic curve of an SOFC showing ideal and observed voltages

2.2.4.3 SOFC durability

The high temperature of SOFC operation exposes cell components to harsh conditions, such as rapid change of temperature, possibility of feed fuel interruptions (fuel shortage) hence anode re-oxidation, and impurities carried in or produced as by-products of hydrocarbon fuel reactions. The occurrence of those interruptions may lead to physical or chemical changes, such as thermal expansion and shrinkage, particle agglomeration, building up of deleterious by-products, cracking and delamination across SOFC components. During the course of SOFC operation, each of these processes can slowly or rapidly lead to the degradation of SOFC performance [34, 35, 37, 38]. These degradation processes have to be minimised and avoided at some stage of SOFC design, operation and maintenance in order to achieve durable SOFC.

Accelerated Lifetime Testing (ALT) is one possibility to evaluate the durability of SOFCs. There are different methods of ALT testing; current cycling, thermal cycling, redox cycling and tolerance to poisoning by fuel impurities or deleterious by-products. By applying ALT an SOFC cells or stacks can be tested in a shorter time period to evaluate its durability against various harsh operating conditions. The following sub-sections briefly explain the SOFC durability testing conditions.

Current or load cycling is a testing condition when the current output of an SOFC is cycled from high to low load. A high current cycling can induce microstructural and chemical changes in SOFC components which may cause degradation. Heneka and Ivers-Tiffee [39] observed that electrolyte supported SOFCs with NiYSZ anode, ScSZ electrolyte and LSM cathode operated at 950 ^{o}C and subjected to several rapid and high current cyclings suffered from chemical and microstructural changes which caused cathode-electrolyte delamination.

Thermal cycling is a testing condition when SOFC components are subjected to rapid changes in temperature, such as rapid heating from room temperature to, for example, 800 ^{o}C, or vice versa, which may lead to cracking and fuel cell failure [37].

Redox cycling is a testing condition when an SOFC is subjected to partial oxidation caused by disruption in fuel supply, or emergency system shutdown, which leads to the loss of reduced condition at the anode and subsequent re-oxidation and with changes of anode microstructure eventually causes cell degradation and failure [38, 40-43].

Developments of redox-stable SOFCs by electrode infiltrations and by using metal supported cells [10, 11] have shown much improved redox stability of anodes.

Poisoning and fouling by fuel impurities such as sulphur and halide compounds and by products especially carbon deposits, is becoming very important nowadays as efforts to directly feed SOFC with natural gas, bio gas or other hydrocarbons as fuel are increasing.

2.3 Fuelling SOFC with hydrocarbons, minimising carbon deposition

2.3.1 Chemical reactions at SOFC anodes

The phenomena of solid carbon formation on metal surfaces exposed to hydrocarbons have been widely studied in the fields of catalysis and dry corrosion [44-53]. In general iron-based alloys and nickel-based materials undergo carburisation and carbon deposition when exposed to high carbon activity and low oxygen potentials at high temperatures. Therefore it is well expected that carbon deposits, coke or soot be formed on Ni-based SOFC anode surface fuelled by hydrocarbon-based fuels, such as methane, ethane, propane, natural gas, syngas, biogas, or other forms of hydrocarbon fuels.

How does carbon form in an SOFC? Consider the reactions occurring in the SOFC anode compartments where porous Ni based ceramic material is commonly used. Let us take methane, the simplest form of hydrocarbon, as an example of the fuel fed into an SOFC operating at 650-850 ^{o}C. On the anode side, where methane is fed, methane will undergo several reactions such as methane cracking or pyrolysis, dry reforming, steam reforming, or partial oxidation which will also be accompanied by various other reactions among the products of the initial reactions. These reactions start to take place at temperatures around 400 ^{o}C [54].

The main reactions taking place will be strongly determined by the temperature and the composition of the gases present in the system. Several reactions can take place simultaneously. The following section discusses these reactions in more detail. Table 1 presents a list of possible reactions with corresponding thermodynamic data which may occur in an anode of solid oxide fuel cells [55].

The first group of reactions is endothermic methane reforming which produces carbon mono- (or di-) oxide and hydrogen and water; these reactions can be of steam reforming type, or dry reforming or water gas shift reaction depending on the exact composition of gases present at the anode. These reactions preferably take place at temperatures above 650 ^{o}C.

The second group is the highly exothermic partial or complete chemical oxidation of methane. Considering their highly negative Gibbs free energy values and large equilibrium constants, these reactions can take place quite readily in the anode compartment. The reactions can take place even when there is only a trace of oxygen present in the anode compartment. However, when the SOFC gas feed does not contain oxygen and is completely sealed from traces of air leaking into the fuel compartment, these reactions are unlikely to occur.

Table 1 Chemical reactions at SOFC anode [55]

Chemical reactions				Thermodynamic data at different temperatures					No.
				Parameters	600 °C	700 °C	800 °C	900 °C	
CH_4 + H_2O	←→	$CO + 3H_2$	partial steam reforming	ΔH ($kJ\ mol^{-1}$)	211.55	211.01	210.01	208.71	**Eq. 2.18**
				ΔG ($kJ\ mol^{-1}$)	13.07	-9.64	-32.27	-54.79	
				Kp	$1.65x10^{-1}$	3.30	$3.72x10^{1}$	$2.75x10^{2}$	
				E^o (V)	-0.07	0.05	0.17	0.28	
$CH_4 + 2\ H_2O$	←→	$CO_2 + 4H_2$	complete steam reforming	ΔH ($kJ\ mol^{-1}$)	175.11	175.63	175.74	175.45	**Eq. 2.19**
				ΔG ($kJ\ mol^{-1}$)	6.47	-12.88	-32.26	-51.63	
				Kp	$4.1\ x10^{-1}$	4.91	$3.72x10^{1}$	$1.99x10^{2}$	
				E^o (V)	-0.03	0.07	0.17	0.27	
$CH_4 + CO_2$	←→	$2CO + 2H_2$	dry reforming	ΔH ($kJ\ mol^{-1}$)	260.25	260.49	260.421	260.04	**Eq. 2.20**
				ΔG ($kJ\ mol^{-1}$)	4.60	-23.82	-52.25	-80.66	
				Kp	0.54	17.6	300.3	$3.24x10^{3}$	
				E^o (V)	-0.024	0.12	0.28	0.40	
$CO + H_2O$	←→	$CO_2 + H_2$	Water Gas Shift Reaction	ΔH ($kJ\ mol^{-1}$)	-36.43	-35.36	-34.29	-33.24	**Eq. 2.21**
				ΔG ($kJ\ mol^{-1}$)	-6.60	-3.24	0.01	3.154	
				Kp	2.48	1.49	$9.99x10^{-1}$	$7.24x10^{-1}$	
				E^o (V)	0.03	0.02	0.00	-0.02	
Partial and complete Oxidations									
$CH_4 + ½\ O_2$	←→	$CO + 2H_2$	partial oxidation	ΔH ($kJ\ mol^{-1}$)	-19.54	-17.36	-15.17	-12.87	**Eq. 2.22**
				ΔG ($kJ\ mol^{-1}$)	-196.07	-216.41	-236.97	-257.74	
				Kp	$5.37x10^{11}$	$4.14x10^{11}$	$3.43x10^{11}$	$3.00x10^{11}$	
				E^o (V)	1.02	1.12	1.23	1.34	
$CH_4 + O_2$	←→	$CO + H_2 + H_2O$	partial oxidation	ΔH ($kJ\ mol^{-1}$)	-261.70	-258.73	-255.36	-251.44	**Eq. 2.23**
				ΔG ($kJ\ mol^{-1}$)	-399.12	-415.02	-431.25	-447.81	
				Kp	$7.54x10^{23}$	$1.90x10^{22}$	$9.80x10^{20}$	$8.70x10^{19}$	
				E^o (V)	1.03	1.08	1.12	1.16	
$CH_4 + 2O_2$	←→	$CO_2 + 2H_2O$	complete oxidation	ΔH ($kJ\ mol^{-1}$)	-784.56	-778.96	-772.12	-763.95	**Eq. 2.24**
				ΔG ($kJ\ mol^{-1}$)	-807.78	-810.74	-814.33	-818.62	

				Kp	2.12x10^{48}	3.30x10^{43}	4.35x10^{39}	2.82x10^{36}	
				E^{o} (V)	1.05	1.05	1.05	1.06	
Carbon deposition									
CH_4	**←→**	$C + 2H_2$	pyrolysis or cracking	ΔH (kJ mol^{-1})	87.88	89.11	90.10	90.92	**Eq. 2.25**
				ΔG (kJ mol^{-1})	-5.57	-16.34	-27.23	-38.20	
				Kp	2.16	7.54	2.12x10^{1}	5.03x10^{1}	
				E^{o} (V)	0.014	0.04	0.07	0.10	
$CO + H_2$	**←→**	$C + H_2O$	reverse carbon gasification	ΔH (kJ mol^{-1})	-135.79	-135.96	-135.97	-135.82	**Eq. 2.26**
				ΔG (kJ mol^{-1})	-10.38	4.00	18.38	32.76	
				Kp	4.18	6.10x10^{1}	1.27x10^{-1}	3.48x10^{-2}	
				E^{o} (V)	0.05	-0.02	-0.10	-0.17	
2CO	**←→**	$CO_2 + C$	Boudouard reaction	ΔH (kJ mol^{-1})	-172.22	-171.32	-170.26	-169.07	**Eq. 2.27**
				ΔG (kJ mol^{-1})	-16.97	0.76	18.39	35.92	
				Kp	1.04x10^{1}	9.11x10^{-1}	1.27x10^{-1}	2.52x10^{-2}	
				E^{o} (V)	0.088	-0.00	-0.10	-0.19	

The third group of reactions are carbon producing reactions, of which endothermic methane pyrolysis or cracking (Eq.2.25) is very important; this is essentially decomposition of methane to produce solid carbon and hydrogen. Pyrolysis reactions take place at temperatures higher than 600 ^{o}C and become more favourable at higher temperatures. The other carbon producing reactions which may occur at 600 ^{o}C to 700 ^{o}C are reverse carbon gasification or carbon monoxide reduction (Eq. 2.26) and carbon monoxide disproportionation (Eq. 2.27). Eq.2.27 is also known as Boudouard reaction. The values of ΔH, ΔG, and Kp in Table 1 show that temperature plays a very important role in determining which reactions are favoured at a certain condition. At temperatures below 700 ^{o}C all three carbon forming reactions are favoured. Therefore, for an SOFC operating at 550-700 ^{o}C, since ΔG values are negative, all three carbon forming reactions may take place. However, at temperatures higher than 700 ^{o}C the reverse carbon gasification and Boudouard reaction are not favourable, therefore for an SOFC operating at 750-850 ^{o}C, the most probable source of carbon deposition is methane pyrolysis or cracking.

Besides all the reforming and carbon forming reactions, the desired reactions to take place and produce electricity in the SOFC are the electrochemical oxidations of fuels. Of course the main electrochemical oxidation taking place in a hydrocarbon fuelled SOFC is the electrochemical oxidation of hydrogen. In addition, CO and C as the products of the reforming reactions are also likely to undergo electrochemical oxidation Eq.2.4 and Eq.2.5 [56, 57], provided that the SOFC anode poses the catalytic activity for that carbon oxidation. It is argued that 1) CO is readily converted to CO_2 and H_2 via fast Water Gas Shift reaction, and 2) the rate of electrochemical oxidation of CO and C are relatively slow compared to that of H_2, therefore in calculation or modelling studies, H_2 is usually the only fuel component considered to undergo electrochemical oxidation [58]. There is a twofold advantage when the anode in the SOFC is capable of electrochemically oxidising CO and C with a comparable rate to the electrochemical oxidation of H_2, the first is from improvement of electrical power and the second is from lowering carbon deposition.

2.3.1.1 Mechanism of carbon deposition

The formation of solid carbon on an SOFC anode surface can lead to various consequences ranging from partial coverage of active catalytic surface [44, 59], anode pore blockage or a complete blockage of anode channel in a microtubular SOFC operating with 100% CH_4 [60]. All those conditions can contribute to a mild to severe cell degradation and even cell failure. However, in the case of formation of a small amount of graphitic carbon, enhancement of electrochemical performance was observed [35, 61, 62]. In this section the types of carbon deposited and how carbon deposition occurs in the catalysts for steam reforming of hydrocarbons are outlined to provide a background to understanding the carbon deposition in SOFC operation.

In steam or dry reforming reactors, at a temperature range of 600-900 ^{o}C, as presented in Table 1 thermodynamics predict the formation of carbon from decomposition of CH_4, CO reduction by H_2 (or reverse carbon gasification,) and CO disproportionation (Boudouard reaction). On nickel catalysts the carbon formed can lead to the formation of carbon whiskers which involves several intermediate steps including dissociative adsorption of hydrocarbon, nucleation of highly reactive carbon atom (C_α), diffusion and dissolution of the adsorbed carbon atoms in the nickel crystal and nucleation of the whiskers from the Ni surface [46, 63]. Some carbon atoms do not diffuse or dissolve into nickel particles but form carbon polymers, films (C_β) or filaments which encapsulate the nickel particles. Accumulation of this type of carbon (C_β) may lead to deactivation of the nickel catalytic activity. C_β is less reactive than C_α, therefore harder to gasify and tend to accumulate [51]. Other types of carbon deposits are vermicular filaments (C_V) and graphitic crystalline platelets (C_C). The different forms of deposited carbon with different reactivities are presented in Table 2 [46].

The proposed steps of carbon formation from the endothermic CH_4 decomposition and from the exothermic CO disproportionation are outlined in the diagram in Figure 2.8 [46, 47]. Factors which affect carbon formation on catalyst surface are numerous. The catalysts, catalyst supports, temperature, pressure and the gas composition are among the factors which affect the type and severity of carbon formation [48-51, 64]. The presence of other metals along with the Ni catalyst, the types of oxide compounds in the catalyst support or the presence of an inhibiting agent, such as carbonyl sulphide in a gas mixture can also affect the rate of carbon formation [47-53, 65-67]. Among the steps of carbon formation on catalyst surface, the first step, the dissociative adsorption of hydrocarbon is considered the rate limiting step [51], therefore the presence of the catalyst sites which are active for the adsorption of hydrocarbon plays an important role in the process of carbon formation. However, in different environment of catalyst surface, such as in steam reforming over noble metal surface, carbon diffusion and dissolution may be the rate limiting step. The rate of whisker carbon formation on noble metals was found to be much less compared to that on nickel; this is attributed to the carbon formed being less easily dissolved on the noble metals [64].

$$CH_4 \rightarrow C_{\alpha\,(a)} + 4H_{(a)}$$

$$\begin{array}{lllll} CO_{(a)} & \rightarrow & C_{\alpha\,(a)} + O_{(a)} & & \\ C_{\alpha\,(a)} & \rightarrow & \text{C in Ni} & \rightarrow & C_v \\ & \rightarrow & Ni_3C_{(s)} & & \\ & \rightarrow & C_{\beta\,(s)} & \rightarrow & C_{c\,(s)} \end{array}$$

Figure 2.8: Formation, transformation and gasification of carbon on nickel (a, g, s refer to adsorbed, gaseous and solid states respectively) [46, 47]

Table 2 Forms and reactivities of carbon species on nickel catalyst [46]

Structural type	Designation	Temperature of formation (°C)	Peak temperature (°C) for reaction with H_2
Adsorbed, atomic (surface carbide)	C_α	200-400	200
Polymeric, amorphous films or filaments	C_β	250-500	400
Vermicular filaments, fibres or whiskers	C_V	300-1000	400-600
Nickel carbide (bulk)	C_γ	150-250	275
Graphitic (crystalline) platelets of films	C_C	500-550	550-850

With regards to the temperature of formation such as listed in Table 2, in SOFCs operating with hydrocarbon fuels, amorphous filaments, C_β, vermicular filaments, C_V, or graphitic crystalline platelets, C_C, are the most probable carbon forms.

2.3.1.2 C-H-O ternary diagram

The phenomena of carbon deposition can be explained in terms of a ternary diagram representing the composition of carbon, hydrogen and oxygen in the mixture as represented in Figure 2.9 [68-70]. With reference to the diagram in Figure 2.9, carbon is formed in the carbon rich region where % C (s) > 10^{-6} % C. Using this C-H-O diagram, it can be predicted whether carbon will be formed in a specific SOFC operating conditions. This ternary C-H-O diagram also helps to explain the concept of minimising carbon formation by adding excess H_2O or CO_2. Reaction-wise, the presence of excess H_2O or CO_2 in the SOFC enhances carbon steam gasification and reverses Boudouard reaction, hence inhibit carbon formation. Viewed in the ternary C-H-O diagram, adding H_2O or CO_2 shifts the position of the gas composition away from the 'carbon deposition region' towards the 'no carbon deposition region'. Another way of representing a condition with regards to carbon deposition is by calculating carbon activity. Carbon activities from reactions described in Eq. 2.25, Eq. 2.26 and Eq. 2.27 are represented by equations Eq. 2.28, Eq. 2.29, and Eq. 2.30 as follows [22]:

$$\alpha_{c,\mathrm{CH}_4} = K_2 \frac{p_{\mathrm{CH}_4}}{{p_{H_2}}^2}$$ **Eq. 2.28**

$$\alpha_{c,CO-H_2} = K_3 \frac{p_{CO} p_{\mathrm{H}_2}}{p_{H_2O}}$$ **Eq. 2.29**

$$\alpha_{c,\mathrm{CO}} = K_1 \frac{p_{CO}^2}{p_{CO_2}}$$ **Eq. 2.30**

Where K_1, K_2, K_3 represent the equilibrium constant of reactions Eq. 2.25, Eq. 2.26 and Eq. 2.27 respectively. It is defined that if $\alpha = 1$ the system is in equilibrium and no carbon is formed, whereas if $\alpha > 1$ the system is not in equilibrium and carbon is formed. Thermodynamically any condition with H_2O/CH_4 ratio > 1 will prevent carbon formation. In practice a minimum of 2:1 steam to carbon ratio (H_2O/CH_4) is needed to prevent carbon formation.

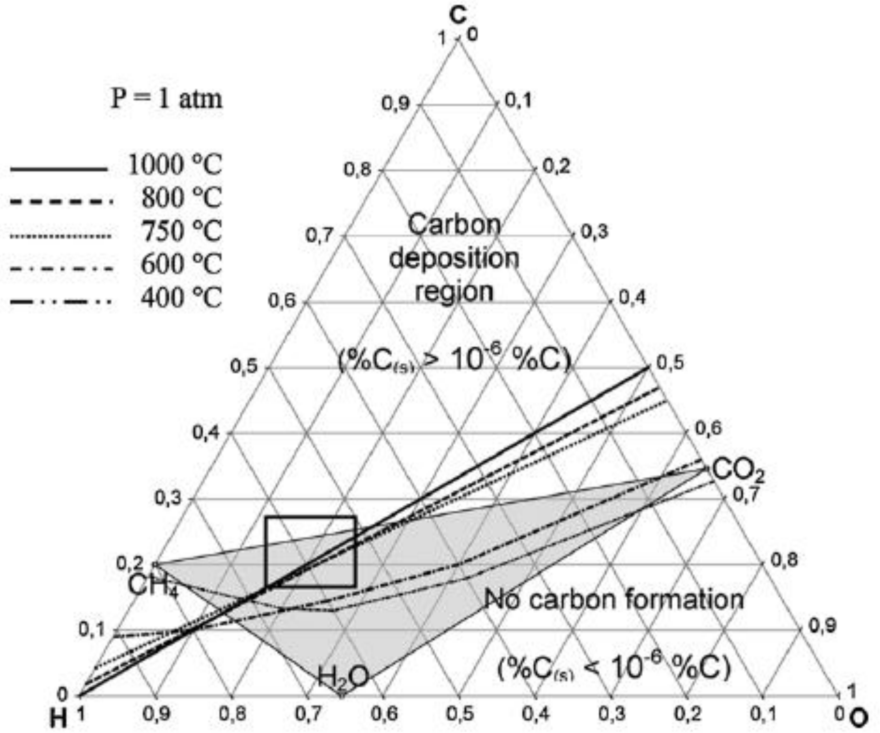

Figure 2.9: C-H-O ternary diagram at different operating temperature [69]

2.3.2 The modes of reforming in SOFC operation

2.3.2.1 External steam reforming

With those reactions explained above, to operate an SOFC with hydrocarbons and avoid rapid SOFC degradation relating to carbon formation, an external reformer (ER) to facilitate the main reforming reactions is usually fitted prior to the SOFC unit [71, 72]. In this way, a high steam to carbon ratio or frequent catalyst regenerations for the external reformer can be provided without disturbing the SOFC unit. The SOFC is fed by the reformate, which consists of a mixture of H_2 and CO and poses less possibility for carbon formation compared to the fuel feed which contains CH_4. However, fitting an

ER significantly reduces the overall efficiency of an SOFC plant, therefore attempts to operate SOFCs using direct internal reforming with minimised carbon formation have been the main research topics for hydrocarbon fuelled SOFCs.

2.3.2.2 *Internal steam reforming*

There are three main modes of operating SOFC with internal reforming; internal steam reforming (based on Eq. 2.18 and Eq. 2.19), internal dry reforming (based on Eq. 2.20) and internal partial oxidation (based on Eq. 2.22 and Eq. 2.23). In each of the internal reforming mode, the water gas shift reaction (Eq. 2.21) is usually considered as one of the reactions taking place in the SOFC anode because of its negative Gibbs free energy value at 600-800 ^oC and of its equilibrium constant being 2.48 at 600 ^oC and 1 at 800 ^oC.

When biogas is used as the SOFC fuel, dry reforming is considered to be the main reaction taking place in the SOFC anode, although the presence of steam as a product of electrochemical reaction cannot be neglected and will also facilitate steam reforming to take place. In many studies, two modes, dry and steam reforming, or three modes, including partial oxidation, are deliberately combined to achieve better SOFC performance and minimise carbon formation.

2.3.2.3 *Minimising carbon deposition in internal steam reforming SOFC*

In the SOFCs operating with hydrocarbon fuels, the study to minimise carbon formation has been an important and most researched topics for decades. In this section the main findings from several selected studies are presented. Most studies emphasized that excess steam or additional air is required to safely operate the SOFCs (without carbon formation). However for fuel cell to operate with high efficiency, additional H_2O should be kept low since H_2O is the product of the electrochemical reaction and high H_2O concentration reduces Nernst potential as represented by Eq. 2.13. Several studies indicated that it is possible to reduce the steam to carbon provision while still maintaining low carbon deposition by modifying the anode catalytic properties [73-75].

Carbon formation boundary in SOFC operations has been extensively studied [21, 22, 68, 76-78]. The study by Sangtongkitcharoen et al. [22] used thermodynamic analysis to calculate the boundary condition for carbon deposition. The boundary was defined as the condition having a carbon activity value =1. The study indicated that in the oxygen ion conducting SOFC the minimum H_2O/CH_4 ratio to avoid carbon formation decreases as temperature increases. Due to the availability of water as the electrochemical reaction product in the anode, the value of minimum H_2O/CH_4 required in direct internal reforming mode is lower than that required in external reforming mode. It was also revealed that proton conducting SOFC is not practical to use in reforming mode of SOFC since water is produced at the cathode side therefore the requirement for addition of steam in the anode feed becomes large and impractical.

Effects of current drawing in reducing carbon formation in SOFC operation has also been predicted in the study by Sangtongkitcharoen et al. [22]. Indeed, this was also supported by several experimental studies [79-82]. The study by Alzate-Restrepo and Hill [79] revealed that less carbon was deposited on NiSYZ SOFC operating under current drawing mode compared to that deposited under OCV mode. The type and stability of the deposited carbon was also affected by SOFC operating mode. Removal of the deposited carbon under current drawing mode both by temperature programmed hydrogenation (TPH) and temperature programmed oxidation (TPO) was easier compared to the removal of carbon deposited under OCV mode. The study by Liu and Lin [80, 81] revealed that anode supported NiYSZ SOFC operating with humidified methane and natural gas showed no carbon deposition after 90 hours of cell testing at 0.6 V producing 350 mW cm^{-2} even at low fuel utilisation. Results of these studies suggested that carbon formed during current drawing was most likely removed by both oxygen anion and water produced in the anode. A recent study involving Raman Spectroscopy on carbon deposition on patterned NiYSZ anode by Li [82] suggested that the carbon types which participates in the carbon electrochemical oxidation is mostly of the crystalline graphitic type.

2.3.2.4 Modification of SOFC anodes for use in steam reforming mode

Although current drawing mode is able to remove the deposited carbon in an SOFC operation, the extent to which and how much carbon can be removed rely on the competition between the rate of carbon formation and the rate of carbon consumption. In many cases, the rate of carbon formation is higher than the rate of carbon consumption even during current drawing, and that the amount of carbon deposited is still unacceptable. Therefore the development of SOFC materials, specifically modification of carbon tolerant SOFC anodes has been a research area with growing interests. Several studies have been conducted such as studies to develop anode barrier layer [83, 84], NiYSZ with $SrLaTiO_3$ oxide anodes [85], or Ni/Cu-based anode [44, 86-88] and modification of Ni-based catalysts using other metals such as Ba [89], Bi, Co, Mo, Fe [74, 75, 88] Ru [90, 91], Rh [92-94], Au [95] or Sn such as reported by Nikolla et al. [73, 96-99] and those reported by other researchers [100-103] to form bimetallic catalysts. A review of Ni-based catalyst for methane steam reforming was carried out by Wu et al. [104]. Four of those studies involving bimetallic catalysts reported the use of Sn-modified NiYSZ catalysts in SOFC operating with steam methane reforming. Among the four studies on Sn/NiYSZ, three studies observed reduced carbon formation during the SOFC operating condition. However, the study by Singh and Hill [102] reported that the Sn-impregnated NiYSZ did not show significant improvement in either the SOFC durability or carbon tolerance when the SOFC was operating on 3% humidified CH_4 and on dry CH_4.

The phenomena of carbon deposition in SOFC operation is so important that several groups of researchers have been actively developing special carbon deposit sensors based on gravimetry and electronic conductivity [105], Raman Spectroscopy [106-108] or evolved gas measurement [109] to enable in situ measurements of carbon deposition during SOFC operation.

2.3.3 Biogas fuelled SOFCs

Studies on the direct utilisation of biogas as fuel in SOFC in dry reforming mode have been continuously attracting attention. Reports by Kendall, Staniforth and Ormerod in the UK [60, 110, 111] are among the early studies with experimental work which used real biogas to fuel electrolyte supported SOFCs. To date more than 5 groups of researchers in the UK, Thailand, Japan, China, Greece, Italy, Switzerland, Germany and the USA have reported promising results of utilising biogas in SOFC and integrating the SOFC in combined heat and power generations. The following section describes and evaluates published reports on biogas fuelled SOFCs.

2.3.3.1 Catalysts for CH_4 dry reforming

Dry reforming, represented by Eq. 2., as a means of hydrogen production from hydrocarbon has been studied for quite a long time. As early as 1928 Fischer and Tropsch studied CO_2 reforming of methane over a number of base metal catalysts, they found that nickel and cobalt were the preferred catalysts. Several further studies were carried out on nickel film as catalysts. Rostrup-Nielsen et al [64] studied and compared catalytic activities of alumina stabilized magnesia supported Rh, Ru, Ir, Ni, Pt and Pd in steam and dry reforming reactions at 550 ^{o}C. Excess steam and CO_2 in the 4:1 ratio of $H_2O:CH_4$ or $CO_2:CH_4$ were used in the study. The results suggested that all of the observed metals showed 3x to 10x less activity in dry reforming compared to that in steam reforming reactions. Only Ni showed less decrease in activity on going from steam reforming to dry reforming.

The effects of catalyst supports and Sn promotion on dry reforming of CH_4 over supported Pt catalysts have been studied by Stagg et al. [112]. The results revealed that at 800 ^{o}C Pt on ZrO_2 support showed higher conversion rate compared to that obtained from Pt on SiO_2 support. It was proposed that zirconia as the catalyst support plays a significant role in promoting the dissociation of CO_2 and increasing the CO production. After evaluation of several special techniques of Sn promotion on Pt/ZrO_2 catalysts, it was revealed that, when Sn alloy formation is controlled not to disrupt ZrO_2 availability, Sn was found to reduce carbon deposition and increase the Pt/ZrO_2 catalyst stability.

The effects of varying temperature and the ratio of CO_2: CH_4 feed in dry reforming over Ce-promoted Ni catalyst with ɣ-alumina support have been investigated. A study by Fakeeha et al [113] is an example. Their results indicated that within the range of 773K to 848K, increasing the temperature led to increased conversions of both CH_4 and CO_2 gases; while decreasing CO_2: CH_4 ratio led to decreased conversion of CH_4, decreased H_2 yield, and increased conversion of CO_2. The study did not mention observation of catalyst durability or carbon formation. Xu [114] studied biogas reforming for H_2 production using Ni/Co bimetallic catalysts supported on γ-Al_2O_3 modified by La_2O_3. The results revealed that operating at 800 ^oC a stable catalyst performance of 290 hours was obtained for 7Ni3Co/LaAl with CH_4 and CO_2 conversion close to 94%. The coking rate was 0.095 mg g_{cat}^{-1} h^{-1}.

Guerra et al., [54] also investigated dry reforming of CH_4 on NiYSZ SOFC anode chips varying the temperature, CO_2/CH_4 ratio, CH_4 flow rate and the catalyst mass. The results indicated that dry reforming was very poor at temperature lower than 450 ^oC. At temperatures higher than 620$^-$800 ^oC NiYSZ showed good reforming ability especially with $CO_2:CH_4$ ratio $\geq$ 1. At $CO_2:CH_4 \leq 1$ reforming was slow. The NiYSZ catalyst showed stable performance for 70 hours when $CO_2:CH_4$ ratio was maintained at 1.5 to 2.

The above explanation represents a few examples of studies performed regarding production of H_2 using dry reforming method. A recent and comprehensive review on production of H_2 using dry reforming reaction which covers the important issues encountered and the various catalysts employed was conducted by Alves et al. [115]. While modelling and thermodynamic analysis of carbon dioxide reforming have also been studied such as by Akpan et al. [116] and Nikoo and Amin [117].

2.3.3.2 Performance of electrolyte supported SOFC

SOFC fuelled by real landfill gas was studied by Staniforth and Kendall [110, 111] and Staniforth and Ormerod [118] using electrolyte supported NiYSZ-based microtubular SOFC. In the first study [110] it was reported that the power produced from SOFCs depends on the landfill sites. The difference was attributed to different biogas composition. The highest power obtained was 70 mW at 0.5 V. The SOFC was able to operate for 3 hours. It was mentioned that sulphur poisoning was affecting the SOFC performance; when sulphur was removed the SOFCs lifetime was increased to 6.5 hours. However, the SOFC still suffered from low dry reforming conversion. Adding air helped to partially oxidise the available methane and increased SOFC electrochemical performance. In the second study [111, 118] it was reported that operating the SOFC with a mixture of 1:1 CO_2 and CH_4 gave better performance compared to that obtained from 100 % natural gas fuelled SOFC. Even at 4:1 CO_2:CH_4 significant power was still produced, whereas in a combustion engine 1:1 CO_2:CH_4 is the composition with the lowest limit of CH_4 that can be used to produce power.

Shiratori and Sasaki [119-121] studied electrolyte supported Ni-ScSZ-based SOFC operating at 1000 ^{o}C with real biogas of CO_2:CH_4 = 0.55 and containing 1.62 volume %

of water. It was reported that at constant current operation of 200 mA cm^{-2} a stable potential of 0.9 V was obtained for 50 hours. Doping the NiScSZ anode with Mg increased the rate of reforming but decreased the electrochemical performance. The decrease in electrochemical performance was due to the SOFCs ohmic resistance increase caused by the NiMgScSZ.

Other groups of researchers studied electrolyte supported high temperature NiYSZ/YSZ/LSM and intermediate temperature NiYSZ/GDC/LSM planar SOFC, fuelled by simulated biogas [122, 123]. In these studies a ratio of 1:1 CO_2:CH_4 was chosen to minimise carbon formation. The operating temperature was 875 °C and 650 °C for the high and intermediate temperature SOFC respectively. It was reported that the NiYSZ/YSZ/LSM cell showed stable operation for 600 hours while the NiYSZ/GDC/LSM was stable for 400 hours. At constant 0.45 V operation, 70 mW cm^{-2} and 18 mW cm^{-2} were obtained from NiYSZ/YSZ/LSM and NiYSZ/GDC/LSM SOFCs respectively.

2.3.3.3 Performance of anode supported SOFC

Anode supported SOFCs showed much higher electrochemical performance than the electrolyte supported SOFCs delivered. The effects of humidification and adding air on the performance of NiYSZ-based SOFC was studied by Xu et al. [124] Their results indicated that coke was severely formed on NiYSZ SOFC operating in dry reforming mode, and that humidification and adding air reduced coke formation. When the SOFC was operating at 750 °C, with 1:1 CO_2:CH_4 and 1.5x cathode gas flow, they obtained 0.994 V OCV and 313 mW cm^{-2} maximum power. At 850 °C they obtained 547 mW cm^{-2} maximum power density and a stable operation was obtained for

100 hours which degraded badly after 40 minutes exposure to 20 ppm H_2S. Coating the NiYSZ anode with Ni-CeO was able to temporarily prolong the SOFC life. The cell performance on the Ni-CeO coated anode cell recovered after the H_2S feed was removed but that on uncoated anode the performance loss was permanent.

A study by Takahashi [125] investigated the thermo mechanical reliability of SOFC fuelled by biogas, while Leonide and A. Weber [126] reported that biogas obtained from a supercritical water gasification pilot plant fed to an anode supported SOFC could produce 0.8 W cm^{-2} at 750 ^{o}C. The biogas used had low CH_4 content but had H_2 added and humidified with 4:1 steam to carbon ratio.

The group of researchers at Politecnico di Turino Italy has been engaged in probably the most extensive study of biogas fuelled SOFCs. Their studies at least cover the followings;

- Effects of biogas type (bio-CH_4 and bio-H_2) on electrochemical performance [127]
- Effects of SOFC design (electrolyte supported (ES) and anode supported (AS)) SOFCs and effects of planar and tubular SOFCs on electrochemical performance [128]
- Modelling biogas fuelled SOFC performance using tubular SOFC [128]
- Durability of anode supported planar NiYSZ SOFC fuelled by varied composition of simulated biogas [129]
- Effects of flow fuel rates and composition, current loads and fuel utilisation on electrochemical performance of tubular SOFCs [130]

The results revealed that the bio-H_2 fuel was successfully utilised without carbon formation but the bio-CH_4 fuel showed carbon deposited on both types of SOFC. Addition of air to the fuel feed improved the reforming and reduced carbon deposition. The results suggested that anode supported SOFC perform better than electrolyte supported SOFC due to more surface area available for dry reforming to take place. At 800 ^{o}C operating temperature and 70%-80% fuel utilisation, a maximum efficiency of 48% (LHV) was achieved with bio-H_2 (50:50 CO_2/H_2) fuel and 30% (LHV) was achieved with bio-CH_4 (40:60 CO_2/CH_4) fuel.

The durability study by Lanzini et al. [129] revealed that electrochemical performance degradation was apparent within 150 hours of operation at 300 mA cm^{-2} and 60% fuel utilisation. At the end of 300 hours operation, a post mortem analysis of the anode under SEM showed formation of much filamentous carbon from operating the SOFC at a 1:1 CO_2:CH_4 ratio. Figure 2.10 shows the carbon filaments formed which have 30-40 nm diameters. On the contrary, no carbon filaments were observed post testing of the SOFC with 2:1 CO_2:CH_4 ratio; however cell degradation was observed suggesting that carbon deposition was not the only cause of cell degradation in the SOFC operation with biogas fuel. It was proposed that anode reoxidation associated with the high CO_2 (oxidant) content was one of the causes of cell degradation.

In their study, Guerra et al. [130] indicated that maximum power was achieved at a 1:1 ratio of CO_2:CH_4. At fuel utilisation of 25% and CO_2:CH_4 = 1 they obtained 20% overall (LHV) efficiency. At CO_2:CH_4 > 1 fuel cell performance was slightly reduced.

The highest overall efficiency of 43% was obtained from operating the SOFC at 17.5A current load with 70% fuel utilisation.

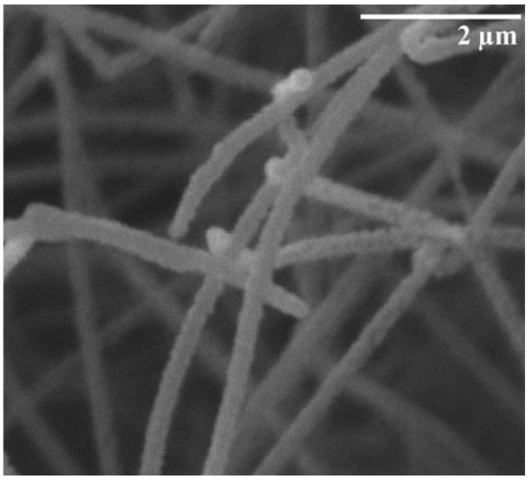

Figure 2.10: Carbon filaments formed on SOFC anode substrate post testing on simulated biogas (1:1 volume ratio of CO_2:CH_4) at 800 °C [129]

The group of researchers at the University of St Andrews who has been actively carrying out research *"on improving biogas utilisation in SOFC"* reported that Ni/Rh infiltrated into $LaCaCeTiO_3$ anode scaffolds showed improved catalytic activities towards biogas reforming and promising tolerant to sulphur poisoning [94]. Most recently, they reported a success in producing a high performance SOFC anode which showed 1.43 W cm^{-2} maximum power density at 750 °C as the SOFC was fuelled by biogas with anode off gas recirculation. The anode was $BaZr_{0.1}Ce_{0.7}Y_{0.1}Yb_{0.1}O_3$-delta (BCZYYb) infiltrated Ni-YSZ. They reported that *"no any obvious carbon deposition was found after operation for 50 hours at 750 °C"* [131].

2.3.3.4 Performance prediction from modelling and simulation

Performance of SOFCs fuelled by biogas has been studied using modelling and simulation either based on thermodynamic properties only or based on thermodynamic and kinetic properties. Predictions of carbon formation boundaries [21], estimation of SOFC electrochemical performance and efficiency [58, 69, 132-135] and feasibility of integrating SOFC in a combined heat and power plant [136, 137] have been studied. Although CO and H_2 are the main products of CH_4 dry reforming and both gases can be electrochemically oxidised, most studies presented in this section, except that performed by Ni [138] and Elizalde-Blancas [134], consider only H_2 for electrochemical oxidation in the SOFC, assuming CO to be continuously converted to H_2 by the fast water gas shift reaction. Regarding feed gas humidification, most studies presented in this section emphasized that provision of steam is required to avoid carbon formation. Besides, to obtain high performance, an equimolar composition of CO_2:CH_4 is recommended to fuel the SOFC. Brief descriptions and results of several studies are presented in the following.

In 2006, Assabumrungrat et al. [21] studied the boundary of carbon formation for dry reforming of methane in SOFC operation. The results suggested that the required CO_2:CH_4 ratio to prevent carbon formation increased with increasing temperature. The results also indicated that additional air is less attractive compared to that of water in reducing carbon deposition in the dry reforming reaction mixture. In addition, H_2O was found to be more effective compared to CO_2 in reducing carbon formation in methane internal reforming at low temperatures but the effects of both oxidants are comparable at high temperatures.

Van Herle et al. [132, 133] compiled biogas production data in Europe and presented thermodynamics of the biogas reforming, electrochemical conversion processes and a complete energy balance to predict the feasibility of the utilisation of biogas in SOFC co-generators. The report included a case study of the use of biogas (obtained from a farm in Switzerland) as SOFC fuel with equimolar air added in the feed to avoid carbon formation. The modelling and simulation using SOFC stacks of 100 anode supported planar cells (each with 100 cm^2 effective area) operating at 800 ^oC and 80% fuel utilisation suggested that it is feasible to produce 3.5 kW electrical power with 4.1 kW heat. This report claimed that an overall 85.9% efficiency, based on 100% methane inlet power, could be obtained.

Girona et al. [69] studied modelling and experimental evaluation of anode supported NiYSZ-based SOFC with LSM cathode operating at 800 ^oC. They developed two interconnected models to simulate the behaviour of the cell, the electrochemical model and the temperature field model. H_2 was the only reagent they considered for electrochemical reaction assuming CO to be always converted to H_2 and CO_2 via the fast water gas shift reaction. In the experimental part, the SOFC was fuelled by simulated biogas of 1:1 ratio of CO_2:CH_4 humidified with 6% steam. Using a total fuel flow rate of 17 ml min^{-1} cm^{-2} and with the cathode exposed to air at 41 ml min^{-1} cm^{-2}, they obtained maximum power densities of 210 mW cm^{-2} when the SOFC was fuelled by biogas and 230 mW cm^{-2} when the SOFC was fuelled by 3% humidified H_2. The model predicted that to prevent carbon deposition the SOFC should be operated at 0.6 V with 4.8 ml min^{-1} cm^{-2} CH_4 flow rate which corresponds to a power density of 160 mW cm^{-2}.

Elizalde-Blancas et al [134] performed numerical modelling of anode supported SOFCs operating at 800 °C on biogas produced in bio-digesters. The reforming model takes into account internal steam reforming and water gas shift reactions. The electrochemical model considers both CO and H_2 as the sources for current generation. The results suggested that it is feasible to operate SOFCs using biogas from fermenting the biomass from water lily (which produced 3:2 volume ratio of CO_2:CH_4) and from cactus (which produced 85:15 volume ratio of CO_2:CH_4) with 1.6% air added. The maximum power density obtained from operating SOFC with biogas from water lily was 550 mW cm^{-2} and was twice higher compared to that obtained from a 30% pre-reformed CH_4 fuel. Even the biogas from fermenting cactus biomass, which has a low heating value due to the low CH_4 composition, showed 1.5x higher maximum power density compared to that obtained from a 30% pre-reformed CH_4 fuel.

In 2013, Wongchanapai et al. [135] evaluated the performance of direct-biogas fuelled SOFC in a micro gas turbine system using system modelling and simulation. The model for internal reforming considered steam reforming, dry reforming and partial oxidation. While H_2 was considered as the only reagent to undergo electrochemical oxidation, CO was assumed to be consumed by the fast water gas shift reaction. It was reported that operating the SOFC at 800 °C, using a biogas composition of CO_2:CH_4 = 2:3, with 75% fuel utilisation and 400 mA cm^{-2} it is possible to operate the SOFC with 50% CHP efficiency. However, it was addressed that steam at a steam to carbon ratio of 2 was needed in the fuel feed to minimise carbon formation.

Santarelli and Lanzini, [58] developed a mathematical model of a tubular SOFC operating on biogas and predicted that direct biogas SOFC provided a good performance and ensured good conversion of the methane fuel. Similar to the experimental results reported by other researchers, the model predicted that the 1:1 CO_2:CH_4 produced the best performance.

Ni [138] developed a two dimensional model to simulate performance of SOFC fuelled by CH_4 and CO_2 mixtures. The study considered the rate of CO electrochemical oxidation being in the same order of magnitude as that of H_2 electrochemical oxidation. The model included the electrochemical oxidation of both H_2 and CO. The constructed model indicated that water gas shift reaction is negative due to low CO concentration. The study concluded that SOFC operation with CO_2:CH_4 gas feed is possible and provided a suitable catalyst for CO electrochemical oxidation is present, higher electrochemical performance can be obtained than that obtained from electrochemical oxidation of H_2 only.

Further to modelling biogas fuelled SOFC performance, a techno-economic analysis of a CHP incorporating a biogas fuelled SOFC plant in a waste water treatment plant has been performed by Trendewicz and Braun [137]. The proposed SOFC system includes a biogas pre-treatment, anode recirculation and a waste heat recovery unit. The system offers 51.6% net electrical efficiency and 87.5% CHP efficiency.

Most recently, Siefert and Litster [136] reported their results of an exergy and economic analysis of a power plant that incorporated an SOFC system utilising biogas as fuel. It was concluded that, provided the SOFC unit cost is close to \$3400 m^{-2} (within a factor of two of DOE-SECA cost target), it is viable to generate electricity at a waste water treatment plant with at least 60% overall efficiency. This would make an AD-SOFC system to be more economically viable than other systems in which the biogas is utilised in an internal combustion engine or micro gas turbine.

2.3.3.5 Summary of previous studies in biogas fuelled SOFC

Techno-economic analysis of a CHP integrating a biogas fuelled SOFC system using modelling and simulation concluded that operation of SOFC fuelled by biogas in a waste water treatment plant is feasible with predicted overall efficiency of 60% to 87.5% [136, 137]. Simulations of the performance direct biogas fuelled SOFCs have shown promising results. While biogas impurities such as sulphur can be overcome by desulphurisation prior to feeding the biogas to the SOFC, carbon formation remains the main issue to solve. The challenge is to establish stable operation of the SOFC without carbon formation. In these simulation studies, to minimise carbon formation, steam reforming or partial oxidation modes of SOFC operation were added, sacrificing SOFC efficiency. A durability study by Lanzini [129] showed that using a high, ≥2, CO_2/CH_4 ratio reduced carbon formation however the presence of excess CO_2 induced cell degradation due to anode re-oxidation. A summary of the SOFC performance described in this section is presented in Table 3.

Table 3 Summary of Literature on Performance of SOFCs fuelled by biogas

First Author	Yr	Ex.	Si	Bio-M	Bio-H	T °C	CD.	U_f	Dur .h	Eff.%	ES	AS	Pla	Tu	DR	SR	PO	AR	C form	Ref.
Staniforth. J.,	1998	√		√		800	70 mW		3						√	3%				[110]
Staniforth. J.,	2000	√		√		850	150mW		8						√					[111]
Staniforth. J.,	2002	√		√		850									√					[118]
Kendall, K.,	2002	√		√										√			√		√	[60]
Van Herle, J.,	2004		√	√		800	0.5	80		38.2e					√		√		N/A	[132]
Van Herle, J.,	2004		√	√		800	0.23	80		48.7e		√	√				√	√	√	[133]
Lanzini, A.,	2010	√		√ (200h)	√ (350h)	800	0.5 (as) 10 (es)	33 (as) 14 (es)			√	√	√		√	√		√		[127]
Shiratori, Y.,	2010	√		√		1000	0.2		50			√	√		√				√	[121]
Xu, C.,	2010	√		√		850	547mW		100			√	√		√					[124]
Lanzini, A.,	2011	√		√	√	800		70-80		30e		√		√	√					[128]
Leonide, A.,	2011	√		√		750	800mW		150			√				√				[126]
Papadam, T.,	2012	√				875	70 mW		600				√							[123]

Girona, K.,	2012	√	√	√		800	210mW	30							√	√				[69]
Lanzini, A.,	2013	√				800	300mA	60	300			√	√		√				√	[129]
Ni, M.,	2013		√	√		800	0.8	70				√	√			√	√			[138]
Guerra, C.,	2013	√		√		800		70	0.01	43.4o		√		√	√			√		[130]
Elizalde-Blancas, F.,	2013		√	√		800	550mW	70	0.56			√	√			√				[134]
Santarelli, M.,	2013	√		√		800		70		43.4o		√		√	√					[58]
Guerra, C.,	2014	√		√		620-800	0.3	60	70			√	√		√				√	[54]
Siefert, N. S.,	2014		√	√		800	0.7	80		60.0o					√	√		√	N/A	[136]
Manenti, F.,	2015		√	√		800 – 950									√	√				[72]
Ma, J.,	2015	√	√	√		750	1.250A/ 0.8V	50	50			√	√		√	√		√		[131]

Note: CD = current density; Uf = fuel utilisation ; Cap = capacity ; DR = dry reforming; SR = steam reforming; PO = partial oxidation; AR = Anode off gas Recirculation; C form = whether carbon formation was detected; e = electrical t=thermal; o=overall

2.3.4 Modification of catalytic properties of SOFC anodes

Despite the high activity of nickel towards carbon formation, to date NiYSZ cermets are still the most commonly used SOFC anodes. Other anode types, such as Cu-based anodes or mixed ionic-electronic conductive oxides, have shown better performance towards minimising carbon formation; however they still suffer from several drawbacks such as low catalytic activity towards electrochemical oxidation and hydrocarbon reforming, low mechanical strength, or incompatible thermal coefficient of expansion with other SOFC components.

In terms of catalytic dry reforming reactions, previous experimental studies have shown important results as follow;

- Compared to Rh, Ru, Ir, Pt and Pd, Ni showed the least decrease on catalytic activity on going from steam reforming to dry reforming reactions.
- Compared to silica, zirconia as a catalyst support for Pt showed better activity towards CO_2 dissociation in dry reforming reaction, leading to less carbon formation.
- NiYSZ anodes have shown acceptable performance in SOFC operation with internal dry reforming of biogas but needed excess steam or air added to minimise carbon formation. It is desirable to operate SOFC with minimised carbon formation without having to add excess steam or air.
- Modifications of NiYSZ to form bimetallic catalyst have been studied and showed promising results.
- SnNiYSZ bimetallic SOFC anodes have shown promising results for suppressing carbon formation during steam reforming of methane.

- There is an opportunity to increase power produced from biogas fuelled SOFC by modifying the NiYSZ anode catalytic properties in such a way that CO electrochemical oxidation is promoted. This way, double benefits can be expected; more power and less carbon deposition. Consumption of CO through electrochemical oxidation shifts the equilibrium of reactions Eq. 2.26 and Eq. 2.27 to the left and reduces the carbon formation. The current challenge is to select the suitable ‘second’ metal and to establish the suitable technique to form the desired bi-metallic NiYSZ anode.

Theoretical studies regarding the catalysis of dry reforming and mechanism of carbon deposition in SOFC operation are lacking. Most of the studies come from those of catalytic reforming reactions for H_2 production. Fortunately a group of researchers at the University of Michigan, the USA, conducted a thorough study on Sn/Ni catalysts for reducing carbon formation in internal steam reforming, from which the similar case in dry reforming can be approached. In explaining the theory behind the Sn/NiYZ capability to enhance carbon tolerance Nikola et al. performed in depth analysis of carbon surface chemistry in relation to Sn/Ni surface alloying using Density Functional Theory (DFT) supported by various methods of catalyst characterisation and reactor studies [96-99, 139]. They identified several possible routes to carbon tolerant catalysts as follows:

- minimising the catalyst sites which promote carbon nucleation,
- reducing the rate of carbon dissolution in the catalyst, and
- increasing the rate of C-O bond formation (carbon oxidation) hence enhancing the rate of carbon removal.

Sn/Ni bimetallic catalyst is reported to display the first and the third properties. Their theory was supported by a more recent study conducted by Helveg, Sehested and Rostrup-Nielsen [140]. The studies by Nikolla et al. demonstrated that at a certain Sn concentration, Sn/Ni alloys display the potential to displace the under-coordinated nickel sites which act as the preferred sites for carbon nucleation, besides Sn/Ni alloys also show the capability of enhancing the rate of carbon oxidation therefore increase the rate of carbon removal hence improved carbon tolerance. Following the above explanations, in this study, it is proposed to investigate the effects of Sn-infiltrated NiYSZ anode on the electrochemical performance of the SOFC fuelled by simulated biogas under dry reforming mode. To the best of the author’s knowledge this study has not been performed before. To illustrate the scope of relevant studies already performed relating to modifications of nickel catalysts in steam and dry reforming applications, Table 4 is presented.

Table 4 Recent literature involving Ni-bimetallic catalysts and Sn for steam and dry (CO_2) reforming

	Catalytic SR Reaction	Catalytic DR Reaction	SOFC with SR	SOFC with DR
Sn/Ni	[51, 52, 98, 105]		[73, 101-103]	None previously, ’ but in this study
Sn-Pt on ZrO_2 and SiO_2 supports		[112]		
Mg-NiYSZ	[141]			[120]
CeO-NiYSZ **CeO-ZrO_2**	[142]	[113, 115, 116, 143]	[144]	[124]
Co-Ni γ-Al_2O_3		[114]		
Fe-NiGDC				[74]
Ni/Rh LaCaCeTiO_3i		[94]		[94]
BCZYYb/Ni-YSZ				[131]

Chapter 3

Methods & Materials

3.1 Overview

This chapter describes the materials and the laboratory methods used in this work. The laboratory methods include preparation of SOFCs for electrochemical performance testing, brief procedures for electrochemical testing, monitoring of outlet gas compositions, methods of Sn-infiltration, and the techniques used for materials characterisation. Since developing the electrochemical testing and Sn-infiltration procedures forms a part of the thesis, the detailed procedures for electrochemical testing and Sn infiltration are described in Chapter 4 and Chapter 5 respectively.

3.2 Materials

The SOFC tested in this work were of NiYSZ-based anode supported cells. Commercially available half cells of anode and electrolyte layers from Ningbo Institute of Material Technology and Engineering - NIMTE China [145], containing 50:50 wt.% NiO:YSZ, were used as our main samples. The anode is 400 µm anode supported NiYSZ and the electrolyte is 10 µm 8 mol% yttria stabilized zirconia. Cathode layers were hand painted using in house lanthanum strontium manganite (LSM) inks. Dense silver paste and pure silver wire were used for current collection from both anode and cathode surface. The dense silver paste was also used for sealing the SOFC onto the alumina cell holder. Tin compounds were used for doping the SOFC anode. A list of the materials used with relevant specifications is given in Table 5.

Table 5 List of materials used

Function	Materials	Manufacturer and product number
Anode	NiYSZ	SOFC half cells from NIMTE
Electrolyte	YSZ	SOFC half cells from NIMTE
Cathode	LSM powder	Praxair (La0.8Sr0.2MnO3)
	YSZ powder	TOSOH (TZ-8YSZ)
	Cathode ink vehicle	Heraeus V737
Current collectors	Dense Ag paste	DAD-87
	0.25 mm Ag wire	Scientific Wire company
SOFC sealants	Dense Ag paste	DAD-87
	Ceramic seal	Cerama bond 552-VFG
	Glass seal 1	Schott glass G018-311
	Glass seal 2	Saint Gobain
SOFC cell holder	Alumina (macor) cylinder	ALMATH ALM3023, ALM2014
Dopants	$SnCl_2$. 2 H_2O	Sigma Aldrich 431508
	SnO_2	Sigma Aldrich 244651
	Ethanol	Fisher Scientific (E/0650DF/17)
Fuel gases	Hydrogen	BOC
	Methane, CH_4	BOC
	Carbon dioxide, CO_2	BOC
	Helium, He	BOC
TPO	Graphite	Sigma Aldrich

3.3 Methods

3.3.1 SOFC manufacturing steps

Referring to Figure 3.1 and Figure 3.2, starting with the half-cell, the cathode active layer of LSM-YSZ was carefully painted on top of the electrolyte layer. The first cathode layer was sintered at 1100°C for three hours at 3 ^{o}C heating rate. The following step was painting a second cathode layer, which consists of pure LSM, on top of the first layer. The second layer was sintered at 1150°C for three hours also at 3 ^{o}C heating rate. The cathode ink which contains LSM powder and V-737 ink vehicle, was made using an 'EXAKT' three roll mill machine. The effective cathode area was 2.0 cm^2.

As illustrated in Figure 3.2 and 3.3, silver wires (6 strands of 0.25 mm Ag wire, Scientific Wire Company) as the current collectors on both cathode and anode were attached to both anode and cathode surface using dense silver paste (DAD-87).

A double cylinder alumina tube was used as the cell holder. The outer diameter of the larger and smaller cylinders is 30 mm and 20 mm respectively. Each alumina cylinder is 3 mm thick. The top view of the cell holder is pictured in Figure 3.2. The full cell was mounted and properly sealed on the top of the cell holder using the dense silver paste with the anode facing downwards towards the fuel inlet and cathode facing upwards exposed to ambient air. The silver paste seal was dried overnight at 120 °C. On the following day, the dried seal was examined against any defects that may have formed and become visible after drying. Any defects found needs to be fixed at this stage, to minimise problems at the subsequent stages.

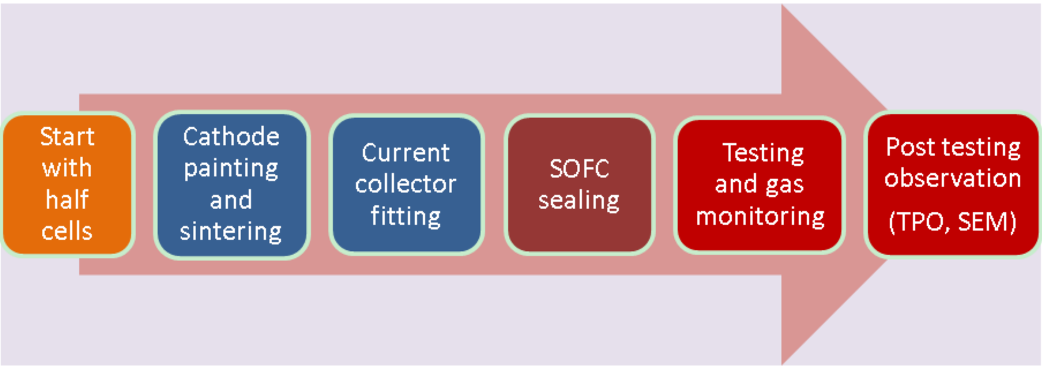

Figure 3.1: Main stages of SOFC preparation

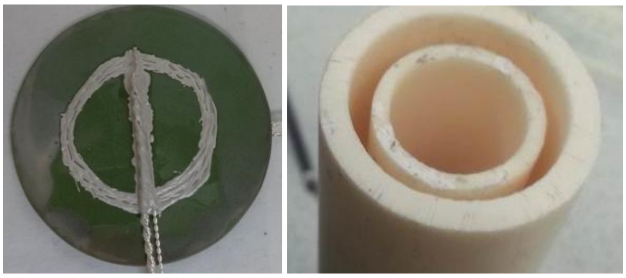

Figure 3.2: SOFC anode side (left) and the ceramic double cylinder SOFC holder (right)

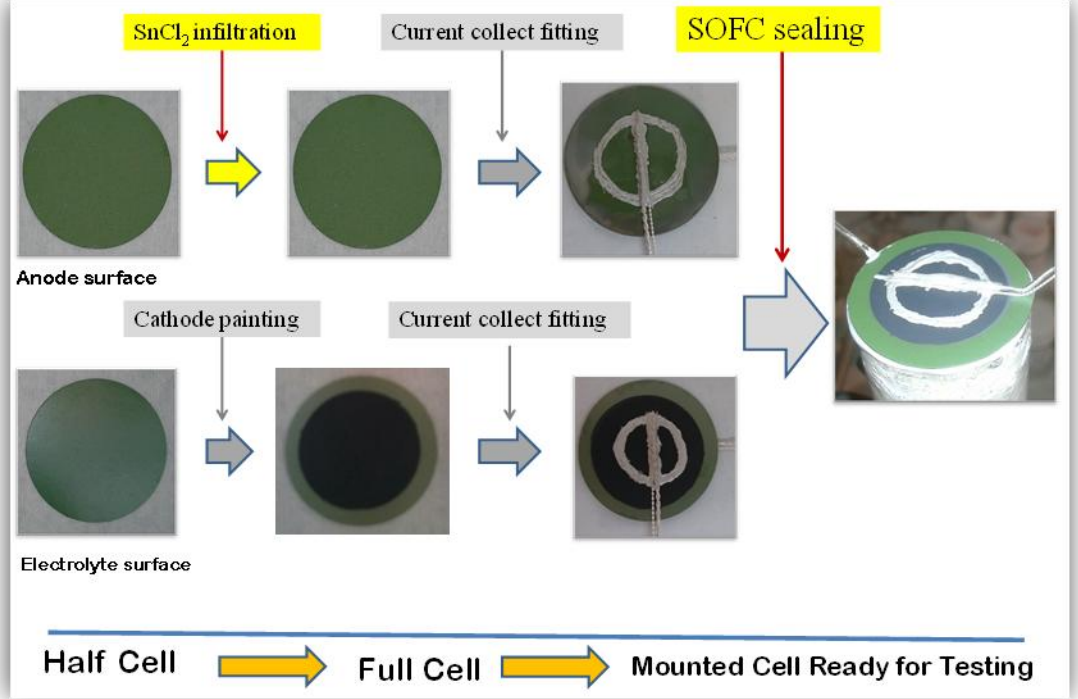

Figure 3.3: Step by step SOFC preparation process

3.3.2 Electrochemical performance test

The cell holder (cell housing) with an SOFC mounted to it as depicted on the right in **Figure 3.3** was placed horizontally in the tunnel furnace. The tunnel furnace with the test system is illustrated in Figure 3.4 and Figure 3.5. The base of the cell holder was connected to the fuel feed. The fuel flows in the inner tube towards SOFC anode surface. The unreacted fuel and the product gas flow out through the space in between the double cylinders.

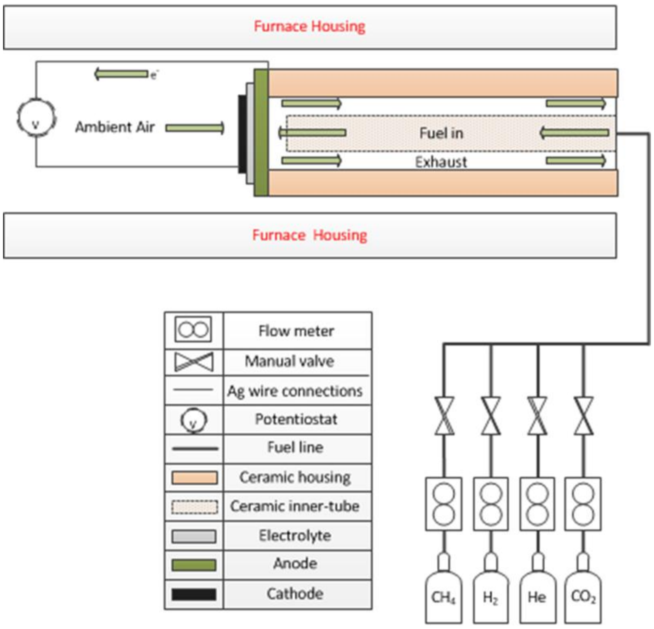

Figure 3.4: Schematic diagram of the test rig (the diagram courtesy of N.McDonald)

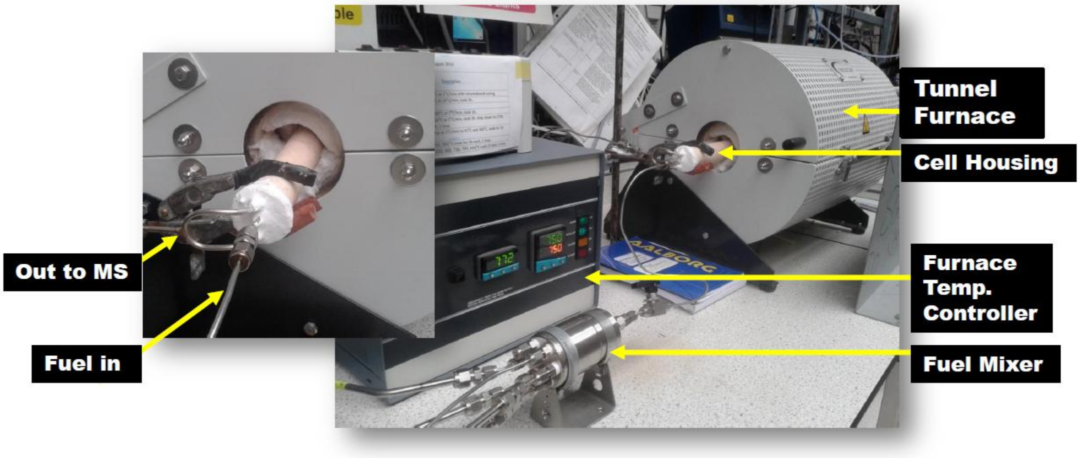

Figure 3.5: SOFC test rig with tunnel furnace; insert is the fuel inlet and outlet position

Cathode surface was exposed to ambient air. The rig was connected to four gas feeds; methane, hydrogen, helium and carbon dioxide with independent mass flow controller as illustrated in Figure 3.6. For electrochemical tests using hydrogen, the flow rate used was 21 ml min^{-1} of hydrogen and 7 ml min^{-1} of helium. For the tests using biogas, the flow rate used was 7 ml min^{-1} of carbon dioxide, 14 ml min^{-1} of methane and 7 ml min^{-1} of helium. The biogas flow rate used was chosen so carbon deposition is thermodynamically expected as outlined in the C-H-O ternary diagram in Figure 3.. All tests were performed at 750 ^{o}C. The test rig was connected to a Solartron 1247 test station for electrochemical performance measurements and to an MKS Cirrus mass spectrometer for monitoring the outlet gas composition.

Figure 3.6 Mass flow controllers

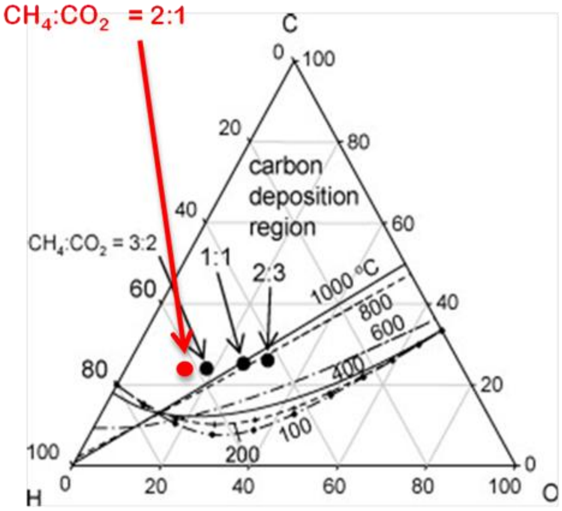

Figure 3.7 C-H-O ternary diagram, red dot shows the position of the biogas fuel used (CH_4 : CO_2 = 2:1)

3.3.3 SOFC outlet gas monitoring using a quadrupole mass spectrometer

Mass Spectroscopy is an analytical technique used to identify elements or compounds in a given sample. During Mass Spectroscopy analysis, the sample is ionised by a beam of electrons, this ionisation method is known as electron impact, and the ions formed are classified according to their mass to charge ratios. From here, the mass to charge ratios are analysed, in our case a quadrupole mass analyser is used, the ions identified and an amplified signal sent by the detector records a spectra. The mass to charge ratios appear on the spectra as a function of intensity which shows the mass of each component and the relative amounts of various components in a given sample. In this study, outlet gas stream was monitored using a 'Minilab-' and 'Cirrus-MKS' Quadrupole Mass Spectrometer analyser. More detailed explanations about the method of Mass Spectra calibration and monitoring the outlet gas composition can be obtained in Dhir [35].

3.3.4 Sn-infiltration on SOFC anode surface

Three methods of infiltration were approached; these are pipette drop and sonic immersion using Sn-dopant solution and powder blending using SnO_2 powder. To prepare the Sn-dopant solution, tin in the form of solid $SnCl_2.2\ H_2O$ was dissolved in 95% ethanol and placed in an ultrasound bath for 15 minutes to dissolve all the $SnCl_2$ particles. Fresh solution was always prepared for Sn-infiltration. The concentration of $SnCl_2.2\ H_2O$ was 10% wt/vol. A brief explanation of the three doping method is given below; a more detailed account of each of these methods is explained in Chapter 5.

In pipette drop infiltration, using a 2.5 ml plastic syringe fitted with a needle this dopant solution was carefully dropped on to the middle part of the NiYSZ anode surface. The drop was allowed to dry in air for 30 minutes; then drying was continued in a drying oven kept at 70 ^oC for 15 minutes. A further drying at 100 ^oC for 1 hour was performed before calcinations in air at 600 ^oC for 2 hours. The heating and cooling rate for calcinations was kept at 2 $^oC\ min^{-1}$. This infiltration, drying and calcinations steps were repeated several times until the desired amount of Sn/Ni was sufficiently deposited onto the NiYSZ anode surface.

In the sonic-immersion infiltration, 6 anode discs were immersed in a beaker glass containing $SnCl_2$. $2H_2O$ solution. The beaker glass was placed in an ultrasound bath at 40 ^oC for 1 hour. At 15, 30 and 60 minutes of immersion two discs were consecutively withdrawn from the $SnCl_2.2H_2O$ solution and were dried and calcined in the same procedure as the drying and calcinations procedures outlined above.

Powder blending method was used to dope Sn on NiO powder right from the beginning of Ni/YSZ anode support preparation. For this method of infiltration, Sn in the form of fine SnO_2 powder was used as Sn-precursor. A certain amount of SnO_2 powder, to make 1-5 weight % of Sn over Ni, was added to the NiO/YSZ mixture for pellet pressing. The presence of Sn in the early stage of NiYSZ powder preparation was expected to provide a homogeneous distribution of Sn/Ni in the bulk NiYSZ powder.

3.3.5 Temperature programmed oxidation

The quantity of carbon formed during dry reforming mode of SOFC operation was measured using a Temperature Programmed Oxidation (TPO) method where the sample is placed in a quartz tube and heated to 900 ^oC at a rate of 10 ^oC while it is exposed to a mixture of 10 ml min^{-1} oxygen and 40 ml min^{-1} helium. Mass spectrometry analysis, which accompanies the TPO experiment, measures the change in partial pressures of the exit gases from the TPO quartz tube. More details about the calculations and mass spectrometer calibration can be found in [35]. A series of known amount of carbon samples, in this case graphite and carbon black powder, including blank samples, were run to obtain corresponding mass spectra of CO_2 to construct a calibration curve. A plot of CO_2 peak area against the weight of each standard carbon should show a linear relationship and give a factor of carbon weight per unit area of CO_2 peak. Then a known quantity of a tested SOFC is run for TPO using exactly the same operating condition for TPO calibration. Approximately 70 to 80 % (in terms of anode surface area) of a tested SOFC was used for TPO, the remaining 20 to 30 % was used for anode microstructure characterisations.

3.3.6 Anode materials characterisation

3.3.6.1 TGA/DSC

TGA is a technique used to examine and predict the chemical and physical changes during heating up in a controlled atmosphere in a closed furnace. During the TGA examination the mass of the substance is monitored as a function of temperature or time. In this work, TGA was used to examine the physical changes of $SnCl_2$. 2 H_2O crystals, as the Sn precursor for Sn-infiltration of the SOFC anodes. An amount of 10 mg of $SnCl_2$. 2 H_2O sample was placed in the TGA chamber. The atmosphere in the chamber was maintained with a mixture of 200 ml min^{-1} N_2 and 50 ml min^{-1} O_2. The sample was heated from ambient temperature to 900°C at 10^oC min^{-1} heating rate. The weight loss and the enthalpy changes as a function of temperature were recorded throughout.

3.3.6.2 XRD

X-ray powder diffraction (XRD) is an analytical technique used for phase identification of a crystalline material and can provide information on unit cell dimensions. Usually the analysed material must be in finely ground, homogenized for average bulk composition to be determined. In this work XRD was used to examine the NiO and ZrO_2 phases on the non-infiltrated and Sn-infiltrated SOFC anodes. The sample, in the form of reduced SOFC anode disc was used in this work.

3.3.6.3 SEM/EDX

SEM of the microstructure of the cell sample was performed using a JEOL 7000 and Hitachi Tabletop Microscope TM3030 Plus. The samples were unpolished fractured SOFC anodes. Prior to SEM measurements, the samples were coated with gold nanoparticles to make them conductive. Both back scattered electron (BSE) and secondary electron (SE) were employed to observe the cross-sectional and surface morphology. The other purposes of SEM examination were to examine the presence of Sn on Sn-infiltrated SOFC anode and deposited carbon on tested SOFCs. EDX elemental mapping with BSE mode was used to identify the element's distribution in the samples.

3.3.6.4 XRF

X-ray fluorescence is a method to determine the qualitative and quantitative element composition using X-rays. It is based on X-rays hitting atoms, causing a secondary radiation that is characteristic for each element in the periodic system. The collision of X-rays with atoms can result in the removal of electrons from various shells leaving vacant positions behind. These vacancies are subsequently filled by electrons from higher energy shells and the excess energy of these electrons is emitted as secondary X-ray fluorescence radiation. When an electron from the L shell substitutes a vacancy in the K shell, Kα radiation is emitted. K_β radiation is emitted when an electron from the M shell moves to the K shell. When an electron from the M shell substitutes a vacancy in the L shell Lα is emitted. Each element has characteristic energies for the secondary X-ray fluorescence. In this work XRF was used to characterise the Sn-infiltrated SOFC anodes in terms of chemical composition, especially Sn-content. Samples in the form of SOFC anode discs were analyzed with the optimum excitation using Rhodium tube with a voltage of 60 kV and a current of 67 mA. The analyzer crystal LiF220 ensures that in combination with the 0.23° collimator, the best separation is achieved for adjacent elements. The XRF machine used was XRF_90_S8_Tiger.

3.3.6.5 X-ray Photoelectron Spectroscopy XPS

In this work, XPS was used to quantitatively analyse the average surface chemistry of SOFC anode samples. It is able to measure the composition, atomic concentrations and the chemical state of the elements on the surface to 20 nm depth. All elements except H_2 and He can be detected. Running an XPS scan is typically accomplished by firstly exciting a sample surface with mono-energetic Al kα x-rays causing photoelectrons to be emitted from the surface. Then an electron energy analyzer is used to measure the energy of the emitted photoelectrons. From the binding energy and intensity of a photoelectron peak, the elemental identity, chemical state, and quantity of a detected element can be determined. The XPS results in this work were obtained at the LENNF (Leeds EPSRC Nanoscience and Nanotechnology Facility) in Leeds University.

Chapter 4

Electrochemical Performance Baseline with Hydrogen Fuel

4.1 Overview

This chapter presents results from exploring suitable procedures for SOFC testing in terms of SOFC sealing on the cell housing, SOFC heating-up prior to testing, anode reduction and the choice of fuel flow rate. Using the chosen procedures, it then continues to present the cell electrochemical performance on hydrogen which will be used as the baseline to evaluate the cell performance on biogas.

4.2 SOFC test set-up

A schematic diagram of the SOFC manufacturing steps performed in this study is presented in Figure 3.. As described in Chapter 3, commercially available half cells containing anode supports and electrolyte layer were purchased from NIMTE, China. The first manufacturing step performed in the laboratory is LSM cathode layers painting and sintering, followed by Ag-wire current collector fitting, SOFC sealing onto the cell housing and SOFC electrochemical testing with simultaneous outlet gas monitoring using a mass spectrometer.

This section highlights important precautions on SOFC preparation steps obtained from our practice which should be carefully exercised to minimise cell testing failure associated with faulty operation. These small but important steps were found to have minimised the number of inconsistent results which could be conflicting during data analysis.

4.2.1 Cathode painting and sintering

Two layers of LSM/YSZ cathode were hand painted onto the electrolyte side of the half cell. The first layer was the LSM-YSZ composite intended for a good bonding between the YSZ electrolyte and the LSM cathode layer and extension of the ion conductivity phase into the cathode for performance improvement. The second layer was the pure LSM layer intended to provide a good electronic conductivity for current collection. Each cathode layer was sintered separately. The chemical composition and the sintering temperature profile of each cathode layer were described in Chapter 3. As a general rule, a consistent procedure to maintain constant cathode area, thickness and microstructure should always be followed for each SOFC cathode painting and sintering. These are as follows;

- Having a fixed template for cathode painting so the cathode area is consistently constant
- Having the same brush strokes applied for each cathode layer so cathode thickness is constant
- Applying the same heating profile for the sintering so that the same cathode microstructures are maintained, and
- Carefully storing and labelling the full SOFC to minimise damage caused by cross contamination.

4.2.2 Current collector attachment

The precautions taken in the SOFC preparation steps for current collector fitting are addressed in this section. These are small but important steps which have minimised the number of irreproducible results which led to ambiguities in data analysis. These are listed as follows:

- maintaining the same Ag wire thickness for current collection in all cell tests,
- ensuring that good connections are made along the current collector wires,
- keeping current and voltage connections separated and making sure that short circuiting is prevented.

During preparation for an SOFC test, it has to be ensured that the cell holder, the SOFC seal and the fuel inlet and outlet lines are gas tight. A way of checking gas tightness along the testing line is by using a bubble flow meter and a mass spectrometer**.** A gas tight system will show consistent identical flow rates of the gas measured at the inlet and outlet points of the fuel cell. Helium is usually used for this test since it is inert and poses very small health and safety risks.

4.2.3 The sealing of the SOFCs on to the cell holder

The sealing of the SOFC cell on to the cell housing was performed in such a way that it ensured a strong bond between the surfaces was produced during manufacturing stages and lasted as long as the SOFC operation at 700-850^{o}C. To achieve this, the sealant material should be able to demonstrate its chemical stability, suitable material strength, and compatible thermal expansion characteristics with the cell materials throughout the cell operation. Most of SOFC cell test failures encountered in our study come from the failure in SOFC sealing. An imperfect SOFC sealing can be observed as seal cracks, cell cracks or a combination of both, such as illustrated in Figure 4.1. Depending on the severity, these seal or cell cracks may allow air to diffuse into the anode compartment and subsequently alter the reactions occurring at the anode site. These effects may be observed as a reduced OCV or reduced current produced. As such, obtaining a strong bond and a gas tight seal is of paramount importance during the preparation stage of an SOFC for performance testing.

Several attempts with different ceramic adhesives and different seal curing techniques were made to seal the SOFC discs on to the ceramic cell housing. Various types of problem were encountered. Figure 4.1 represents the problems encountered which were seal delamination, cell crack or excessive seal expansion. Seven seal types as listed in Table 6 below were tried.

Table 6 List of sealing types used

No.	**Seal type**	**Abbreviation**
1.	Silver paste – thin seal	Ag-thin
2.	Ceramabond	Cera
3.	Saint Gobain Sealant	SGo
4.	Schott Glass Sealant	SGl
5.	Schott-glass combined with ceramabond	SGl-Cera
6.	Schott glass combined with silver paste	SGl-Ag
7.	Silver paste-thick seal	Ag-thick

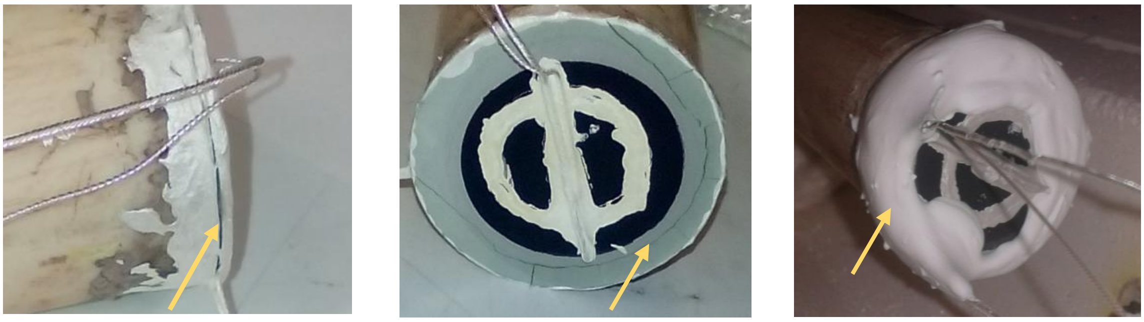

(a) Thin Ag seal delaminated **(b) Cell cracked** **(c) Ceramabond excessive seal expansion**

Figure 4.1: Various cases of seal misfunction and cell cracks at 750-800 °C operating temperature.

Alumina based ceramic sealants, glass sealant, and silver paste sealants are among those adhesives which were explored. A simplified list of each sealant's performance is presented in Table 7.

4.2.4 Observations on SOFC seals

Table 7 Qualitative results of SOFC sealing trials at 750-800 °C operating temperature

Trial No.	Sealing type	Observation
1.	Silver paste-thin seal	• Very good adhesion • Fully dense • Thinning of some seal caused gas leak
2.	Ceramabond	• Very good adhesion • Porous, hence not gas tight • Often causes cell crack • Excessive seal expansion may occur at too rapid curing rate
3.	Saint Gobain sealant	• No adhesion especially post testing (when the cell was cooled down) • Seal reacts with Ag wire, developing leak during testing, then flame was observed and Ag wire disrupted • Tests on small pieces of macor and cells, also on small pieces of ZrO_2 plate and cells confirm that this seal shows no adhesion and even shows some sign of repelling Ag wires.
4.	Schott Glass sealant	• Good adhesion on horizontal mount • On vertical mount (supporting tube in horizontal position), it needs support to avoid the seal drifting down and leaving holes/leaks at the bottom part of the cell (especially during seal curing at 850 °C).
5.	Schott glass and ceramabond Sch-CB	• Incompatible thermal expansion coefficient, hence the seal almost always cracked
6.	Schott glass and Ag Paste Sch-Ag	• Not showing good repeatability, very good in 3 trials, the 4th trial showed seal crack
7.	Ag paste only-thick seal	• Very good in 5 trials • Seal is dense and shows no seal or cell crack during heating up and cell testing. However some seal crack was observed during cooling down. • Seal curing at 120 °C overnight is very important to minimise seal failure during testing.

Table 8 presents results of an approach to rate the sealing quality of each seal trialled. This result suggested that the thick silver paste is the most suitable sealant for the anode supported SOFC used in this study. Therefore this thick silver paste was used for our SOFC sealing in the subsequent manufacturing steps.

Table 8 Rating results of SOFC sealing trials at 750-800°C operating temperature

Sealing Type	**Performance Criteria**				
	Adhesion	Density	Chemical Stability	Cost	Overall
Ag-thin seal	3	2	3	2	10
Cera	3	1	3	3	10
SaGo	1	3	1	1	6
ScGl	2	3	3	1	8
ScGl-Cera	2	3	2	2	9
ScGl-Ag	3	2	2	1.5	8.5
Ag-thick seal	3	3	3	2	11

Note: 3 = very good; 2 = good; 1 = bad

4.2.5 SOFC heat-up

The temperature profile for heating up the SOFC is presented in Figure 4.2. The SOFC heat-up was performed without gas flow to allow for a dense Ag seal to form. The Ag seal was cured at 800 °C for 1 hour. Heating was performed from ambient temperature with a rate of 5 °C min^{-1}. After Ag seal curing at 800 °C, the test rig was brought to operating temperature of 750 °C. Only at this stage Helium and H_2 were gradually introduced. The rate of heating and the manner of H_2 introduction are among the critical points that need to be carefully addressed.

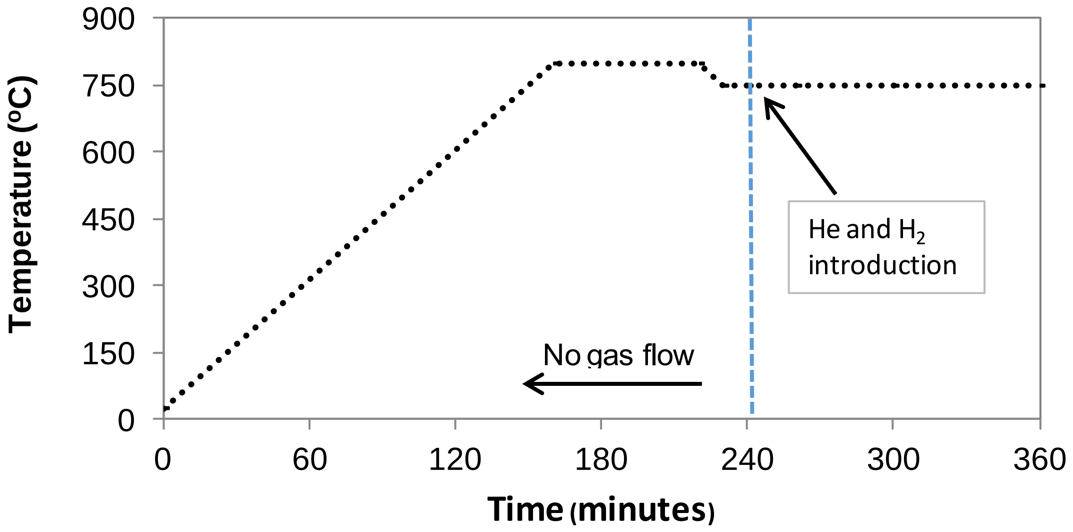

Figure 4.2: SOFC heat-up profile

The rate of heating can affect the SOFC microstructure and sealing quality. A rapid heating rate is desired as this will be the favoured condition for the real SOFC applications. However too fast a heating may pose a risk of cell cracks or seal cracks. A slow heating rate is not desired as it makes inefficient operation. Therefore a careful selection of heating rate has to be made to allow for an efficient operation while also minimising cell and seal cracks.

The manner H_2 is introduced into the SOFC affects the anode microstructure and further affects the SOFC performance. The effects are related to the seemingly simple but yet delicate process of reduction of nickel oxide to form nickel metal in the SOFC. It was reported that for microtubular SOFCs reduced at 650-800 °C, higher temperature of H_2 introduction improved mechanical strength [146] and also increased electrochemical performance [61]. A study by Li et al. [147] reported that both temperature and duration of the reduction on H_2 affect the NiYSZ anode electrochemical performance. It was shown that reduction at 650 ^{o}C gave the best SOFC electrochemical performance compared to that performed at 550 ^{o}C and 750 ^{o}C. When the NiYSZ was reduced at 550 ^{o}C, the SOFC polarisation resistance decreased from 2.4 to 1.9 Ω cm^2 as reduction time was increased from 60 to 300 minutes. Other study reported that different reduction temperature and H_2 partial pressure affect the electronic conductivity of the reduced NiYSZ anode [148]. They studied the reduction at 400 ^{o}C, 600 ^{o}C and 800 ^{o}C with 100% H_2 and with 10% H_2. They obtained the highest and most stable electronic conductivity from the reduction at 800 ^{o}C with 10% H_2. Recently, a study by Simonsen et al. showed that heating rate and reduction temperature affect the NiYSZ microstructure [149]. Their study used environmental transmission electron microscopy (ETEM) to observe reduction of NiO-YSZ at 800 ^{o}C with low H_2 partial pressure. They observed the presence of nano-pores Ni-YSZ at 300-400 ^{o}C but coarser, denser nickel with larger pores formed at 800 ^{o}C. They also observed that reduction of NiO-YSZ occurs slower than that of NiO. These studies on NiYSZ anode reduction indicated that reduction temperature, rate of heating, duration, partial pressure of H_2 as reducing agent and the nature of the nickel anode (the presence of YSZ) affect the anode microstructure and subsequently affect the SOFC electrochemical performance. Therefore keeping the anode reduction conditions constant throughout the experiments is of paramount importance to obtain consistent SOFC electrochemical performance results.

In this study, 750 ^{o}C is chosen as the SOFCs anode reduction temperature to keep it the same with the SOFC operating temperature. The SOFC operating temperature was selected based on the working temperature of YSZ electrolyte and also based on the possibility of carbon deposition as described in Chapter 3. The heat-up rate was determined by the requirement of slow heating to avoid cell and seal crack. The SOFC is heated up to 800 ^oC at a rate of 5 ^oC min^{-1} without any gas flowing to allow for Ag seal to cure and form a dense seal. The H_2 partial pressure used for reduction was kept the same as that for the SOFC operation as presented in Table 9. The duration of 6 hours was determined from preliminary observation of OCVs which revealed that OCV values were relatively constant after 3 hours of operation. This was also supported by Li et al. [147] who studied the reduction of similar NiYSZ based SOFCs and observed that 4 to 5 hours were required to completely reduce the anodes at 550^oC.

It is known that reduction of nickel oxide by H_2 at 750 ^oC is exothermic [150, 151]. Rapidly introducing H_2 may lead to formation of hot spots on the SOFC anode. To minimise any hot spot originated from nickel oxide reduction within the anode surface, introduction of H_2 at 750 ^oC was performed gradually and only after gradually introducing Helium. The presence of hot spot may lead to formation of undesirable anode microcracks. SOFC being cracked and failed to proceed to the subsequent testing steps were observed during our work that it was decided to minimize the possibility of any cracks by introducing H_2 gradually.

4.2.6 Sequence of electrochemical performance measurements

All electrochemical performance measurements were started with open circuit voltage (OCV) mode. A stable OCV value of 1.1 ±0.1 V was considered acceptable. We used a test response which shows only 5 mV change within an hour of measurement as a rough guide for a stable value. With our fuel cell samples this stable performance was achieved in 5 hours of operation. Increasing OCV values may indicate improving anode microstructure (or incomplete anode reduction process) while unstable OCV usually indicates unstable current collectors fitting or relates to the presence of some cracks on the cell. When unstable OCV was observed the cell test was terminated. Once a stable OCV was obtained, the subsequent test sequences were performed; these are measurements of polarisation curve (or I-V curve), impedance spectra and potentiostatic measurements over up to 26 hours.

Performance stabilisation took up to 20 hours. To end the H_2 stabilisation, I-V curve and EIS and a final OCV on H_2 were measured for 1 hour. A stable final OCV value (similar to initial OCV values) indicates that no cell crack occurred during operation.

4.2.6.1 Two feed flow rates

Due to the frequent occurrence of seal leaking, it was a common practice in our group to use high fuel flow rate to compensate for the leaks. A total flow rate of 60 ml min^{-1} to 100 ml min^{-1} H_2 was used for preliminary cell testing. The first few electrochemical tests were performed using 60 ml min^{-1} H_2 and 40 ml min^{-1} He; for convenience this condition is called Case A. However, as the problem of seal leaking was overcome, and the mass spectra showed that when 60 ml min^{-1} H_2 was fed, only 5% of H_2 was utilised. It was decided to reduce the total H_2 flow rate so a higher fuel utilisation and better gas analysis can be obtained. The lower fuel flow rate or lower number of moles of fuel feed will allow for a small change in a gas component's partial pressure to be detected and registered by the Mass Spectrometer to produce better spectra. This is so because the intensity of each mass spectrum corresponds to the component's partial pressure; it follows that when total pressure (or flow rate) is low any small change of a component's partial pressure will be more clearly observed.

For the flow rate of Helium, the lowest value which can be used was dictated by the capacity of the mass flow controllers. For 100 ml min^{-1} capacity of mass flow controllers used in this study, the manufacturer recommends 5 ml min^{-1} is the lowest flow rate to maintain accuracy of the measurement results. In order not to operate the mass flow controllers at the lowest limit, it was decided to use a higher flow rate than the lowest recommended value. The flow of 7 ml min^{-1} Helium and 21 ml min^{-1} H_2 was chosen to give the total gas flow rate of 28 ml min^{-1}. This is the condition of Case B. The summary of the two conditions are presented in Table 9.

Table 9 Conditions of the two feed flow rates

	Flow rates (ml min^{-1})			
	H_2	He	Total	**H_2 partial pressure**
Case A	60	40	100	0.60
Case B	21	7	28	0.75

Comparison of performance of the two fuel flow rates were performed to ensure that the better fuel flow rate was chosen for subsequent tests with biogas. To evaluate the SOFC performance, two SOFCs were tested with Case A and four SOFCs were tested with Case B.

The change of feed gas flow from Case A to Case B involved two factors, H_2 flow rate and H_2 partial pressure. According to Nernst equation, a decrease in H_2 flow rate decreases the SOFC potential and an increase in H_2 partial pressure increases the SOFC potential. This was what occurred in the SOFC on changing from Case A to Case B. At least two changes with opposite effects on the Nernst potential are expected. To predict the fuel cell performance, a fuel cell model (FCM) developed by Tsai [78, 152] was used to simulate the Nernst potentials at OCV and the polarisation curves during current drawing. The results of the simulation and experiments are presented in Section 4.4 following the mass spectra.

4.3 Mass spectra of SOFC outlet gases

Monitoring of the SOFC outlet gas composition was performed using a Quadrupole Mass Spectrometer. Figure 4.3 & Figure 4.4 represent the mass spectra of H_2 which have been converted to a curve of H_2 concentration over the duration of electrochemical performance tests for the SOFCs with Case A and Case B, respectively. The charts show the SOFC outlet gases detected over a fraction of electrochemical performance measuring time from 25-26 hours. Each chart shows 4 sequences of electrochemical performance measurements designated as sections A, B, C and D. These sections from left to right represent the measurement sequence as follow; constant 0.7 V operation, two sweeps of I-V curve, impedance at different voltage, and OCV. The I-V curve measurement was performed with a decreasing voltage sweep followed by an increasing voltage sweep between OCV and 0.4V and back to OCV. The red dotted lines in Figure 4.3 and Figure 4.4 highlight the H_2 concentrations (partial pressures) as the SOFC was operated at OCV and at 0.7 Volt.

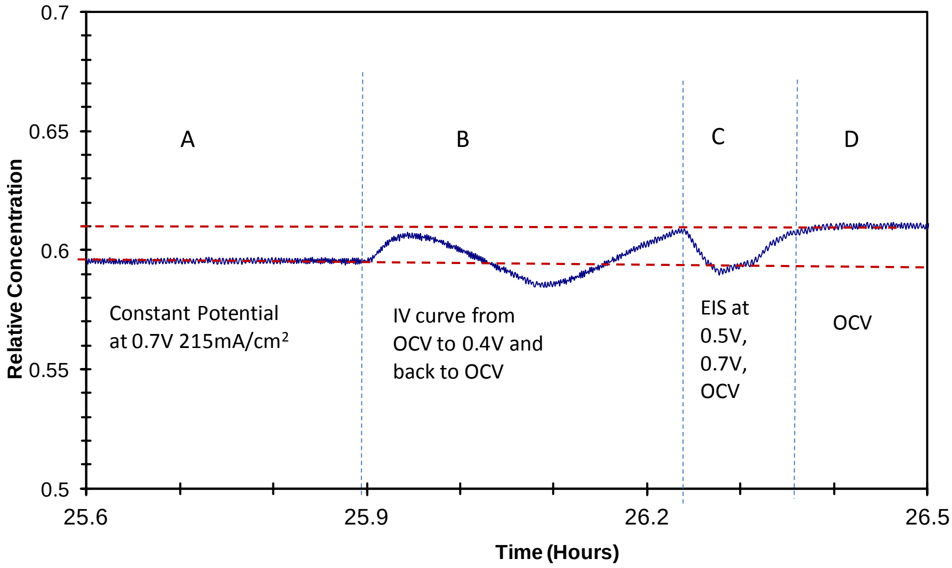

Figure 4.3: Concentration of H_2 at fuel cell outlet obtained from Case A

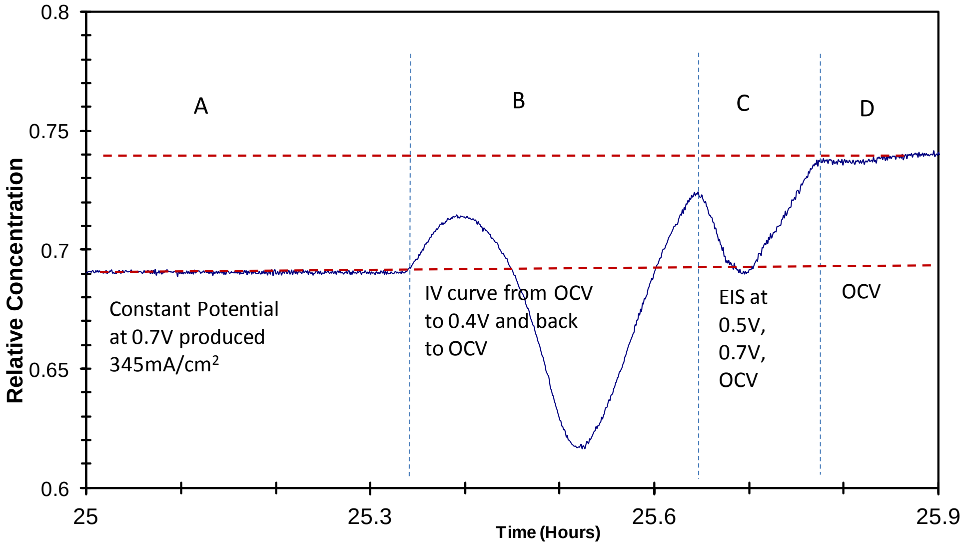

Figure 4.4: Concentration of H_2 at fuel cell outlet obtained from Case B

It is clearly shown that during the constant voltage of 0.7 V, section A, when H_2 is consumed by electrochemical oxidation reaction a low level of H_2 is present. Whereas during OCV measurement, section D, when practically no H_2 is consumed (or H_2 is equally consumed and regenerated) a higher level of H_2 is present. Also as voltage is gradually decreased and increased during I-V curve measurement, section B, a gradual decrease and increase of H_2 level is observed. The lowest point of H_2 level represents the H_2 level at 0.4 V which is the lowest voltage value applied.

It is noticed that in Figure 4.4 there is a difference of H_2 level at OCV shown by section D to the H_2 level shown by the start and end points of section B (the I-V curve). We can attribute this phenomenon to the fact that the OCV state recorded by the Mass Spectrometer at Section D resulted from a steady OCV condition of more than 2 minutes measurement whereas that obtained during I-V curve measurement was obtained from a dynamic measurement of 30 s for each voltage increment. While this 30 s is sufficient for the Solartron potentiostat machine to record steady current and voltage, this is not so for the Mass Spectrometer to record steady SOFC outlet gas composition due to the time needed for the gas to travel from the SOFC to the Mass Spectrometer analysis chamber. Therefore we can observe the right trend of H_2 level decreasing and increasing again in the I-V curve section but the real value recorded will have a certain degree of inaccuracy.

From Figure 4.3 & Figure 4.4, by comparing H_2 levels in section A and D, fuel utilisation values ($U_{f\ MS}$) at 0.7 V can be calculated as follows:

$$U_{f\ \mathrm{MS\ at\ 0.7\ V}} = ([H_2]_{\mathrm{at\ OCV}} - [H_2]_{\mathrm{at\ 0.7\ V}}) \;/\; [H_2]_{\mathrm{at\ OCV}}$$

We obtained for SOFC No.1 (Case A)

$$U_{f\ \mathrm{MS\ at\ 0.7\ V}} = (0.610-0.595) / 0.610 = 2.46\%$$

And for SOFC No.3 (Case B)

$$U_{f\ \mathrm{MS\ at\ 0.7\ V}} = (0.740-0.690) / 0.740 = 6.76\%$$

Similarly, fuel utilisation at 0.5 V (or at maximum power density) can be calculated as follows:

SOFC A.1 (Case A number 1)

$$U_{f\ \mathrm{MS\ at\ 0.5\ V}} = (0.610\text{-}0.585) / 0.610 = 4.10\%$$

SOFC B.1 (Case B number 1)

$$U_{f\ \mathrm{MS\ at\ 0.5\ V}} = (0.740\text{-}0.610) / 0.740 = 17.57\%$$

The trend of the fuel utilisation value obtained from calculation using mass spectra agrees with that calculated from the fuel cells' electrochemical output. However, it is interesting to note that the nominal values of the fuel utilisation obtained from mass spectra appeared lower than those obtained from electrochemical performance. The fact that not only H_2 was present in the mass spectrometer analyser chamber, but Helium and water vapour were also present, makes it possible that the percent change of H_2 composition recorded by the mass spectrometer appeared lower than the actual percent change occurring in the fuel cell outlet gas line. Nevertheless, obtaining the trend of the gas composition change is sufficient for this study.

4.4 Electrochemical performance

4.4.1 Prediction of electrochemical performance using fuel cell model

Electrochemical performance of the SOFC operations with Case A and Case B were calculated using the fuel cell model (FCM) developed by Tsai [152]. The model is zero dimensional and based on Nernst equation and calculations of the voltage losses related to activation, Ohmic and concentration losses. Since H_2 and He fed into the SOFC were dry gases, and the simulation only works with a certain value of H_2O input to the equation, a value of 0.5% H_2O was input for both Case A and Case B as the initial partial pressure of water so a reasonable simulation result can be obtained. At ambient temperature, a fuel gas flow saturated with water vapour contains 3% water vapour. The figure 0.5% was chosen as a value which is much less than 3% (or much closer to a dry condition of 0%). Figure 4.5 presents the results of the FCM predictions. The insert shows a small, 4 mV, difference of OCV values; 1.211 V and 1.215 V for Case A and Case B respectively, with Case B shows a slightly higher OCV than Case A does. However, since the amount of H_2 in Case A is three times more than that in Case B, as current density increased the FCM model predicts Case A to produce slightly higher voltage, due to smaller concentration polarisation. Overall, the simulation predicted a slightly better performance produced from Case A.

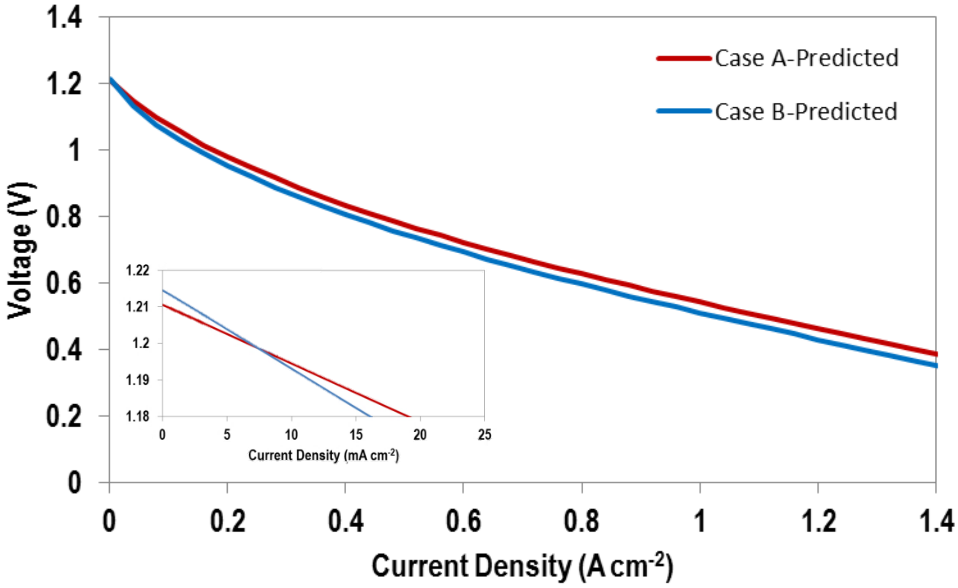

Figure 4.5: Predicted polarisation curve obtained from Tsai's FCM simulation.

4.4.2 Measured electrochemical performance

4.4.2.1 Measured open circuit potential (OCV)

Open circuit potential (OCV) was measured for 6 hours at the beginning of a cell test to allow for a complete anode reduction and any anode microstructure changes. From all of the cells being tested, OCV increased from 0.0 V to approximately 1.1 V within the first hour of introduction of hydrogen. It then stabilised and reached almost constant value within the subsequent 3 hours. The last 2 hours of OCV measurement was performed to ensure that less than 5 mV OCV change was observed. A stable OCV means the cell is well sealed and no cracks have propagated during heat-up phase. Figure 4.6 represents profiles of OCV during the first 6 hours of measurement, obtained from SOFC-A1 and SOFC-B1. Apparently SOFC-A1 gave higher OCV values (1.140 V) than SOFC-B1 did (1.080 V). The lower measured values compared to the predicted values may be caused by the low percentage (0.5%) of steam input to the FCM model, such as mentioned in section 4.4.1. Although the feed was dry H_2 and Helium, the way that H_2 was gradually introduced into the SOFC system may have produced a significantly higher value of steam than 0.5% in the SOFC anode. With higher than 0.5% steam presence in the anode, a lower OCV is expected from the measurement. In addition to the observed OCV values being lower than the predicted values; the fact that Case A gave higher OCV than Case B did is contrary to the values predicted by the FCM. This may indicate that other factors than H_2 partial and total pressures play a role in determining the actual cell potential. These factors can come from kinetics related to the fuel cell anode microstructure and porosity. Further explanations to this phenomenon are presented in the following sections.

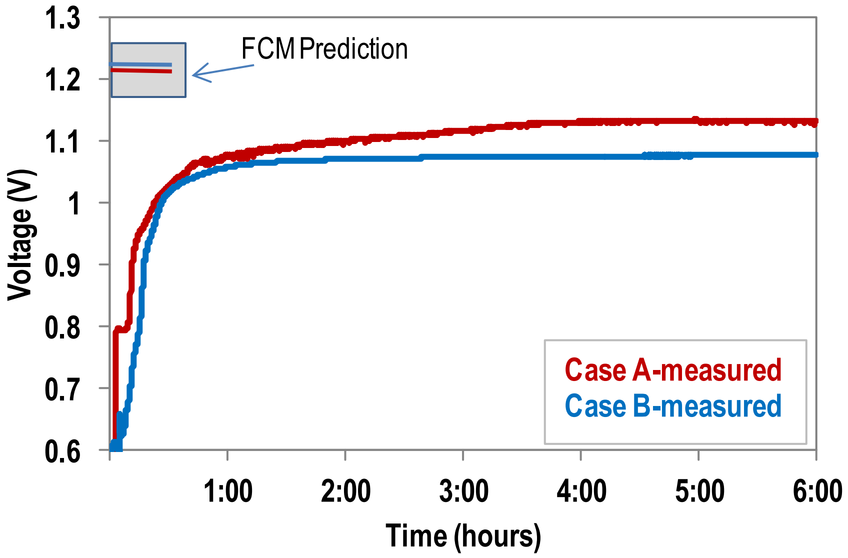

Figure 4.6: Measured OCV obtained from SOFC-A1 and SOFC-B1

4.4.2.2 Polarisation and power density curves

To obtain the performance of the cell as a function of current density, several polarisation curve measurements were performed. The measurements were performed by drawing current at continuously decreasing voltage from OCV down to 0.4 V and back to OCV. The measurements were performed at 6 hours, 12 hours, 19 hours and 26 hours. It was observed that electrochemical performance increased gradually from 6 to 26 hours of operation. The highest increase occurred during 6 to 13 hours operation. The increase in electrochemical performance was minimal during 6 to 13 hours. This significant increase of electrochemical performance during 6 to 13 hours and smaller increase during 13 to 26 hours of operation may be caused by the state of anode reduction and subsequent improvement of anode microstructure. Improvements of anode microstructure may results in better gas diffusion, electrochemical oxidation and electronic conduction. With the more complete NiO anode reduction, there will be at least two factors affected i) more nickel sites for electronic conduction and electrochemical oxidation, and ii) more pores for better gas diffusion. The two factors improve the electrochemical reactions, hence improve electrochemical performance, such as explained by Li et al.[147], Monzon and Laguna-Bercero [148], and Simonsen et al. [149]. Details of the explanation were discussed in section 4.2.5. In addition, according to Li et al. [147] NiYSZ reduction at 550 ^{o}C was completed in 4 to 5 hours, while these results showed that reduction at 750 ^{o}C needed at least 13 hours to complete. This can be related to the exothermic nature of NiO reduction [150, 151] which implies that at higher temperature, 750 ^{o}C instead of 550 ^{o}C, NiO reduction takes place more slowly.

Effects of contact time

Figure 4.7 presents the polarisation curves for Case A (SOFC-A1) and Case B (SOFC-B1) at 6 hours and 26 hours to show the cell performance improvement over 26 hours of operation. The figure also shows the results of the simulation run using the fuel cell model FCM [78, 152]. According to the simulation, as current density increases, Case A showed a slightly better performance. This means that as current density increases, polarisation resistance of Case A increases more slowly than that of Case B does. This is expected since three times more H_2 is present in Case A. The predicted better performance with Case A can be explained as follows;

- increase in current density increases H_2 consumption.
- The consumption of H_2 causes H_2 concentration depletion.
- Having 3x more H_2 available, the remaining H_2 in Case A is still high compared to that in Case B, although H_2 partial pressure in Case A is 20% less than that of Case B.

- Thus the effect of H_2 consumption in Case A results in less concentration polarisation, hence it is predicted that overall SOFC performance with Case A is slightly higher than that of Case B.

Contrary to the FCM predictions, the experiments showed that Case A gave significantly higher OCVs and higher polarisation losses which are contrary to the predictions obtained from FCM model. As was mentioned in previous section, other factors than H_2 partial and total pressures, such as those related to anode microstructures and fluid flow phenomena, may have contributed to the actual performance of these SOFCs. A possible explanation to these phenomena is the factor of contact time. The followings section includes the H_2 contact time in the SOFC anode into consideration.

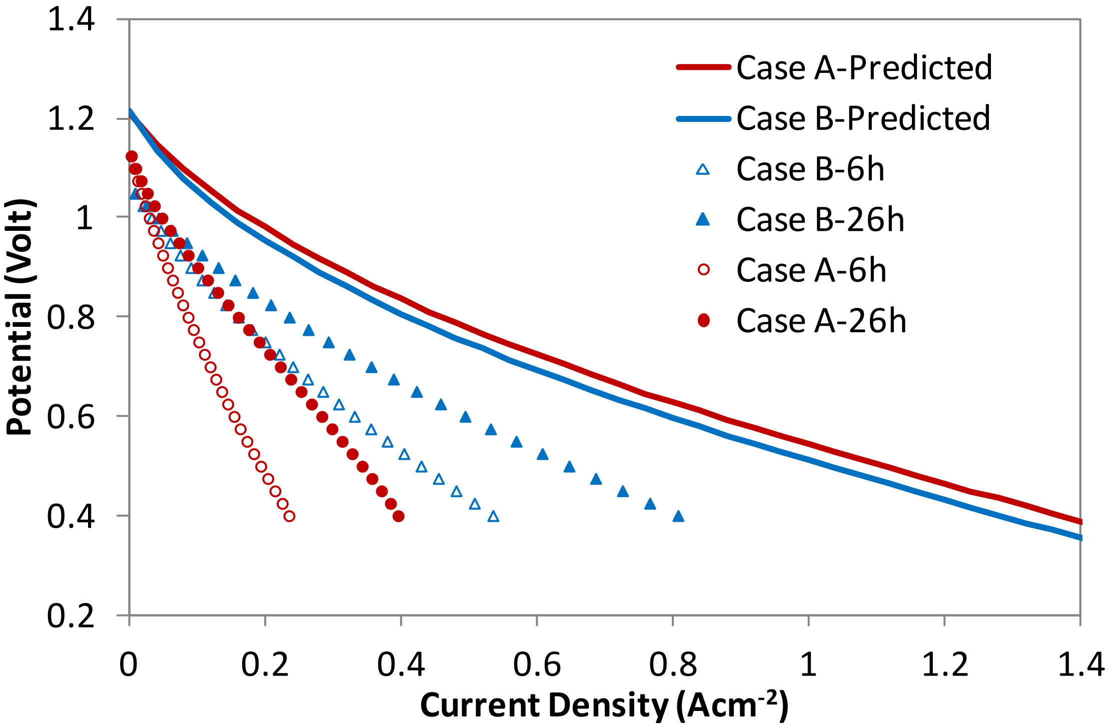

Figure 4.7: Comparison of polarisation curves of Case A and Case B obtained in the lab and predicted by Nernst's equation.

Assuming the fuel cell anode as a simple plug flow reactor [153] having a specific reactor volume determined by the anode's effective area, thickness and pore volume, the contact time of H_2 in Case A and Case B were calculated. The contact time is the reactor volume divided by the H_2 flow rate. The calculated contact time values are presented in Table 10. It is seen that the contact time for H_2 in Case B is almost three times longer than that in Case A. Given that a certain duration of time is needed for H_2 to diffuse into the anode pores, adsorb on nickel surface and eventually undergo electrochemical oxidation on the nickel surface near the electrolyte layer, it is expected that a longer contact time will result in a better chance for H_2 to undergo electrochemical oxidation more effectively, hence produce higher electrochemical performance.

Figure 4.8 a) and b) show polarisation curves for SOFC-A1 (Case A) and SOFC-B1 (Case B). According to Huang [154] who studied fuel utilisation (U_f) and fuel sensitivity of SOFCs based on calculations using Faraday's law and Nernst potential, the effects of fuel flow rate on the cell electrochemical performance is significant only at high values of $U_f \geq 80\%$. Nakajima et al. [155] also observed a significant effect of U_f on polarisation curves as U_f decreased from 80% to 40% but no significant effect as U_f decreased from 40% to 27%. However, in this study a significant effect of fuel feed flow rate was observed at such a low value of $U_f \leq 30\%$, therefore other factors may have been present and contribute to these polarisation characteristics. In addition Nakajima et al. [155] also observed a significant increase of electrochemical performance as H_2 partial pressure was increased from 0.2 to 0.33 but not so as the partial pressure was increased from 0.33 to 0.5. Therefore an increase of H_2 partial pressure from 0.6 to 0.75 in this study is not predicted to give a significant effect of increase in electrochemical performance. Again other factors than H_2 partial and total pressure may have contributed to the observed increase of electrochemical performance on changing the feed flow rates from Case A to Case B. The contact time, as explained above, may be one of the factors involved in these observed phenomena.

Another possible factor that may contribute to the low performance of the SOFCs from Case A compared to that from Case B is the presence of 40 ml min^{-1} helium in case A which is 5.7x higher than the helium present in Case B. This high flow rate of helium in Case A may have contributed to lowering the actual operating temperature, hence lowering the overall SOFC performance. In this work, the thermocouple for measuring and controlling the operating temperature was placed outside the SOFC at approximately 3 mm distance from the SOFC cathode side. This arrangement was set to maintain a safe condition; that is to prevent short circuiting between the thermocouple and the SOFC surface or the silver current collector wires. This way the actual temperature of the SOFC at the anode side was not measured. This absence of the data of actual anode temperature measured at each test makes it unable to present the effect of the difference in helium flow rates on the overall SOFC electrochemical performance. For future works it is recommended that a good deal of effort be made to be able to measure the temperature at the anode side so more detailed behaviour of the SOFC can be investigated and more understanding for better SOFC design can be achieved.

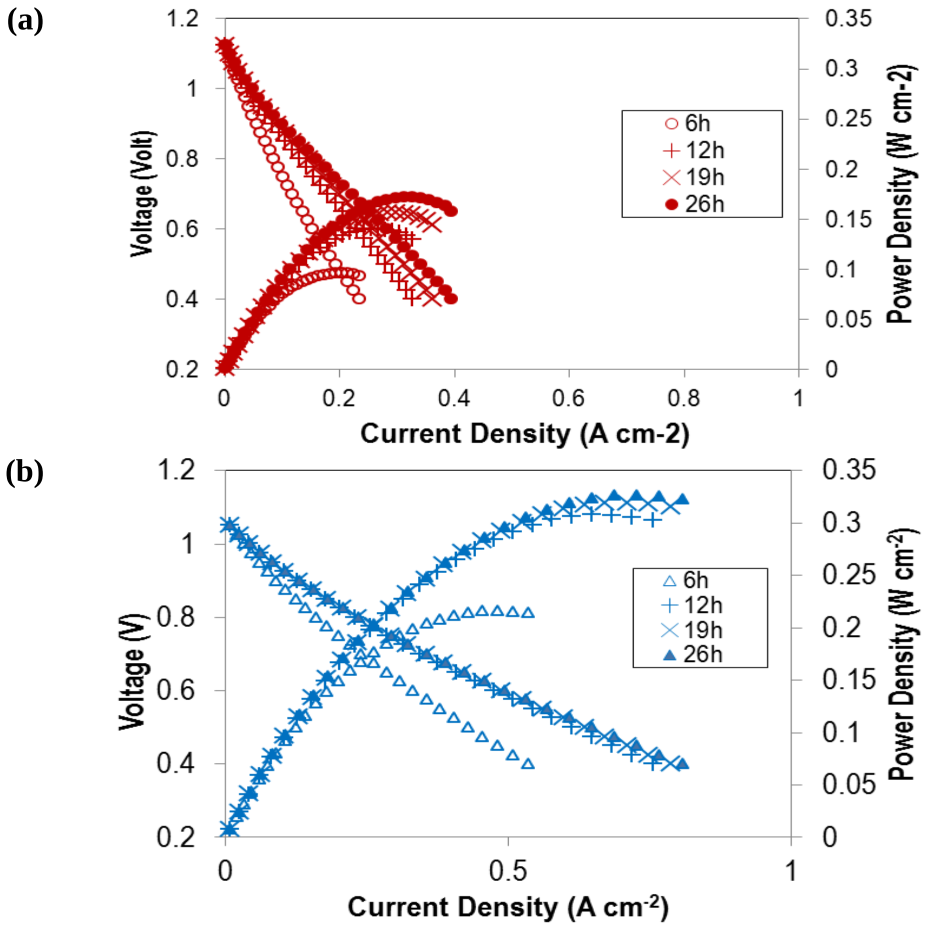

Figure 4.8: Electrochemical performance of (a) SOFC-A1 and (b) SOFC-B1

Table 10 lists the values of contact time, OCV, area specific resistance (ASR) at 0.8 V, current density and power density at half OCV values obtained from 2 repeats of SOFC tests with Case A and 4 repeats of SOFC tests with Case B. It is shown that SOFC-A1 and A2 gave maximum power of 172 mW cm^{-2} to 185 mW cm^{-2} and less than 9% fuel utilisation, while SOFC-B1 to –B4 gave 326 mW cm^{-2} to 420 mW cm^{-2} maximum power and between 46% and 55% fuel utilization. It is observed that a difference of 100 mW cm^{-2} maximum power density was observed between the lowest and the highest performing SOFC-Bs; this may be due to unavoidable variation in the actual effective cathode area of the first SOFCs manufactured. The nature of cathode hand painting and application of dense silver paste for current collections in the SOFC preparation stages may have contributed to this variation in the electrochemical performance among the SOFC-Bs. Nevertheless, all SOFC-Bs consistently showed much higher electrochemical performance compared to SOFC-As did.

Table 10 SOFC electrochemical performance operating on H_2 at 750 ^oC (26 hours)

Cell No.	H_2 Feed Flow rate (ml min^{-1} cm^{-2})	Contact time* (s)	OCV (V)	CD at max PD (A cm^{-2})	Max PD (mW cm^{-2})	ASR at 0.8V (Ω cm^2)	U_f at max PD (%)	CD at 0.7V (A cm^{-2})	U_f at 0.7V (%)
A1.	30.0	0.020	1.140	0.312	172	1.63	7.92	220	5.58
A2.	30.0	0.020	1.167	0.328	185	1.47	8.32	247	6.27
B1.	10.5	0.057	1.080	0.686	326	0.89	49.73	343	25.37
B2.	10.5	0.057	1.000	0.648	346	0.67	46.97	400	30.00
B3.	10.5	0.057	1.020	0.650	333	0.75	47.12	358	28.27
B4.	10.5	0.057	1.050	0.760	420	0.55	55.09	519	37.48

Note: CD = current density PD = power density U_f = fuel utilisation

4.4.2.3 Current produced at 0.7 V

The chart in Figure 4.9 shows the current produced during the 26 hours of operation at 0.7 V from six SOFCs tested with Case A and Case B. While SOFC with Case A gave a final current of 220mA indicating 5.58% fuel utilisation, SOFC with Case B gave a higher final current of 350 mA indicating 25.37% fuel utilisation. It would be ideal to obtain 85% fuel utilisation with the SOFC operating with Case B. The SOFC will produce current as follows:

$$(85\%) / (25.37\%) * 350 \text{ mA} = 1172 \text{ mA cm}^{-2} \text{ at } 0.7 \text{ V}$$

$$\text{or power as much as} = 0.7 \text{ V} * 1172 \text{ mA cm}^{-2} = 820 \text{ mW cm}^{-2}.$$

Based on the above result from Case B, the tested SOFCs can be categorised as in the low performance category. In other words these SOFCs still need improvements in order to demonstrate higher fuel utilisation and produce higher power. Which specific

SOFC properties need to be improved? These can be analysed using data of Electrochemical Impedance Spectroscopy (EIS) presented in the next section.

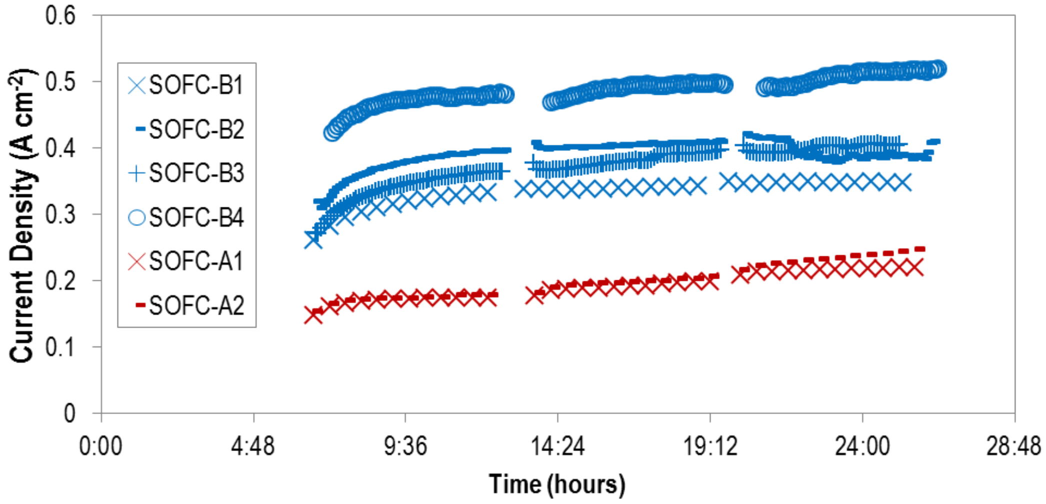

Figure 4.9: Current produced at 0.7 V from SOFCs with Case A and Case B

The results presented here also showed that feeding more fuel than the amount that can be electrochemically reacted in an SOFC may not necessarily increase the electrochemical performance but only wastes fuel. Therefore operating an SOFC with a low fuel utilisation is undesirable. However, operating an SOFC with too high fuel utilisation, for example 95% is not recommended since this will give 5% unreacted H_2 in the anode compartment. Too low H_2 partial pressure in the anode poses the risk of nickel anode to re-oxide. Therefore SOFC operating with 85% fuel utilisation is recommended and considered safe with regards to minimising the wasted fuel and also minimising the possibility of nickel re-oxidation [154].

4.4.2.4 Electrochemical Impedance Spectroscopy (EIS)

Electrochemical Impedance Spectroscopy measurements were carried out at OCV and 0.7 V every six hours of operation. The measurements were performed with a frequency sweep from 1 MHz to 0.1 Hz. Figure 4.10 presents the spectra at 6 hours and at 26 hours of operation, a) during OCV and b) during 0.7 V. The spectra show the Ohmic, $R_{Ohm,}$ and polarisation resistance R_p for the SOFC operated with Case A and Case B. The Ohmic resistance, $R_{Ohm,}$ is the point of intersection between the impedance semicircle (curve) and the real Z axis at high frequency region. The Polarisation resistance, R_p, is determined from the point at which the curve intersects the real (Z) axis at low frequency region minus the value of R_{Ohm} [156]. Figure 4.10b illustrates these features. R_{Ohm} represents the Ohmic resistance of the electrolyte, anode, cathode and current collectors. The value of polarisation resistance, R_p, represents the accumulated resistance from various kinds of reactions from fast reactions such as electronic and ionic charge transfer to slow reactions such as diffusion and mass transfer. These fast and slow reactions can appear in a Nyquist plot as several discreet or overlapping semicircles depending on the nature and the rate of each reaction that contributes to the overall fuel cell reactions.

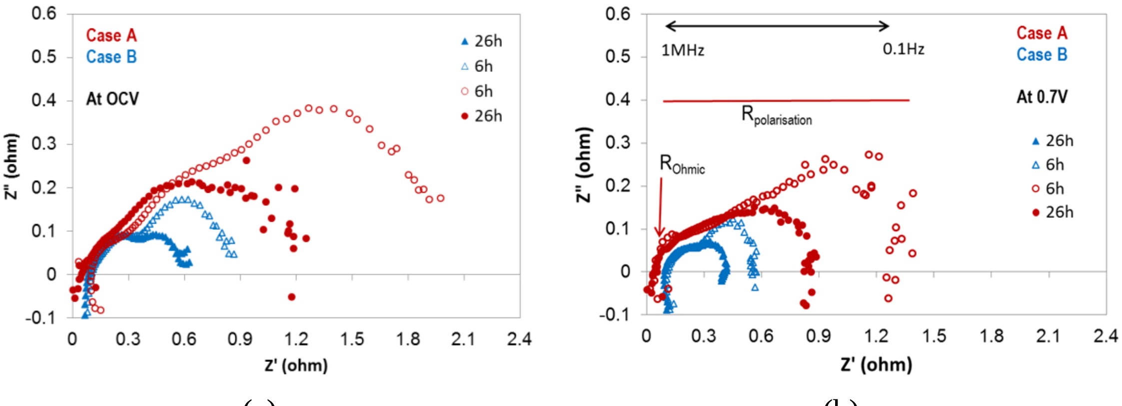

(a) (b)

Figure 4.10: EIS spectra at (a) OCV and (b) 0.7 V of SOFC-A1 (Case A) and B1 (Case B)

From Figure 4.10, it is observed that the values of R_{Ohm} of the SOFCs operating under Case A and Case B are acceptable. They all show $R_{Ohm} < 0.1\ \Omega\ cm^2$. Leonide et.al [156] reported R_{Ohm} of SOFCs similar to the ones used in this study as 0.15 Ω cm^2. They performed an extensive study of EIS spectra of anode supported NiYSZ based SOFCs fuelled by H_2 to find out the effects of various anode and cathode gas compositions and SOFC operating temperature on the EIS spectra. Their cell geometry was 1.5 mm thick anode with 10 µm electrolyte, 7 µm CGO interlayer and 45 µm LSCF electrolyte layer. The observation was under OCV mode. They used the distribution on relaxation time (DRT) method to identify at least three different processes occurring at each of the SOFC anode and cathode. They identified that the EIS spectra at high frequencies ranging from 1 kHz to 1 MHz are attributed to gas diffusions coupled with charge transfer reaction and ionic transport, while at frequencies of 4-20 Hz the EIS spectra are related to gas diffusion in anode substrate and at frequencies of 0.3-10 Hz the EIS spectra are related to gas (or air) diffusion in cathode side. When 10 ml min^{-1} cm^{-2} H_2 at 0.625 partial pressure and N_2:O_2 mixtures at the cathode side were used at 800 ^oC, they reported the SOFC's R_{Ohm} being 0.15 Ω cm^2 and the R_p being 0.38 Ω cm^2. As there are similarities in the cell geometry and operating conditions used in Leonide's work, these values of R_{Ohm} and R_p can be used as references in this study.

Figure 4.10 showed that the R_{Ohm} obtained are relatively constant both in Case A and Case B; in other words there are no significant Ohmic resistance change observed on changing the operating conditions from Case A to Case B, nor it is observed during operation at 6 hours and 26 hours. However, it is interesting to observe polarisation resistances decreased quite significantly both on going from Case A to Case B and on operating from 6 hours to 26 hours. The observed R_p value for Case B, 0.42 Ω cm^2, is only slightly higher than that obtained in Leonide's study which was 0.38 Ω cm^2. As presented in Table 11, in Case A at OCV, polarisation resistance decreased from 2.1 to 1.2 Ω cm^2; while at 0.7 V it decreased from 1.4 to 0.9 Ω cm^2 . In Case B at OCV polarisation resistance decreased from 0.9 to 0.6 Ω cm^2 ; whereas at 0.7 V it decreased from 0.6 to 0.4 Ω cm^2. As explained above, the polarisation resistance is related to the mass transfer properties of the system. A lower R_p means the mass transfer or gas diffusion is easier to take place. These improvements in mass transfer or gas diffusion properties may be caused by several factors such as improvements in the anode reduction state, the porosity or the tortuousity of the anode pores for gas diffusion [134].

Table 11 SOFC resistances obtained from EIS spectra of Case A and Case B

Case A						**Case B**					
R_{Ohm} (Ω cm^2)		**R_{total} (Ω cm^2)**				**R_{Ohm} (Ω cm^2)**		**R_{total} (Ω cm^2)**			
At OCV	**At 0.7 V**	**At OCV**		**At 0.7 V**		**At OCV**	**At 0.7 V**	**At OCV**		**At 0.7 V**	
		6 h	26 h	6 h	26 h			6 h	26 h	6 h	26 h
0.050	0.057	2.10	1.20	1.40	0.90	0.087	0.094	0.90	0.60	0.60	0.42

Further study on the EIS of these SOFCs operating with controlled conditions of anode and cathode gas flow rate may help to uncover the phenomena observed. In this study it is sufficient to obtain this evidence that the SOFC with Case B showed much lower polarisation resistance than the SOFC with Case A did. Consequently the SOFC with Case B showed higher electrochemical performance. Therefore, the SOFCs tested with Case B will be used for subsequent tests in biogas fuel.

4.5 Conclusions

The NiYSZ anode supported SOFCs were prepared by hand painting the LSM cathode layers onto the ready-made half cells. This preparation stage was followed by attaching silver wires, which function as current collectors, onto the anode and cathode surfaces using silver paste. Subsequent sealing of the SOFC onto the double alumina cylinder cell holder using thick Ag seal and curing the Ag seal for 1 hour at 800 ^{o}C with 5 ^{o}C min^{-1} heating rate were successful and produced gas tight SOFCs ready for testing.

The SOFC heating-up procedure at 5 ^{o}C min^{-1} without gas flow followed by gradually introducing Helium and H_2 gases at 750 ^{o}C, produced a good condition for subsequent electrochemical performance testing, without any seal or cell cracks observed during SOFC testing.

The gradual decrease of the SOFC polarisation resistance hence gradual improvement of SOFC performance over 26 hours of operation may be related to better anode porosity, and more continuous electrochemical conduction paths due to more complete anode reduction at prolonged SOFC operation.

The SOFCs being tested with Case B, showed consistently higher electrochemical performance compared to those tested with Case A. Comparison of the polarisation curves obtained from experiments with those obtained from fuel cell simulation indicated that these tested SOFCs show good activation for hydrogen electrochemical oxidation with low Ohmic resistance. However, the SOFCs suffered from much concentration polarisation at increased current density which indicated that H_2 depletion occurred in the anode functional layer while much H_2 remained unreacted in the anode compartment.

Electrochemical Impedance Spectroscopy (EIS) and Area Specific Resistance (ASR) measurements revealed that the SOFCs tested with Case B demonstrated much lower polarisation resistances; hence much higher power produced across 0.0-1.4 A cm^{-2} current densities. This lower polarisation resistance may be attributed to better (longer) contact time which allowed sufficient time for H_2 molecules to adsorb on Ni surfaces. Consequently, the H_2 in the SOFCs with Case B 'appear' to undergo electrochemical oxidation more easily, hence lower charge transfer resistance and generally lower polarisation resistance.

The condition of Case B is used for subsequent electrochemical performance testing on biogas. The average values of electrochemical performance of the four SOFCs tested with Case B were 367 mA cm^{-2} at 0.7 V with 0.71 Ω cm^2 ASR at 0.8 V. The average value of their Ohmic resistance was 80 mΩ cm^2.

Chapter 5

Tin-infiltration on SOFC Anodes

5.1 Overview

This chapter describes Ni/Sn alloy properties, applications, and methods of Ni/Sn alloy formation. It then describes the method of Sn-infiltration used in this work to obtain Ni/Sn alloy in the SOFC anodes. The chapter concludes with the Sn-infiltrated anode material characterisation. Sn-infiltration on NiYSZ-based SOFC anodes is aimed to provide stable Ni/Sn alloy(s) which will improve the catalytic activity of NiYSZ towards biogas reforming by minimising C-C bond formation and maintaining good properties of NiYSZ as SOFC anodes with respect to electrochemical conductivity and porosity. To obtain the Ni/Sn alloy, Sn and Ni-metals need to be in contact with each other in a controllable atmosphere at elevated temperature for a certain length of time. The SOFC test condition at 750 ^{o}C with H_2 or CH_4 as gas feed is expected to be a suitable condition for formation of Ni-Sn alloys. Approximately, a 1% weight Sn over Ni in the bulk SOFC anode is targeted to be obtained from Sn-infiltration.

5.2 Overview of Ni/Sn alloy properties and applications

5.2.1 Ni/Sn phase diagram

The binary phase diagram for the Ni/Sn system has been intensively investigated since the 1930s. Several reassessments of the phase diagram were carried out in the 1980s. The most recent reassessment was performed by Schmetterer and co-workers in 2007 [157]. Their study into the detailed phase transformations within the Ni/Sn system has resulted in the re-assessed Ni/Sn phase diagram as presented in Figure 5.1. At least five Ni/Sn phases, namely Ni_3Sn_LT, Ni_3Sn_HT, Ni_3Sn_2_LT, Ni_3Sn_2_HT and Ni_3Sn_4, exist at various Ni/Sn compositions and temperatures as illustrated in Figure 5.1.

According to the Ni/Sn diagram presented in Figure 5.1, it is possible to obtain Ni/Sn alloy during the SOFC anode reduction at 750°C, provided that the SOFC anode is adequately infiltrated by a suitable Sn precursor.

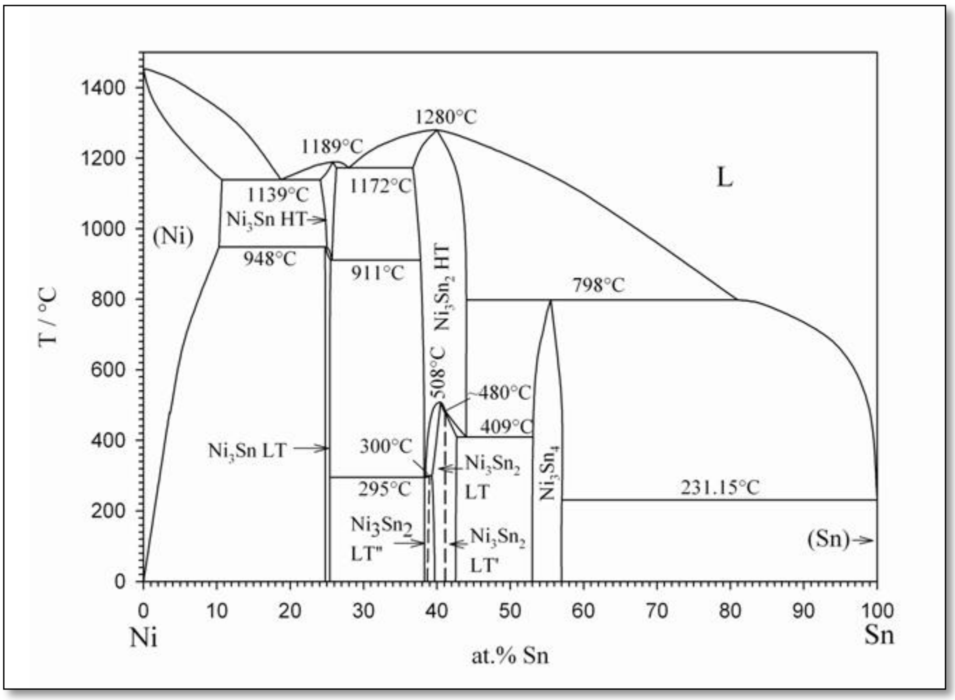

Figure 5.1: Ni/Sn phase diagram [157]

Enthalpies of formation, $\Delta_f H$, of Ni/Sn compounds have been measured using direct reaction calorimetry by Vassilev et al. [158]. All five Ni/Sn phases show slight exothermic reactions with $\Delta_f H$ values ranging from -21 to -35 kJ mol^{-1} while solid Ni (f.c.c. Ni) and liquid Sn were used as standard states. Table 12 presents the standard enthalpy values for each Ni/Sn phase obtained from corresponding alloying conditions. Vassilev and co-workers utilised electron probe microanalysis and high and room temperature XRD to verify the compositions of the alloys.

Table 12 Enthalpies of formation of different Ni/Sn phases [158]

Ni-Sn phases	$\Delta_f H$ (kJ mol^{-1})	Alloying conditions	Comments
Ni_3Sn_LT	-24.4 ±1.2	670 ^{o}C, 6 hours	
Ni_3Sn_HT	-21.0 ±02.4	1059 ^{o}C, 15 min	
Ni_3Sn_2_LT	-29.0 ±0.9	455 ^{o}C, 6 hours	Also contains Ni_3Sn_4 (26)%, Ni_3Sn (3%), pure Ni (12%)
Ni_3Sn_2_HT	-35.0 ±0.2	1015 ^{o}C, 15 min	
Ni_3Sn_4	-29.8 ±1	573 ^{o}C, 7 hours	

5.2.2 Ni/Sn applications

5.2.2.1 As a catalyst for hydrocarbon reforming

As was described in Chapter 2, Sn has been used as a dopant for Ni catalysts to reduce carbon formation in hydrogen production from methane steam reforming [48-51]. Sn-promoted Raney-nickel catalysts have also been used as a replacement for platinum-based catalysts in aqueous phase reforming of biomass derived hydrocarbons such as ethylene glycol, sorbitol, or glycerol [52]. Nikolla et al. [96-98] reported that they "*identified Sn/Ni surface alloy as a potential carbon-tolerant reforming catalyst"*. Their reactor studies showed that *"Sn/Ni was much more carbon-tolerant than monometallic Ni in the steam reforming of methane, propane, and iso-octane at moderate steam to carbon ratio.*

5.2.2.2 As a high temperature corrosion resistant material

For their excellent features of mechanical properties and chemical and tarnish resistance, Ni/Sn alloys have found applications in the fields which require corrosion resistant materials. The alloys have been produced for several commercial uses such as in electroplating as a base coating underneath a chrome plating [159], as a potential alternative to lead free solder and in special stainless steel materials where Ni/Sn is added to obtain high corrosion resistant stainless steel for severely corrosive environments [160, 161].

5.2.2.3 As anodes in Li-ion batteries and in SOFCs

Other uses of Ni/Sn alloys are in the field of Li-ion batteries [162, 163]; Ni/Sn-alloys in Li-ion battery anodes showed higher current capacity compared to the anodes without Ni/Sn. More recently, compared to the performance obtained with NiYSZ anodes, Sn-doped NiYSZ-based SOFC anodes have been reported to show better performance in SOFC fuelled by methane and iso-octane, in steam reforming mode [73]. Nikolla [99, 139] stated that their Sn-doping on NiYSZ anode formed Ni/Sn surface alloys and Bogolowski [103] clearly stated that their Sn-doping on NiYSZ anode formed a Ni/Sn alloy of the Ni_3Sn_2 phase.

5.3 Methods of Ni/Sn alloy formation

5.3.1 Previous studies, general methods of Ni/Sn alloy formation

Depending on the applications, various different methods of Ni/Sn alloy formation have been used. Huber [52] used decomposition of tri-butyl-Sn-acetate in Raney-nickel to improve catalytic activities of Raney-nickel for reforming of biomass derived hydrocarbons. Nikolla [73, 96, 97, 99, 139] and Kan [100, 101] used incipient wetness impregnation of NiO powder followed by calcinations and reduction at high temperature to obtain Sn-doped NiYSZ SOFC anodes. Other methods of alloying such as electrodeposition of a mixture of Ni and Sn salt solutions [159-161], formation of a solid metal solution followed by heat treatment [164], arc melting of a mixture of pure Ni and Sn metals [157, 158] have been developed to obtain Ni/Sn alloys. Table 13 presents these methods with the operating conditions used for Ni-Sn alloying.

Table 13 Methods of Ni/Sn alloy formation

No.	Ni/Sn alloy applications	Alloy formation methods	References
1.	Promoter for Ni catalysts in production of H_2 via aqueous phase hydrocarbon reforming	Decomposition of tri-butyl Sn acetate	[52]
2.	High corrosion resistant materials	Metal powder milling at room temperature for 5 hours and heat treatment for at least 10 minutes at 800-1100 ^{o}C	[164]
3.	Lead free soldering	Arc melting a mixture of pure Ni (sheet) and Sn (rod or ingot)	[157, 158]
		Heat treatment of pure Ni and Sn (powder) mixture in a shield quartz tube at 1050 ^{o}C for 6 days	[157, 158]
4.	Anode in Li-ion batteries	Electrodeposition of a mixture of Ni and Sn salt solutions at room temperature using different cathode current densities.	[159] [160, 161]
5.	Anode in SOFC	Impregnation of NiO powder by incipient wetness technique followed by calcinations and reduction	[101]; [97-99, 139]
		Melting stoichiometric amount of Ni and Sn metals in a centrifugal casting oven	[103]

Various proven methods of Ni/Sn alloy formation were described. In principle it is possible to obtain a Ni/Sn alloy as long as Ni and Sn metals are in good contact with each other and contained in a controlled inert or reducing atmosphere at high temperature. The Ni and Sn precursors are not limited to the metallic state but can be in the form of salts or oxides as long as appropriate processes are performed to bring those salts or oxides into the metal form. A temperature as low as 455 ^{o}C with 6 hours contact time or 1000 ^{o}C with only 15 minutes contact time is sufficient to form the desired Ni-Sn alloy. Regarding the Ni/Sn alloy formation for SOFC anodes, the suitable methods would be the incipient wetness impregnation (or infiltration) of NiO powder such as reported by Kan [100, 101] and Nikolla [97-99, 139], or an adapted version of the incipient wetness impregnation for use with ready sintered anode discs.

5.3.2 Methods of Sn-anode infiltration

Three methods of infiltration were approached. Pipette drop and sonic immersion using Sn-dopant solution and powder blending using SnO_2 powder. To prepare the Sn-dopant solution, tin in the form of $SnCl_2.2\ H_2O$ was dissolved in 95% ethanol and placed in an ultrasound bath for 15 minutes to dissolve all the $SnCl_2$ particles. For a successful Ni/Sn alloy formation on the sintered SOFC anode, several criteria of the anode and dopant material such as listed below should be taken into consideration;

i. the sintered anode should have continuous pores throughout the bulk anode,
ii. the dopant should be in a form of solution; a suspension or emulsion may not be as effective in transferring the dopant throughout the pores,
iii. the solution should show pH-neutral; otherwise a slightly acidic or basic dopant solution may totally or partially dissolve the NiYSZ anode and significantly alter the anode microstructure,
iv. the dopant solution should be able to wet the NiYSZ pores and be easily dried leaving well distributed thin films of solid dopant salt adhering to the pore wall,
v. the dopant solution should not cause any harmful side reactions with any component (element) in the NiYSZ anode,
vi. the thin solid dopant should be able to calcine (react with O_2 to form oxides), and

vii. the thin film of dopant oxide should further be able to reduce to a metal state and form an alloy with the Ni substrate.

5.3.2.1 Pipette drop (P-drop)

In pipette drop infiltration, using a 2.5 ml plastic syringe fitted with a needle this dopant solution was carefully dropped on to the middle part of the NiYSZ anode surface. The drop was allowed to dry in air for 30 minutes; then drying was continued in a drying oven kept at 70 °C for 15 minutes. A further drying at 100 °C for 1 hour was performed before calcinations in air at 600 °C for 2 hours. The heating and cooling rate for calcinations was kept at 2 °C min^{-1}. This infiltration, drying and calcinations steps were repeated several times until the desired amount of Sn/Ni was sufficiently deposited onto the NiYSZ anode surface. Figure 5.2 represents the temperature profile for drying and calcinations of the Sn-infiltrated SOFC anodes.

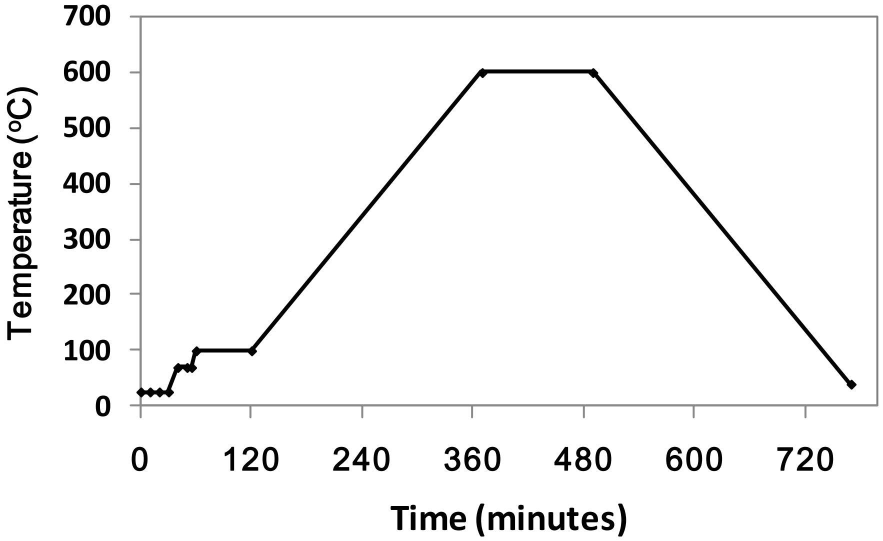

Figure 5.2: Temperature profile for calcinations of Sn-infiltrated SOFC anodes

5.3.2.2 Sonic immersion (S-imm)

In the sonic-immersion infiltration, 6 anode discs were immersed in a beaker glass containing $SnCl_2.2H_2O$ solution. The beaker glass was placed in an ultrasound bath at 40 ^oC for 1 hour. At 15, 30 and 60 minutes of immersion two discs were consecutively withdrawn from the $SnCl_2.2H_2O$ solution and were dried and calcined in the same procedure as the drying and calcinations procedures outlined above.

5.3.2.3 Powder blend (P-blend)

To explore possibilities of infiltration on NiO powder in in-house anode support manufacturing, a third method of infiltration was tried, i.e. the powder blending method. This method was used to dope Sn on NiO powder right from the beginning of Ni/YSZ anode support preparation. The aim was to produce Sn/Ni SOFC anodes using in-house manufacturing method [28]. For this method of infiltration, Sn in the form of fine SnO_2 powder was used as Sn-precursor. A certain amount of SnO_2 powder, to make 1-5 weight % of Sn over Ni, was added to the NiO/YSZ mixture for pellet pressing. The presence of Sn in the early stage of NiYSZ powder preparation was expected to provide a homogeneous distribution of Sn/Ni in the bulk NiYSZ powder. The application of this doping method should not be limited to manufacturing anode support using pellet pressing but this procedure should also be suitable for other manufacturing methods such as tape casting or extrusion. Figure 5.3 represents a simplified illustration of the three infiltration methods attempted.

(a) Pipette-drop **(b) Sonic immersion** **(c) Powder blend**

Figure 5.3: Illustration of pipette-drop, sonic-immersion and powder-blend infiltration methods

Between the two methods of infiltration attempted on sintered anode discs, the pipette drop method was the one which can be used for further observations of SOFC electrochemical performance. The sonic immersion technique was found to interfere with subsequent manufacturing stages; the infiltration caused delamination of electrolyte and cathode layers. On sonic immersion of anode support discs, electrolyte layer delamination was thought to have been related to the formation of a thin SnO layer on the anode surface where the YSZ electrolyte is later coated. This thin SnO layer blocked the supposedly continuous interface layer of YSZ electrolyte and NiYSZ anode, caused interlayer mismatch of the thermal expansion coefficient and subsequent electrolyte delamination. Likewise, on sonic immersion of half cells, cathode layer delamination was later observed and this is thought to have been caused by formation of a thin SnO layer on the electrolyte surface where the cathode is deposited. Again, the SnO layer prevented the formation of a supposedly continuous interface layer of YSZ electrolyte and LSM-YSZ cathode, causing the cathode layer to flake off.

Table 14 presents a summary of the results of the two methods of infiltration plus the trial of powder blending method.

Table 14 Observations of three infiltration techniques

Types	**Results**	
	Positive points	Negative points
P-drop	The amount of Sn infiltrated can be directly calculated and measured. Flexible, in that it can be performed on anode supports, anode-electrolyte half cells, or full cells.	In lab scale and using manual pipette drop, it requires careful attention and can only be done one cell at a time
S-imm	Can be performed on several cells simultaneously. Sn distribution over anode surface is expected to be homogenous across the anode surface	SnO layer formed on electrolyte side causes electrolyte and cathode layers to delaminate
P-blend	Can be performed during early stage of anode support manufacturing and quite promising for bulk manufacturing.	Currently in our lab, it cannot be further studied due to not yet established electrolyte screen printing and co-sintering procedures. As an Sn precursor, SnO_2 was better than $SnCl_2.2H_2O$. The latter caused longer drying and grinding time.

With the powder blending method, further examination of the infiltrated SOFCs were not possible since it could not be supported by subsequent manufacturing stages required to enable cell testing. The method of electrolyte screen printing on anode active layer and co-sintering of anode and electrolyte layers still produced slightly curved half-cells with some cell cracks and micro-cracks. Since optimising those stages of SOFC manufacturing (electrolyte screen printing and co sintering) were beyond the scope of this work, this powder blending technique could not proceed to the SOFC testing stages.

5.3.3 Characterisation of Sn precursor

5.3.3.1 TGA/DSC of $SnCl_2.2H_2O$ as a Sn precursor

To be able to closely predict chemical and physical changes occurring during the Sn-infiltration and calcinations, thermogravimetric analysis was performed on $SnCl_2$ $2H_2O$ powder which was used as a precursor to the Sn metal. An amount of 10mg $SnCl_2$. $2H_2O$ sample was placed in a small alumina crucible in the TGA sample holder. A mixture of N_2 (at 200 ml min^{-1}) and O_2 (at 50 ml min^{-1}) was allowed to pass through the $SnCl_2$. $2H_2O$ salt sample to observe the weight and enthalpy changes during heating from ambient temperature through to 900 ^{o}C. The heating rate was set at 10 ^{o}C min^{-1}. Figure 5.4 shows thermogravimetric analysis curves of heating $SnCl_2.2H_2O$ in a 4:1 volume ratio of N_2:O_2 from ambient temperature to 470 ^{o}C. The curve from 470-900 ^{o}C was not shown as it showed constant weight and enthalpy values, indicating a stable oxide, SnO_2, was formed.

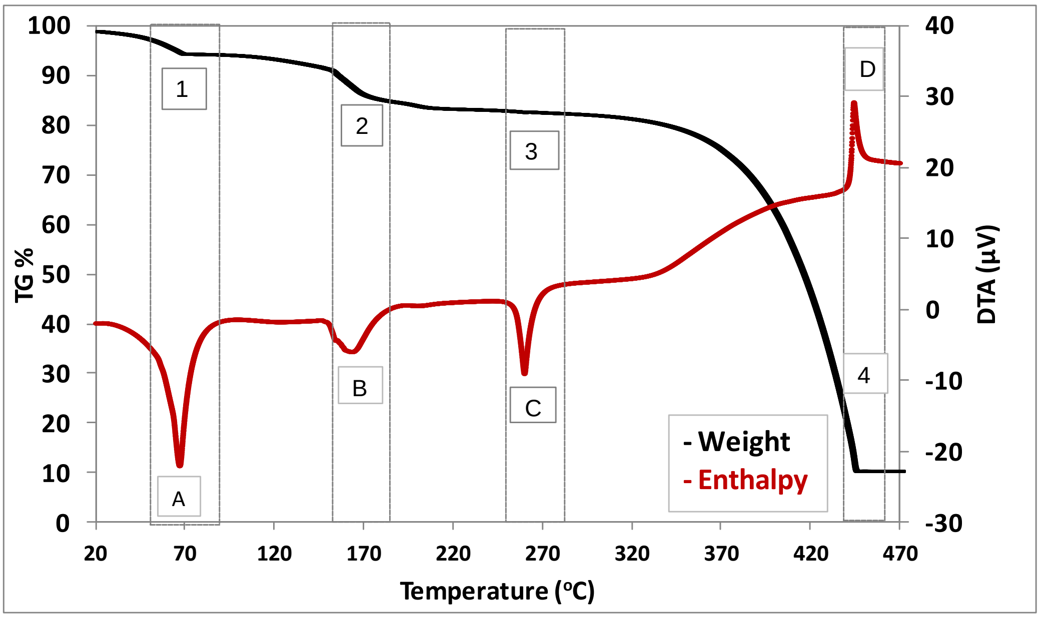

Figure 5.4: TG% and DTA of $SnCl_2.2H_2O$ at 10 ^{o}C min^{-1} heating rate

The black coloured curve in Figure 5.4 represents the sample weight (TG %) relative to the original weight while the red coloured curve represents the differential thermal changes. Three regions of significantly sharp weight loss are found in the TG% curve. These are marked as region 1 (70 ^oC, 95.26%), region 2 (170 ^oC, 85.56%) and region 4 (320-450 ^oC, 80-10%). One region of gradual weight loss is marked as region 3. Meanwhile 4 significant thermal changes are observed; these are three troughs of endothermic reaction marked with A, B, C, and one peak of exothermic marked with D. A gradual thermal change is seen between C and D.

The two weight losses at region 1 and 2 correspond to the two endothermic troughs at A and B. The mass loss at region 1 which corresponds to trough A in enthalpy change and occurred at 70 ^oC corresponds to evaporation of moisture adhering to the surface of $SnCl_2.2H_2O$ crystals, whereas the weight loss at region 2 with corresponding endothermic trough B correlates to evaporation of 2 moles of water molecules from each mole of $SnCl_2$ crystals. At the end of region 2, the remaining weight is very close to the calculated initial weight minus the loss of 2 moles of water (84%). The loss of 2 moles of water in $SnCl_2.2H_2O$ will make 16% weight loss and will leave 84% weight of $SnCl_2$ remaining.

At 247 ^oC the $SnCl_2$ starts to melt. The endothermic trough C indicates the enthalpy of melting of $SnCl_2$. At 350 ^oC the $SnCl_2$ starts to evaporate quite rapidly but some $SnCl_2$ also starts to react with O_2 to form the unstable SnO and further react with O_2 to form stable SnO_2. Had all $SnCl_2$ reacted with O_2 to form SnO_2 and no $SnCl_2$ evaporation occurred, 66.5% (corresponding to the weight which would remain when all

$SnCl_2.2H_2O$ decomposes to SnO_2) would have been observed on TG%. However there was no sign of any TG% shoulder at 66.5% meaning some $SnCl_2$ did evaporate. At 450 ^oC the evaporation of $SnCl_2$ ended, no more weight loss was observed and 10% of the weight of the initial $SnCl_2.2H_2O$ was left as SnO_2 (yellowish white in colour, boiling point 623 ^oC)

The next region of weight loss occurring between 280-450 ^oC is a gradual loss followed by a rapid loss. At region C (280 ^oC) a small endothermic trough is observed but weight loss is not so obviously observed. It means that no significant chemical reaction is occurring. However the gradual weight loss shows a small endothermic through at C and the rapid weight loss did not show sharp endothermic or exothermic reactions. On the contrary, there is an exothermic peak at D without weight loss recorded. This region from C to D is considered to correspond to partial calcinations from $SnCl_2$ (to SnO and SnO_2) but accompanied by vaporisation of $SnCl_2$. Vaporisation of $SnCl_2$ seems to be faster than calcinations between 370-420 ^oC.

5.3.4 Chemical reactions involved in the Sn-infiltration stages

Based on the TGA and DSC curves and visual observations, the proposed reactions occurring during drying and calcinations are listed in Table 15. Table 15 also lists the proposed reduction and alloy formation reactions preceding the cell testing.

Table 15 Proposed reactions occurring during calcinations, reduction and alloying

Infiltration stage	Reactions
Drying at 70 °C and 100 °C (Solvent evaporation)	$C_2H_5OH_{(liq)} \rightarrow C_2H_5OH_{(vap)}$ $H_2O_{(liq)} \rightarrow H_2O_{(vap)}$
First stage calcinations up to 200 °C (anhydrous $SnCl_2$ formation)	$SnCl_2.2H_2O \rightarrow SnCl_2 + 2H_2O_{(vap)}$
Further heating to 600 °C during calcinations ($SnCl_2$ evaporation and calcinations)	$SnCl_{2\,(solid)} \rightarrow SnCl_{2\,(liq)}$ Partial $SnCl_{2\,(liq)} \rightarrow SnCl_{2\,(vap)}$ Partial $SnCl_2 + \frac{1}{2} O_{2\,(g)} \rightarrow SnO + Cl_{2\,(g)}$ $SnO + \frac{1}{2} O_{2\,(g)} \rightarrow SnO_2$
Reduction with H_2 at 750 °C	$SnO_2 + 2\,H_{2\,(g)} \rightarrow Sn + 2\,H_2O_{(vap)}$ $NiO + H_{2\,(g)} \rightarrow Ni + H_2O_{\text{vap)}}$
Alloy formation at 750 °C	Ni + Sn → Ni-Sn alloys

5.4 Results

5.4.1 Gravimetric analysis of Sn-infiltrated SOFC anodes

Figure 5.5 presents results of averaged SnO_2 weight gained from 13 samples of anode supports treated with repeated infiltration. The 13 samples were firstly doped with 2 drops of dopant and then dried and calcined. The samples weight was measured post calcinations. Then these samples were given 2 more drops of dopant and dried, calcined and weighed. The procedure was repeated until 28 drops of dopant were added. Since the weight gain was measured post calcinations, the Sn compound obtained was SnO_2 since SnO_2 is the more stable oxide between the two most commonly occurring Sn-oxides, stannous oxide (SnO) and stannic oxide (SnO_2). Figure 5.5 shows that increasing the number of drops of dopant solution resulted in a consistent gain of weight of SnO_2. This indicates that the pipette drop method is repeatable and reliable to use as an infiltration method.

Each drop of dopant solution was 20 µl and contained 1.05 mg of Sn in the form of $SnCl_2.2H_2O$. How much weight of SnO_2 expected can be calculated from the concentration of Sn in dopant solution. This can then be compared against the actual SnO_2 obtained. Since each SOFC disc (button cell) contains 50% NiO and the average weight of one anode support disc is 1240 mg, it follows that one anode support contains 620 mg of Ni.

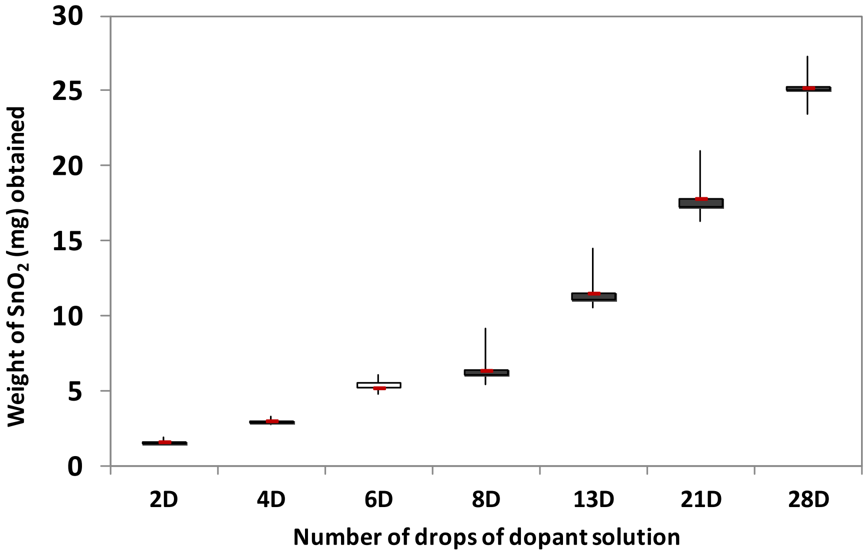

Figure 5.5: Weight of SnO_2 obtained after Sn infiltration on SOFC anodes

From these data, the Sn/Ni weight % in each SOFC infiltrated with a number of drops of dopant solution can be predicted. Figure 5.6 presents two pairs of comparison between predicted and experimental data; the first pair is the Sn/Ni weight % (black) and the second pair is the SnO_2 weight (red) obtained. Comparison of SnO_2 weight (red triangles) shows that roughly 30-40% of SnO_2 is lost. Consequently, roughly 30-40% of Sn/Ni weight % is also lost. This loss is associated with the partial evaporation of $SnCl_2$ as explained by TG% and DSC curves in Figure 5.4. However, not all $SnCl_2$ evaporated, a substantial part of $SnCl_2$ was able to react with O_2 to form unstable SnO which then turned to more stable SnO_2. Figure 5.6 shows that 60-70% SnO_2 was deposited on the anode surface. This yield of SnO_2 is significantly higher than the SnO_2

obtained in heating up pure $SnCl_2.2H_2O$ during TGA measurement. The reason for this higher yield of SnO_2 in the actual infiltration may well be associated with a slower rate of evaporation of liquid $SnCl_2$ occurring in anode pores. This leaves more molecules of liquid $SnCl_2$ on the anode pores to be in contact with O_2 to form a thin solid film of SnO_2. This slower rate of $SnCl_2$ evaporation may be associated with several factors as follows;

- the geometry of the anode pores,
- the slower ramp rate during calcinations,
- the stagnant air present in calcinations compared to flowing N_2:O_2 which was used in TGA/DSC analysis

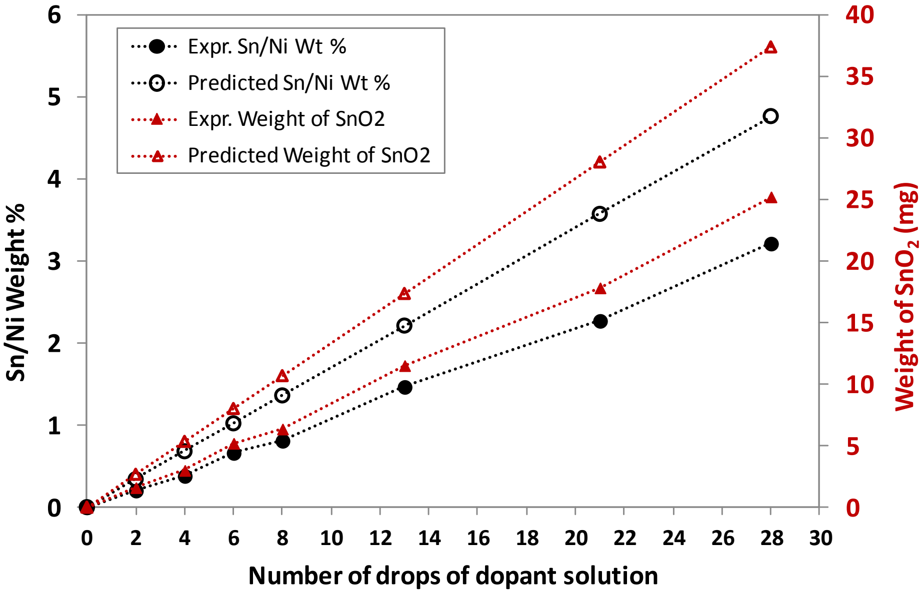

Figure 5.6: Weight percent of Sn/Ni in Sn-infiltrated SOFC anodes

From the chart in Figure 5.6 it is observed that to obtain 1% weight Sn/Ni in the bulk SOFC anodes, 6 to 10 drops of dopant is needed on 1 piece of SOFC with roughly

600 mg of Ni content in the anode. This is the base to which different dopant amounts are infiltrated onto the SOFC anodes tested for biogas fuel such as presented in Chapter 8.

5.4.2 Characterisation of Sn-infiltrated anode

5.4.2.1 XRD

Figure 5.7 represents overlapped XRD spectra of a 6D- Sn infiltrated SOFC anode and the non-infiltrated anode surface. The sample was examined in the disc form (not powdered). According to gravimetric analysis, this sample contained 0.7 weight % Sn/Ni or 0.34 Atomic % Sn. Referring to the Ni-Sn phase diagram in Figure 5.1 at 750 ^{o}C alloying temperature as used in our study, the possible phases of Sn-Ni alloy formed are Ni_3Sn_LT, Ni_3Sn_2LT, and Ni_3Sn_2_HT depending on the Ni-Sn atomic composition.

The spectra show the characteristic peaks of Ni and YSZ along the 2θ values. However, the XRD spectra of the 6D Sn-infiltrated NiYSZ do not show any obvious presence of Ni/Sn phases. This is understandable since according to the Sn/Ni phase diagram any Sn in Ni alloy at <5 atomic % would be soluble in the Ni phase, in other words there will be no Sn/Ni phase observed. Even with the 28D-Sn-infiltrated anodes sample, the anode with the highest load of Sn, no Sn/Ni phase will be observed as the 28D-Sn-infiltrated anode only contain 4.77 weight % Sn or 2.3 atomic % Sn, which is still lower than the 5 weight % Sn minimum limit of XRD detection.

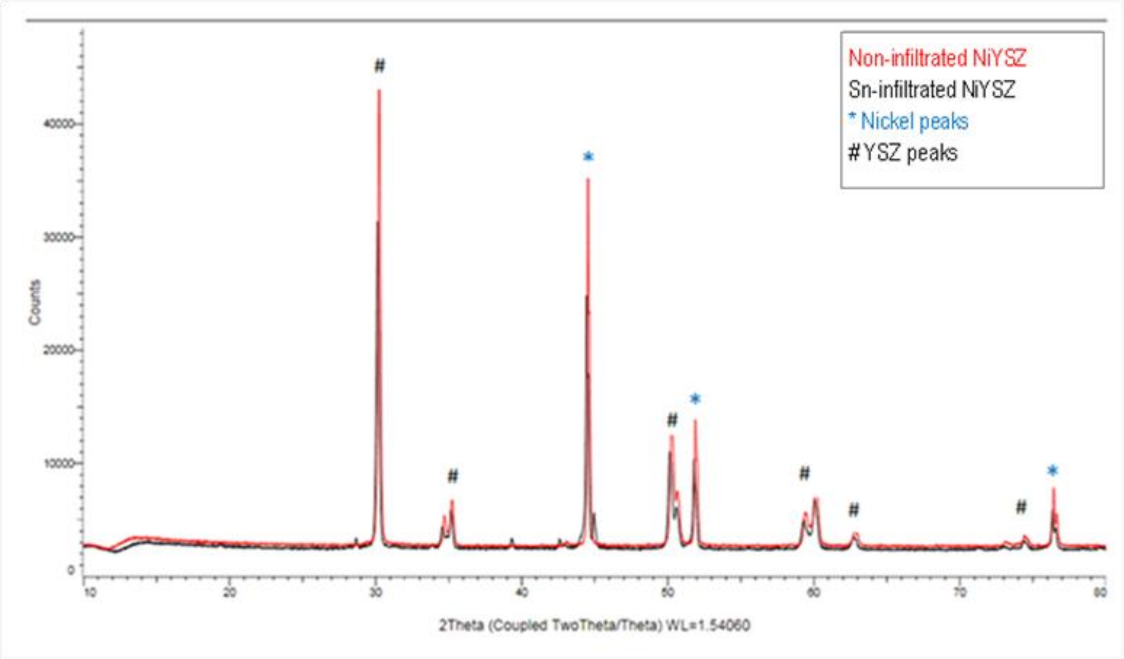

Figure 5.7: XRD spectra of SOFC anodes, 6D SnNiYSZ and NiYSZ

5.4.2.2 <u>SEM and EDX</u>

SEM/EDX was used to characterise the cell microstructure. Figure 5.8 a) shows part of the anode and electrolyte layer while Figure 5.8 b) represents the anode surface showing the distribution of Ni-rich parts and Zr-rich parts.

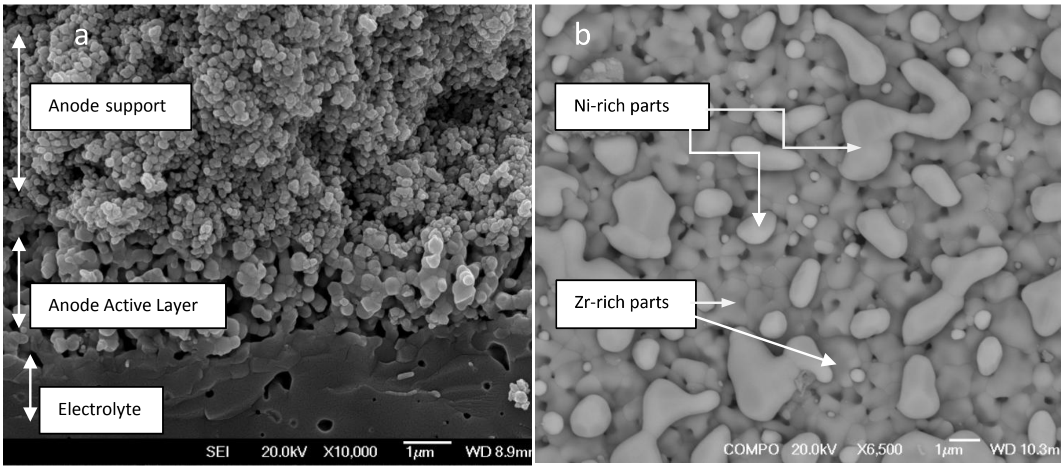

Figure 5.8: (a) a cross sectional area of a reduced Sn-infiltrated NiYSZ cell showing part of the anode support, anode active and electrolyte layers and (b) anode surface showing Ni-rich and Zr-rich parts.

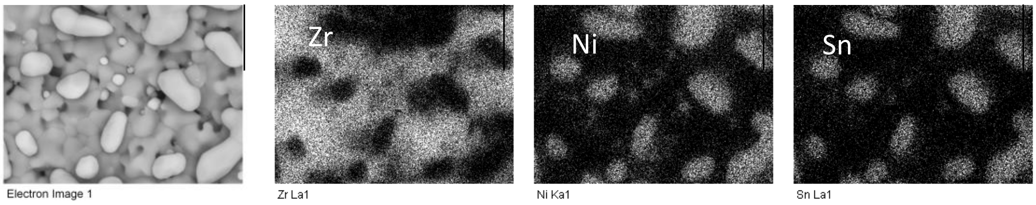

Figure 5.9: EDX map of the 6D-SnNiYSZ anode surface showing the distribution of Zr, Ni and Sn

Figure 5.9 shows EDX mapping of Zr, Ni and Sn on the 6D Sn-infiltrated anode surface. This image shows that on the anode surface Zr forms a more continuous part compared to Ni. It is also shown that anode pores are of less than 1µm diameter. The EDX map confirms that Sn is present and well distributed over the Ni particle sites. The image was taken from a 6D-Sn-infiltrated and reduced NiYSZ anode surface.

5.4.2.3 XRF and XPS

Table 16 represents the chemical composition of 28D-Sn-infiltrated SOFC anode support obtained from X-ray fluorescence spectra of an anode support sample infiltrated with 28 drops of $SnCl_2$ dopant solution. The sample used for XRF was not powdered, but it was the anode surface of a half cell. Considering that the XRF probe only analyses the anode surface layer down to 125 µm for this sample (while the whole anode thickness is 500 µm) and the infiltration was performed by pipette drop method on the anode surface, it is expected that the surface will show a higher Sn content compared to that in the bulk anode which is represented by gravimetric analysis. Therefore it is expected that XRF identified a higher weight % of Sn/Ni of 9.99% instead of 4.77% as it was presented in Figure 5.6.

Table 16. Chemical composition of 28D-Sn-infiltrated SOFC anode obtained from XRF

Atomic symbol	Atomic Number	Weight %	Atomic
Ni	28	48.07	
Zr	40	46.48	
Sn	50	4.80	
Y	39	0.65	
Atomic ratio Ni:Sn			20.3 : 1
Atomic % Sn			4.71
Weight % of Sn/Ni		9.99	

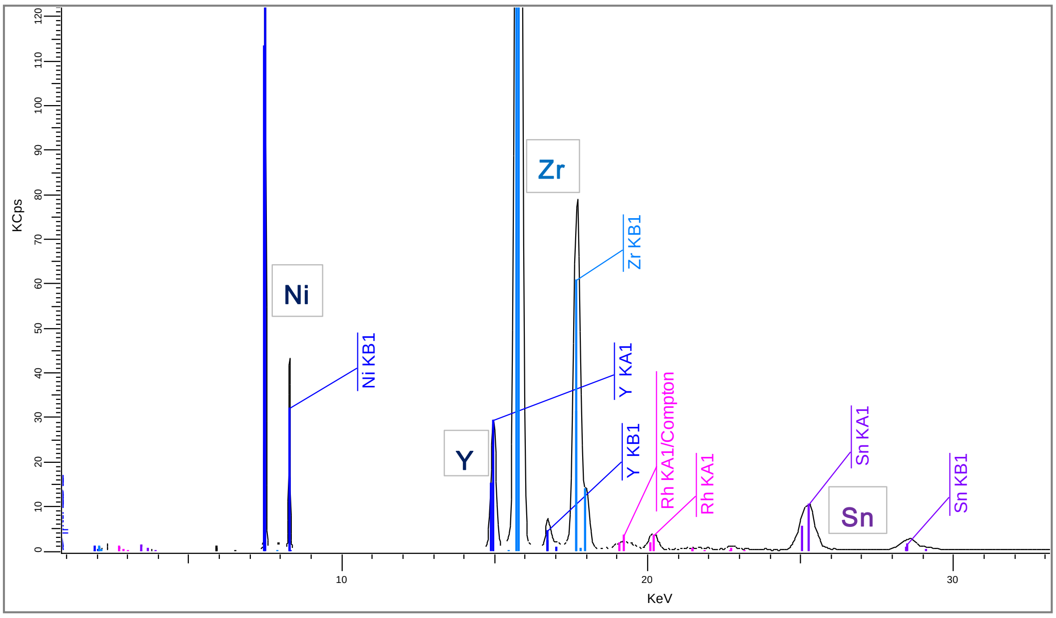

Figure 5.10: X-ray fluorescence spectra of 28D-Sn-infiltrated anode

Figure 5.10 represents the X-ray fluorescence spectra corresponding to Table 16. The spectra show each element's peak of principal line KA1 accompanied by KB1. The KA1 peaks of Ni, Y, and Zr are at 7.47 keV, 14.9 keV and 15.75 keV respectively. A pair of peaks of Sn KA1 and KB1 appear at 25.3 keV and 28.5 keV. Although rhodium is not on the list of the SOFC anode component, it appear in these spectra since the XRF detector we used contained Rh.

Table 17 shows the chemical composition obtained from XPS of 28D-Sn-infiltrated SOFC anode. It is shown that as high as 59.72 weight % Sn/Ni is identified by XPS. Taking into account that XPS analysis measures only a sample surface layer down to 20 nanometres deep, this high value of 59.72 weight % Sn/Ni indicates that the Sn content is highest on the anode surface compared to 9.99 weight % obtained from XRF and 4.77% obtained from gravimetric analysis.

Table 17 Chemical composition of 28D-Sn-infiltrated NiYSZ anode obtained from XPS

Ni 2p %	O 1s %	Sn 3d %	Zr 3d %	At Ni:Sn	At % Sn	Wt % Sn/Ni
15.34	38.38	5.13	5.02	2.99 : 1	25	67.61

5.5 Discussion and Conclusion

Following the various methods of obtaining Ni-Sn alloys which have been utilized both commercially and in research stage, a procedure for Sn-infiltration on sintered NiYSZ based SOFC anodes was developed. Sn-infiltration on a sintered SOFC anode was carried out using the pipette drop method of $SnCl_2.2H_2O$ solution containing 1mg Sn per drop (20µL) of the dopant solution. Repeatability of the method was confirmed by gravimetric analysis of 13 pieces of SOFC anodes being infiltrated by 2 to 28 drops of dopant solution showing a consistently linear increase of weight of SnO_2 obtained as the number of drops was increased. Roughly 60-70% of Sn contained in the dopant solution added was deposited as SnO_2 in the anode after repeated infiltration and calcinations. The 30-40% SnO_2 loss was associated with partial evaporation of $SnCl_2$ during temperature ramping up from 247-600 ^{o}C when $SnCl_2$ melted and partly vaporized.

Analysis of chemical composition of the 28 drops Sn-infiltrated SOFC anode using XRF and XPS revealed that Sn was detected with the highest concentration of 67.61 weight % Sn/Ni on the anode surface (within tens of nanometers distance from the anode surface), a lower concentration of 9.99 weight % Sn/Ni was found at a quarter of the way through the bulk anode (125 µm), and an average concentration of 0.7 weight % Sn/Ni was found in the total bulk anode of 500 µm thickness.

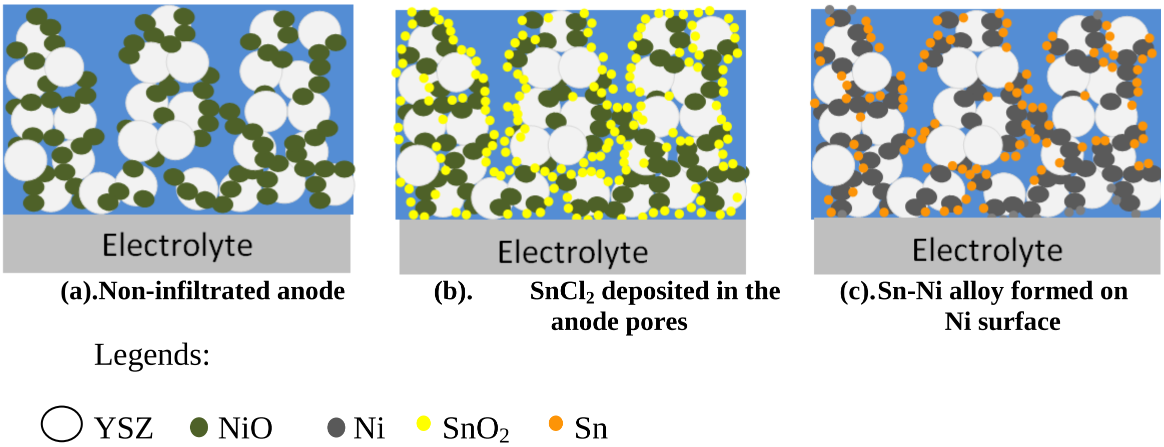

(a).Non-infiltrated anode **(b). $SnCl_2$ deposited in the anode pores** **(c).Sn-Ni alloy formed on Ni surface**

Figure 5.11: Schematic model of Sn-infiltration on SOFC anode

Figure 5.11 represents a schematic diagram of the proposed NiYSZ anode conditions before and after Sn-infiltration in cross sectional view. In Figure 5.11a) the anode before infiltration is represented showing NiO-zirconia particles, in b) the sites where $SnCl_2$ particles being deposited are shown, and in c) NiSn alloy formed after anode reduction are represented showing Sn particles being distributed mostly over Ni particles as supported by EDX maps in Figure 5.9. It is possible that the distribution of NiSn alloy is high on the anode surface and low towards the bulk anode and anode-electrolyte interface as represented by the figures of Ni-Sn composition obtained from three methods of analysis listed in Table 18.

Table 18 Summary of Sn content in 28D-SnNiYSZ anode

	Gravimetry	XRF	XPS
Representative	Bulk anode, 500 µm thick	Anode surface to 125 µm deep	Anode surface to 20 nm deep
Weight % Sn/Ni	4.77	9.99	67.61
Atomic % Sn	2.30	4.71	25.00

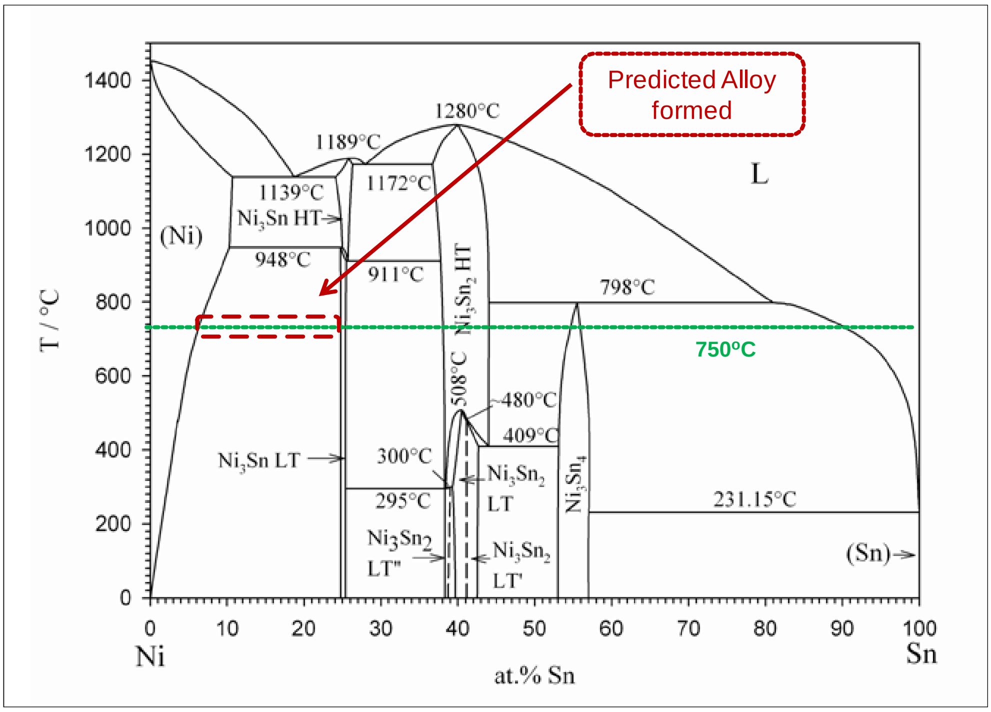

Figure 5.12: Ni/Sn phase diagram showing the expected Ni/Sn alloy phase which can be obtained from Sn-infiltrated SOFC anode

Based on the values of atomic % Sn listed in Table 18, it can be deducted that the most possible Ni/Sn alloy phase obtained from the 28D-Sn-infiltrated anode is Ni_3Sn-LT as illustrated in Figure 5.11. SOFC anodes infiltrated with a higher amount of Sn are expected to yield Ni/Sn alloy phases with a higher Sn content such as Ni_3Sn_2 or Ni_3Sn_4 phases. While SOFC anodes infiltrated with a lower amount of Sn, especially when Sn atomic % < 5, may not form an alloy, but the Sn may be soluble in the Ni phase such as depicted in Figure 5.11. This explains why the Sn/Ni alloy phase is not detected by XRD, the reason being Sn atomic % < 5 and Sn become soluble in the Ni phase.

Chapter 6

Dry Reforming of Biogas on SOFC Anodes

6.1 Overview

This chapter presents results from exploring the activity of NiYSZ in the SOFC anode samples, of both non-infiltrated and Sn-infiltrated, to catalyse dry reforming of biogas. The catalytic activity of NiYSZ was measured in terms of CH_4 and CO_2 conversion and the amount of H_2 and CO gases produced. The effects of operating temperature and CO_2:CH_4 ratio in the feed composition on the H_2 and CO gases produced were observed. This chapter serves as a preliminary investigation towards feasibility of operating the SOFCs directly on biogas under dry reforming mode. Carbon deposition was clearly observed during most of the dry reforming investigations; results of this carbon deposition is presented in Chapter 9.

6.2 Method of dry reforming

Small pieces of 2-4 mm length/width SOFC anode supports or SOFC full cells weighing 500-785 mg were placed in the middle of a quartz reactor and used as the catalyst for dry reforming. The dimension of the quartz reactor was 12 mm inner diameter with 1.5 mm wall thickness. Ni in the NiYSZ anode is the component expected to catalyse dry reforming. Since the anode part of these SOFC pieces comes in the oxide form, anode reduction using a mixture of 1:4 volumetric flow rate of H_2 and Helium was carried out prior to dry reforming procedure.

The quartz reactor was placed in a tunnel furnace with programmable temperature controller. Simulated biogas combined with Helium was fed into the quartz reactor. The outlet gas line was connected to a Quadrupole Mass Spectrometer to monitor the outlet gas composition. Figure 6.1 shows the test rig for dry reforming reaction, with the tunnel furnace, temperature controller, and mass flow controllers for the fuel supply. The quartz reactor pictured here is not the actual size used for dry reforming but just for illustration of how it is positioned in the tunnel furnace.

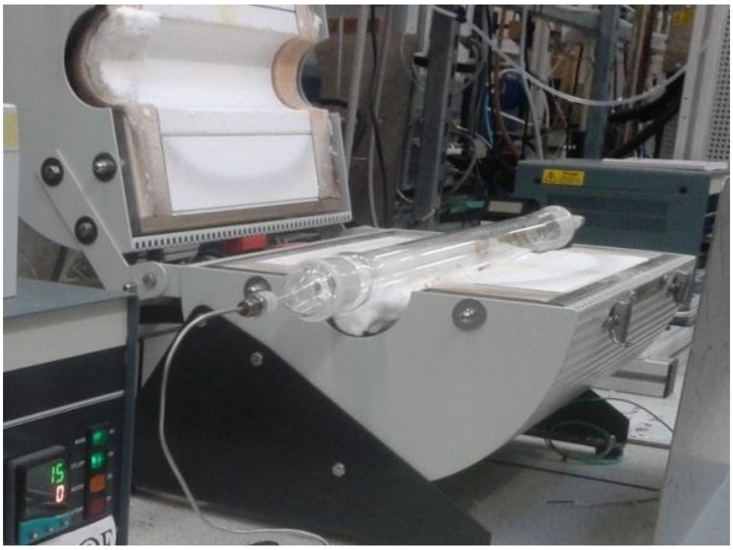

Figure 6.1: The rig configuration used for dry reforming of simulated biogas

6.3 Results

6.3.1 Anode reduction profile

Reduction of SOFC anode was carried out by feeding a mixture of 10 ml min^{-1} H_2 and 40 ml min^{-1} Helium into the quartz tube reactor and heating the quartz reactor to 900 ^{o}C at a rate of 10 ^{o}C min^{-1}. The SOFC anode reduction temperature profile and the partial pressure of un-reacted H_2 flowing out of the quartz reactor is presented in Figure 6.2. The results in Figure 6.2 was obtained from reducing 500 mg NiYSZ anode support pieces. Figure 6.2 shows that anode reduction started at approximately 500 ^{o}C and continued to 900 ^{o}C. This reduction profile is similar to what was reported by Guerra et al. [54]. It is shown that there are two reduction regions, a fast reduction region at temperatures 500<= T <= 750 °C and a slow reduction region at 750 to 900 °C. During the fast reduction rate H_2 partial pressure dropped to 75% the original level. Then during the slow reduction, H_2 partial pressure was gradually resumed to the original level within 1.1 hour. Reduction was completed within 2.5 hours from the start of the heating up.

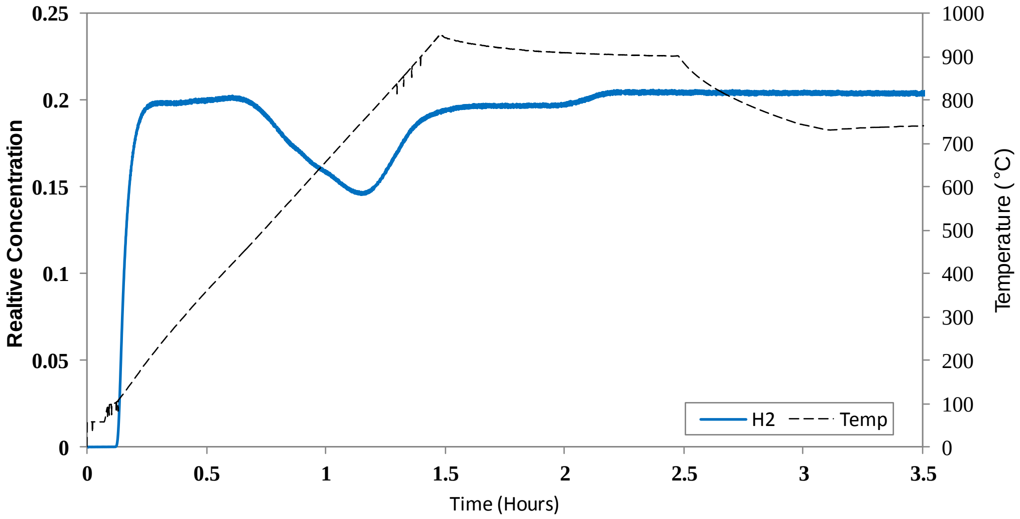

Figure 6.2: Concentration of H_2 as anode reduction progresses

6.3.2 Dry reforming on non-infiltrated anode

6.3.2.1 Percentage of conversion at 750 °C and 1:1 CO_2:CH_4 ratio

The first trial of dry reforming was performed on 500 mg non-infiltrated anode support pieces fed with equal number of moles of CO_2 : CH_4 and a low flow rate of helium to minimize the effects of dilution associated with the presence of helium. Figure 6.3 shows partial pressures of outlet gases resulted from biogas dry reforming on the non-infiltrated SOFC anode support with 1:1 CO_2 : CH_4 feed (22.5 ml min^{-1} CO_2:

22.5 ml min^{-1} CH_4:and 5 ml min^{-1} He) at 750 °C. Biogas feed was introduced at 750 °C. It is shown that as soon as the biogas was introduced, the dry reforming reaction instantly took place producing H_2 (blue curve) and CO (yellow curve). After the first five minutes of biogas introduction approximately 25 vol.% CH_4 and 18 vol.% CO_2 remained (which corresponds to 44% of CH_4 and 60% of CO_2 conversion) and 30 vol.% CO and 18 vol.% H_2 were produced. After 6 minutes of biogas introduction, equilibrium was established which resulted in almost constant levels of CO and CO_2 partial pressures but a slight decrease in H_2 partial pressure which corresponds to a slight increase of CH_4 partial pressure. Although the values of CH_4 and CO_2 conversions are lower compared to those reported in literature [54, 113], the results in Figure 6.3 showed that the pieces of non-infiltrated SOFC anode supports have significant catalytic activities towards dry reforming reactions with dry gas feed (without adding steam into the gas feed).

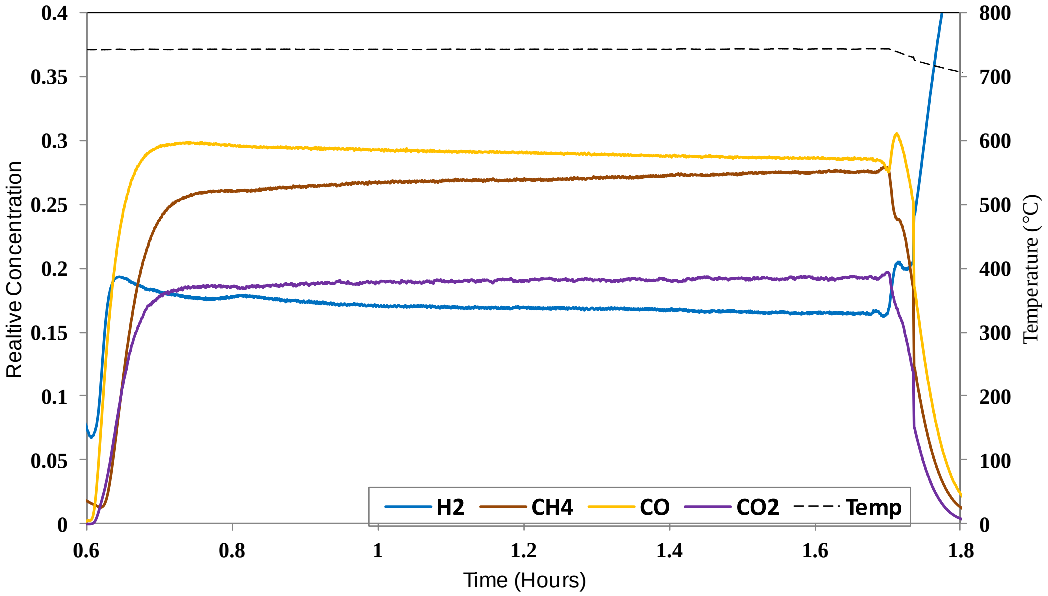

Figure 6.3: Mass spectra of outlet gases from dry reforming of 1:1 CO_2:CH_4 at 750 °C on non-infiltrated NiYSZ anode support

6.3.2.2 The effects of operating temperature

Figure 6.4 shows mass spectra of dry reforming product gases at different operating temperatures, obtained from 785 mg non-infiltrated SOFC full cell. The biogas feed composition was 1:2:2 volume ratio of CO_2:CH_4:He which was the composition intended to be used for the SOFC operation. The spectra show almost equimolar H_2 and CO produced at 800 ^oC but slightly higher CO produced at 750 ^oC and 700 ^oC. At 650 ^oC very little (less than 3%) CO and H_2 were produced which means that the activity of this NiYSZ full cell pieces at 650 ^oC is very low hence may not provide sufficient CO and H_2 for SOFC operation. At 750^{o}C, the planned temperature to operate the fuel cell, approximately 5 vol.% H_2 and 7 vol.% CO are produced. The H_2 and CO partial pressures are low compared to those obtained from anode support pieces such as presented in Figure 6.3; nevertheless these results show that at 750 ^oC H_2 and CO are present as the dry reforming products and thus available for electrochemical reactions under fuel cell operation.

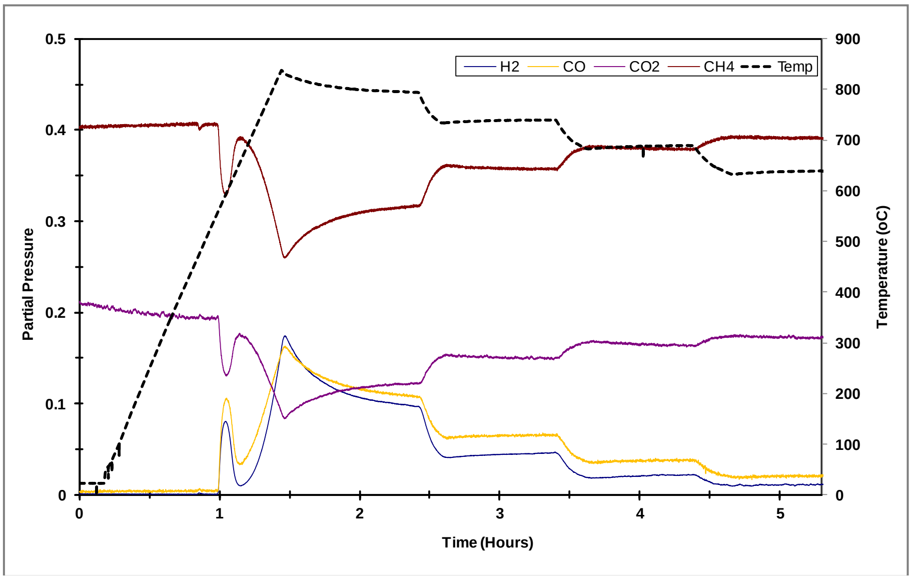

Figure 6.4: Mass spectra of outlet gases from dry reforming on non-infiltrated NiYSZ full cells at 650 - 800 ^oC

Figure 6.5 shows % conversion of CO_2 and CH_4 at different temperatures while Figure 6.6 shows partial pressures of CO and H_2 produced. In Figure 6.5 it is shown that CO_2 conversion was higher than CH_4 conversion, this phenomenon is in agreement with that observed by Stagg et al. [112]. Stagg and co-workers reported that, compared to SiO_2, ZrO_2 as a Pt catalyst support for dry reforming of CH_4 plays a good role in promoting CO_2 dissociation. In this work the ZrO_2 in NiYSZ may have acted as a promoter for CO_2 dissociation. In Figure 6.5. at 800°C, CO_2 conversion was 40% while CH_4 conversion was only 20%. Figure 6.5 and Figure 6.6 show that dry reforming of CH_4 is significantly affected by temperature; increasing temperature from 750°C to 800°C resulted in two folds of increase of CO_2 and CH_4 conversion and twice the amount of CO and H_2 produced. The very low CO and H_2 produced at 700°C and especially at 650°C indicate dry reforming on this NiYSZ anode from full cell pieces at 700°C and 650°C are not efficient. This finding is an important input in selecting suitable SOFC operating temperature for direct biogas reforming.

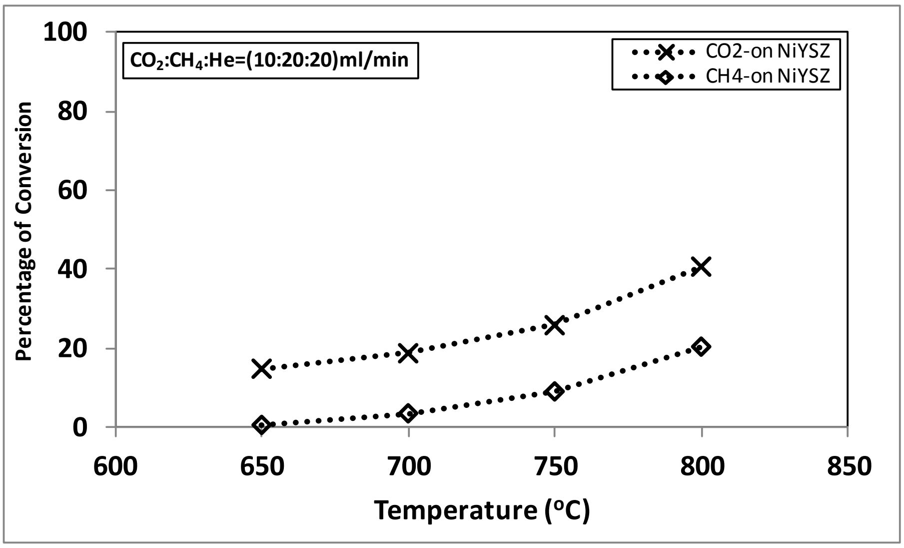

Figure 6.5: Percent conversion of CO_2 and CH_4 at 650-800 °C

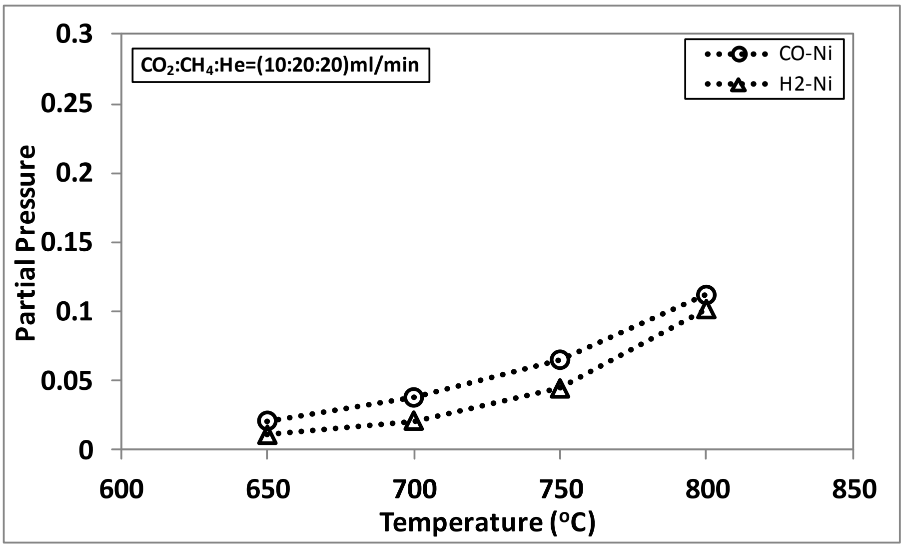

Figure 6.6: Partial pressure of CO and H_2 produced at 650-800 ^oC

6.3.3 Dry reforming on Sn-infiltrated anodes

6.3.3.1 The effect of temperature

Figure 6.7 shows the effect of operating temperature on the outlet gas composition obtained from 500 mg 6D Sn-infiltrated SOFC full cell. Within the temperature range of 800^{o}C to 650^{o}C, compared to the gas composition presented in Figure 6.4, a similar trend is observed in Figure 6.7; that is the unreacted CO_2 and CH_4 are lowest at 800^{o}C, and that the unreacted gas feed gradually increased and showed the highest values at 650^{o}C. Both Figure 6.4 and Figure 6.5 also show that a decrease of 50^{o}C resulted in the decrease of H_2 and CO produced by approximately 50%. It is interesting to compare the level of H_2 and CO partial presures represented by the blue and yellow colored curves in Figure 6.4 (representing non-infiltrated NiYSZ) and Figure 6.7 (representing Sn-infiltrated NiYSZ). The results of Sn-infiltrated NiYSZ shows twice or higher H_2 and CO produced than that of non-infiltrated NiYSZ. This shows that Sn-infiltration improves dry reforming of CH_4 and increases the H_2 and CO production.

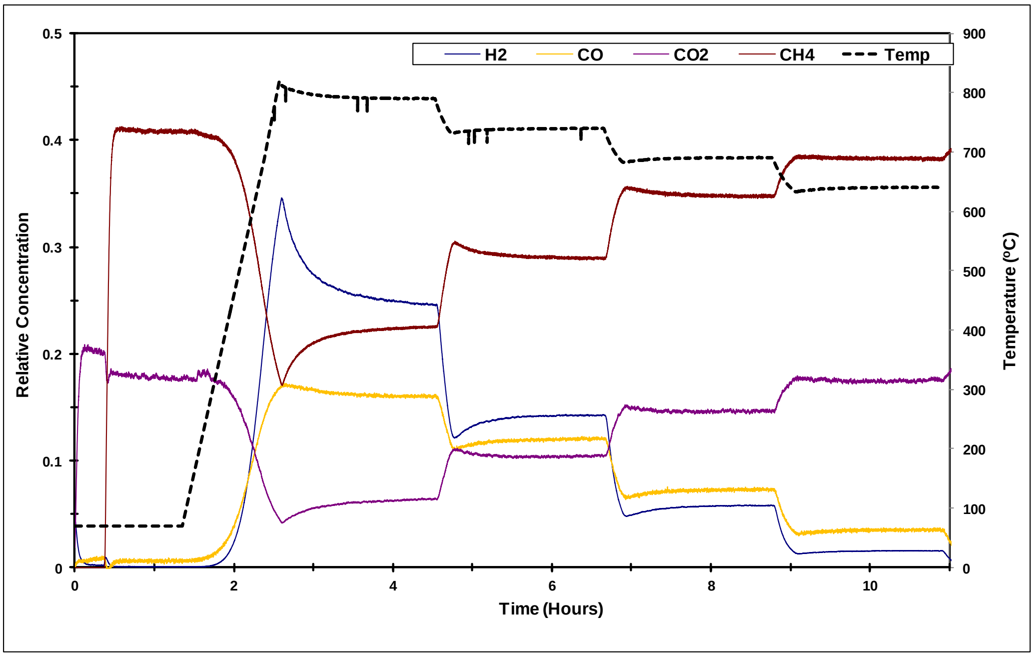

Figure 6.7: Mass spectra of outlet gases during dry reforming on 6D Sn-infiltrated NiYSZ full cell at 650-800 °C

6.3.3.2 <u>The effect of different feed composition</u>

Figure 6.8 shows effect of different feed compositions on the outlet gas composition. The spectra were obtained from 500 mg 4D Sn-infiltrated anode support. The total volume of gas feed was kept at 50 ml min^{-1} with constant 5 ml min^{-1} helium flow and varied flow rates of CO_2 and CH_4. Figure 6.8 shows that the highest level of H_2 and CO produced is at 1:1 ratio of CO_2:CH_4 feed which is expected from stoichiometry, but this is also in agreement with literature [54, 113]. Figure 6.8 also shows that at CO_2:CH_4 = 1:2 H_2 produced is slightly higher than that from CO_2:CH_4 = 1:1, and CO produced is only slightly lower. This is a good indication for the planned SOFC operation; in that the SOFC is feasible to operate at 750°C and with CO_2:CH_4 = 1:2 to produce sufficient amount of CO and H_2 for electrochemical oxidation.

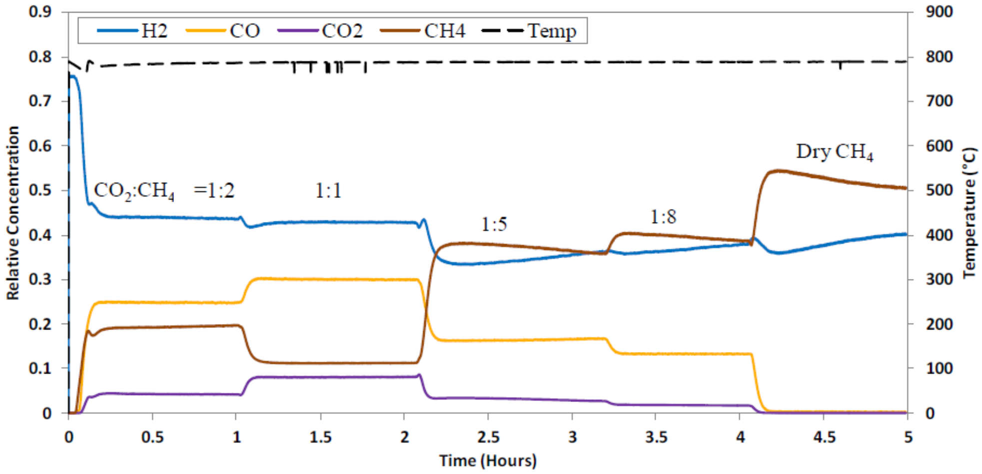

Figure 6.8: Mass spectra of outlet gases during dry reforming on 4D Sn-infiltrated NiYSZ full cell at 800°C and varied CO_2:CH_4 ratio

Figure 6.9 and Figure 6.10 are the same experimental results with those in Figure 6.8 but presented in bar charts. Figure 6.9 and Figure 6.10 show that it is the amount of CO produced which linearly corresponds to the different CO_2:CH_4 ratio in the feed; while H_2 produced was not linearly affected by CO_2:CH_4 ratio. The amount of CO produced decreases as the CO_2 concentration in the feed was decreased. This can be explained by the general understanding that dry reforming reaction, represented by Eq. 2.20, occurs via at least two reactions namely methane cracking, Eq. 2.25, which produces C and H_2, and oxidation of C by CO_2 to form CO which is also known as reverse Boudouard reaction (reverse Eq. 2.27). For convenience, below are the three chemical reactions copied from Table 1 in Chapter 2. Considering these three reactions it is clear that in a closed system, the amount of CO produced is directly affected by the available CO_2.

$$\mathbf{CH_4 + CO_2} \leftrightarrow 2\,CO + 2\,H_2 \quad \text{dry reforming} \qquad \text{(Eq. 2.20)}$$

$$\mathbf{CH_4} \leftrightarrow C + 2\,H_2 \quad \text{pyrolysis or cracking} \qquad \text{(Eq. 2.25)}$$

$$\mathbf{C + CO_2} \leftrightarrow 2\,CO \quad \text{Reverse Boudouard} \qquad \text{(Reverse Eq. 2.27)}$$

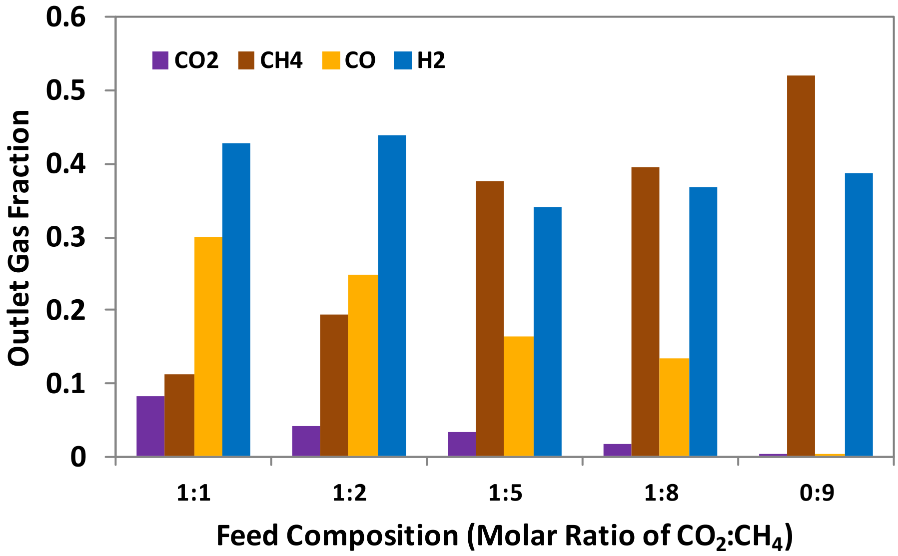

Figure 6.9: Dry reforming product gas fraction on 4D Sn-infiltrated NiYSZ full cell at 800°C at varied CO_2 : CH_4 ratio

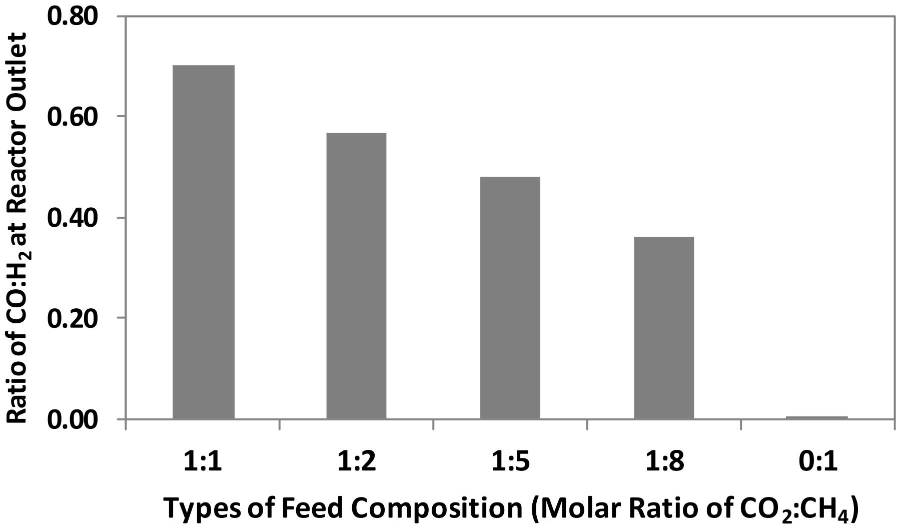

Figure 6.10: Ratio of CO:H_2 on 4D Sn-infiltrated NiYSZ full cell at 800°C and varied CO_2 : CH_4 ratio

For an equilibrium dry reforming reaction without steam, the ratio of CO to H_2 present in the product stream is expected to be 1. Figure 6.9 and 6.10 show that the ratio of CO : H_2 produced being less than 1; this may indicate that carbon is formed during the dry reforming reaction. Results and discussion on this carbon formation is presented separately in Chapter 9.

6.4 Discussion and Conclusion

Pieces of non-infiltrated SOFC anode supports and non-infiltrated and Sn-infiltrated SOFC full cells were tested as catalysts for dry reforming reactions. Dry reforming on pieces of non-infiltrated anode support produced more H_2 and CO compared to that on pieces of SOFC full cell. This is due to Ni particles in pieces of anode supports are more exposed to the gas feed than those Ni particles in pieces of SOFC full cells. Pieces of anode support has Ni particles exposed to gas feed on both sides of the disc while pieces of SOFC full cells has only one side exposed.

It was shown that at the observed temperature range (650 ^{o}C to 800 ^{o}C) Sn-infiltrated SOFC anodes produced more H_2 and CO (or higher CO_2 and CH_4 conversions) compared to non-infiltrated ones. On both non-infiltrated and Sn-infiltrated anodes, more H_2 is produced at higher temperature (800^{o}C) than at lower temperatures of 650 – 750 ^{o}C. It was observed that at 750 ^{o}C and 1 : 2 : 2 ratio of CO_2 : CH_4 : He approximately 5 vol.% H_2 and 7 vol.% CO were produced on non-infiltrated SOFC anode while 15 vol.% H_2 and 13 vol.% CO were produced on 6D Sn-infiltrated SOFC anode. Although rather low, the presences of H_2 and CO in these dry reforming reactions are considered sufficient for further investigation of the non-infiltrated and Sn-infiltrated SOFC electrochemical performance.

As expected from stoichiometry, observation of dry reforming at different CO_2 : CH_4 ratios shows that equimolar feed of CO_2 : CH_4 produced the most CO and H_2 compared to other feed compositions. The amount of CO produced is much affected by the composition of CO_2 in the feed. Rough comparison of dry reforming on 6D and 4D Sn-infiltrated SOFC anodes (Figures 6.7 and 6.8 respectively) shows that the Sn loading is another determining factors (other than temperature and gas composition) for the amount of H_2 and CO produced.

As a base for evaluation of SOFC operation with direct biogas feed, these results of dry reforming on SOFC anode pieces have shown that infiltration of SOFC anode with Sn dopant increased the yield of dry reforming products, namely H_2 and CO, therefore Sn-infiltration is promising to be used in improving electrochemical performance of SOFC operating on biogas.

Chapter 7

Electrochemical Performance of Non-infiltrated SOFC Fuelled by Biogas

7.1 Overview

This chapter presents results of operating the SOFCs on simulated biogas using the total fuel feed flow rate of 28 ml min^{-1} as recommended by the results in Chapter 4. The biogas composition used was 1:2 CO_2:CH_4 ratio and the operating temperature was 750 ^{o}C. Helium was added at 25% volumetric flow rate to the total flow rate. These SOFC tests on biogas were performed immediately after the stabilisation performance of SOFCs B1, B2, B3 and B4 on H_2 fuel with the results presented in Chapter 4.

7.2 Mass spectra of the SOFC outlet gases

The SOFC outlet gases composition was monitored using a quadrupole mass spectrometer. Figure 7.1 illustrates the composition of the fuel cell outlet gases obtained from monitoring the SOFC-B1. The picture shows three regions of measurement. Region A which corresponds to OCV, region B which shows a change of H_2, CO and CO_2 compositions corresponding to I-V curve measurements, and region C which shows constant compositions of H_2, CO and CO_2 corresponding to constant potential operation of the SOFC. It can be observed that very little H_2 and CO were produced from the dry reforming of the biogas feed. The quantities of H_2 and CO produced were compared to the dry reforming product composition predicted by a simulation program known as NASA Chemical Equilibrium Program (CEA2) simulation which was used as a reference by several researchers [65, 78, 152].

Since dry reforming and electrochemical oxidation reactions in hydrocarbon system are occurring in equilibrium, having certain k values such as presented in Table 1, only a certain part of these already low H_2 and CO obtained from the dry reforming reaction were electrochemically oxidised; consequently only low current and power were produced. These are presented in the I-V curves and constant potential (potentiostatic) curves explained in section 7.3.2.

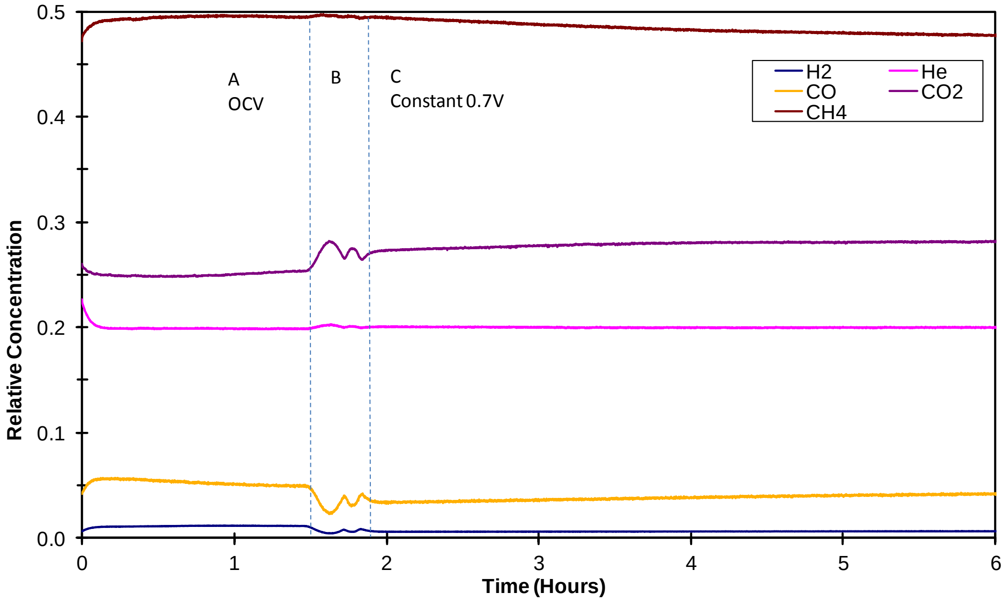

Figure 7.1: Dry reforming product gas composition of the non-infiltrated SOFC-B1 at 750 °C

7.3 Electrochemical Performance

7.3.1 Prediction of electrochemical performance using fuel cell model

A simulation was run to predict the product gas composition resulting from dry reforming of the biogas feed using a software known as the NASA ‘Chemical Equilibrium Program CEA2’ [65, 152]. This NASA CEA2 software was developed based on the minimised Gibbs free energy calculation. According to the simulation using this software, the dry reforming produced a gas mixture with the composition shown in Table 19. Then the gas product composition obtained from the NASA CEA2 simulation was used to predict the polarisation curve with a fuel cell model incorporating Nernst equation [152] developed in the lab; this is called 1st FCM simulation.

Table 19 SOFC outlet gas composition, measured vs. prediction[#1] (at 750 °C) in equilibrium (OCV)

Gas components	Feed	Product partial pressure, predicted by CEA2 simulation	Product partial pressure, (Mass spectra) of SOFC-B1
CO_2	0.25	0.01649	0.24800
CH_4	0.50	0.01833	0.49600
He	0.25	0.12958	0.19800
H_2O	0	0.03900*	na
H_2	0	0.44667	0.01300
CO	0	0.19717	0.05120
C (gram)	0	0.15675	Na
Total	1.000	1.004	1.006

Note * H_2O was not supplied to the feed in the experiment but needs to be specified in order for the fuel cell model to work.

Table 19 lists the gas composition of the dry reforming product obtained from mass spectra and the predicted dry reforming products obtained from simulation software. It is interesting to note that the simulation predicted H_2 and CO as products with the partial pressure of H_2 twice higher than that of CO, which means that carbon is likely to form; the mass spectra show the partial pressure of CO almost four times that of H_2. This can be a sign that the anode, in the SOFC operation, acts not only as a dry reforming catalyst but can possibly act as an electrochemical catalyst for carbon oxidation which allow for formation of more CO than H_2 at OCV. It is also noted that there is a large difference between the two compositions. The simulation showed thirty times more H_2 with four times more CO partial pressure than the real dry reforming did. This indicates that the particular SOFC is a low performing dry reforming catalyst.

Using the real dry reforming product composition, a second FCM simulation was run. The results are presented in Figure 7.2 It is observed that with a very low concentration of H_2 produced from dry reforming, a low OCV value of 0.930 V is expected.

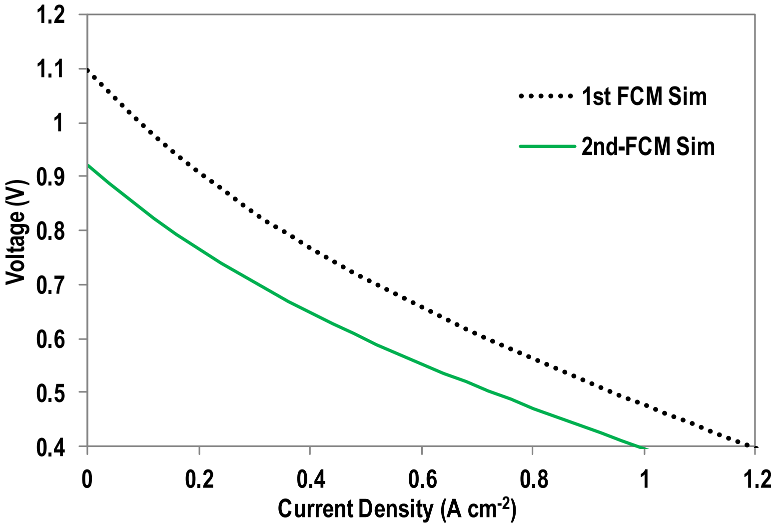

Figure 7.2: First and second FCM simulation results

7.3.2 Measured electrochemical performance

Figure 7.3 shows the polarisation curves obtained from the FCM simulations along with the experimental results obtained from testing four SOFC-Bs. It is interesting to observe the experimentally obtained OCV and the 2nd FCM simulated results since they are in good agreement. Comparing between the OCV values obtained from the 2nd FCM simulation, it is revealed that the tested SOFC performs well in terms of OCV, this means that the SOFC system shows good catalytic activity towards electrochemically oxidising the available H_2 in the SOFC anode. However it is the low dry reforming activity of these SOFC anodes and the voltage loss associated with mass transfer or diffusion that cause the large electrochemical performance gap. The polarisation curves show that the SOFC can cope with 0.1 A cm^2 current drawing but not with a higher rate of current drawing. In Chapter 4, where results of fuelling the SOFCs by H_2 are presented, it is already observed that there is a gap between the polarisation curves predicted by the fuel cell model and that obtained from the experiment. The experimental results show good agreement in terms of OCV but much higher potential loss at high current densities than the predicted results do.

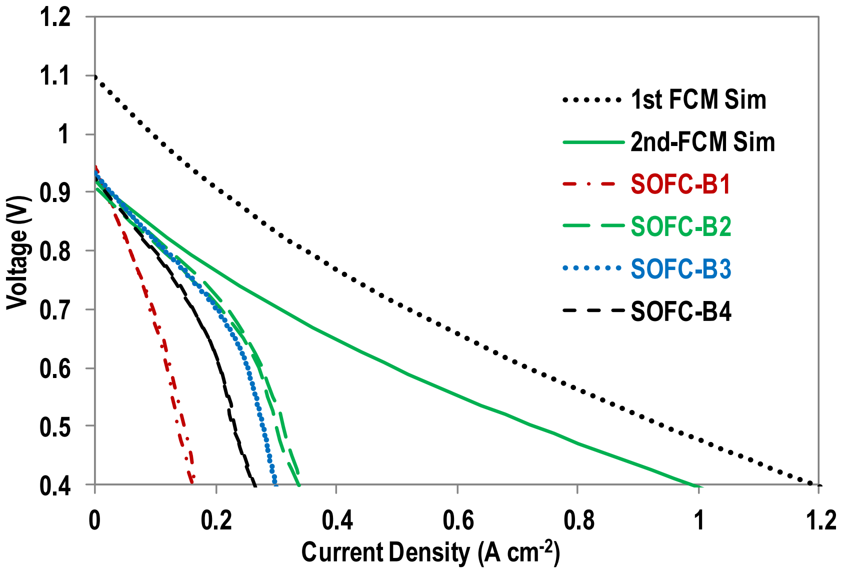

Figure 7.3: Performance of SOFC-Bs compared with results obtained from two simulations

More detailed results of the electrochemical performance of the SOFC-Bs are presented in the next sections.

7.3.2.1 Open Circuit Potential

Open circuit potentials were measured at the beginning of the electrochemical performance measurement sequence. The OCVs were measured for 90 minutes before switching the electrochemical test sequence to the I-V curve measurements. For OCV measurements in biogas, the duration was chosen so as to allow for the stable flow of biogas to replace the H_2 remaining in the feed gas line and in the cell anode compartment. The longer the duration the better is the replacement of H_2 by biogas feed. However, with regards to the possibility of carbon formation, the longer the OCV is held the more chance for carbon to be formed. Formation of carbon at an early stage of the SOFC testing, especially if it is severe, may prevent subsequent electrochemical performance measurements from being tested successfully, therefore this should be avoided. To allow for stable biogas flow and to minimise the possibility of 'too early' carbon formation, 90 minutes were chosen as the duration for OCV measurements. The OCV values of the four SOFCs tested over 90 minutes measurements are presented in Figure 7.4. It is observed that on switching from H_2 to biogas fuel, the OCV decreased from slightly over 1.0-0.96 V except for SOFC-B4 which decreased to 0.93 V. Results obtained from SOFC-B1 showed a small error caused by the test rig running out of Helium supply, resulting in a temporary increase of OCV. However as the Helium flow was resumed the OCV value was back to the normal and stable condition. It is observed that stable OCV were obtained after 30 minutes of operation on biogas.

In all the four non-infiltrated SOFC tested, OCV values of the biogas system are lower than those obtained in the H_2 system (see Figure 4.6). The reason for this decrease in OCV is a lower H_2 partial pressure available in this biogas system due to a low conversion in the biogas reforming. In fact this low OCV is predicted by the 2nd-FCM simulation presented in Figure 7.3.

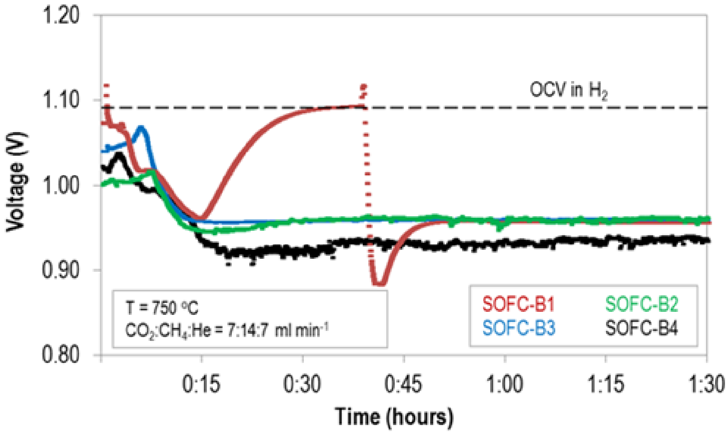

Figure 7.4: OCV of four SOFCs fuelled by biogas with OCV in H_2 as reference

7.3.2.2 Polarisation (I-V) and power density curves

To evaluate electrochemical performance of the un-doped SOFCs under current loading, current obtained at different values of SOFC potentials were measured in an I-V curve or potentio-dynamic mode of polarisation measurement. The SOFC potential was incrementally reduced, by 25 mV from OCV value to 0.4 V and back to OCV. Figure 7.5 presents the polarisation and power density curves measured immediately after the OCV measurement (red coloured) and after 22 hours of operation (black coloured). Among the four SOFCs, SOFC-B2 (Figure 7.5 b) demonstrated the highest maximum power density of 170 mW cm^{-2} at 270 mA cm^{-2} current density, while SOFC-B1 (Fig 44a) showed the lowest maximum power density of 75 mW cm^{-2} at 130 mA cm^{-2}.

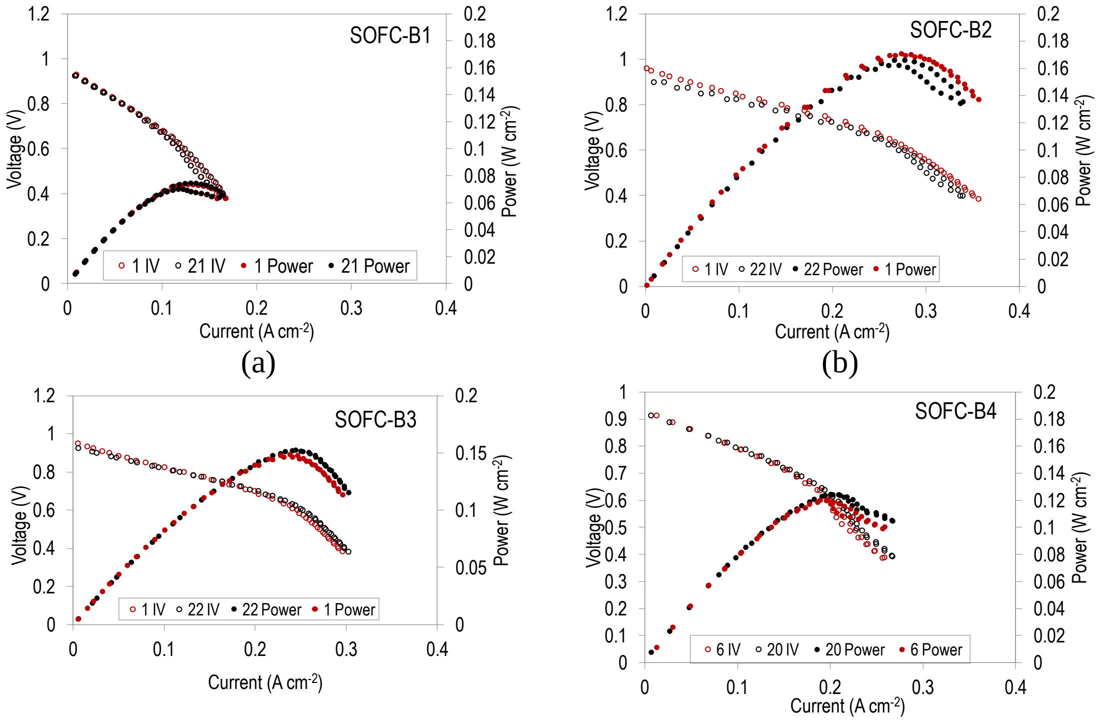

(a) (b)

(c) (d)

Figure 7.5: Polarisation and power density curves of four SOFCs fuelled by biogas

Compared to the maximum power densities obtained from fuelling the SOFCs with H_2 (Figure 4.9b), these maximum power densities obtained in biogas are low. This is already predicted by the low OCV obtained as described in the previous sub-section. Again the main cause for this low power produced is the low conversion of the biogas reforming. In terms of maximum power density values over 22 hours of operation, quite stable performance was observed in SOFC-B1, while a slight decrease of 9 mW cm^{-2} maximum power density was seen in SOFC-B2 and a slight increase of 4 mW cm^{-2} was observed in SOFC-B3 and SOFC-B4.

7.3.2.3 Constant potential measurement

The SOFC performance on biogas over 22 hours of operation at constant 0.7 V is presented in Figure 7.6. The average current produced is 0.154 A cm^{-2}. This current is low compared to that produced on H_2 fuel, 0.355 A cm^{-2}. Figure 7.6. also shows that performance of each SOFC is stable, no significant degradation over 22 hours of operation, except for SOFC-B2 which showed 22 mA cm^{-2} current decrease from initial current of 220 mA cm^{-2} or 10% degradation over 22 hours. This performance decrease is also shown in maximum power density values displayed in Figure 7.5. The blue lines inserted on the top left side are the corresponding currents in H_2 as presented in section 4.4.2.3 .

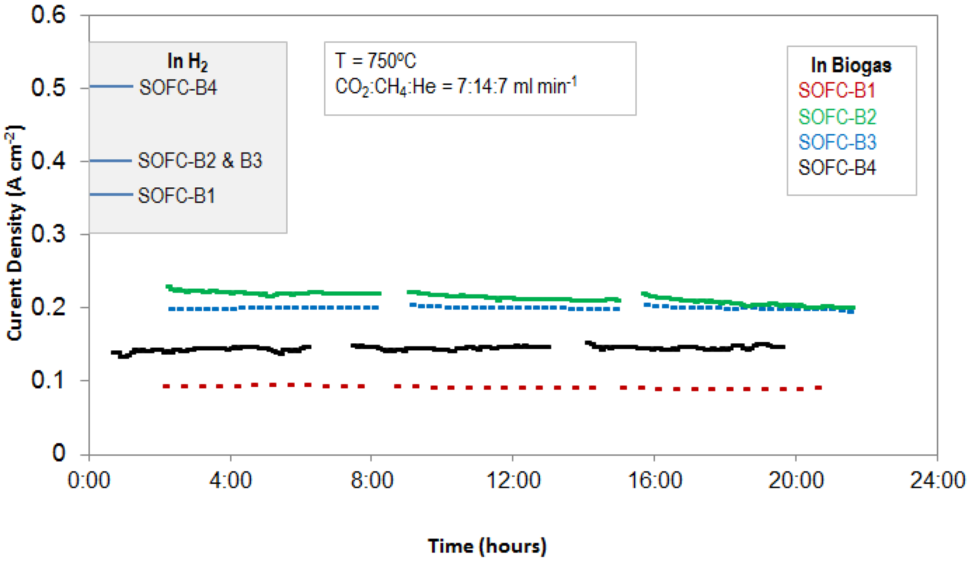

Figure 7.6: Current produced for 22 hours (at 0.7 V) from four SOFCs fuelled by biogas.

Figure 7.7 shows current produced by SOFC-B1 fuelled by biogas, operated for 150 hours at 0.7 V. The current produced is stable showing no degradation. OCV, i-V curves and impedance spectra were taken every 12 hours or 6 hours during the 150 hours of operation, hence the evidence of slightly increased currents observed each time the constant voltage measurement was started.

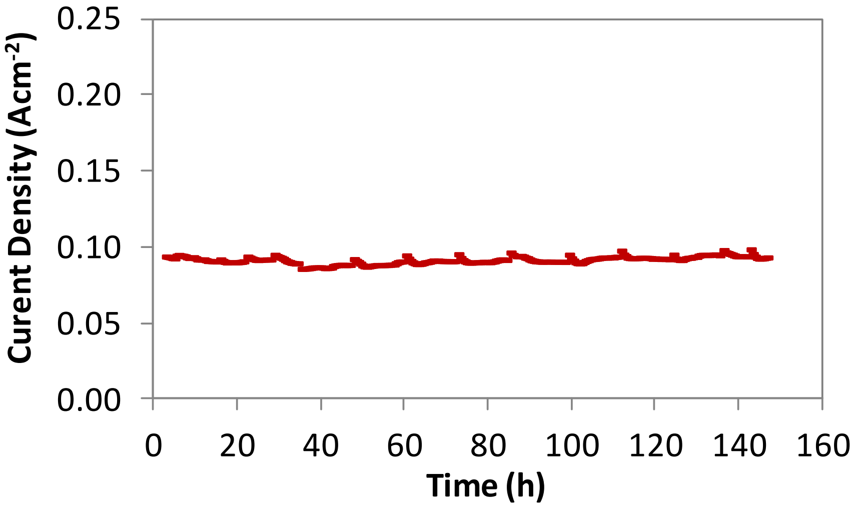

Figure 7.7: Current produced for 150 hours (at 0.7 V) from SOFC-B1 fuelled by biogas

7.3.2.4 Electrochemical Impedance Spectra Measurements

Figure 7.8 presents a sample of the EIS spectra obtained from the SOFC-B1 operation on biogas compared to those obtained on H_2. The EIS spectra was run from 1 MHz to 0.1 Hz. Referring to the labelling of the resistances in Figure 4.10 in Chapter 4, it is observed that the Ohmic resistance obtained from biogas operation is the same with that obtained from H_2 operation. As reported in several studies, changes in NiYSZ microstructure, such as the emergence of microcracks or partial re-oxidation of nickel, even carbon deposits which dissolves into nickel structure can be observed via an increase in ohmic resistance [105, 165]. Since there is no change in ohmic resistance observed it can be concluded that the anode microstructure is stable during the operation of the SOFC on H_2 and on biogas.

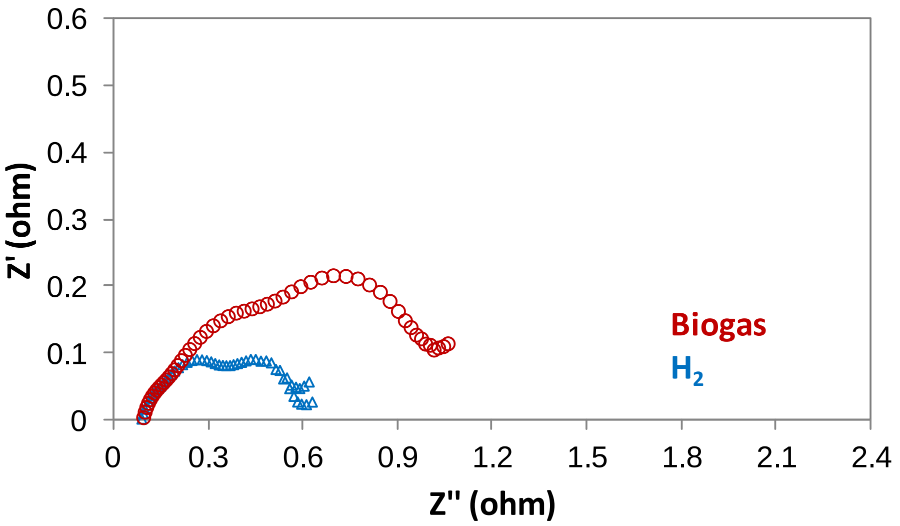

Figure 7.8: EIS spectra of SOFC-B1 obtained in H_2 (26 hours) and biogas (22 hours) at OCV

However there is a significant increase in polarisation resistance observed in operation on biogas which indicates poor mass transfer or diffusion. This is in fact supported by the data of dry reforming product composition obtained from the mass spectra. Very low concentrations of H_2 and CO were observed in the mass spectra, these conditions cause poor mass transfer. Insufficient CO and H_2 present for electrochemical oxidation reaction results in the increase of polarisation resistance. In this SOFC operation on biogas, the increase in polarisation resistance caused by the poor dry reforming adds to the poor diffusion characteristics of the anodes which is observed and discussed in Chapter 4.

7.3.2.5 SEM images

Figure 7.9 shows the appearance of one of the non-infiltrated SOFC ready for testing, post testing and appearance of the anode side post-testing on biogas. The figure shows that the anode surface post testing on biogas appeared grey and clean without signs of carbon deposited. To further investigate the anode surface with regard to carbon deposition, the tested cell was fractured and prepared for SEM observations.

(a) (b) (c)

Figure 7.9: SOFC appearance a) pre-test b) post-test and c) anode side post-22 h test on biogas

Figure 7.10 shows the SEM images of the SOFC anode surface pre- and post-testing on biogas. **Figure 7.10** a) and b) show the SE (secondary electron) images while c) and d) show BSE (back scattered electron) images. The image of the pre-tested anode surface was taken from the SOFC anode reduced in H_2 for 24 hours. It is observed that there is a change of the appearance of Ni-rich phases (the whitish part in the SE image or the dull parts in the BSE image) in the SOFC anode surface. The Ni-rich phases are more clearly distinguished in the tested cell than that in the pre-tested cells. This may be a result of the NiO being more completely reduced and more easily distinguishable from the un-reduced NiOYSZ. Another important result from these SEM images is that there is no clear indication of the appearance of carbon post-22 hours biogas test. This is confirmed, especially when the SEM images in Figure 7.10 b and d are compared with Figure 2.10, which shows carbon filaments formed on a NiYSZ SOFC anode after 300 hours operation at 800^{o}C using 1:1 CO_2 : CH_4 ratio. A more detailed analysis of carbon deposition on these tested SOFCs using quantitative measurement method known as TPO (Temperature Programmed Oxidation) is presented in Chapter 9.

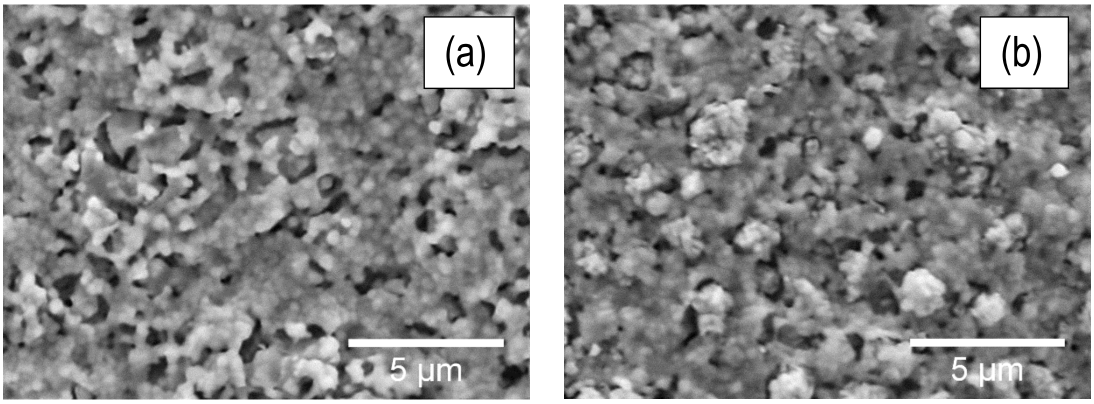

(a). Reduced anode pre-test (SE) **(b). SOFC-B3 post-test on biogas (SE)**

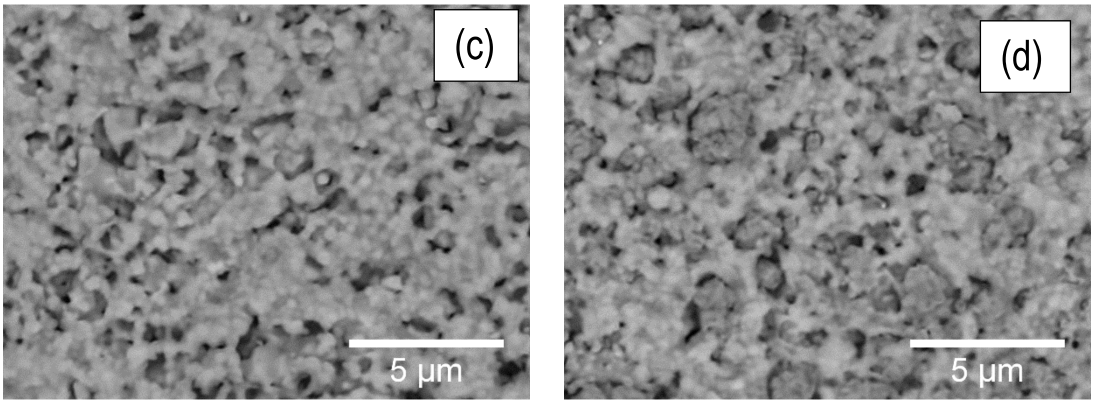

(c). Reduced anode pre-test (BSE) **(d). SOFC-B3 post-test on biogas (BSE)**

Figure 7.10: SEM images of SOFC-B3 pre- and post-22 hours test on biogas

7.4 Conclusion

Operation of the SOFCs in biogas showed low electrochemical performance compared to that obtained in H_2 fuel. Results from monitoring the SOFC outlet gases show that this low electrochemical performance is caused by the low concentration of H_2 and CO produced from the biogas dry reforming reactions. Comparison of the polarisation curves obtained from the experiments with those obtained from the 2nd FCM simulation, using the outlet gas composition obtained from mass spectra, showed that the observed OCV value matched the predicted value but voltage loss became larger as current increased. This indicates that mass transfer is poor and polarisation resistance is high. This explanation is supported also by EIS spectra. The similar and low values of Ohmic resistances on biogas fuel with those observed on H_2 fuel indicate that under the tested conditions the anode microstructure is stable and there are low risks of carbon deposition or anode re-oxidation. Regarding carbon deposition, a detailed analysis, which gives comparisons with carbon formed during dry reforming on anode pieces in a quartz reactor and during SOFC operation, is presented in Chapter 9.

Chapter 8

Electrochemical Performance of Tin-infiltrated SOFC Fuelled by Biogas

8.1 Overview

This chapter presents results of operating the Sn-doped SOFCs on simulated biogas using the fuel feed flow rate of 14 ml min^{-1} CH_4, 7 ml min^{-1} CO_2 and 7 ml min^{-1} Helium, giving 1:2 CO_2:CH_4 ratio and a total of 28 ml min^{-1} gas flow rate. The operating temperature was 750 ^{o}C. The SOFCs were infiltrated with pipette drop method varying the amount of Sn dopant with 2 drops, 4 drops, 6 drops and 10 drops and designated as SOFC types 2D, 4D, 6D and 10D respectively. At least three cells were tested for each type of Sn-infiltrated SOFC. Each test lasted 26 hours on H_2 and 22 hours on biogas giving a total of 48 hours of test duration. To represent durability of the SOFCs, one 10D-Sn-infiltrated SOFC was tested for 150 hours on biogas, another was tested for 176 hours on H_2.

8.2 Summary of electrochemical performance on H_2

Results of the electrochemical performance tests on H_2 are presented in Table 20. The first row represents the performance of non-infiltrated SOFCs which is discussed in Chapter 4.

Table 20 Summary of electrochemical performance on H_2

Cell types	Weight % Sn/Ni	OCV (V)	Constant 0.7 V		Resistances (mΩ cm^2)			
					at OCV		at 0.7 V	
			Current (A)	Power (W)	Ohmic	Total	Ohmic	Total
SOFC-Bs (0Ds)	0.00	1.040	0.380	0.260	90	600	90	420
SOFC-2Ds	0.20	1.020	0.380	0.260	70	450	90	400
SOFC-4Ds	0.38	1.040	0.420	0.300	80	370	90	350
SOFC-6Ds	0.66	1.000	0.370	0.260	60	440	60	440
SOFC-10Ds	1.02	1.020	0.290	0.200	70	610	80	500

Note: the values listed above are the average values

Referring to results in Table 20, it can be seen that Sn infiltration with ≤ 1% weight Sn/Ni causes no decrease in electrochemical performance on H_2. In fact SOFC-4Ds showed the highest current and power produced at 0.7 V among all the SOFCs tested. This highest current is related to the lowest total cell resistance and more specifically related to the lowest polarisation resistance, considering that the cells' Ohmic resistances are relatively constant for all cell types. These results are encouraging that Sn infiltration at ≤ 1 % weight of Sn/Ni does work for SOFC fuelled by H_2.without causing any decrease in the electrochemical performance on H_2 compared to that of the non-infiltrated SOFCs. This means that the Sn infiltration still retains the properties of the SOFC in terms of Ohmic resistance and catalytic activities towards H_2 electrochemical oxidation. The next sections present results of fuelling the SOFCs with biogas

8.3 Mass Spectra of SOFC outlet gases

Figure 8.1 represents typical mass spectra obtained from operation of a Sn-infiltrated SOFC; this one is from SOFC-6D-1. The mass spectra show the first 6 hours of operation which consists of 3 regions of electrochemical performance measurements; regions A, B and C. Region A corresponds to 90 minutes OCV measurement, region B to I-V curve and impedance measurements, and region C corresponds to current drawing at constant 0.7 V. The biogas feed is 14 ml min^{-1} CH_4, 7 ml min^{-1} CO_2 and 7 ml min^{-1} Helium which corresponds to the partial pressures of CO_2, CH_4, He of 0.25 ; 0.50; 0.25 respectively. A significantly higher CO and H_2 concentrations are observed in Figure 8.1 compared to the CO and H_2 obtained from the SOFC-B1 presented in Figure 7.1. This means dry reforming occurs with much more biogas converted to CO and H_2 in Sn-infiltrated SOFC than that in non-infiltrated SOFCs.

During OCV, the CH_4 (brown) and CO_2 (purple) lines in Figure 8.1 appear at approximately 0.3 and 0.15. Compared to the initial composition of 0.5 vol.% CH_4 and 0.25 vol.% CO_2, the vol.% of CH_4 and CO_2 at region A represents a rough indication that approximately 40% CH_4 and CO_2 are consumed in biogas dry reforming reaction.

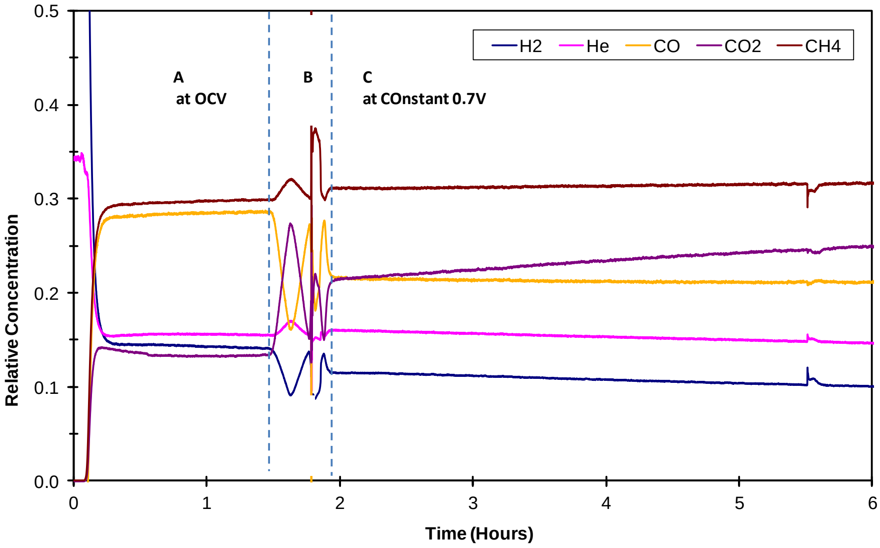

Figure 8.1: Typical mass spectra of outlet gases of a Sn-infiltrated SOFC fuelled by biogas.

Region B shows the gas partial pressures during I-V curve and EIS measurements. The I-V curve measurements were performed by incremental decrease of cell voltage from OCV to 0.4 V and back to OCV, hence the observed decrease and subsequent increase of H_2 (blue curve) and CO (orange curve) partial pressures. These trends are expected, for both H_2 and CO are proposed to undergo electrochemical oxidations. The partial pressures of H_2 and CO are shown to decrease as current increases meaning that electrochemical oxidation of H_2 and CO take place in the SOFC anode. The partial pressure of CO_2 which shows the opposite trend of firstly increasing and subsequently decreasing manner can serve as an evidence of CO electrochemical oxidation taking place in the anode. However this proposed explanation is still subject to further investigations since it is argued that this behaviour of CO and CO_2 partial pressures with response to current change may also be associated with the fast water gas shift reaction. In other words, it was not the electrochemical reaction of CO which caused the decrease of CO level as current was increased, but rapid depletion of H_2 caused by H_2 electrochemical oxidation. It is argued that this depletion of H_2 shifts the water gas shift reaction to the right, consuming CO while producing more H_2. However, this water gas shift reaction is more likely to occur in a steam reforming environment. In an SOFC operating under dry reforming mode, the water gas shift reaction is likely to be suppressed.

Region C shows mass spectra during current drawing at a constant potential of 0.7 V. At this region, any electrochemically oxidisable components available at the anode interface will be consumed to produce electrons. Here the partial pressures of CO and H_2 are shown to have decreased from those at OCV, which indicate that CO and H_2 are consumed by electrochemical oxidation reactions to produce CO_2 and H_2O. As expected, the partial pressure of CO_2 is shown to have increased. Figure 8.1 doesn’t show H_2O curve since before reaching the analytical chamber of the mass spectrometer, H_2O condenses along the SOFC outlet gas pipeline. Therefore the H_2O partial pressure detected by the mass spectrometer won’t be able to represent the true H_2O composition; hence H_2O curve is not presented in Figure 8.2.

It is interesting to observe the CO (orange) and CO_2 (purple) curve in this Region C; while the level of CO is constant over the 4 hours duration, the level of CO_2 is gradually increasing. This can be an early sign that at least a part of carbon deposits present on the anode surface may undergo electrochemical oxidation producing CO and pushing the already existing CO to oxidise to CO_2.

Figure 8.2 a) shows CO partial pressures in the SOFC outlet obtained from the first 30 minutes of OCV measurements of 3 Sn-infiltrated SOFCs in biogas compared to 2 non-infiltrated SOFCs. Figure 8.2 b) and c) show partial pressures of CO and H_2 during the 60 – 105 minutes operation on biogas.

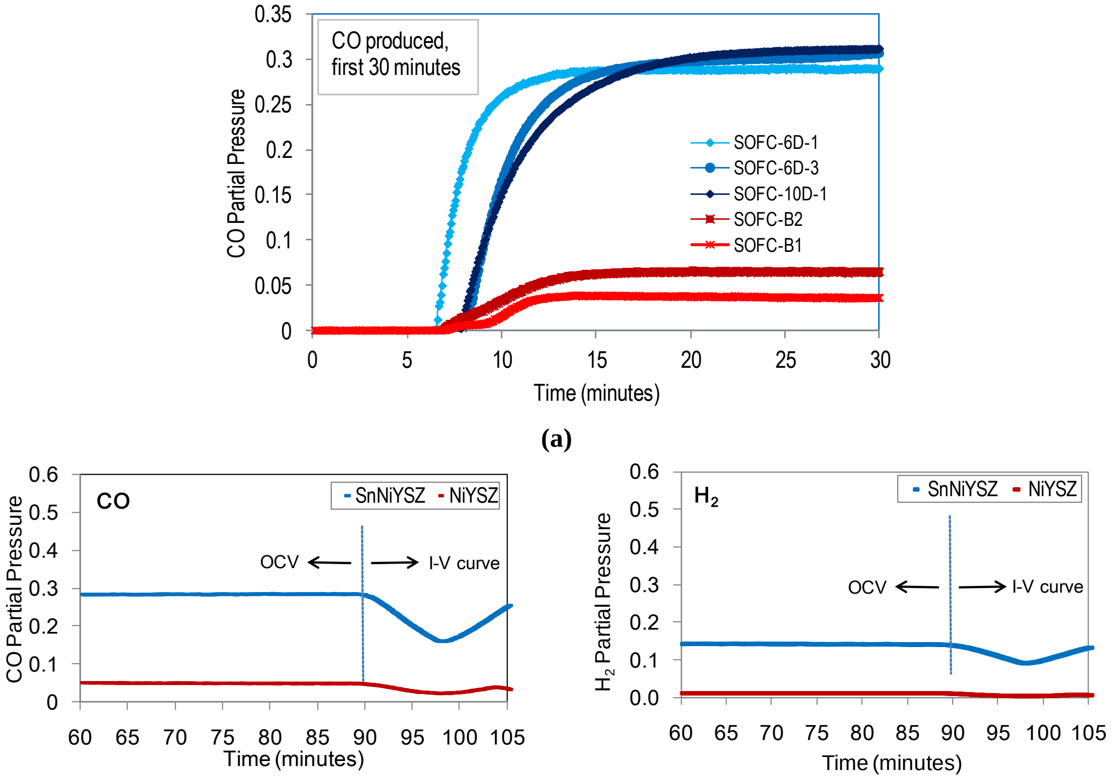

(a)

(b) **(c)**

Figure 8.2: Partial pressures of SOFC outlet gases (a) CO at OCV, (b) CO at OCV and IV curve and (c) H_2 at OCV and IV curve measurements.

Figure 8.2 b) shows that at 90 minutes operation, when I-V curve was started, both CO and H_2 partial pressures responded accordingly to the change in current density. Figure 8.2 a), b) and c), show the significant difference of SOFC outlet gas compositions which contributed to the markedly different electrochemical performance of the Sn-infiltrated

SOFCs compared to those of the non-infiltrated SOFCs, as will be presented in detail in the following sections.

How can Sn-infiltrated SOFC anode increase the conversion rate of dry reforming? This will be discussed under discussion and conclusion section of this chapter.

8.4 Electrochemical Performance on Biogas

8.4.1 Prediction of electrochemical performance using fuel cell model

Composition of the SOFC outlet gas obtained from the mass spectra of Sn-infiltrated SOFC discussed in section 8.3 is tabulated in Table 21. The composition obtained from operating biogas on Sn-infiltrated SOFCs is compared to the predicted (ideal) composition and the measured composition obtained from non-infiltrated SOFCs presented in Chapter 7.

Table 21 SOFC outlet gas composition (in partial pressure), measured vs. prediction$^{\#2}$ (at 750 ^{o}C) in equilibrium (OCV)

Gas components	Feed	Product, predicted by CEA2 simulation	Product, of non-infiltrated SOFC-B1	Product, of Sn-infiltrated SOFC-6D-1
CO_2	0.25	0.01649	0.24800	0.1329
CH_4	0.50	0.01833	0.49600	0.289
He	0.25	0.12958	0.19800	0.157
H_2O	0	0.03900*	na	na
H_2	0	0.44667	0.01300	0.143
CO	0	0.19717	0.05120	0.285
C (gram)	0	0.15675	Na	Na
Total	1.000	1.004	1.006	1.007
% Conversion*		44.67	1.30	14.30

* : to avoid much error on calculation due to extremely different values of CH_4 partial pressures displayed in column 3 and 4, calculation of % conversion was slightly altered from those in Chapter 6; here it is calculated as % (1/2 mole H_2 produced /mole CH_4 in the feed).

The measured SOFC outlet gas composition was then used as input for the fuel cell model [78, 152]. There are now three sets of results of fuel cell model simulation as follow;

1. 1st FCM simulation: using the biogas dry reforming product composition predicted by reforming simulation software. This simulation is based on equilibrium compositions which is an ideal case.
2. 2nd FCM simulation: using the dry reforming product composition obtained from mass spectra of a non-infiltrated cell (SOFC-B1)
3. 3rd FCM simulation: using the dry reforming product composition obtained from mass spectra of a Sn-infiltrated cell (SOFC-6D-1)

The results of the simulations are presented in Figure 8.3. It is shown that with the outlet gas composition obtained from Sn-infiltrated SOFC a closer to ideal polarisation curve (blue coloured) is obtained.

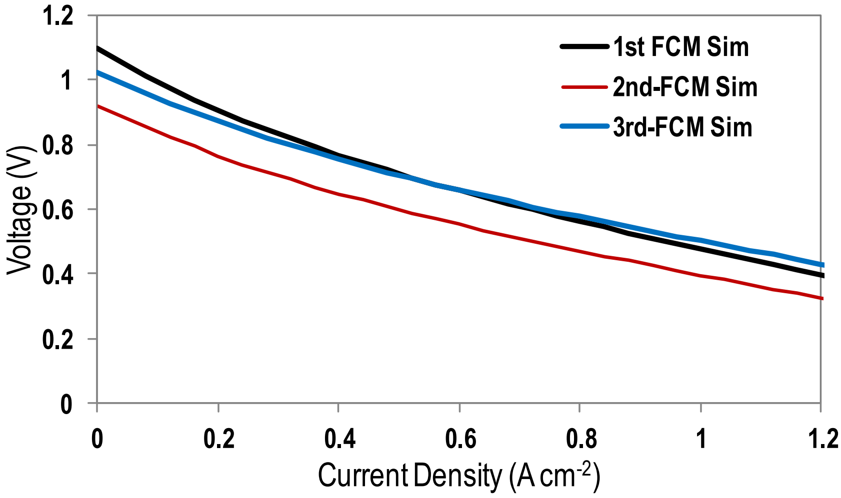

Figure 8.3: Predicted polarisation curves obtained from three modes of simulation.

8.4.2 Measured electrochemical performance

Figure 8.4 shows the polarisation curves obtained from FCM simulations compared to the actual results obtained from testing a non-infiltrated SOFC (-B2) and a Sn-infiltrated SOFC (-4D-2). The charts in Figure 8.4 shows good agreements of polarisation curve obtained from SOFC-4D-2 with that predicted by 3rd FCM simulation. In fact OCV values obtained in SOFC-4D-2 was 15 mV higher than that predicted by the simulation. Potential losses at high current density (concentration polarisations) were observed but these were also observed in fuelling the SOFCs with 50% fuel utilisation in H_2. So, these concentration polarisations were originated from the base fuel cell, not from the Sn-infiltration.

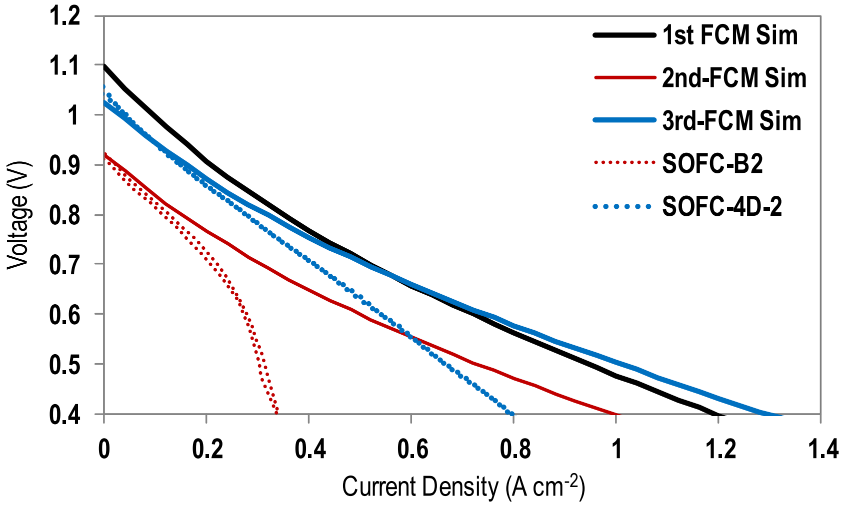

Figure 8.4: Measured vs. predicted polarisation curves of Sn-infiltrated and non-infiltrated SOFCs.

8.4.2.1 Open circuit potential

Results of the OCV measurements of the Sn-NiYSZ SOFCs with varied amount of Sn are presented in Figure 8.5. The figure shows 4 sets of the OCV profiles obtained from 2D-, 4D-, 6D-, and 10D-NiYSZ. Each set was represented by two SOFCs. The OCV profiles indicate that OCV fluctuates during the first 25 minutes of measurements which corresponds to the gradual switch of fuel feed from H_2 to biogas. A common trend of OCV decrease was observed but the decrease was followed by a subsequent increase and eventually it reached a stable and slightly higher value compared to the initial value obtained in H_2. On average, 10 – 20 mV increase of OCV was gained from switching to biogas. The trend observed in the OCV profiles of these Sn-infiltrated SOFCs is the opposite to that observed in the non-infiltrated SOFCs, represented in Figure 7.4, where an overall decrease from 1.05 V to 0.93 V was observed on switching the fuel gas from H_2 to biogas. Since OCV is the first indication of a fuel cell performance, this constant value or slight increase in OCV is a good indication that electrochemical performance of the Sn-doped SOFC in biogas remained constant or slightly increased as the fuel was switched to biogas. As suggested by Nernst equation, higher OCV values can be originated from higher flow rate or partial pressure of the electrochemically oxidisable gases; H_2 and CO. A more detailed analysis will be given in the following sections.

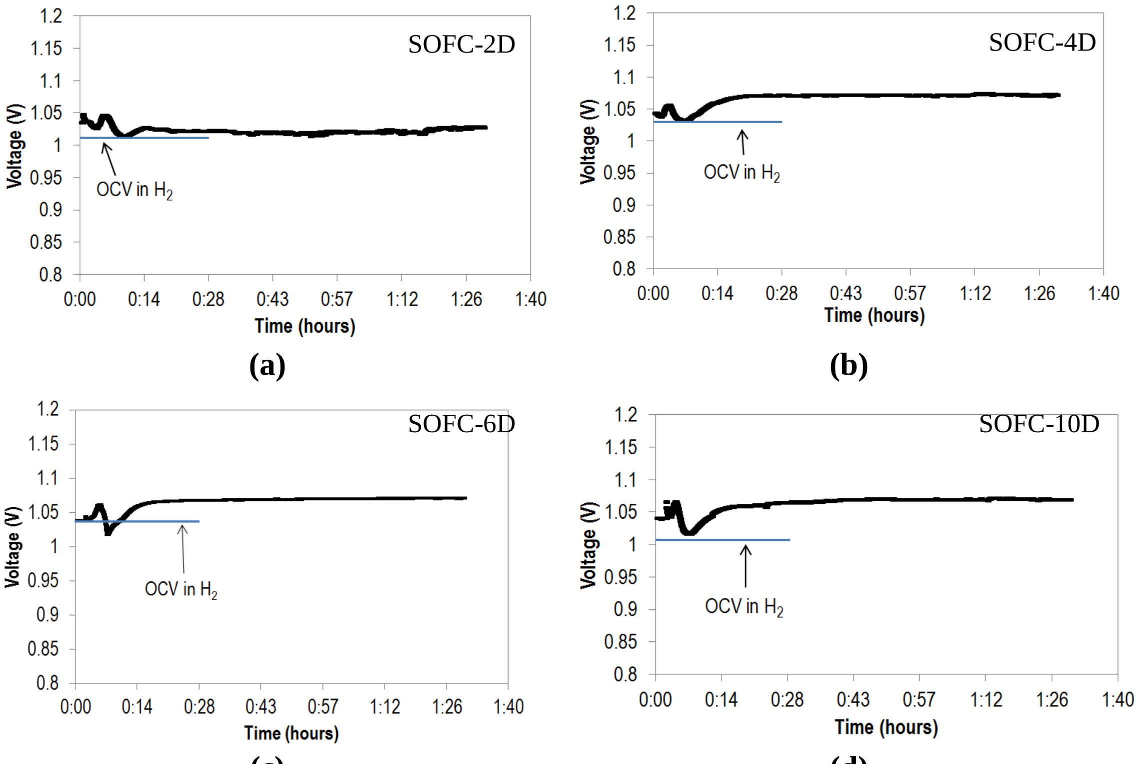

(a) (b)

(c) (d)

Figure 8.5: OCV values obtained from Sn-infiltrated SOFCs fuelled by biogas

8.4.2.2 Polarisation and Power density

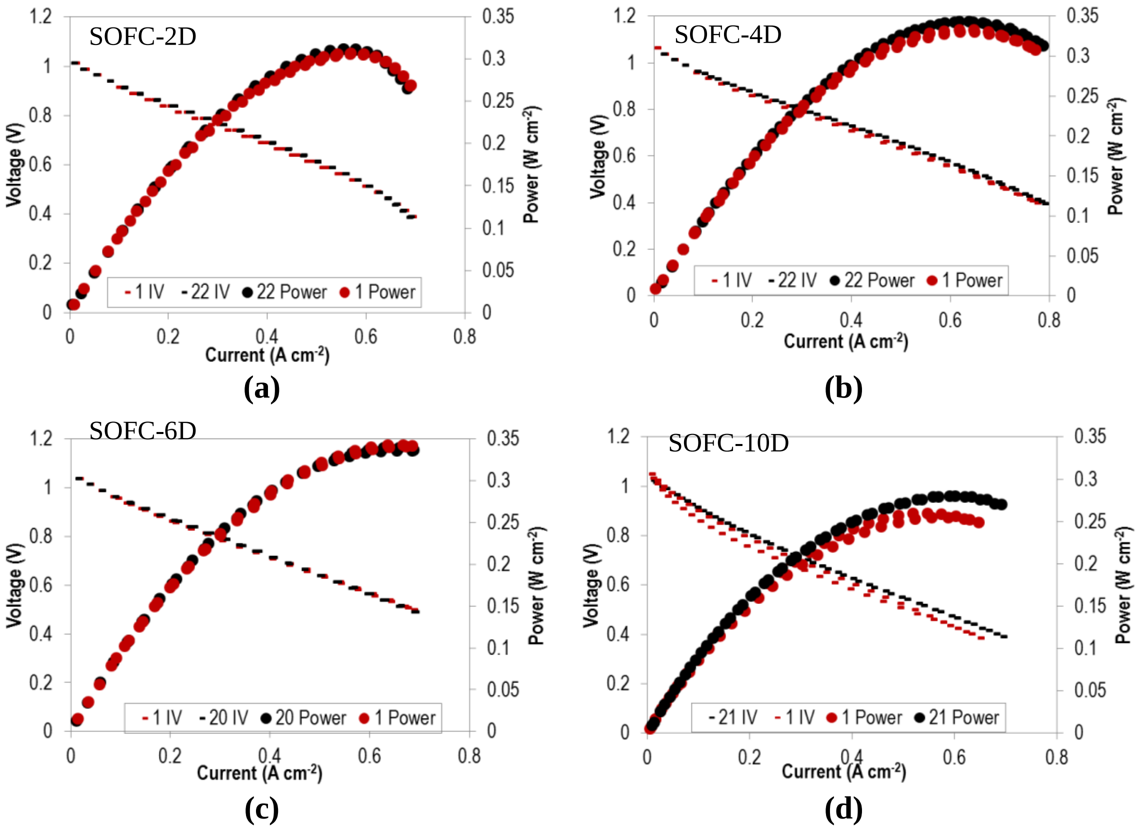

Figure 8.6: Polarisation and power density curves of Sn-infiltrated SOFCs fuelled by biogas

The polarisation curves of the four sets of Sn-doped SOFCs are presented in Figure 8.6. These sets of polarisation curves were recorded during the first 2 hours (just after the 90 minutes OCV, red coloured) and the last hour (black coloured) of the 22 hours of operation in biogas. It can be seen that each Sn-doped SOFC shows maximum power densities of 300 mW cm^{-2} or higher. Within 22 hours of operation, all Sn-infiltrated SOFCs showed a stable or slightly increased performance, except that of the 6D-1 SOFC, which showed a slight decrease in performance. The highest increase of performance is shown by SOFC-10D which indicates that 10 drops infiltration seems to block porosity and thus stretches the time it takes for the anode to properly reduce. This phenomenon is more clearly observed in Figure 8.7.

8.4.2.3 Durability at 22 hours and 150 hours

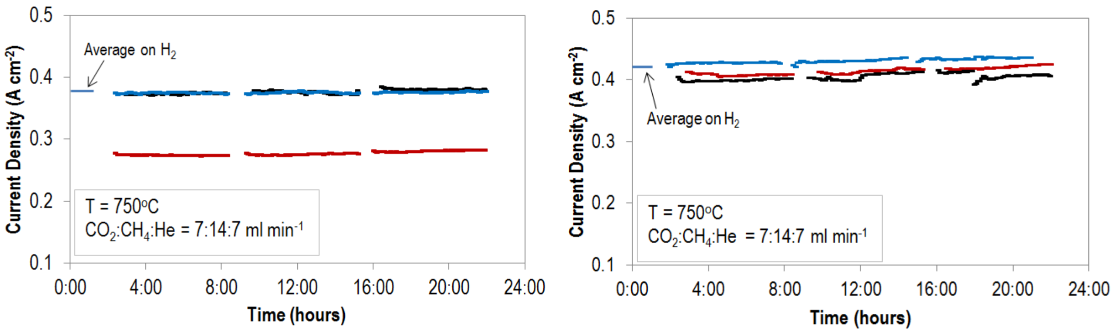

(a) SOFC 2Ds **(b) SOFC 4Ds**

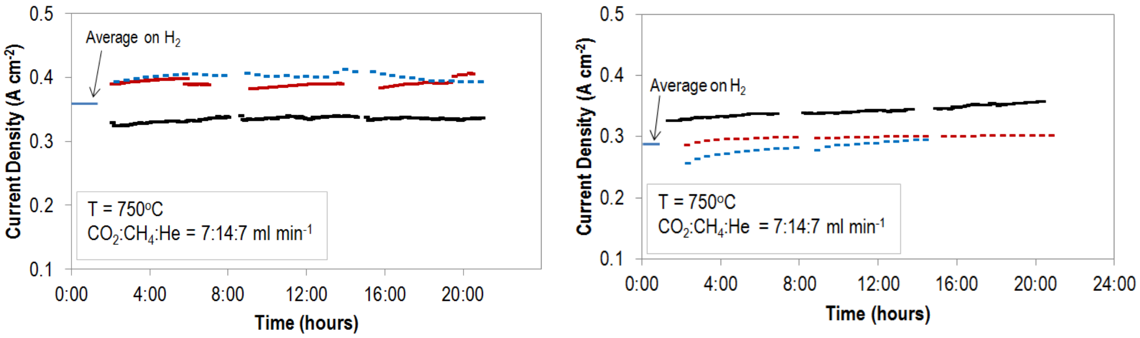

(c) SOFC 6Ds **(d) SOFC-10Ds**

Figure 8.7: Current density at 0.7 V from Sn-infiltrated SOFCs fuelled by biogas

From Figure 8.6 and Figure 8.7 it is observed that on going from SOFC-2D to -4D, and -6D there is an increase in current and power produced but from SOFC-6D to -10D there is a slight decrease of current and power. Again it seems that the 10D infiltration causes parts of anode pores to block. Other possible effect is that the 10D infiltration reduces the active sites of nickel surface for H_2 electrochemical oxidation, hence lower current produced and higher concentration over-potential observed at higher current densities.

While most of the SOFCs were tested for 22 hours on biogas, one of the 10D Sn infiltrated SOFCs was tested for 150 hours. Figure 8.8 shows current and power produced over 150 hours test which includes 26 hours baseline test on H_2. The regions marked A, B and C represent long periods of OCV. The A region was almost 20 hours of OCV which was accidentally observed due to the test was 'safety shut down' following a malfunction of a neighbouring cell test channel which occurred over a weekend. It was interesting to see the accident did not cause cell failure. Cell performance degradation was observed but the performance gradually increased and stabilised. Regions B and C were purposely observed OCV for 6 and 12 hours which confirmed that considerably long OCV did not cause this Sn-infiltrated cell performance to degrade. This is a promising indication that Sn-infiltrated SOFC does resist carbon formation even during OCV, when no current to electrochemically oxidise carbon and no production of water from H_2 electrochemical oxidation is produced. This Sn-infiltrated SOFC seems to have the ability to promote chemical oxidation of carbon formed with the presence of 0.5 ratio of CO_2:CH_4.

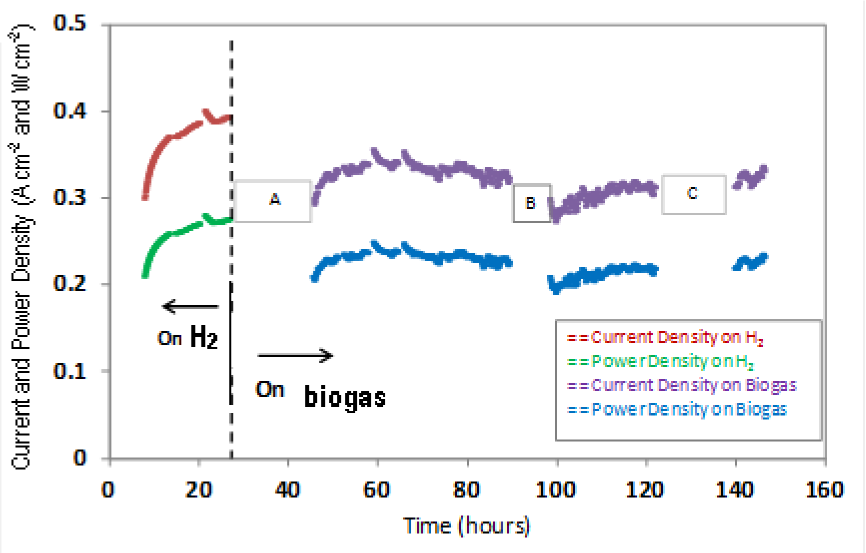

Figure 8.8: Current and power densities at 0.7 V of 10D-Sn-infiltrated SOFC fuelled by biogas

8.4.2.4 Electrochemical Impedance Spectra (EIS)

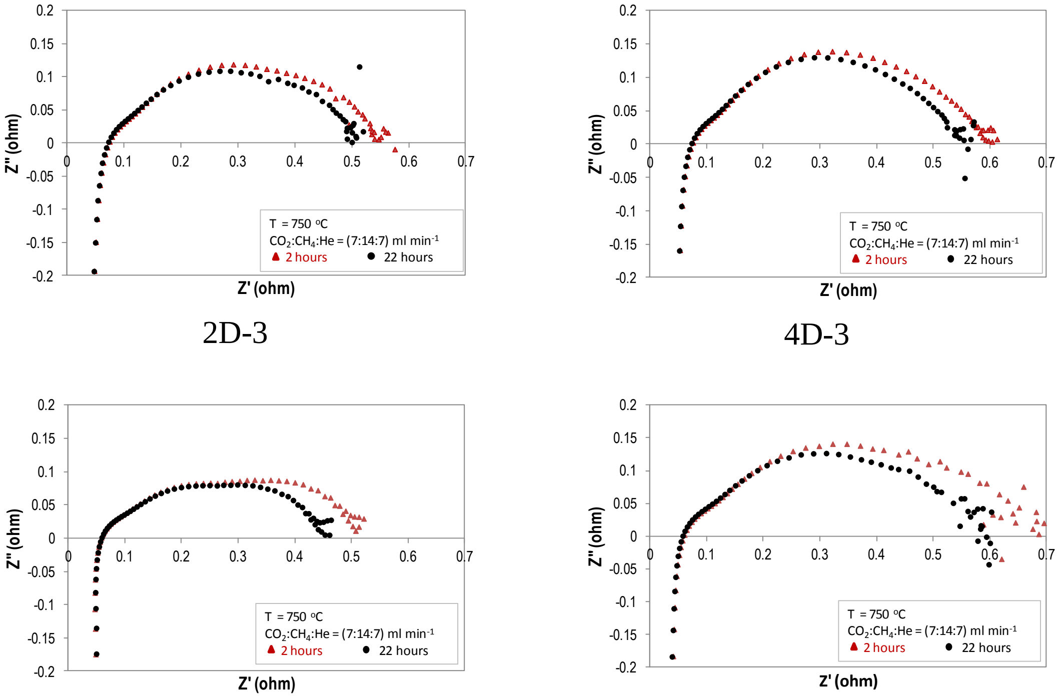

2D-3 4D-3

6D-6 10D-2

Figure 8.9: EIS Spectra at OCV of Sn-infiltrated SOFCs fuelled by biogas

EIS spectra of the Sn-infiltrated SOFCs are presented in **Figure 8.9.** The highest and lowest frequencies displayed in the spectra were 10 MHz and 0.1 Hz respectively. The EIS spectra obtained from 2D, 4D, 6D and 10D Sn-infiltrated SOFC anodes show consistently low Ohmic resistance and also considerably low polarisation resistances compared to the polarisation resistances displayed by non-infiltrated SOFCs in Figure 7.8. in Chapter 7. In fact the polarisation resistances of these Sn-infiltrated SOFCs in biogas are comparable to those demonstrated by non-infiltrated SOFCs in H_2. These impedance spectra also confirm results shown in Figure 8.6 and Figure 8.7 regarding the improvements of performance of the SOFCs observed over 22 hours of operation.

8.5 SEM images of anode surface

Figure 8.10 shows the appearance of anode surface under SEM comparing the anode microstructure pre- and post- 22 hours test on biogas. Although not quantitatively proven, it is observed that more anode pores were formed during the test. The images also revealed that there is no visible carbon formed on the anode surface during the test. A further analysis of the tested cells using Temperature Programme Oxidation was carried out to quantify the trace carbon formed. The results are presented in Chapter 9.

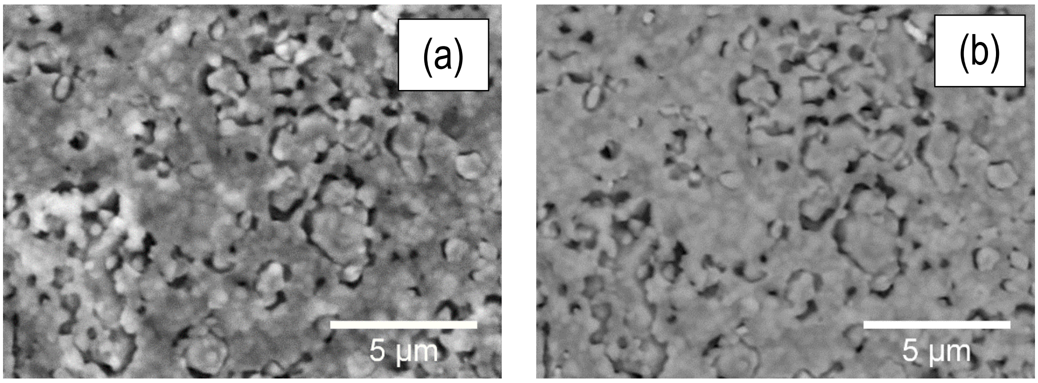

(a). SOFC-4D reduced anode, pre-test (SE) **(b). SOFC-4D reduced anode, pre-test (BSE)**

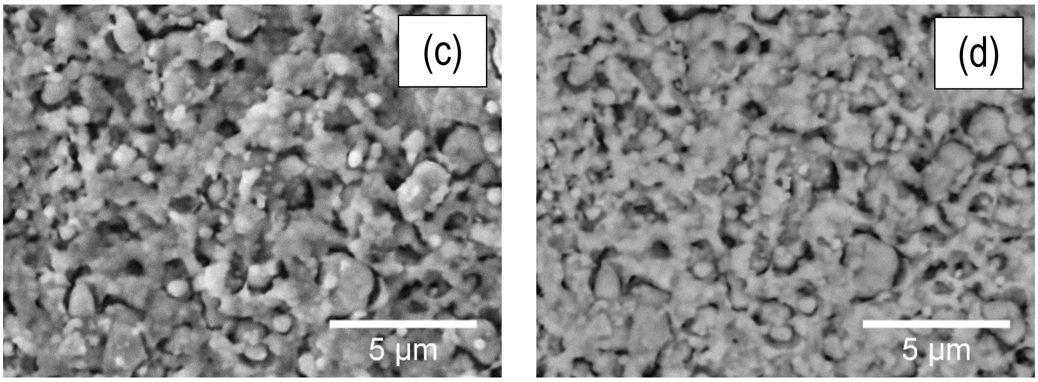

(c) SOFC-4D 3 post-22 hours in biogas (SE) **(d) SOFC-4D 3 post-22 hours in biogas (BSE)**

Figure 8.10: SEM images of Sn-infiltrated SOFC anode pre- and post-22 hours test on biogas

Another set of SEM images is presented in Figure . These images are representatives of (a) Sn-infiltrated anode surface pre-test, (b) a non-infiltrated anode surface post-150 hours test on biogas, (c) Sn-infiltrated anode post-150 hours tests on H_2 and (d) Sn-infiltrated anode post-150 hours test on H_2. It is observed that 150 hours test both on biogas and on H_2 displayed much different microstructures. The Sn-infiltrated SOFCs showed distinctive nickel particles, similar to those shown in Figure 5.9. The distinctive nickel particles are not so clearly observed on the anode surface of the non-infiltrated SOFC displayed in Figure b. Further examinations using higher resolution SEM or TEM may help to clarify what exactly was happening to these Sn-infiltrated and non-infiltrated NiYSZ anode during the 150 hours period of test on H_2 and on biogas.

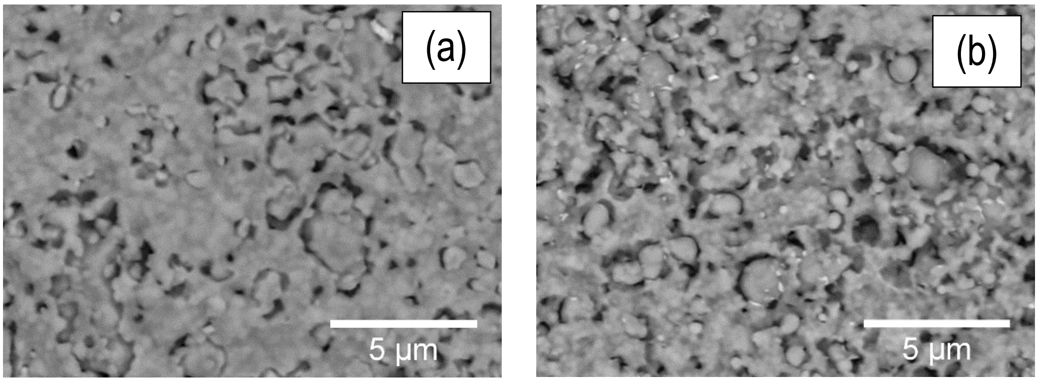

(a) 4D Sn-infiltrated anode, pre-test **(b) Non-infiltrated SOFC post 150 hours on biogas**

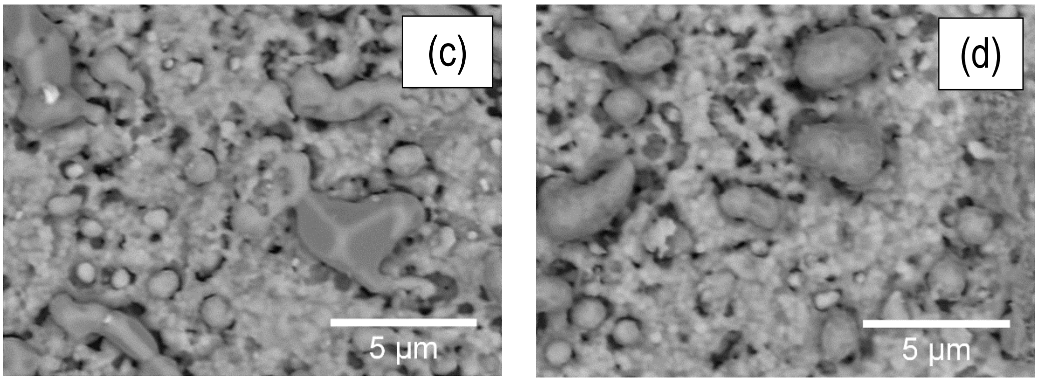

(c) 10D Sn-infiltrated SOFC post 176 h test on H_2 **(d) 10D Sn-infiltrated SOFC post 150 hours test on biogas**

Figure 8.11: SEM images of SOFC anode surface pre- and post-150 hours test on H_2 and biogas

8.6 Summary of SOFC electrochemical performance

Figure shows the summary of the electrochemical performance of all the SOFCs tested represented by current produced at 0.7 V. The current produced both on the non-infiltrated and the Sn-infiltrated SOFCs fuelled by H_2 are not much varied, taking note that SOFC-4Ds showed slightly higher while SOFC 10Ds showed slightly lower current than other SOFCs. It is the current produced on biogas fuel that was much varied with the level of the current produced from non-infiltrated SOFCs significantly lower than that from the Sn-infiltrated SOFCs. These results are quite encouraging: especially the results from SOFC-4Ds which showed that Sn-infiltrated SOFCs have shown much improved performance on biogas without having to lose their performance on H_2.

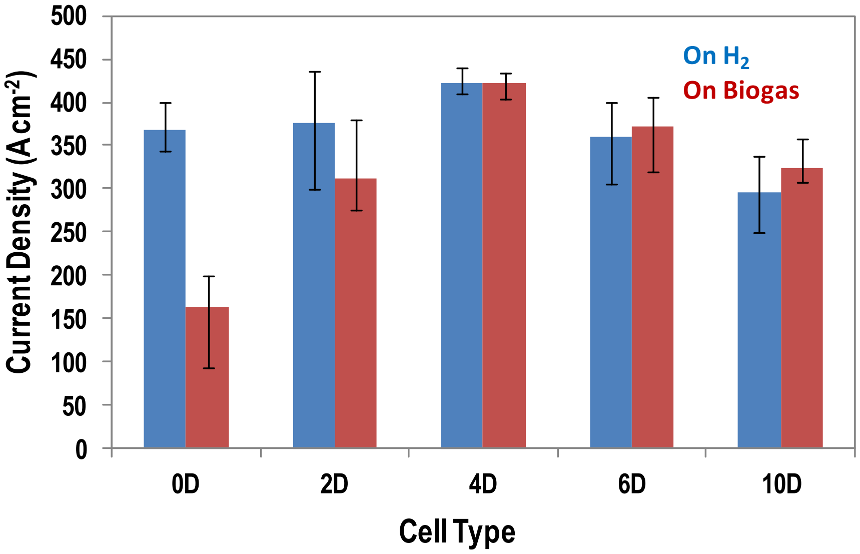

Figure 8.12: Summary of current density at 0.7 V obtained from all of the tested SOFCs

8.7 Discussion and Conclusion

Summary of the electrochemical performance revealed that Sn-infiltrated SOFCs showed significant improvement of current density produced on biogas and the ability to retain current density on H_2. The SOFCs showed stable operation on biogas for 22 hours and 150 hours without visible carbon formation.

Sn-infiltrated SOFCs with varied Sn contents were manufactured and electrochemically tested on biogas fuel using exactly the same test conditions as those used for testing the non-infiltrated SOFCs. The Sn-content in the SOFC ranges from 0.2 to 1.0 % weight Sn/Ni. It was observed that all Sn-infiltrated cells (2D, 4D, 6D, and 10D) showed significant improvements of electrochemical performance on biogas while still retaining the performance on H_2. It was found that the 4D Sn infiltrated SOFC, corresponding to 0.38 % weight Sn/Ni gave the best electrochemical performance on both H_2 and biogas, producing 420 mA cm^2 current density at 0.70 Volt.

Mass spectra of the Sn-infiltrated SOFCs showed that the improved electrochemical performance was related to the higher conversion of dry reforming reaction on Sn-infiltrated SOFCs compared to that on non-infiltrated SOFCs. While Trimm [51] and Nikolla et.al [98] reported that under steam reforming reactions the presence of Sn on supported Ni catalysts slightly suppressed steam reforming but significantly reduced the amount of deposited carbon, the results in this study showed the opposite effect on the reforming part but with similar effect on the carbon deposition. How can Sn-infiltration increase the conversion of dry reforming reaction on NiYSZ catalyst? This may be explained as follows; it is generally understood that hydrocarbon reforming reactions occur via methane cracking and carbon oxidation [51] as represented below;

$\mathbf{CH_4 + CO_2}$	$\leftrightarrow$	$2\,CO + 2\,H_2$	dry reforming	(Eq. 2.20)
$\mathbf{CH_4}$	$\leftrightarrow$	$C + 2\,H_2$	pyrolysis or cracking	(Eq. 2.25)
$\mathbf{C + CO_2}$	$\leftrightarrow$	$2\,CO$	Reverse Boudouard	(Reverse Eq. 2.27)

Methane cracking, which is initiated by a dissociative adsorption of hydrocarbon, on supported Ni catalyst is a structure sensitive reaction. It was found that under coordinated (or step edge) Ni surface sites are more active than closed packed Ni sites

[99, 140]. The non-infiltrated SOFC samples used in this study may have very small active Ni sites that they showed low conversion of dry reforming. However as Sn was infiltrated on the NiYSZ catalyst, the Sn/Ni surface alloy was formed. As suggested by Nikolla et.al [99] this Sn/Ni surface alloy '*is more efficient than Ni in the preferential formation of C-O rather than C-C bonds*. As a consequence, the carbon formed on Sn/Ni catalyst surface is rapidly oxidised to CO. The rapid oxidation of carbon shifts the methane cracking reaction to the right, producing more carbon and hydrogen, which in turn increase the overall conversion of dry reforming reaction.

Predictions of SOFC electrochemical performance using FCM simulation were compared to those obtained from the SOFC tests and presented in Figure 8.4. It was revealed that the polarisation curve obtained from the Sn-infiltrated SOFC is in good agreement with that predicted by 3rd FCM simulation. This confirms that the experimental observations are in agreement with theoretical calculations.

From the SOFC outlet gas composition monitored using a quadruple mass spectrometer during the SOFC electrochemical tests; it was observed that at OCV 14.3% CH_4 conversion was achieved during the electrochemical performance test of SOFC-6D-1. This value is eleven times higher compared to the CH_4 conversion achieved in non-infiltrated cells. However overall improvement of the electrochemical performance on Sn-infiltrated cells was found to be twice to four times only which means that at least 50 % of H_2 and CO produced were wasted as outlet gas without being electrochemically oxidised. This indicates that, in SOFC operation using direct biogas in dry reforming mode, there are rooms to improve other factors than catalytic activity of the anode towards dry reforming reactions. Those factors as anode substrate porosity and anode particle size, which can significantly affect anode TPB boundary length, are examples of important factors to investigate in the future along with more Sn-infiltration techniques and more anode characterisations.

Chapter 9

Carbon Deposition

9.1 Overview

This chapter describes results of observations and measurements of quantity of carbon deposited on the SOFC anodes during SOFC operation fuelled by biogas described in Chapters 7 and 8. Presenting carbon deposition results in one chapter is aimed for clearer comparisons across different conditions of non-infiltrated and Sn-infiltrated SOFC anodes. Observation of SOFC anode appearance post testing was used as a preliminary method, observation of SEM micrographs was used for more detailed examination. The method used to measure the quantity of carbon deposited was Temperature Programmed Oxidation (TPO). The details of the procedure to perform TPO are presented in Chapter 3. As a reference and comparison, the observations of anode pieces pre- and post-dry reforming in the quartz glass reactor as described in Chapter 6 are also presented in this chapter.

9.2 Appearance of NiYSZ SOFC anodes

9.2.1 Pre- and post-dry reforming in the quartz tube

The appearance of catalysts was observed after dry reforming reaction in the quartz tube with the dry reforming results described in Chapter 6. It was obvious that carbon was deposited during dry reforming reaction, especially on NiYSZ anode support pieces. While on pieces of full fuel cell, formation of carbon was not that obvious. Below are pictures which show the appearance of the catalysts after dry reforming. Figure 9.1 shows pieces of non-infiltrated NiYSZ anode supports (referring to dry reforming performance in Figure 6.3) which were turned into carbon containing crumbs (upper right), and pieces of non-infiltrated full fuel cells (lower right) which did not show carbon formed after 5.5 hours of dry reforming at 650-800^{o}C and at feed composition of CO_2:CH_4:He = 10:20:20 ml min^{-1} (referring to dry reforming conditions in Figure 6.4). It is apparent that anode support pieces have more nickel particles exposed (on both sides of the disc) while full fuel cell pieces have fewer nickel particles exposed (only on one side of the disc). This indicates that the more free NiYSZ anode surface exposed to biogas in the anode support pieces have made carbon formation, from methane cracking reaction, much faster than that in the full fuel cell pieces. The weight of carbon, pictured in Figure 9.1 upper right, obtained after dry reforming on 500 mg of non-infiltrated anode support was 1200 mg (240% of the original weight of the catalyst). Referring to the lower right picture of Figure 9.1, this shows that even in dry reforming in a quartz reactor (without current drawing) carbon formation on the non-infiltrated SOFC full cell was slow. This supports evidence that the pieces of non-infiltrated SOFC full cell performed poorly in biogas dry reforming.

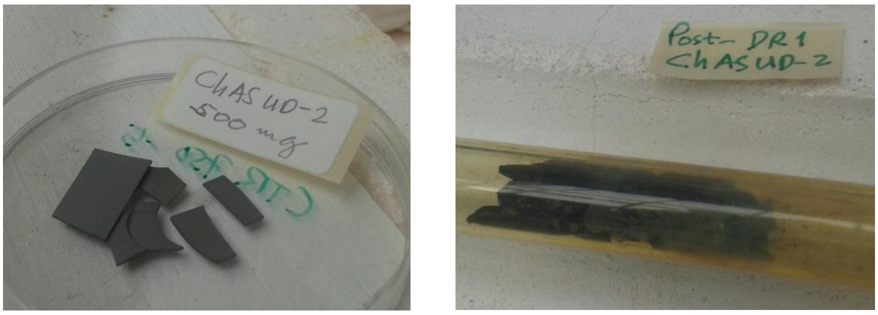

Anode supports before dry reforming Anode supports after dry reforming

Full cell pieces before dry reforming Full cell pieces after dry reforming

Figure 9.1: Appearance of catalysts before and after dry reforming in the quartz tube

9.2.2 Appearance of SOFC anodes post-electrochemical test on biogas

Figure 9.2 shows the appearance of five SOFC anodes from tested SOFCs, which represents all SOFC types, post-electrochemical test on biogas. It was observed that after 22 hours of operation on biogas the anodes still appeared clean without significant carbon formation observed. Figure 9.2 e) and f) show the anode side of SOFC-10D-2 pre- and post-test on biogas for 150 hours. It was observed that 10 drops of Sn-infiltration on the SOFC anode surface seems to be excessive (not able to be absorbed in the anode pores) that a whitish colour of possibly SnO_2 deposits appeared on the edge of the anode. Parts of the anode edge post-testing for 150 hours on biogas appeared black which resembles carbon but SEM image of this particular SOFC presented in **Figure** did not confirm it was carbon. Further quantitative analysis of carbon deposition presented in section 9.3.2 showed a very low rate of carbon deposition on this SOFC-10D-2 anode.

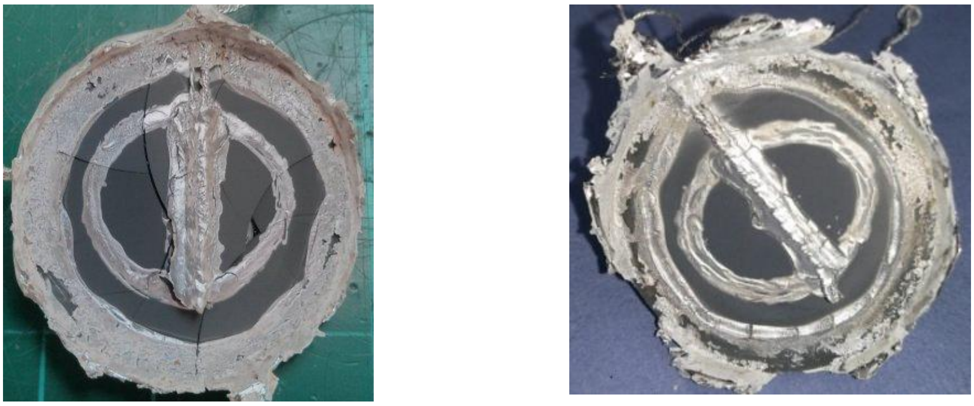

(a) SOFC-B2, post-22 hours on biogas

(b) SOFC-2D-1, post-22 hours on biogas

(c) SOFC-4D-2, post-22 hours on biogas

(d) SOFC-6D-6, post-22 hours on biogas

(e) SOFC-10D-2, pre-test

(f) SOFC-10D-2, post-150 hours on biogas

Figure 9.2: Appearance of SOFC anode surface post testing under dry reforming mode

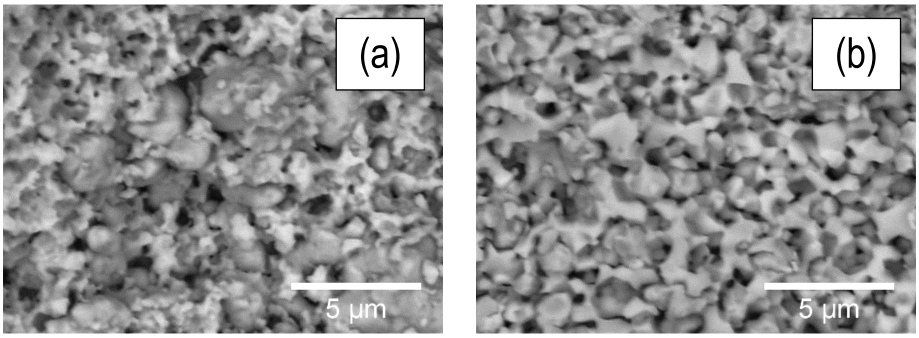

(a) SEM image of SOFC-10D-2 AS **(b) SEM image of SOFC-10D-2 AFL**

Figure 9.3: SEM images of SOFC-10D-2 post-150 hours test on biogas (a) anode support (b) anode functional layer.

Figure 9.3 shows SEM images of cross sectional area of SOFC-10D-2 both at anode support and anode functional layer parts. This figure indicates clear NiYSZ grains and shows no sign of carbon deposition compared to the micrograph in Figure 2.10 which shows formation of much carbon filaments even at a condition milder (CO_2 : CH_4 = 1:1) than the biogas composition used in this work (CO_2 : CH_4 = 1:2).

9.3 TPO Results

9.3.1 Carbon deposition from non-infiltrated SOFCs

The details of TPO measurement method is presented in Chapter 3. Below are pictures of the test rig and quartz tube which were used for TPO measurement and an example of 6.6 mg graphite powder in a ceramic bowl ready for TPO calibration.

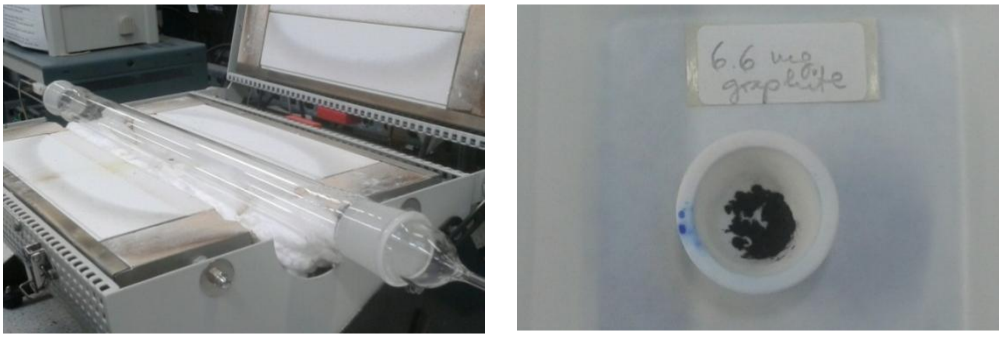

(a) The TPO reactor **(b) A known amount of graphite for TPO calibration**

Figure 9.4: (a) The TPO reactor and (b) a known amount of graphite for TPO calibration

TPO calibration was carried out to obtain several data points for construction of a calibration curve. Figure 9. presents the CO_2 peaks evolved during TPO of different quantity of pure graphite. It was observed that the pure graphite was consistently oxidised at approximately 850^{o}C. One of the carbon standard used for calibration was carbon black. It was shown that carbon black, known to have some part of amorphous solid, oxidised at a lower temperature of 720^{o}C. This is expected since amorphous carbon is more reactive (easier to gasify) compared to graphitic carbon, such as implied by the reactivities of the different types of carbon which is presented in Table 2. Although Table 2 lists the reactivities in hydrogen environment, a similar trend is expected of the reactivities of carbon in oxidation reaction.

Data of CO_2 peak area obtained from calibration of graphite as presented in Figure 9.5 were used to construct a calibration curve. From this calibration curve a linear relationship between the weight of graphite and CO_2 peak area was obtained. It was found that 1 mg of graphite corresponds to 0.697 units of CO_2 peak area. This value was used as a factor to calculate the quantity of carbon deposited in the SOFC anode samples using the CO_2 peak area obtained from TPO of the samples and the exact weight and cell area of each tested SOFC sample.

Amount of C deposited (mg carbon / cm^2 SOFC) =

CO_2 peak area / 0.697 x 1 mg / (surface area of SOFC anode sample in cm^2) Eq. 9.1

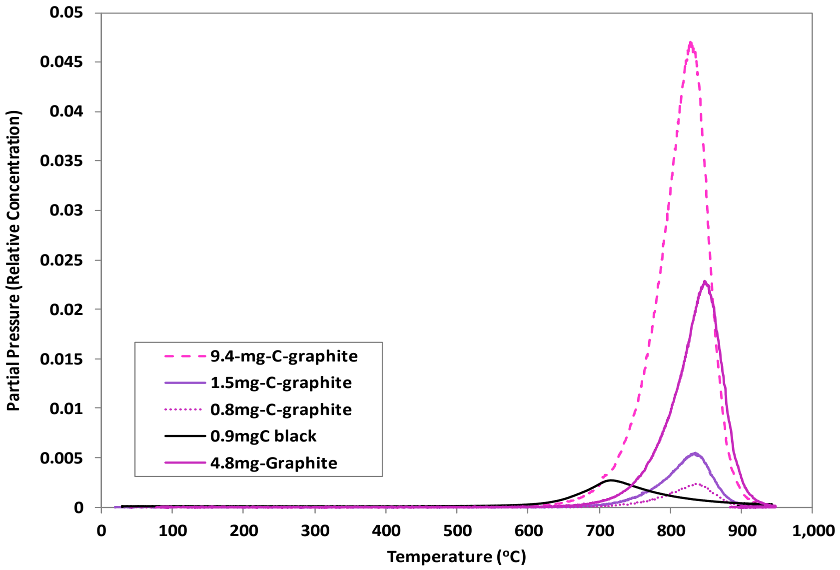

Figure 9.5: CO$_2$ peaks obtained from TPO calibration of standard carbon (graphite powder)

Figure 9. shows TPO results of three non-infiltrated SOFCs. It is observed that SOFC-B3 and B4 showed almost no carbon detected. While SOFC-B1 which was operated for 150 hours on biogas showed a very low amount of carbon (0.21 mg carbon cm^{-2}). TPO result of SOFC-B2 was not included here since the mass spectrometer had its filament burnt out while the TPO was measured hence no adequate data were obtained.

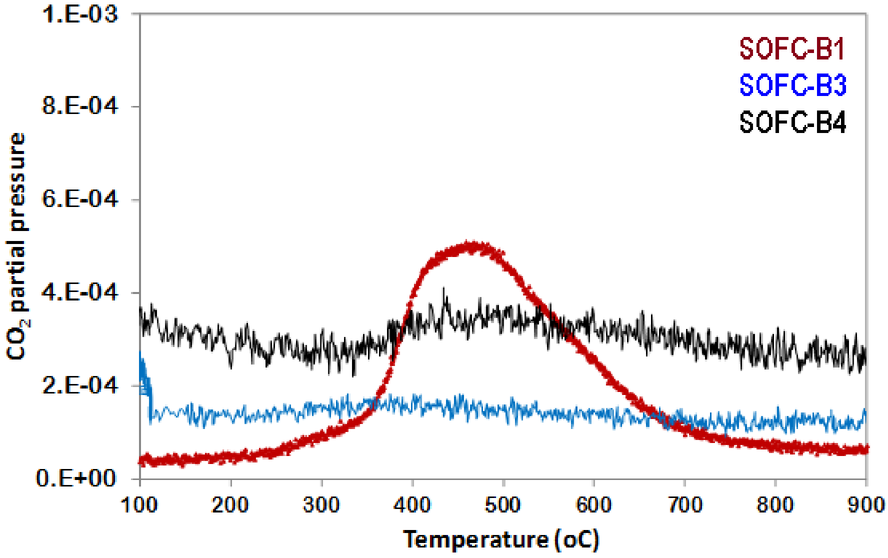

Figure 9.6: CO$_2$ peaks obtained from TPO of non-infiltrated SOFCs (SOFC-B1, B3 and B4)

9.3.2 Carbon deposition from Sn-infiltrated SOFCs

Results from the first series of TPO measurements of SOFC-B1 (0D), SOFC-2D-1, SOFC-4D-2, SOFC-6D-1, and SOFC-10D-2 are presented in Figure 9.. The curve for SOFC-B1 (0D) is the same red curve appearing in Figure 9.6. The green coloured curve represents CO_2 peak from SOFC-10D-2 which was operated for 150 hours on biogas. The shape of the curves of SOFCs 0D, 2D, 4D and 6D indicate a small quantity of amorphous carbon, forming CO_2 peak at 450 ^{o}C, was similarly formed during each SOFC operation.

The green curve obtained from SOFC-10D-2 which was operated for 150 hours, shows a split peak forming a smaller amount of amorphous carbon at 350 ^{o}C and a larger amount of graphitic carbon at 700 ^{o}C. These green CO_2 peaks correspond to a total of 0.14 mg carbon cm^{-2} or 0.0009 mg carbon cm^{-2} h^{-1}. Knowing that the average weight of an SOFC anode support in this work is 1240 mg, and the anode diameter is 30 mm; it follows that the anode weight per cm^2 is

$$1240 \text{ mg} / (3.14 \text{ x } 1.5^2) \text{ cm}^2 = 175.5 \text{ mg}.$$

Therefore on SOFC-10D-2 the rate of carbon deposition per mg catalyst per hour is

$$0.14/(150 \text{ x } 175.5) = 5.3 \text{ x } 10^{-6} \text{ mg carbon mg}_{cat}^{-1} \text{ h}^{-1}$$

$$= 5.3 \text{ x } 10^{-3} \text{ mg carbon g}_{cat}^{-1} \text{ h}^{-1}$$

The above rate of carbon deposition on SOFC anode operating on biogas is very low compared to the reported rate of carbon deposition, that was 0.095 mg g$_{cat}^{-1}$ h^{-1} over 290 hours, of dry reforming on alumina supported 7Ni3Co/LaAl catalyst at 800^{o}C [114].

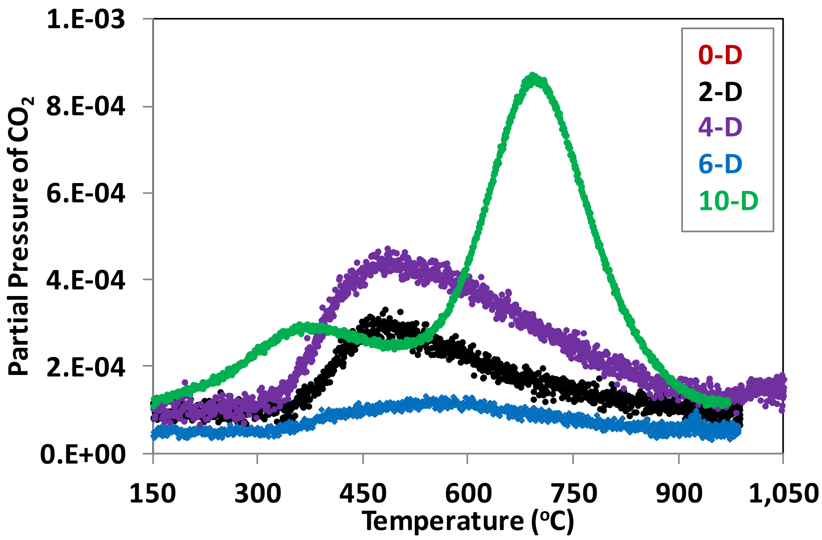

Figure 9.7: CO_2 peaks obtained from TPO of Sn-infiltrated SOFCs, first series

To the best of the author's knowledge most literature reported only relative comparisons of carbon formation among the tested cells of their own samples using TPO curves derived from mass spectra without stating the quantity of the deposited carbon. Therefore comparison of the above rate of carbon deposition couldn't be adequately made with other reports on tested SOFCs.

To confirm the results obtained in the first series of TPO measurements, a second series of TPO measurements was carried out for these samples; SOFC-B4 (0D), SOFC-2D-3, SOFC-4D-3, SOFC-6D-6, and SOFC-10D-4. Results from the second series of TPO measurements are presented in Figure 9.. Low/weak peaks of amorphous carbon were observed at 450 °C on all tested cells. On tested SOFC-6D-6 another low peak of carbon, possibly graphitic carbon, was observed at 820 °C. Considering the green TPO curve of SOFC 10D-2 in Figure 9.7 which represents a very small rate of carbon deposition, overall TPO results presented in Figures 9.7 and 9.8 show very low levels of carbon deposition observed during SOFC operation on biogas.

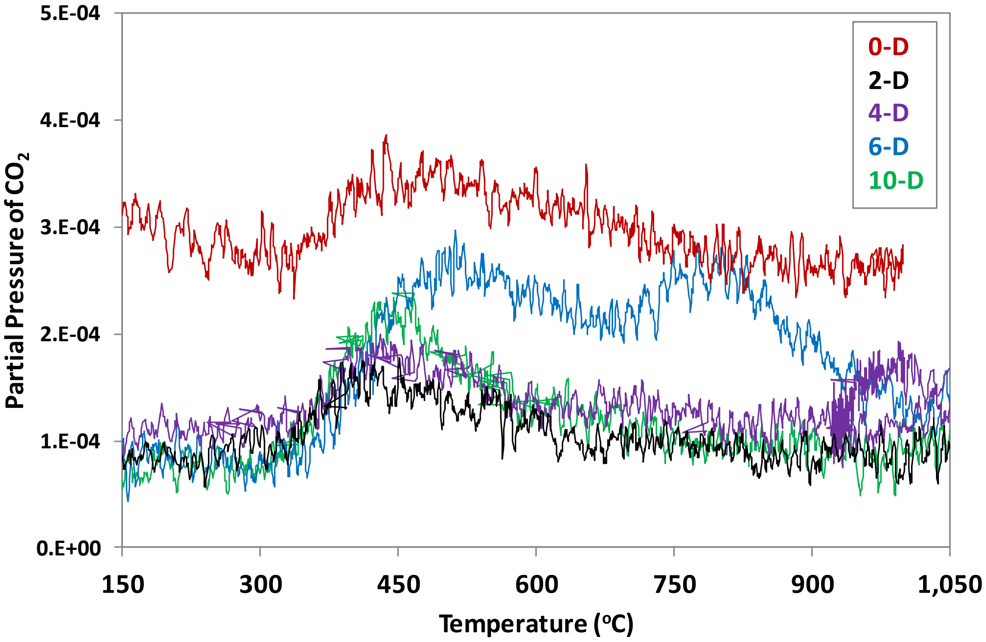

Figure 9.8: CO_2 peaks obtained from TPO of Sn-infiltrated SOFCs, second series

9.4 Discussion and conclusion

Despite being operated at the conditions where much carbon deposition is expected, visual observations and SEM images of the tested non-infiltrated and Sn-infiltrated SOFCs showed very low level of carbon deposition. These phenomena of low carbon deposition can be explained as follows;

- The non-infiltrated SOFCs have low activity towards biogas dry reforming. They showed very low conversion of CH_4 (1.3 % CH_4 conversion as listed in Table 21), hence the observed low carbon deposition
- The Sn-infiltrated SOFCs show good activity towards biogas dry reforming. They showed CH_4 conversion of 14.3 % (referring to Table 21). However the much higher CH_4 conversion observed on Sn-infiltrated SOFC anodes did not produce much carbon deposition. This may occur when the Sn-infiltrated SOFC anodes have the ability to oxidise the carbon formed with a higher rate than the

non-infiltrated anodes do. Similar to what was reported by Nikolla et al. [99] the ability of Sn infiltrated SOFC anodes to catalyse carbon oxidation combined with their ability to lower the rate of C-C bond formation forms the overall ability of Sn-infiltrated SOFC anodes in SOFC operation fuelled by biogas with low carbon deposition.

Nikolla et al. [96, 97, 99] carried out extensive studies on carbon surface chemistry related to reforming reactions and carbon deposition on Ni and Sn/Ni alloy. Figure 9. was adapted from Nikolla et al. [99] which shows their results of *"calculated maximum rates of C-H bond activation in methane, C-C bond formation, and C-O bond formation plotted as a function of temperature and for Ni and Sn/Ni surface alloy"*. It is observed that while C-H bond activation in methane is the rate limiting step for methane reforming both on Ni and Sn/Ni surfaces, the C-O bond formation (for carbon oxidation) is faster on Sn/Ni than that on Ni surface. In contrast, the C-C bond formation (for formation of carbon filaments or coke) is slower on Sn/Ni compared to that on Ni surface.

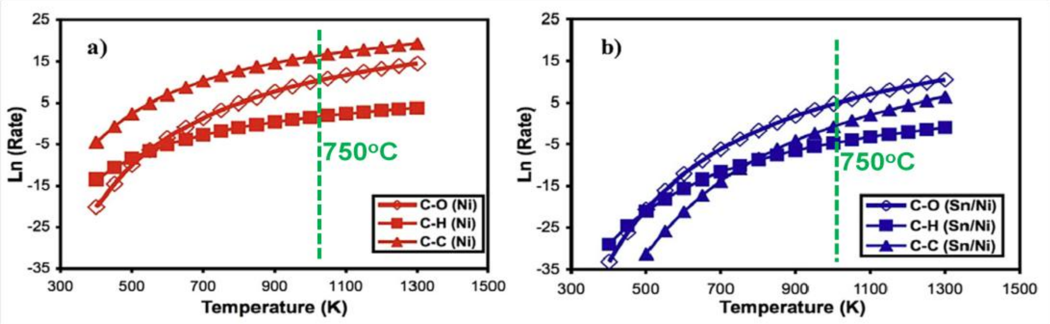

Figure 9.9: Results of DFT calculations of C-O, C-H, C-C bond formation rate on Ni and Sn/Ni surfaces [99]

Furthermore, they have also identified that the preferred sites for carbon formation on Ni surface is the step edge or the under coordinated site. According to Nikolla et al. [99]

“The Sn atoms increase the chemical potential of carbon at the under-coordinated sites and decrease the thermodynamic driving force for the carbon atoms to approach these sites. This mechanism by which Sn improves the tolerance of the catalyst to the carbon-induced deactivation is very similar to the mechanism proposed previously for Au and S additives [166]”.

A more recent review by Helveg et.al [140] on whisker carbon formation supported the argument, of *Sn atoms increasing the chemical potential of carbon at the under-coordinated (step edge) sites*, such as presented by Nikolla. They agreed that alloying (similar to what was carried out in this Sn-infiltration presented in this thesis) can be an alternative route for engineering the step site properties in relation to preventing carbon formation.

Chapter 10

Conclusions & Further work

10.1 Overview

This thesis presents results of a study to develop a technique for Sn-infiltration on NiYSZ based SOFC anodes, evaluate catalytic and electrochemical performance of the SOFCs in biogas dry reforming mode, and evaluate degradation and tendency to form carbon during electrochemical testing. Hundreds of experiments have been conducted in order to establish the Sn-infiltration method and the reliable testing procedure. Results have shown that Sn-infiltrated NiYSZ-based SOFC can be operated on simulated biogas with significantly higher electrochemical performance and low carbon deposition, given the anode is adequately modified

10.2 Summary of Conclusions

10.2.1 Establishing the electrochemical performance testing procedure

Important points to obtain reliable results of electrochemical performance are:

- ✓ To keep SOFC test set-up free of gas leakage. Gas tight sealing of the SOFC onto SOFC cell holder can be obtained from correctly applying dense silver paste using appropriate procedure.
- ✓ To keep consistent SOFC heat-up and H_2 introduction procedure to maintain stable and reproducible condition of NiYSZ microstructure for reliable electrochemical test results.

The SOFCs tested with Case B showed consistently higher performance with lower polarisation resistance compared to those tested with Case A. This indicates that for the tested SOFCs sufficient contact time for H_2 to adsorb onto nickel is needed to allow for effective electrochemical oxidation.

10.2.2 Sn- Anode infiltration

It was found that pipette drop method of Sn infiltration onto sintered anode surface is effective to obtain low Sn/Ni concentration. The infiltration used 10 % weight/volume $SnCl_2.2H_2O$ solution in 95 % ethanol. Repeated Sn infiltration using pipette drop method with 2-drops to 28-drops $SnCl_2$ solution resulted in 0.2 to 4.8 % wt Sn/Ni infiltrated onto SOFC anodes. The presence of Sn/Ni surface alloy on infiltrated NiYSZ anode was confirmed by gravimetry, XRF, SEM/EDX and XPS.

10.2.3 Electrochemical performance measurement with outlet gas monitoring

It was observed that electrochemical performance of non-infiltrated SOFCs dropped significantly on switching the fuel from H_2 to biogas. Measurements of SOFC outlet gas using mass spectrometry was useful to reveal that the low electrochemical performance was caused by the low ability of the non-infiltrated SOFCs to convert biogas to H_2 and CO which can then be electrochemically oxidised on the anode site. The mass spectra also showed that, in contrast to non-infiltrated SOFCs, at 750 ^oC and 1:2 CO_2 : CH_4 ratio, Sn infiltrated SOFCs show eleven times higher ability to convert biogas into H_2 and CO. Therefore higher electrochemical performance was obtained from Sn infiltrated SOFC. Despite the higher conversion of biogas obtained on Sn-infiltrated SOFCs, carbon was not significantly formed on Sn-infiltrated SOFCs.

Results of electrochemical impedance spectra (EIS) show that there are improvements on Ohmic and polarisation resistances obtained from adequately Sn-infiltrated SOFCs. These improvements were observed when the SOFCs were operated on H_2 as well as on biogas. Further study with more detailed evaluation of electrochemical performance involving EIS will be useful to reveal electrochemical phenomena more accurately and to uncover other roles that Sn-infiltration play than enhancing biogas reforming and reducing carbon formation.

In addition, predictions of the fuel cell performance (polarisation curves) using fuel cell model simulation derived from NASA Chemical Equilibrium Program (CEA2) were performed. The simulation helped predict fuel cell performances under different gas feed flow rates and compositions and therefore provided arguments for more grounded analysis of the actual fuel cell performance obtained from the experiments. Simulations to predict polarisation curves were performed for five conditions as follows; H_2 at low flow rate, H_2 at high flow rate, biogas at ideal condition, biogas at lower (1.3 %) and at higher (14.3 %) methane conversion. The polarisation curves obtained experimentally were compared with the corresponding simulation results which concluded that the experimental results are in good agreement with predicted results from the simulation.

10.2.4 Carbon deposition

Visual observations of the tested SOFCs and SEM image examinations did not show any carbon deposited during the 22 hours and 150 hours SOFC operations fuelled by biogas. Quantitative measurements of deposited carbon using Temperature Programmed Oxidation showed very low rates of 5.3×10^{-3} mg carbon g_{cat}^{-1} h^{-1} and 6.4×10^{-3} mg carbon g_{cat}^{-1} h^{-1} carbon deposition on a Sn-infiltrated and non-infiltrated SOFC tested for 150 hours respectively.

10.3 Main Points

1. Tin anode infiltration using simple pipette drop method was successfully performed on sintered NiYSZ anode surface, forming Sn/Ni surface alloy. The presence of Sn/Ni surface alloy, on the Sn-infiltrated SOFC anode was confirmed by inference and combining results obtained by gravimetry, XRF, SEM/EDX and XPS.
2. Results of measuring and comparing electrochemical performance of the non-infiltrated SOFCs versus a series of Sn-infiltrated SOFCs showed that, fuelled by biogas, the Sn-infiltrated SOFCs gave much higher electrochemical performance compared to non-infiltrated SOFCs did.
3. Non infiltrated SOFCs operating on biogas showed an average performance of 150 mA cm^{-2} current density at 0.70 Volt. The best performance was obtained on SOFC-B2 which gave 200 mA cm^{-2} current density at 0.70 Volt.
4. It was observed that the 4D Sn infiltrated SOFCs, corresponding to 0.38 % weight Sn/Ni gave the highest electrochemical performance on both H_2 and biogas, producing an average of 420 mA cm^2 current density at 0.70 Volt.
5. Mass spectra of the SOFCs outlet gas revealed that higher electrochemical performance obtained on Sn-infiltrated NiYSZ SOFCs was related to the higher conversion rates of dry reforming on Sn-infiltrated NiYSZ SOFCs (14.3%) compared to that on the non-infiltrated SOFCs (1.34%).
6. It is proposed that Sn-infiltration improved the catalytic activity of original NiYSZ SOFC anode for operation under dry reforming mode because Sn/Ni surface alloy '*is more efficient than Ni in the preferential formation of C-O rather than C-C*

bonds [99]. As a consequence, the carbon formed on Sn/Ni catalyst surface is rapidly oxidised to CO. The rapid oxidation of carbon shifts the methane cracking reaction to the right, producing more carbon and hydrogen, which increases the overall conversion of dry reforming reaction.

7. All of the SOFCs tested showed very low ohmic resistance of 80 mΩ cm^2 but varied values of polarisation resistance; with Sn-infiltrated SOFCs consistently showed lower polarisation resistances. These phenomena showed that Sn-infiltration enhances the catalytic activities of the NiYSZ anodes for dry reforming reactions.
8. Both the non-infiltrated and Sn-infiltrated SOFCs were able to operate stably for 22 hours and 150 hours in the simulated biogas with very low carbon deposition.
9. SEM images of all of the SOFC anodes tested for 22 hours on biogas showed no carbon filaments. TPO measurements of tested SOFCs showed very low carbon deposition. The highest quantity of carbon deposited on a non-infiltrated SOFC fuelled by biogas was 0.17 mg carbon cm^{-2} or 6.4×10^{-3} mg carbon g_{cat}^{-1} h^{-1} observed on SOFC-B1 operated for 150 hours. Despite being exposed to prolonged (20 hours) OCV, 10D Sn-infiltrated SOFC fuelled by biogas which was operated for 150 hours showed 0.14 mg carbon cm^{-2} or 5.3×10^{-3} mg carbon g_{cat}^{-1} h^{-1}.
10. With regard to the low carbon deposition obtained on Sn-infiltrated SOFC, it is proposed that Sn atoms displace the low coordinated (step edge) sites for nucleation and growth of whisker carbon [51, 73, 99, 140, 167].

10.4 Further work

Based on the results presented in this thesis, it is suggested that future work be performed on these areas:

1. Study the ability of SnNiYSZ in H_2, CH_4, CO and CO_2 adsorption and desorption; this will lead to more understanding of the roles played by SnNiYSZ in the catalytic activity and selectivity towards the main reactions taking place in SOFC anode.
2. Study electrochemical performance, including EIS, of Sn-infiltrated SOFCs at various operating conditions to provide sufficient data for analysis of sensitivity of fuel cell performance towards temperature, feed compositions and cathode gas conditions. This study will help reveal more detailed roles, both in chemical and electrochemical reaction steps, played by Sn-alloying of the SOFC anode.
3. Explore the ability of SnNiYSZ SOFC fuelled by direct biogas containing sulphur, chloride and other impurities to evaluate SnNiYSZ resistance against poisoning caused by those impurities.
4. Evaluate SnNiYSZ catalyst life using accelerated testing method such as redox, load and thermal cycling. Perform more extensive characterisation of SnNiYSZ alloy pre- and post-testing to obtain more detailed alloy properties (e.g. TEM, XPS, XRD, Mossbauer spectroscopy).
5. Explore Sn-infiltration on NiScSZ or Ni-anode combined with other electrolytes of intermediate temperature SOFC.
6. Explore the ability of SnNiYSZ SOFC fuelled by other hydrocarbon -based fuel
    a. higher hydrocarbons (propanes, butanes)
    b. biomass derived hydrocarbons (such as ethylene glycol, glycerol, sorbitol)

7. Develop mathematical model based on carefully designed experiments to obtain accurate kinetic parameters which can be used to assist in designing better performing biogas fuelled SOFCs.
8. Explore Ni/Sn catalysts infiltration on YSZ scaffold to achieve SOFCs with higher power density and more redox stable. [168]

References

1. Atanasiu, M., *The Status of SOFC R&D in the Fuel Cell and Hydrogen Joint Undertaking Program.* ECS Transaction, 2015. **68**(1): p. 3-14.

2. Kadowaki, M., *Current status of National SOFC Projects in Japan.* ECS Transaction, 2015. **68**(1): p. 15-22.

3. White, B.M., Lundberg, Wayne L., Pierre, Joseph F.,, *Accomplishments, Status, and Roadmap for the US Department of Energy's Fossil Energy SOFC Programme.* ECS Transactions, 2015. **68**(1): p. 23-28.

4. *Fuel Cell Hand Book 7th Edition.* EG & G Technical Srvices, , 2004.

5. Larminie, J., Dicks, A.,, *Fuel Cell Systems Explained.* John Wiley and Sons, 2003.

6. Singhal, S.C., K. Kendall,, *High Temperature Solid oxide Fuel Cells.* Elsevier,, 2003.

7. Fergus, J.W., Hui, R., Li, X., Wilkindon D.P., Zhang, J.,, *Solid Oxide Fuel Cells, Materials Properties and Performance.* CRC Press,, 2009.

8. Taufiq, B.N., Kikuchi, Y., Ishimoto, T., Honda, K., Koyama, M.,, *Sensitivity Analysis for the Efficiency Improvement of a Light Integrated GAsification Fuel Cell Power Plant.* ECS Transaction, 2015. **68**(1): p. 333-342.

9. Wachsman, E.D. and K.T. Lee, *Lowering the Temperature of Solid Oxide Fuel Cells.* Science, 2011. **334**(6058): p. 935-939.

10. Leah, R., et.al., *Low-cost, REDOX-stable, Low-temperature SOFC Developed by Ceres Power for Multiple Applications:Latest Development Update.* ECS Transaction, 2013. **57**(1): p. 461-470.

11. Leah, R.L., M.,, *Towards a fully redox-stable SOFC: Cell Development at Ceres Power.* ECS Transactions, 2013. **57**(1): p. 849-856.

12. Leah, R., Bone, A., Lankin, M., Selcuk, A., Rahman, M., Clare, A., Rees, L., Phillip, S., Mukerjee, S., Selby, M.,, *Ceres Power Steel Cell Technology: Rapid Progress Towards a Truly Commercially Viable SOFC.* ECS Transaction, 2015. **68**(1): p. 95-107.

13. Leah, R., Lankin, M., Bone, A., Mukerjee, S., Selby, M.,, *Kinetics of Internal Methane Reforming on the Anodes of Low Temperature Ceres Power Steel Cell SOFCs.* ECS Transactions, 2015. **68**(1): p. 1137-1149.

14. *Ceres Power Holdings - A change of power.* www.cerespower.com, 2015.

15. Foger, K., Payne, R.,, *Ceramic Fuel Cells BlueGen - Market Introduction Experience.* 11th European Fuel Cell Forum, 2014.

16. Wang, X., et al., *Thermodynamic analysis of glycerol dry reforming for hydrogen and synthesis gas production.* Fuel, 2009. **88**(11): p. 2148-2153.

17. Santarelli, M., *Harvesting energy from waste water treatment plant.* 2015.

18. Dudley, B., *BP Statistical Review of World Energy - June 2015.* 2015(64th Ed): p. 42.

19. Steinberger-Wilckens, R., *Sustainable and Renewable Energy Future.* 2015: p. 24.

20. Wachsman, E.D., C.A. Marlowe, and K.T. Lee, *Role of solid oxide fuel cells in a balanced energy strategy*. Energy & Environmental Science, 2012. **5**(2): p. 5498-5509.

21. Assabumrungrat, S., N. Laosiripojana, and P. Piroonlerkgul, *Determination of the boundary of carbon formation for dry reforming of methane in a solid oxide fuel cell.* Journal of Power Sources, 2006. **159**(2): p. 1274-1282.

22. Sangtongkitcharoen, W., et al., *Comparison of carbon formation boundary in different modes of solid oxide fuel cells fueled by methane.* Journal of Power Sources, 2005. **142**(1–2): p. 75-80.

23. *SOFC.* Fuel Cell Today, 2013. **www.fuelcelltoday.com/technologies/sofc**.

24. Brett, D.J.L., et al., *What Happens Inside a Fuel Cell? Developing an Experimental Functional Map of Fuel Cell Performance.* Chemphyschem, 2010. **11**(13): p. 2714-2731.

25. Wilson, J.R., et al., *Three-dimensional reconstruction of a solid-oxide fuel-cell anode.* Nature Materials, 2006. **5**(7): p. 541-544.

26. Bujalski, W., *Solid Oxide Fuel Cells.* Lecture Material, University of Birmingham, 2010.

27. Kendall, K., *Progress in Solid Oxide Fuel Cell Materials.* International Materials Review, 2005. **50**: p. 257-264.

28. McDonald, N.M., Watton, J., Dhir, A., Steinberger-Wilckens, R.,, *The Manufacture and Testing of Ni-10Sc1CeSZ Anode Supported SOFCs for Intermediate Temperature Operation.* European Fuel Cell Forum, 2014. **11th**: p. B0913.

29. Xia, C., *Electrolytes.* In Solid Oxide Fuel Cells Ed. Fergus. J. W., CRP Press, 2009.

30. Jiang, S.P., Jian Li,, *Cathodes.* In Solid Oxide Fuel Cells Ed. Fergus. J. W., CRP Press, 2009.

31. McEvoy, A., *Anodes.* In High Temperature Solid Oxide Fuel Cells Ed. Singhal, S. C., and Kevin Kendall, Elsevier,, 2003.

32. Zhao, F. and A.V. Virkar, *Dependence of polarization in anode-supported solid oxide fuel cells on various cell parameters.* Journal of Power Sources, 2005. **141**(1): p. 79-95.

33. Yang, Z., and Jeffrey W. Fergus, *Interconnects.* In Solid Oxide Fuel Cells Ed. Fergus, J. W., et al, CRC Press,, 2009.

34. Kendall, K., *Progress in Microtubular Solid Oxide Fuel Cells.* International Journal of Applied Ceramics, 2010. **7**(1): p. 1-9.

35. Dhir, A., *Improved Micro Tubular Solid Oxide Fuel Cells.* Ph D Thesis, University of Birmingham, 2009.

36. Pollet., B.G., *PEM Fuel Cells.* Lecture Material, University of Birmingham, 2010.

37. Bujalski, W., C.M. Dikwal, and K. Kendall, *Cycling of three solid oxide fuel cell types.* Journal of Power Sources, 2007. **171**(1): p. 96-100.

38. Dikwal, C.M., W. Bujalski, and K. Kendall, *Characterization of the electrochemical performance of micro-tubular SOFC in partial reduction and oxidation conditions.* Journal of Power Sources, 2008. **181**(2): p. 267-273.

39. Heneka, M.J. and E. Ivers-Tiffee, *Influence of High Current Cycling on the Performance of SOFC Single Cells.* Journal of Fuel Cell Science and Technology, 2012. **9**(1).

40. Waldbillig, D., A. Wood, and D.G. Ivey, *Electrochemical and microstructural characterization of the redox tolerance of solid oxide fuel cell anodes.* Journal of Power Sources, 2005. **145**(2): p. 206-215.

41. Waldbillig, D., A. Wood, and D.G. Ivey, *Thermal analysis of the cyclic reduction and oxidation behaviour of SOFC anodes.* Solid State Ionics, 2005. **176**(9-10): p. 847-859.

42. Monzon, H. and M.A. Laguna-Bercero, *Redox-cycling studies of anode-supported microtubular solid oxide fuel cells.* International Journal of Hydrogen Energy, 2012. **37**(8): p. 7262-7270.

43. Keyvanfar, P. and V. Birss, *Optimization of Infiltration Techniques Used to Construct Ni/YSZ Anodes.* Journal of the Electrochemical Society, 2014. **161**(5): p. F660-F667.

44. Gorte, R.J., J.M. Vohs, and S. McIntosh, *Recent developments on anodes for direct fuel utilization in SOFC.* Solid State Ionics, 2004. **175**(1–4): p. 1-6.

45. Baker, R.T.K., et al., *Nucleation and growth of carbon deposits from the nickel catalyzed decomposition of acetylene.* Journal of Catalysis, 1972. **26**(1): p. 51-62.

46. Bartholomew, C.H., *Mechanisms of catalyst deactivation.* Applied Catalysis A: General, 2001. **212**(1–2): p. 17-60.

47. Alstrup, I., et al., *Carbon formation on nickel and nickel-copper alloy catalysts.* Materials and Corrosion-Werkstoffe Und Korrosion, 1998. **49**(5): p. 367-372.

48. Rostrup-Nielsen, J. and D.L. Trimm, *Mechanisms of carbon formation on nickel-containing catalysts.* Journal of Catalysis, 1977. **48**(1–3): p. 155-165.

49. Trimm, D.L., *Catalyst design for reduced coking (review).* Applied Catalysis, 1983. **5**(3): p. 263-290.

50. Trimm, D.L., *Coke formation and minimisation during steam reforming reactions.* Catalysis Today, 1997. **37**(3): p. 233-238.

51. Trimm, D.L., *Catalysts for the control of coking during steam reforming.* Catalysis Today, 1999. **49**(1–3): p. 3-10.

52. Huber, G.W., J.W. Shabaker, and J.A. Dumesic, *Raney Ni-Sn catalyst for H-2 production from biomass-derived hydrocarbons.* Science, 2003. **300**(5628): p. 2075-2077.

53. Millward, G.R., et al., *The influence of oxide layers on the initiation of carbon deposition on stainless steel.* Oxidation of Metals, 2001. **56**(3-4): p. 231-250.

54. Guerra, C., et al., *Optimization of dry reforming of methane over Ni/YSZ anodes for solid oxide fuel cells.* Journal of Power Sources, 2014. **245**(0): p. 154-163.

55. Zhang, X., et al., *Conversion of methane to syngas in a solid oxide fuel cell with Ni–SDC anode and LSGM electrolyte.* Fuel, 2002. **81**(8): p. 989-996.

56. Habibzadeh, B., *Understanding CO oxidation in SOFC's using Nickel Patterned Anode.* PhD Thesis, University of Maryland, USA, 2007.

57. Yao, W., *Hydrogen and Carbon Monoxide Electrochemical Oxidation Reaction Kinetics on Solid Oxide Fuel Cell Anode.* PhD Thesis, University of Waterloo, Canada, 2013.

58. Santarelli, M., et al., *Direct reforming of biogas on Ni-based SOFC anodes: Modelling of heterogeneous reactions and validation with experiments.* Journal of Power Sources, 2013. **242**: p. 405-414.

59. Kee, R.J., *Solid Oxide Fuel Cells with hydrocarbon fuels.* Proceedings of The Combustion Instutite, 2005. **30**: p. 2379-2404.

60. Kendall, K., et al., *Effects of dilution on methane entering an SOFC anode.* Journal of Power Sources, 2002. **106**(1-2): p. 323-327.

61. Dhir, A. and K. Kendall, *Microtubular SOFC anode optimisation for direct use on methane.* Journal of Power Sources, 2008. **181**(2): p. 297-303.

62. Mallon, C. and K. Kendall, *Sensitivity of nickel cermet anodes to reduction conditions.* Journal of Power Sources, 2005. **145**(2): p. 154-160.

63. Baker, R.T.K., *Catalytic growth of carbon filaments.* Carbon, 1989. **27**(3): p. 315-323.

64. Rostrup-Nielsen, J.R., *Production of synthesis gas.* Catalysis Today, 1993. **18**(4): p. 305-324.

65. Khzouz, M., et al., *Characterization and activity test of commercial Ni/Al2O3, Cu/ZnO/Al2O3 and prepared Ni-Cu/Al2O3 catalysts for hydrogen production from methane and methanol fuels.* International Journal of Hydrogen Energy, 2013. **38**(3): p. 1664-1675.

66. Nagai, M., et al., *CO2 reforming of methane on Rh/Al2O3 catalyst.* Chemical Engineering Science, 2007. **62**(18-20): p. 4998-5000.

67. Millward, G.R., et al., *The influence of carbonyl sulphide on the inhibition of filamentary carbon deposition on stainless steel.* Materials and Corrosion-Werkstoffe Und Korrosion, 2003. **54**(11): p. 864-869.

68. Sasaki, K. and Y. Teraoka, *Equilibria in fuel cell gases - II. The C-H-O ternary diagrams.* Journal of the Electrochemical Society, 2003. **150**(7): p. A885-A888.

69. Girona, K., et al., *Carbon deposition in CH4/CO2 operated SOFC: Simulation and experimentation studies.* Journal of Power Sources, 2012. **210**: p. 381-391.

70. Eguchi, K., et al., *Fuel flexibility in power generation by solid oxide fuel cells.* Solid State Ionics, 2002. **152**: p. 411-416.

71. Farhad, S., F. Hamdullahpur, and Y. Yoo, *Performance evaluation of different configurations of biogas-fuelled SOFC micro-CHP systems for residential applications.* International Journal of Hydrogen Energy, 2010. **35**(8): p. 3758-3768.

72. Manenti, F., et al., *Biogas-fed solid oxide fuel cell (SOFC) coupled to tri-reforming process: Modelling and simulation.* International Journal of Hydrogen Energy, 2015. **40**(42): p. 14640-14650.

73. Nikolla, E., Schwank, J., Linic, S.,, *Direct Electrochemical Oxidation of Hydrocarbon Fuels on SOFCs: Improved Carbon Tolerance of Ni Alloy Anodes.* Journal of The Electrochemical Society, 2009. **156**(11): p. B1312-B1316.

74. Kan, H. and H. Lee, *Enhanced stability of Ni-Fe/GDC solid oxide fuel cell anodes for dry methane fuel.* Catalysis Communications, 2010. **12**(1): p. 36-39.

75. Li, K., et al., *Methane on-cell reforming in nickel-iron alloy supported solid oxide fuel cells.* Journal of Power Sources, 2015. **284**: p. 446-451.

76. Sasaki, K. and Y. Teraoka, *Equilibria in fuel cell gases - I. Equilibrium compositions and reforming conditions.* Journal of the Electrochemical Society, 2003. **150**(7): p. A878-A884.

77. Sasaki, K. and Y. Teraoka, *Equilibria in fuel cell gases.* Solid Oxide Fuel Cells Viii (Sofc Viii), 2003. **2003**(7): p. 1225-1239.

78. Tsai, T.I., Du, S., Dhir, A., Williams, A.A., Steinberger-Wilckens, R.,, *Modelling a Methane Fed Solid Oxide Fuel Cell with Anode Recirculation System.* ECS Transactions, 2013. **57**(1): p. 2831-2840.

79. Alzate-Restrepo, V. and J.M. Hill, *Effect of anodic polarization on carbon deposition on Ni/YSZ anodes exposed to methane.* Applied Catalysis A: General, 2008. **342**(1–2): p. 49-55.

80. Liu, J. and S.A. Barnett, *Operation of anode-supported solid oxide fuel cells on methane and natural gas.* Solid State Ionics, 2003. **158**(1–2): p. 11-16.

81. Lin, Y., et al., *Direct operation of solid oxide fuel cells with methane fuel.* Solid State Ionics, 2005. **176**(23-24): p. 1827-1835.

82. Li, W., et al., *Carbon deposition on patterned nickel/yttria stabilized zirconia electrodes for solid oxide fuel cell/solid oxide electrolysis cell modes.* Journal of Power Sources, 2015. **276**: p. 26-31.

83. Lin, Y., Z. Zhan, and S.A. Barnett, *Improving the stability of direct-methane solid oxide fuel cells using anode barrier layers.* Journal of Power Sources, 2006. **158**(2): p. 1313-1316.

84. Pillai, M., et al., *Stability and coking of direct-methane solid oxide fuel cells: Effect of CO2 and air additions.* Journal of Power Sources, 2010. **195**(1): p. 271-279.

85. Pillai, M.R., et al., *Fuel-flexible operation of a solid oxide fuel cell with Sr0.8La0.2TiO3 support.* Journal of Power Sources, 2008. **185**(2): p. 1086-1093.

86. Gorte, R.J. and J.M. Vohs, *Nanostructured anodes for solid oxide fuel cells.* Current Opinion in Colloid & Interface Science, 2009. **14**(4): p. 236-244.

87. Gorte, R.J. and J.M. Vohs, *Catalysis in Solid Oxide Fuel Cells.* Annual Review of Chemical and Biomolecular Engineering, Vol 2, 2011. **2**: p. 9-30.

88. An, W., et al., *Catalytic activity of bimetallic nickel alloys for solid-oxide fuel cell anode reactions from density-functional theory.* Journal of Power Sources, 2011. **196**(10): p. 4724-4728.

89. La Rosa, D., et al., *Mitigation of carbon deposits formation in intermediate temperature solid oxide fuel cells fed with dry methane by anode doping with barium.* Journal of Power Sources, 2009. **193**(1): p. 160-164.

90. Hibino, T., et al., *Ru-catalyzed anode materials for direct hydrocarbon SOFCs.* Electrochimica Acta, 2003. **48**(17): p. 2531-2537.

91. Modafferi, V., et al., *Propane reforming on Ni–Ru/GDC catalyst: H2 production for IT-SOFCs under SR and ATR conditions.* Applied Catalysis A: General, 2008. **334**(1–2): p. 1-9.

92. Ferrandon, M., A.J. Kropf, and T. Krause, *Bimetallic Ni-Rh catalysts with low amounts of Rh for the steam and autothermal reforming of n-butane for fuel cell applications.* Applied Catalysis A: General, 2010. **379**(1–2): p. 121-128.

93. Boaro, M., et al., *Comparison between Ni–Rh/gadolinia doped ceria catalysts in reforming of propane for anode implementations in intermediate solid oxide fuel cells.* Journal of Power Sources, 2010. **195**(2): p. 649-661.

94. Cassidy, M., Gamble, S., Irvine, J.T.S.,, *Application of exsolved structures as a route to more robust anodes for improved biogas utilisation in SOFCs.* ECS Transactions, 2015. **68**(1): p. 2029-2036.

95. Niakolas, D.K., et al., *Au-doped Ni/GDC as a new anode for SOFCs operating under rich CH4 internal steam reforming.* International Journal of Hydrogen Energy, 2010. **35**(15): p. 7898-7904.

96. Nikolla, E., et al., *Controlling Carbon Surface Chemistry by Alloying: Carbon Tolerant Reforming Catalyst.* Journal of the American Chemical Society, 2006. **128**(35): p. 11354-11355.

97. Nikolla, E., J. Schwank, and S. Linic, *Promotion of the long-term stability of reforming Ni catalysts by surface alloying.* Journal of Catalysis, 2007. **250**(1): p. 85-93.

98. Nikolla, E., J.W. Schwank, and S. Linic, *Hydrocarbon steam reforming on Ni alloys at solid oxide fuel cell operating conditions.* Catalysis Today, 2008. **136**(3-4): p. 243-248.

99. Nikolla, E., J. Schwank, and S. Linic, *Comparative study of the kinetics of methane steam reforming on supported Ni and Sn/Ni alloy catalysts: The impact of the formation of Ni alloy on chemistry.* Journal of Catalysis, 2009. **263**(2): p. 220-227.

100. Kan, H., et al., *Improved solid oxide fuel cell anodes for the direct utilization of methane using Sn-doped Ni/YSZ catalysts.* Catalysis Communications, 2009. **11**(3): p. 180-183.

101. Kan, H. and H. Lee, *Sn-doped Ni/YSZ anode catalysts with enhanced carbon deposition resistance for an intermediate temperature SOFC.* Applied Catalysis B-Environmental, 2010. **97**(1-2): p. 108-114.

102. Singh, A. and J.M. Hill, *Carbon tolerance, electrochemical performance and stability of solid oxide fuel cells with Ni/yttria stabilized zirconia anodes impregnated with Sn and operated with methane.* Journal of Power Sources, 2012. **214**: p. 185-194.

103. Bogolowski, N., ; Drillet, Jean-Francois.,, *Development of a coking-resitant NiSn anode for direct methane SOFC.* European Fuel Cell Forum, 2014. **11th**: p. B0501.

104. Wu, H.J., et al., *Ni-Based Catalysts for Low Temperature Methane Steam Reforming: Recent Results on Ni-Au and Comparison with Other Bi-Metallic Systems.* Catalysts, 2013. **3**(2): p. 563-583.

105. Kim, Y., et al., *In Situ Analyses of Carbon Dissolution into Ni-YSZ Anode Materials.* Journal of Physical Chemistry C, 2012. **116**(24): p. 13281-13288.

106. Millichamp, J., et al., *A study of carbon deposition on solid oxide fuel cell anodes using electrochemical impedance spectroscopy in combination with a high temperature crystal microbalance.* Journal of Power Sources, 2013. **235**: p. 14-19.

107. Maher, R.C., et al., *In-operando Raman Characterization of Carbon Deposition on SOFC Anodes*, in *Solid Oxide Fuel Cells 13*, T. Kawada and S.C. Singhal, Editors. 2013, Electrochemical Soc Inc: Pennington. p. 1619-1626.

108. Brightman, E., et al., *Designing a miniaturised heated stage for in situ optical measurements of solid oxide fuel cell electrode surfaces, and probing the oxidation of solid oxide fuel cell anodes using in situ Raman spectroscopy.* Review of Scientific Instruments, 2012. **83**(5): p. 7.

109. Kuhn, J. and O. Kesler, *Method for in situ carbon deposition measurement for solid oxide fuel cells.* Journal of Power Sources, 2014. **246**(0): p. 430-437.

110. Staniforth, J. and K. Kendall, *Biogas powering a small tubular solid oxide fuel cell.* Journal of Power Sources, 1998. **71**(1-2): p. 275-277.

111. Staniforth, J. and K. Kendall, *Cannock landfill gas powering a small tubular solid oxide fuel cell - a case study.* Journal of Power Sources, 2000. **86**(1-2): p. 401-403.

112. Stagg, S.M., et al., *Effect of Promotion with Sn on Supported Pt Catalysts for CO_2 Reforming of CH_4.* Journal of Catalysis, 1998. **178**(1): p. 137-145.

113. Fakeeha, A.H., Alfatish, A.S., Soliman , M.A. , Ibrahim A.A.,, *Effect of changing* CH_4/CO_2 *ratio on* H_2 *production by dry reforning reaction.* World Hydrogen Energy Conference, 2006. **16**.

114. Xu, J., et al., *Biogas reforming for hydrogen production over nickel and cobalt bimetallic catalysts.* International Journal of Hydrogen Energy, 2009. **34**(16): p. 6646-6654.

115. Alves, H.J., et al., *Overview of hydrogen production technologies from biogas and the applications in fuel cells.* International Journal of Hydrogen Energy, 2013. **38**(13): p. 5215-5225.

116. Akpan, E., et al., *Kinetics, experimental and reactor modeling studies of the carbon dioxide reforming of methane (CDRM) over a new – catalyst in a packed bed tubular reactor.* Chemical Engineering Science, 2007. **62**(15): p. 4012-4024.

117. Nikoo, M.K. and N.A.S. Amin, *Thermodynamic analysis of carbon dioxide reforming of methane in view of solid carbon formation.* Fuel Processing Technology, 2011. **92**(3): p. 678-691.

118. Staniforth, J. and R.M. Ormerod, *Implications for using biogas as a fuel source for solid oxide fuel cells: internal dry reforming in a small tubular solid oxide fuel cell.* Catalysis Letters, 2002. **81**(1-2): p. 19-23.

119. Shiratori, Y., T. Oshima, and K. Sasaki, *Feasibility of direct-biogas SOFC.* International Journal of Hydrogen Energy, 2008. **33**(21): p. 6316-6321.

120. Shiratori, Y. and K. Sasaki, *NiO-ScSZ and Ni(0.9)Mg(0.1)O-ScSZ-based anodes under internal dry reforming of simulated biogas mixtures.* Journal of Power Sources, 2008. **180**(2): p. 738-741.

121. Shiratori, Y., et al., *Internal reforming SOFC running on biogas.* International Journal of Hydrogen Energy, 2010. **35**(15): p. 7905-7912.

122. Yentekakis, I.V., T. Papadam, and G. Goula, *Electricity production from wastewater treatment via a novel biogas-SOFC aided process.* Solid State Ionics, 2008. **179**(27-32): p. 1521-1525.

123. Papadam, T., G. Goula, and I.V. Yentekakis, *Long-term operation stability tests of intermediate and high temperature Ni-based anodes' SOFCs directly fueled with simulated biogas mixtures.* International Journal of Hydrogen Energy, 2012. **37**(21): p. 16680-16685.

124. Xu, C., et al., *Tolerance tests of H2S-laden biogas fuel on solid oxide fuel cells.* Journal of Power Sources, 2010. **195**(15): p. 4583-4592.

125. Takahashi, Y., et al., *Thermo-mechanical reliability and catalytic activity of Ni-Zirconia anode supports in internal reforming SOFC running on biogas.* Solid State Ionics, 2012. **225**: p. 113-117.

126. Leonide, A., A. Weber, and E. Ivers-Tiffee, *Electrochemical Analysis of Biogas Fueled Anode Supported SOFC.* Solid Oxide Fuel Cells 12 (Sofc Xii), 2011. **35**(1): p. 2961-2968.

127. Lanzini, A. and P. Leone, *Experimental investigation of direct internal reforming of biogas in solid oxide fuel cells.* International Journal of Hydrogen Energy, 2010. **35**(6): p. 2463-2476.

128. Lanzini, A., Leone, P., Pieroni, M., Santarelli, M., Beretta, D., Ginocchio, S.,, *Experimental Investigations and Modelling of Direct Internal Reforming of Biogases in Tubular Solid Oxide Fuel Cells.* Fuel Cells, 2011. **11**: p. 697-710.

129. Lanzini, A., et al., *Durability of anode supported Solid Oxides Fuel Cells (SOFC) under direct dry-reforming of methane.* Chemical Engineering Journal, 2013. **220**(0): p. 254-263.

130. Guerra, C., et al., *Experimental study of dry reforming of biogas in a tubular anode-supported solid oxide fuel cell.* International Journal of Hydrogen Energy, 2013. **38**(25): p. 10559-10566.

131. Ma, J.J., et al., *Highly efficient, coking-resistant SOFCs for energy conversion using biogas fuels.* Journal of Materials Chemistry A, 2015. **3**(37): p. 19068-19076.

132. Van herle, J., Y. Membrez, and O. Bucheli, *Biogas as a fuel source for SOFC co-generators.* Journal of Power Sources, 2004. **127**(1-2): p. 300-312.

133. Van herle, J., et al., *Process flow model of solid oxide fuel cell system supplied with sewage biogas.* Journal of Power Sources, 2004. **131**(1-2): p. 127-141.

134. Elizalde-Blancas, F., et al., *Numerical modeling of SOFCs operating on biogas from biodigesters.* International Journal of Hydrogen Energy, 2013. **38**(1): p. 377-384.

135. Wongchanapai, S., et al., *Performance evaluation of a direct-biogas solid oxide fuel cell-micro gas turbine (SOFC-MGT) hybrid combined heat and power (CHP) system.* Journal of Power Sources, 2013. **223**(0): p. 9-17.

136. Siefert, N.S. and S. Litster, *Exergy & economic analysis of biogas fueled solid oxide fuel cell systems.* Journal of Power Sources, 2014. **272**(0): p. 386-397.

137. Trendewicz, A.A. and R.J. Braun, *Techno-economic analysis of solid oxide fuel cell-based combined heat and power systems for biogas utilization at wastewater treatment facilities.* Journal of Power Sources, 2013. **233**(0): p. 380-393.

138. Ni, M., *Modeling and parametric simulations of solid oxide fuel cells with methane carbon dioxide reforming.* Energy Conversion and Management, 2013. **70**(0): p. 116-129.

139. Nikolla, E., J. Schwank, and S. Linic, *Measuring and Relating the Electronic Structures of Nonmodel Supported Catalytic Materials to Their Performance.* Journal of the American Chemical Society, 2009. **131**(7): p. 2747-2754.

140. Helveg, S., J. Sehested, and J.R. Rostrup-Nielsen, *Whisker carbon in perspective.* Catalysis Today, 2011. **178**(1): p. 42-46.

141. Liu, Y., Y. Bai, and J. Liu, *(Ni0.75Fe0.25–xMgO)/YSZ anode for direct methane solid-oxide fuel cells.* Journal of Power Sources, 2011. **196**(23): p. 9965-9969.

142. Sutthisripok, W., N. Laosiripojana, and L. Sikong, *Effect of Specific Surface Area and Zr Doping Content on Oxygen Storage Capacity (OSC) and Methane Steam Reforming Reactivity of CeO(2)-ZrO(2).* Solid Oxide Fuel Cells 10 (Sofc-X), Pts 1 and 2, 2007. **7**(1): p. 1769-1777.

143. Nandini, A., K.K. Pant, and S.C. Dhingra, *Kinetic study of the catalytic carbon dioxide reforming of methane to synthesis gas over Ni-K/CeO2-Al2O3 catalyst.* Applied Catalysis A: General, 2006. **308**(0): p. 119-127.

144. Liang, B., et al., *Performance of Ni–Fe/gadolinium-doped CeO2 anode supported tubular solid oxide fuel cells using steam reforming of methane.* Journal of Power Sources, 2012. **202**(0): p. 225-229.

145. Zhang, Y., *Fuel Cell and Energy Technology Division, Ningbo Institute of Materials Technology and Engineering - NIMTE China.* Www.sofc.com.cn, 2014.

146. Troskialina, L., Kendall, K., Dhir, A., Bujalski, W.,,, *Effects of anode reduction methods on flexural strength of mSOFCs.* Book of Abstract for the 8th Annual International Conference - Smart Hydrogen and Fuel Cell Power - NEC - Birmingham UK, 2012(8th): p. 42.

147. Li, T.S., et al., *Effect of reduction temperature on the electrochemical properties of a Ni/YSZ anode-supported solid oxide fuel cell.* Journal of Alloys and Compounds, 2010. **495**(1): p. 138-143.

148. Monzon, H., Laguna-Bercero, M.A.,,, *The Influence of Reduction Conditions on a Ni-YSZ SOFC Anode Microstructure and Evolution.* ECS Transactions, 2015. **68**(1): p. 1229-1235.

149. Simonsen, S.B., Agersted, K., Hansen, K.V., Jacobsen, T., Wagner, J.B., Hansen, T.W., Theil Kuhn, L.,,, *NiO/YSZ Reduction for SOFC/SOEC studied in situ by Environmental Transmission Electron Microscopy.* ECS Transaction, 2014. **64**(2): p. 73-80.

150. L’vov, B. and A. Galwey, *The mechanism and kinetics of NiO reduction by hydrogen.* Journal of Thermal Analysis and Calorimetry, 2012. **110**(2): p. 601-610.

151. Svoboda, K., et al., *Thermodynamic possibilities and constraints of pure hydrogen production by a chromium, nickel, and manganese-based chemical looping process at lower temperatures.* Chemical Papers, 2007. **61**(2): p. 110-120.

152. Tsai, T.I., *Carbon Formation in Solid Oxide Fuel Cells During Internal Reforming and Anode Off-Gas Recirculation.* PhD Thesis - School of Chemical Engineering - University of Birmingham, 2015.

153. You, H.X., et al., *The conversion among reactions at Ni-based anodes in solid oxide fuel cells with low concentrations of dry methane.* Journal of Power Sources, 2011. **196**(5): p. 2779-2784.

154. Huang, K., *Fuel utilization and fuel sensitivity of solid oxide fuel cells.* Journal of Power Sources, 2011. **196**(5): p. 2763-2767.

155. Nakajima, H., T. Kitahara, and T. Konomi, *Electrochemical Impedance Spectroscopy Analysis of an Anode-Supported Microtubular Solid Oxide Fuel Cell.* Journal of the Electrochemical Society, 2010. **157**(11): p. B1686-B1692.

156. Leonide, A., et al., *Evaluation and modeling of the cell resistance in anode-supported solid oxide fuel cells.* Journal of the Electrochemical Society, 2008. **155**(1): p. B36-B41.

157. Schmetterer, C., et al., *A new investigation of the system Ni–Sn.* Intermetallics, 2007. **15**(7): p. 869-884.

158. Vassilev, G.P., Lilova, K.I., Gachon, J.C.,, *Enthalpies of formation of Ni-Sn compounds.* Thermochimica Acta, 2006. **447**: p. 106-108.

159. Moller, P., Rasmussen, J.B., Kohler, S., Nielsen, L.P., , *Electroplated Tin-Nickel Coatings as a Replacement for Nickel to eliminate Nickel Dermatitis.* NASF Surface Technology White Papers, 2013. **78**(3).

160. Rudnik, E., *The influence of sulfate ions on the electrodeposition of Ni-Sn alloys from acidic chloride-gluconate baths.* Journal of Electroanalytical Chemistry, 2014. **726**: p. 97-106.

161. Rudnik, E., G. Wloch, and A. Czernecka, *The Influence of Potential-Current Conditions on the Electrodeposition of Ni-Sn Alloys from Acidic Chloride-Sulphate Solution.* Archives of Metallurgy and Materials, 2014. **59**(1): p. 195-198.

162. Polat, B.D., et al., *Use of Multilayered Ni-Sn and Ni-Sn-C Thin Film Anodes for Lithium-Ion Batteries.* Electrochimica Acta, 2014. **135**: p. 585-593.

163. Mukaibo, H., T. Momma, and T. Osaka, *Changes of electro-deposited Sn–Ni alloy thin film for lithium ion battery anodes during charge discharge cycling.* Journal of Power Sources, 2005. **146**(1–2): p. 457-463.

164. Tongsri, R., Tosangthum, N.,, *Solid state transformation of non-equilibrium Ni-Sn powder with eutectic composition.* Songklanakarin Journal of Science and Technology, 2011. **33**(2): p. 209-2014.

165. Koh, J.H., et al., *Carbon deposition and cell performance of Ni-YSZ anode support SOFC with methane fuel.* Solid State Ionics, 2002. **149**(3-4): p. 157-166.

166. Bengaard, H.S., et al., *Steam Reforming and Graphite Formation on Ni Catalysts.* Journal of Catalysis, 2002. **209**(2): p. 365-384.

167. Abild-Pedersen, F., et al., *Mechanisms for catalytic carbon nanofiber growth studied by ab initio density functional theory calculations.* Physical Review B, 2006. **73**(11).

168. Jiang, S.P., *Nanoscale and nano-structured electrodes of solid oxide fuel cells by infiltration: Advances and challenges.* International Journal of Hydrogen Energy, 2012. **37**(1): p. 449-470.